Investigations of Improved Heat Transfer Instrumentation for Cooled Turbine Stages

Inés Usandizaga Forés
University College, Oxford



Thesis submitted in fulfilment of the requirements for the degree of Doctor of Philosophy at the University of Oxford

Hilary Term 2016

Investigations of Improved Heat Transfer Instrumentation for Cooled Turbine Stages

Inés Usandizaga Forés, University College, Oxford

Thesis submitted in fulfilment of the requirements for the degree of
Doctor of Philosophy at the University of Oxford
Hilary Term 2016

Abstract

This thesis describes the development of heated double-sided thin film gauge configurations for transient heat transfer measurements. By heating the substrate it is possible to measure the heat flux over a range of wall temperatures, which improves the resulting regression and leads to a more accurate determination of the adiabatic wall temperature and the heat transfer coefficient. The heated gauges can be used to measure the heat transfer of a film-cooled high-pressure turbine stage with engine-realistic combustor exit flows (hot-streaks and swirl) in order to study turbine aero-thermal performance in the presence of cooling flows. This thesis also presents the aerodynamic and heat transfer design as well as the mechanical assessment of the first fully cooled turbine stage for the Oxford Turbine Research Facility (OTRF). The high-pressure turbine stage is designed for lean-burn combustor interaction effects and has engine-state external cooling features.

Platinum thin film resistive gauges are the most advanced instrumentation for transient heat transfer measurement where high frequency response is required. Double-sided thin film gauges, consisting of two thin film temperature gauges mounted on either side of an insulating layer, have the advantage that the driving temperature difference is directly determined at the point of interest. A new gauge design is presented, which combines double-sided thin film gauges with the possibility to heat the substrate layer. Two arrangements of heated gauges have been developed, namely double-sided gauges with an underside thin film heater and self-heating double-sided gauges. These gauges yield an improved regression without the need for complex heating systems. The lateral conduction effects have been investigated using analytical models. The performance of different gauge types is quantified based on the quality of the regression. The heated gauge arrangements have been tested in the OTRF under engine-representative conditions on uncooled and cooled MT1 high-pressure nozzle guide vanes. Measurement strategies have been implemented to obtain the time-dependent temperature trace over a range of heating powers and calculate the convective heat transfer. This improved measurement technique allows for an accurate determination of non-dimensional parameters such as the Nusselt number and the film cooling effectiveness.

Three basic abilities are the foundation of craftsmanship. These are the ability to localize, to question, and to open up. The first involves making a matter concrete, the second reflecting on its qualities, the third expanding its sense.

(Richard Sennett, The Craftsman)

Contents

Acknowledgements vii

Nomenclature viii

1 Introduction 1

1.1 Research background 3

1.2 Project overview 5

1.3 Thesis outline 7

2 Review of Transient Facilities and Heat Transfer Measurements 9

2.1 Transient annular turbine test facilities 9

2.2 Heat transfer measurements in transonic high-pressure turbine stages 11

2.2.1 Thin film gauge history and theory 12

2.2.2 Thin film gauge applications and limitations 13

2.3 The Oxford Turbine Research Facility 20

2.3.1 Historical overview 21

2.3.2 LEMCOTEC and SILOET upgrades 23

3 Design of a Cooled High-Pressure Turbine Stage 24

3.1 Design of the SILOET cooled turbine stage 24

3.1.1 Aerodynamic design 24

3.1.2 Scaling from engine conditions 28

3.2 Cooling configuration . . . 30
3.2.1 High-pressure nozzle guide vane . . . 32
3.2.2 High-pressure rotor blade . . . 35
3.3 Stress analysis of the stator without main flow . . . 37
3.4 Mechanical assessment of the rotor blade . . . 41
3.4.1 Modelling of the steady-state stresses . . . 42
3.4.2 Vibrational analysis . . . 55
3.5 Summary turbine design . . . 60

4 Development of Double-Sided Thin Film Gauges for Heat Transfer Measurement 61

4.1 Heat transfer measurements . . . 61
4.1.1 Measuring procedure . . . 63
4.1.2 Measuring a film-cooled turbine stage . . . 64
4.2 Theoretical considerations . . . 65
4.2.1 One-dimensional heat conduction equation . . . 66
4.2.2 Lateral conduction effects of heated gauges . . . 68
4.3 Modelling of the thermal pulse through a multi-layer system . . . 70
4.3.1 Step temperature change and validation . . . 71
4.3.2 Realistic inlet conditions . . . 74
4.4 Analysis of different gauge configurations . . . 82
4.5 Summary . . . 85

5 Modelling and Testing of Double-Sided Thin Film Gauges 86

5.1 Thin film gauge design and manufacture . . . 86
5.2 Heating of double-sided thin film gauges . . . 89
5.2.1 Thin film heater element . . . 89
5.2.2 Self-heating gauges . . . 90
5.3 Calibration of the temperature coefficient of resistance . . . 92
5.4 Data analysis . . . 95
5.4.1 Measurement strategy for thin film gauges with or without underside heater 95

5.4.2 Measurement strategy for self-heating thin film gauges 96
5.4.3 Use of HTA3 amplifier and modification for higher currents 98
5.4.4 Impulse response processing of transient heat transfer signals 100
5.4.5 Regression of heat flux over wall temperature 105
5.5 Gauge preheating and problem of determining initial temperature 106
5.5.1 Thin film heater element 106
5.5.2 Self-heating gauges 111
5.6 Experimental uncertainties 115
5.7 Summary 122

6 Casing Tests and Model Validation 123

6.1 Single-sided thin film gauges 129
6.2 Double-sided thin film gauges 133
6.3 Double-sided thin film gauges with an underside thin film heater 137
6.4 Double-sided thin film gauges with variable heating current 143
6.4.1 Calculating the top gauge temperature 144
6.4.2 Results 145
6.5 Comparison of thin film gauge configurations 152
6.6 Texstan modelling 154
6.7 Summary casing tests 156

7 Heat Transfer Measurements on Uncooled and Cooled Aerofoils 157

7.1 Test conditions 158
7.2 Cooling configuration and coolant delivery 159
7.3 Instrumentation 164
7.3.1 Tunnel and stage monitoring 164
7.3.2 Coolant supply conditions 166
7.3.3 Data acquisition 168
7.4 Uncooled results 169
7.4.1 Single-sided thin film gauges 170

7.4.2 Double-sided thin film gauges 173
7.4.3 Double-sided thin film gauges with an underside thin film heater 178
7.4.4 Double-sided thin film gauges with variable heating current 192
7.5 Cooled results 201
7.5.1 Double-sided thin film gauges with an underside thin film heater 202
7.5.2 Double-sided thin film gauges with variable heating current 212
7.6 Summary aerofoil measurements 218

8 Conclusions **220**

8.1 Summary 220
8.2 Outlook 223

Appendices **225**

A.1 HTA3 Heat Transfer Amplifier 225
A.2 Issues with the reference voltage measurement 227

Bibliography **230**

Acknowledgements

Above all, I would like to thank my supervisor, Thomas Povey, for giving me the opportunity to work on such an exciting project. Thank you for shaping my research skills and for training my critical eye. Paul Beard has been an enormous support during my time at the Osney Lab and I have very much enjoyed our collaboration. I would like to give special thanks to Kam Chana for sharing his vast experience on the OTRF with me.

I am grateful for the guidance from Martin Oldfield on the use of the HTA3. The thin film gauges were designed with the invaluable help of Matthew Collins. Many thanks to Trevor Godfrey for the laborious manufacture and for instructing me in the instrumentation process. The input from Paul Pattinson at the Physics Department is also duly acknowledged. Many thanks to the workshop for their help with all major and minor tasks.

I am indebted to David Cardwell and Sunny Chana for conducting the experiments in the OTRF and for turning the most unnerving part of the thesis into a thoroughly enjoyable experience. I thank my contemporary fellows at the OTRF, Martin Johansson and Benjamin Hall, for answering my numerous questions. Thanks also to Benjamin Kirollos for showing me how to use the IR camera.

For proofreading this thesis I thank Paul Beard and Felix Kahlhoefer, who also helped with various layout problems. I gratefully acknowledge admin support from Kathryn Scott.

Irene Cresci and Holt Wong deserve special thanks for their support in the final stages of this thesis and for being the "bestest" housemates. I would also like to express my gratitude to the Women in Engineering Network, in particular Priyanka Dhopade and Niharika Gurram, for being a group of wonderfully supportive women.

The research on the OTRF was funded by Rolls-Royce. Alexander Matthews and Cuneyt Kenger deserve special acknowledgement for their help with the design of the turbine stage. This thesis has been supported by an Amelia Earhart Fellowship. I am indebted to the Zontians for their generosity and inspiration.

Finally, I would like to thank my parents for backing me and always encouraging me – they are my foundation. I thank Felix Kahlhoefer for supporting me throughout this project. With you by my side, I feel I can achieve anything.

Nomenclature

Latin (uppercase)

Symbol	Unit/value	Definition
A	m^2	Area
C_d	–	Discharge coefficient
E	$\mathrm{N\,m^{-2}}$	Young's modulus
G	$\mathrm{N\,m^{-2}}$	Modulus of rigidity
I	A	Current
K_t	–	Notch factor
K_f	–	Fatigue notch factor
L	m	Characteristic length
N	–	Cycles to failure
R	Ω	Resistance
R	$287\,\mathrm{J\,kg^{-1}\,K^{-1}}$	Specific gas constant
S	–	Stability criterion
S_f	$\mathrm{N\,m^{-2}}$	Fatigue strength
T	K	Temperature
V	V	Voltage
W	J	Work

Latin (lowercase)

a	m	Thickness
c	$\mathrm{J\,kg^{-1}\,K^{-1}}$	Specific heat capacity
d	m	Diameter (or width)
f	Hz	Frequency

Symbol	Unit/value	Definition
g	$9.81\,\mathrm{m\,s^{-2}}$	Acceleration of gravity
h	$\mathrm{W\,m^{-2}\,K^{-1}}$	Heat transfer coefficient
k	$\mathrm{W\,m^{-1}\,K^{-1}}$	Thermal conductivity
l	m	Length
$\dot{m}$	$\mathrm{kg\,s^{-1}}$	Mass flow rate
n	rpm	Rotational speed
p	Pa/bar	Pressure
p	m	Pitch
$\dot{q}$	$\mathrm{W\,m^{-2}}$	Heat flux
r	–	Recovery factor
t	s	Time
u	$\mathrm{m\,s^{-1}}$	Velocity
x	m	Depth (or thickness)

Greek

α	$\mathrm{K^{-1}}$	Temperature coefficient of resistance
α	$\mathrm{m^2\,s^{-1}}$	Thermal diffusivity
β	$\mathrm{K^{-1}}$	Coefficient of volume thermal expansion
Γ	$\mathrm{kg\,K^{1/2}\,s^{-1}\,Pa^{-1}}$	Capacity
γ	–	Ratio of specific heats
η	–	Thermal efficiency
η_f	–	Film cooling effectiveness
λ	–	Non-dimensional film decay rate
μ	$\mathrm{kg\,m^{-1}\,s^{-1}}$	Dynamic viscosity
μ_JT	$\mathrm{K\,Pa^{-1}}$	Joule-Thompson coefficient
ν	$\mathrm{m^2\,s^{-1}}$	Kinematic viscosity
ρ	$\mathrm{kg\,m^{-3}}$	Density
σ	Pa	Stress
σ	$5.67\,\mathrm{W\,m^{-2}\,K^{-4}}$	Stefan-Boltzmann constant
σ_x	Same as x	Uncertainty of x

Dimensionless numbers

Gr	Grashof number
M	Mach number
Nu	Nusselt number
Pr	Prandtl number
Re	Reynolds number
St	Stanton number

Subscripts

ad	adiabatic
aw	adiabatic wall
c	coolant
cal	calibration
conv	convective
exp	experimental
g	gauge
h	hot gas
H	heater
i	initial
inj	injection
iso	isothermal
n	nominal
r	recovery
s	surface
w	wall
x	local
y	yield
0	total (also reference measurement)
1	inlet
3	exit
∞	freestream

Abbreviations

AC	Alternating current
BFPR	Blade feed pressure ratio
BR	Blowing ratio
DC	Direct current
DR	Density ratio
EO	Engine order
FE(A)	Finite element (analysis)
FFT	Fast Fourier transform
HP	High-pressure
HTA	Heat transfer amplifier
HTC	Heat transfer coefficient
IR	Infra-red
LEMCOTEC	Low Emissions Core-Engine Technologies
MFR	Momentum flux ratio
MTO	Maximum Take-Off
NGV	Nozzle guide vane
OTRF	Oxford Turbine Research Facility
PR	Pressure ratio
PS	Pressure side
RAE	Royal Aircraft Establishment
RR	Rolls-Royce
SFC	Specific fuel consumption
SS	Suction side
SILOET	Strategic Investment in Low-Carbon Engine Technology
TATEF	Turbine Aero-Thermal External Flows
TE	Trailing edge
TET	Turbine entry temperature
(H)(DS)TFG	(Heated) (double-sided) thin film gauge
UTS	Ultimate tensile strength

CHAPTER 1

Introduction

The efficient conversion of the chemical energy stored in fossil fuels into mechanical and electrical energy is at the heart of meeting an ever-increasing demand in energy and mobility. Gas turbines, used both to create thrust and to generate electrical power, play a leading role in this field. Their high power density makes them particularly important for aircraft propulsion. Thus, there is a great interest in further increasing their efficiency and specific work output.

The overall efficiency can be improved either by increasing the efficiency of the individual components of a gas turbine or by increasing the thermal efficiency. While the former approach aims to reduce the losses in each step of the thermodynamical cycle, the second approach aims to improve the thermodynamical cycle as a whole in order to increase the achievable efficiency. The key factors for improving the thermal efficiency are the pressure ratio and the turbine entry temperature.

Over the past fifty years, advances in the blade materials and, more importantly, of the cooling technologies have led to an increase in gas temperatures. Nowadays, turbine entry temperatures exceeding 1800 K can be achieved. These temperatures are significantly above the melting point of the blade material and complex cooling systems are needed to manage blade metal temperatures. As a result, the thermal efficiency is currently limited by cooling flow requirements and improved cooling systems may translate into significant performance increases.

The aim of this thesis is to contribute to the study of turbine aero-thermal performance in the presence of cooling flows and in particular the effects of film cooling on heat transfer in

a high-pressure (HP) turbine stage. The hot section of a gas turbine is the most interesting to study, but taking accurate data in an engine is impractical and obtaining engine-realistic conditions in test facilities is very difficult due to the complexity of the engine environment. Consequently, there are still many challenges ahead and significant potential for performance improvement.

Novel measurement techniques are required to assess the impact of the cooling flows on stage aerodynamic and thermal performance. This thesis focuses on the development of gauges to measure the heat transfer. The gauges consist of plasma deposited thin films, allowing ultra-fast-response measurements. They operate accurately at low temperature differences on non-isothermal surfaces and are therefore ideally suited for the instrumentation of fully cooled HP turbine stages in short-duration experimental facilities.

The design and manufacture of a fully cooled HP turbine stage will be presented in this thesis. The nozzle guide vane (NGV) and rotor are representative of a modern shroudless turbine and have state-of-the-art external cooling features. The stage is novel in that it is a first generation design for challenging lean burn inlet conditions. By improving sensor technology it will be possible to understand the interaction of cooling flows with engine-realistic inlet flows. Providing CFD calibration data for this difficult environment may furthermore lead to improvements in engine optimisation.

The Oxford Turbine Research Facility (OTRF) is capable of investigating transonic HP turbine stages at engine-representative conditions of aerodynamics and heat transfer. There are only four such facilities worldwide. Out of these facilities, the OTRF has the unique advantage that it can replicate combustor realistic temperature distortion and swirl. When the new turbine stage is installed, this will be the first experiment of its kind to achieve highly engine-representative flows. The interactions between the combustor and the HP turbine are increasingly important to consider in order to achieve breakthroughs in efficiency.

This chapter aims to provide the background for the research presented in this thesis and to show its importance within the investigation of the heat transfer of fully cooled HP turbine stages subjected to engine-realistic inlet conditions of temperature and swirl in jet engines. In section 1.1 the fundamental thermodynamics of gas turbines are reviewed and the implications

on modern engine design are discussed. Section 1.2 gives an overview over the present work and highlights the research objectives. The chapter finishes with an outline of this thesis (section 1.3).

1.1 Research background

A gas turbine consists of a compressor, a combustion chamber and a turbine. The thermodynamic process is described by the Brayton cycle (see figure 1.1). In a jet engine the air is compressed, heated and expanded to produce a high-velocity propulsive jet. In an ideal (open) Brayton cycle, air is drawn into the compressor from the atmosphere and the pressure is increased isentropically between states 1 and 2', where the prime denotes an ideal isentropic process. The compressed air then passes through the combustion chamber, where fuel is burned to increase the temperature of the air. This heating is assumed to be reversible and isobaric. Between states 3 and 4' the high-temperature gas is expanded isentropically in the turbine to atmospheric pressure. In a real non-isentropic case, losses occur in both the compressor and the turbine, i.e. the energy absorbed by the compressor is increased, while that released by the turbine is decreased. The states reached in the non-isentropic case are denoted without primes and the resulting cycle is indicated by the dashed lines in figure 1.1. In a turbofan engine only a fraction of the thrust for the propulsion of the aircraft comes from the exhaust gas, while the remaining thrust is generated by the fan.

The thermal efficiency η is defined as the specific work output W per energy required to

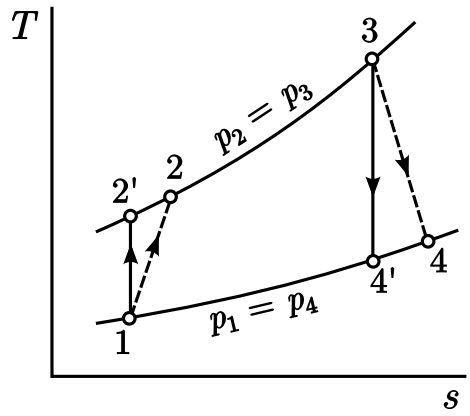

Figure 1.1: Ideal Brayton cycle describing a simple gas turbine system.

obtain it. From an analysis of the ideal Brayton cycle it follows:

$$\eta = 1 - \frac{T_{4'}}{T_3} = 1 - \frac{T_1}{T_{2'}} = 1 - \left(\frac{p_1}{p_2}\right)^{\frac{\gamma-1}{\gamma}} , \tag{1.1}$$

$$W = c_p(T_3 - T_{4'}) - c_p(T_{2'} - T_1) , \tag{1.2}$$

where γ is the ratio of specific heats and c_p the specific heat capacity at constant pressure. T_3 is the turbine entry temperature (TET) and p_2/p_1 the pressure ratio (PR) of the compressor. It follows that for an ideal cycle increasing the TET, or equivalently the PR, leads to an increase of the efficiency.

The performance of a real gas turbine depends on three key factors, namely the compressor PR, the TET and the single component efficiencies. The strive to improve the total performance has boosted the progress in related technologies, like the materials science, and has led to advanced engines with pressure ratios up to 45:1, turbine inlet temperatures exceeding 1800 K and component efficiencies of 85–90% (Saravanamuttoo et al., 2009).

The optimisation of a gas turbine requires a balance of sometimes conflicting factors. For instance, when increasing the PR, less fuel is needed for achieving the same TET, but at the same time the compressor temperatures, which are limited by thermal, mechanical and material considerations, are increased. A higher PR also means a higher coolant temperature, since the turbine cooling flow comes from the later stages of the compressor. A very important parameter in this context is the specific fuel consumption (SFC), the fuel consumption per unit thrust. For example, it is possible to obtain a larger specific thrust at the cost of the SFC by increasing the fuel flow in order to achieve a larger TET.

In effect, the TET has become an important design variable, being limited by the maximum permitted temperature which the highly stressed parts of the turbine are able to withstand for the required life. Modern materials and thermal barrier coatings allow for maximum temperatures of 1300 K in jet engines for civil aircraft. With complex cooling systems combining internal coolant impingement with external surface films, it is however possible to have a TET that is far higher than the allowable metal temperatures and hot gas temperatures over 1800 K have been achieved (Han et al., 2012).

A continuous improvement in turbine cooling is crucial to achieve a further gain in efficiency. Therefore, it is essential to consider the penalty associated with increased cooling flow requirements, including compression and pumping losses and, most importantly, aerodynamic losses of the cooling air mixing with the mainstream flow. Moreover, because the cooling air is extracted from the later stages of the compressor, it is of the utmost importance to reduce the amount of coolant required, in order to increase the thermal efficiency without compromising the engine performance.

The optimisation of a cooling system requires insight into the external aerodynamics and its interaction with the coolant flow as well as an accurate knowledge of the external heat transfer rate. Experimental work is invaluable not only to gain a better understanding of the complex aero-thermal processes inside an engine, but also for the validation of heat transfer predictions and the optimisation of turbine cooling systems.

1.2 Project overview

This section discusses the research objectives of this thesis and puts them into the context of ongoing heat transfer research in the OTRF. The OTRF is a transient annular facility for testing an engine size turbine stage at the correct non-dimensional parameters of aerodynamics and heat transfer so that measurements can be performed under engine-representative conditions. A detailed description of the OTRF is given in section 2.3. The three main objectives of this thesis can be summarised as follows: to design a fully cooled HP turbine stage for the OTRF, to develop improved heat transfer instrumentation for cooled aerofoils and to demonstrate the new instrumentation techniques under engine-realistic conditions in the OTRF.

The new turbine stage is the first fully cooled module to be designed for the OTRF. It is representative of a modern shroudless turbine with lean burn. In a shrouded turbine, neighbouring blades are connected at the tip to form an annular ring, so that the blades and the shroud rotate together and tip losses are reduced. Unshrouded blades, in contrast, do not have this shroud and therefore have a much smaller rotating mass. For a given maximum allowable stress unshrouded blades achieve higher rotational speeds. Current turbofan design aims to

increase the fan diameter and reduce the core diameter, in order to increase the bypass ratio, i.e. the ratio of the air mass flow rate through the bypass duct and the air flow rate through the core of the engine. A smaller core diameter results in a higher operating speed for the turbine, which requires the use of an unshrouded rotor.

Simultaneously, modern combustors have lean premix systems designed to reduce emissions of NO_x, CO and unburned hydrocarbons by premixing the fuel with excess air before ignition. These combustors have highly swirling exit flows, which need to be taken into account when designing the HP turbine stage. The HP NGV and HP rotor have engine-realistic external cooling features, including vane and rotor film cooling and trailing edge (TE) slot cooling as well as the blade root seal leakage flow.

Thin film gauges are an indispensable tool for measuring the heat transfer in a short-duration rotating test rig without disrupting the flow. In order to determine the heat transfer rate on thin walls at low temperature differences, a new gauge concept based on double-sided gauges is required. A central part of the present work consists in developing methods to accurately determine the adiabatic wall temperature and the heat transfer coefficient. To achieve this goal, new heated gauge configurations are considered, which allow to measure the heat transfer rate for different wall temperatures. The resulting distributions of film cooling effectiveness and Nusselt number are important both for the turbine designer and as CFD validation data. The turbine industry is very interested in accurate heat transfer data of engine-realistic geometries under relevant test conditions (that can be scaled to the true engine environment) to improve their design procedure. Although the new turbine stage was not finished in time to be tested within this thesis, tests were carried out on experimental hardware in the OTRF to demonstrate the performance of the new heated gauge configurations.

The results of this work contribute to two major test programmes on the OTRF (see section 2.3). The gauge concept developed for this thesis will be used on a new HP turbine stage currently under installation. The turbine stage designed for this thesis will be tested in late 2016.

1.3 Thesis outline

An overview of the content of the remaining chapters is given below.

Chapter 2 presents transient annular test facilities used to test HP turbine stages under engine-realistic conditions. The use of thin film gauges for heat transfer measurement in transonic experiments is reviewed and the applications and limitations of the gauges are discussed. The focus is on current developments in manufacture, heated configurations and data processing. The principle of operation of the OTRF is described and two major upgrades of the facility are detailed.

In chapter 3 the design of a fully cooled turbine stage using the Rolls-Royce design suite is presented. The design considers aerodynamics, heat transfer, cooling and mechanical requirements of a high performance turbine stage. The fatigue life and the resonance frequencies of the rotor are calculated and a safe operation at the design speed is confirmed. Details on the manufacturing process are given.

Chapter 4 examines the procedure of taking heat transfer data on a film-cooled aerofoil leading to the development of a gauge concept consisting of heated double-sided gauges. A review of thin film gauge theory is given. The gauge theory is extended to include lateral conduction effects in the gauge substrate. A 1D model of the thermal pulse through a multi-layer system is introduced and used to define the gauge design parameters.

The final gauge design and two heating arrangements are presented in chapter 5. The calibration of the gauges and the data analysis required to obtain temperature traces are discussed and the data acquisition system is described. The measurement strategies for each heating arrangement are detailed with an emphasis on the problem of determining the initial temperature of a heated gauge. To address this problem thermal models of the gauge substrate are investigated. The heater performance is assessed in bench tests. An analysis of the experimental uncertainties related to heat transfer measurements using heated gauges is given.

Chapter 6 concerns the demonstration of the new gauge concept under engine-realistic conditions in the OTRF. For this purpose, the turbine casing of a simple nozzle geometry is instrumented with four configurations of thin film gauges to have a back-to-back comparison.

These experiments serve to implement the measurement strategy and to validate the thermal models introduced in the previous chapter. The experimental results are compared with correlations from literature and with a prediction from a boundary layer code.

In chapter 7 the results of heat transfer measurements on uncooled and cooled aerofoils are presented. Six (uncooled and cooled) NGVs are instrumented with thin film gauges. The results include Nusselt number distributions over the surface distance at mid-span. For the cooled NGVs the film cooling effectiveness is presented and the performance of the cooling films is discussed. The results are compared with data from literature.

Finally, in chapter 8 the results are summarised and conclusions are drawn from this study. The thesis finishes with an outlook on future work, in particular regarding the use of heated double-sided gauges for future experiments.

CHAPTER 2

Review of Transient Facilities and Heat Transfer Measurements

The aim of this chapter is to put this thesis into the context of aero-thermal research of cooled turbine stages with an emphasis on heat transfer measurements in an HP turbine stage. Section 2.1 compares the OTRF to other transient annular facilities, which also have the capability to reproduce engine-realistic conditions. Section 2.2 gives an overview of the use of thin film gauges for heat transfer measurements in transonic HP turbine stages. In section 2.3 the OTRF is presented in detail and the latest hardware upgrades are discussed.

2.1 Transient annular turbine test facilities

Modern turbines have complex three-dimensional aerodynamic designs in order to optimise the pressure distribution and minimise the losses (Lakshminarayana, 1996). The designs include highly three-dimensional blade profiles with lean, sweep and twist as well as contoured passage endwalls. The flow-field is viscous, compressible and unsteady. For this reason it can be captured best in annular cascades, which recreate the radial pressure gradient. The addition of a rotor disc makes it possible to investigate the vane-blade interaction and rotating flow phenomena. Moreover, effects that are influenced by relative motion, such as the interaction of the blade with the wake or the tip leakage flow can be represented.

Rotating cascades can be classified as continuous and transient facilities. Continuous facilities (such as engine tests) require a large amount of power and are thus expensive to run. Moreover, instrumentation at extremely high temperatures and pressures in continuous facilities is difficult and unreliable, so that high-resolution measurements are hard to achieve. Transient facilities,

on the other hand, have the advantage that unsteady heat transfer measurements are possible. They are very well suited to take aerodynamic and heat transfer measurements in an engine-representative environment, also because most high-speed turbine flow effects occur at blade passing time scales. This short-duration testing technique was developed by Schultz and Jones (1973) on a shock tube. Nowadays, the transient rigs can be divided into three groups: *shock tunnels*, *piston facilities* and *blowdown facilities*. Each of them can match all non-dimensional parameters relevant to aerodynamics (Mach number, Reynolds number, pressure ratio, non-dimensional speed) and to heat transfer (gas-to-wall temperature ratio) in a running time which ranges from 40 ms to 500 ms. In a transient facility the temperature requirement is not very high: In order to achieve engine-characteristic gas-to-wall temperature ratios of about two, a wall at room temperature will require mainstream temperatures of less than 600 K.

The application of *shock tubes* for film cooling studies was firstly documented by Jones and Schultz (1971). A high-pressure "driver" gas and a low-pressure "driven" gas are separated by a diaphragm in a tube. When the diaphragm bursts a shock wave propagates along the tube, compressing and heating the test gas, which then passes through the turbine stage. The shock tube used in the Turbine Test Facility at Ohio State University (formerly at Calspan (Dunn and Stoddard, 1977)) is presented by Dunn (1986). More recently it has been upgraded to test a cooled 1 1/2 turbine stage (Mathison et al., 2012).

The operation of a *piston tunnel* is explained by Jones et al. (1973). It differs from that of a shock tunnel in that the test gas is heated by isentropic compression rather than by shock compression. The test gas in the piston tube is compressed by a free piston, which is driven by air from a high-pressure supply. When the desired inlet pressure is reached and the air has been heated to the required temperature, the gas is released through a fast acting valve into the working section, where the turbine rotor has already been spun up in vacuum. The air vents through the working section into a dump tank. During a test run steady conditions can be maintained by controlling the volume flow rate that drives the piston. The exit flow of the turbine stage is determined by an adjustable choked throat downstream. A test run ends as the piston reaches the end of the tube. The running time depends on the volume in the piston tube, the mass flow rate through the working section and the inlet total temperature. The Oxford

Rotor was the first such facility used to conduct heat transfer measurements on a linear cascade (Schultz et al., 1977). It was followed by the Pyestock Isentropic Light Piston Facility, which was commissioned by Brooks et al. (1985) and had an annular cascade of NGVs. This facility is now called the Oxford Turbine Research Facility (see section 2.3 for more details).

Finally, there is the Compression Tube Facility in the von Karman Institute for Fluid Dynamics, which was designed by Sieverding and Arts (1992) to investigate the aero-thermal performance of real engine parts and gas turbine components in an annular cascade. It has since been extended to an engine-scale 1 1/2 turbine stage.

Blowdown facilities consist of a high-pressure vessel, which vents through the test section into a dump tank. The running time depends on the size of the supply tank and the mass flow rate. The MIT Blowdown Turbine Facility is described by Epstein and Guenette (1984). It was developed to test film-cooled aircraft turbine stages and used a mixture of foreign gases as the working gas to match the ratio of specific heats in an engine. Prior to each test the turbine rotor is spun up to the design speed and an eddy current brake is employed to hold the shaft speed constant. Nonetheless, there is a drop of the turbine stage Reynolds number due to the pressure decay in the supply tank. The US Air Force Research Laboratory at the Wright-Patterson Air Force Base in Ohio also uses similar facilities for aero-thermal investigations (Haldeman et al., 1992) and has a rig capable of testing a 1 1/2 turbine stage with NGV cooling (Anthony et al., 2012).

2.2 Heat transfer measurements in transonic high-pressure turbine stages

This section focuses on current research on unsteady heat transfer with film cooling. As pointed out by Han et al. (2012), in order to optimise the film cooling performance it is necessary to know in detail the distribution of the Nusselt number and the film cooling effectiveness on turbine blades under unsteady high-turbulence engine flow conditions. These non-dimensional parameters can be inferred from experimental data using rigs that have been scaled to lower pressure and temperature conditions. The heat transfer rate is proportional to a driving temperature difference ΔT. For convective processes Moffat (1998) suggests to calculate ΔT

using the adiabatic wall temperature T_{aw}. The resulting adiabatic heat transfer coefficient h_{ad} depends only on the fluid mechanics:

$$h_{\mathrm{ad}} = \frac{\dot{q}}{\Delta T} = \frac{\dot{q}}{T_{\mathrm{aw}} - T_{\mathrm{w}}} \tag{2.1}$$

with the heat transfer rate $\dot{q}$ and the wall temperature T_{w}.

There are several options to measure the convective heat flux from the surface temperature history if the thermal properties of the substrate are known and an assumption on the temperature distribution in the substrate can be made (calorimetric principle). The current study was carried out in the OTRF. Given the restrictions of an annular, rotating experiment, this section focuses on heat transfer measurement techniques which do not require optical access (as do thermochromic liquid crystals and IR thermography). Thin film gauges have been used for several decades for heat transfer measurements in transient facilities. In the following their historical development and different applications are presented.

2.2.1 Thin film gauge history and theory

Schultz and Jones (1973) pioneered the use of thin film gauges as surface resistance thermometers in short-duration facilities proposed by Vidal (1956). Thin film gauges consist of a metallic film deposited on a semi-infinite material of low conductivity. The heat transfer is obtained from the conduction in a semi-infinite medium. An overview of the history and the development of these gauges at the Osney Laboratory is provided by Jones (1995). For unsteady heat conduction, single-sided gauges can be used to measure the local surface temperature history when operated in constant current mode. Assuming a semi-infinite substrate during the short-duration test, the governing equation is the 1D Fourier equation (see section 4.2). Due to the very low heat capacity of the chosen metal for the gauges, very high frequency measurements are possible.

The first gauges were painted onto machineable glass-ceramic substrates, which made them only practicable on substrates subjected to low stresses. Dunn (1985) extended the use of thin film gauges to a rotating turbine stage (at Calspan) by painting the gauges on Pyrex inserts which were embedded into a metallic turbine blade. This technique caused surface temperature discontinuities which affect the thermal boundary layer. The error in the heat transfer coefficient

introduced by these discontinuities is difficult to correct for in the case of a transitional boundary layer (Schultz and Jones, 1973).

Epstein et al. (1986) continued the development of the thin film gauge instrumentation at MIT by depositing the gauges on a flexible, low conductive sheet which can be bonded to any test surface. Similarly, Doorly and Oldfield (1986) used gauges deposited onto a metal model coated with an electrical insulator to achieve an easy to manufacture and durable result which minimised flow disruption. The theory of multi-layer thin film gauges is reported by Doorly and Oldfield (1987) and will be revised in section 4.2. This technology has been state of the art for many years and it has been used in many heat transfer studies.

2.2.2 Thin film gauge applications and limitations

Thin film gauges have been successfully used on uncooled and cooled NGV and rotor aerofoils and on turbine endwalls in engine-representative environments (see for example (Guo et al., 1998)). The application of thin film gauges on engine parts is limited by the geometry of the substrate. For thin or hollow walls the semi-infinite assumption does not apply. Furthermore, errors are introduced if flat-plate conditions are assumed on a curved surface. The leading edge of an aerofoil is affected by curvature effects, while the trailing edge is often too thin to make a semi-infinite assumption.

Buttsworth and Jones (1997) extended the 1D data analysis to capture radial heat conduction effects on curved surfaces by introducing analytical curvature corrections. Solano and Paniagua (2009) presented an alternative technique to process the temperature data and calculate the heat flux, which takes into account the lateral conduction effects expected in multi-layered systems. By solving the unsteady 2D heat conduction equation on the cross section of a metallic aerofoil with an insulating layer wrapped around it, they obtain an initial temperature distribution. This method was used to assess the pre-run heat flux into cooled rotor blades during spin-up. To simplify the processing they regarded the pre-run and blow-down contributions separately and obtained the resulting heat flux from the superposition of the initial heat flux to the blade due to the pre-run rotation heating and the heat flux calculated during the blow-down for a uniform initial temperature distribution. The 2D heat conduction phenomena on the leading edge and

the trailing edge of a aerofoil demonstrate the limitations of the 1D semi-infinite approach.

These issues also led to the investigation of new gauge types. The direct-heat-flux gauge developed by Piccini et al. (2000) is a single-sided thin film gauge on an insulating layer which is bonded to a high conductivity metal substrate instrumented with thermocouples. As the gauge measures the temperature difference across a layer of known thermal properties, there is no need to make assumptions on the semi-infinite behaviour of the metal substrate. Ideally the thermocouple is located as close as possible to the metal surface, but in principle given the high conductivity of the metal substrate it is possible to use a reduced number of thermocouples. This gauge type is suitable for experiments on thin substrates or for long test times. The direct-heat-flux gauges were used in cold heat transfer tunnel (where cold air is blown through a preheated working section to achieve the correct gas-to-wall temperature ratio) to measure the heat transfer of an NGV in a large-scale annular cascade. Their principle of operation is very similar to that of the double-sided gauges introduced in the next section.

Thin film gauges are also very well suited for the use in unsteady total temperature probes. This application, also known as the dual thin film probe, was first demonstrated by Buttsworth and Jones (1998a). Total temperature probes measure the stagnation temperature at the tip of a hemispherical probe by recording pairs of surface temperature and heat flux values. Given the high frequency response of thin film gauges they are better suited than thermocouple probes to measure unsteady flow phenomena. Thin film gauges are more robust than the probes used for hot-wire anemometry and in comparison to aspiration probes[1] the dimensions of a total temperature probe instrumented with thin film gauges are much smaller. Most importantly there is no need to perform a heat transfer calibration. To determine the total temperature it is necessary to record the heat flux at two distinct wall temperatures. For this reason total temperature probes initiated the application of heated thin film gauges, which will be discussed together with other heated configurations.

[1] Aspiration probes are a development of constant temperature anemometers in a cylindrical probe with a choked orifice downstream (Ng and Epstein, 1983).

Current developments

The aim of current heat transfer research on gas turbine aerofoils is to obtain accurate distributions of Nusselt number and film cooling effectiveness, which can be scaled to engine conditions and used to validate CFD predictions. Testing fully cooled geometries on rotating facilities under engine-realistic conditions, requires further progress in thin film gauge technology. There are three parallel developments in the measurement of surface heat flux with thin film gauges.

The first trend is to increase the spatial resolution of the measurements by reducing the size of the gauges. This improvement is driven by manufacturing technology. The thin film gauges used by Guo et al. (1998) consisted of platinum sensors which were deposited onto a polyimide layer, which was glued onto the test surface. The gauges were manufactured in a photolithography process, whereby a thin layer of platinum ($< 0.04\,\mu$m) was sputtered onto the substrate. The soldering joints, which are away from the measurement location, were connected to the sensors by copper tracks. These tracks were deposited on the platinum in a vacuum chamber using evaporation techniques (see also (Guo et al., 1995)). The resulting copper tracks had a thickness of $0.5\,\mu$m, which made them very frail and inappropriate to use on complex geometries. The gauges had a typical size of 0.1 mm by 2 mm. In comparison to the hand-painted gauges, these gauges were much easier and less time-consuming to manufacture. Also, a considerable reduction in size was achieved (from 0.3 mm by 3 mm). The main advantage, however, was that the automation of the manufacturing process made the gauges much more predictable and uniform, thus avoiding the need to calibrate the thickness and geometric properties.

An alternative manufacturing process was suggested by Thorpe et al. (2004a), who used a laser beam to directly cut the gauge geometry on a previously platinised test surface. The resulting gauges were as small as 0.08 mm by 1 mm.

The width of the connecting tracks limits the spatial resolution of the manufacturing processes presented above. The resistance of these tracks has to be sufficiently low, so that the change in resistance and hence the temperature sensitivity is restricted to the intended gauge area. However, with typical copper thicknesses of around $0.5\,\mu$m the required track width was a multiple of the gauge size. Anthony (2002) designed high spatial density gauge arrays to resolve

turbulent spots in transitional boundary layers. These arrays consisted of a number of gauges connected in series to a single power source, thus significantly reducing the space requirements for connecting tracks. While the spacing between the gauges was as low as 0.2 mm, differential amplifiers had to be used to measure individual gauge voltages (as the end of the gauge was not at ground potential). Also, the failure of one gauge could render the whole array useless.

Collins et al. (2015a) have achieved a significant reduction in the track size by using a pre-laminated copper-polyimide sheet with an 18 µm thick copper layer. The platinum sensor is sputtered in a photolithography process on the copper-polyimide sheet, on which the geometry of the copper tracks has been etched. The manufacturing process is otherwise relatively similar to that of Guo et al. (1995). More details on this process are given in section 5.1. The width of the tracks is now limited by the resolution of the etching process and the tracks can be as thin as 0.1 mm. Nonetheless, the new tracks have still proven to be much more robust and resistant to bending. The results are intricate gauge patterns of very high spatial resolution (limited by the size of the platinum sensor).

The second issue with thin film gauges concerns the requirement of the 1D semi-infinite assumption, which is not applicable in hollow geometries or near the leading edge and trailing edge of an aerofoil. Instead of accounting for curvature and finite substrate effects or using additional thermocouples, one could use double-sided thin film gauges. The first double-sided gauge was presented by Epstein et al. (1986). It consists of two thin film temperature gauges mounted on either side of a thin insulating layer, which is glued to the anodised surface of a metal blade. This gauge has the advantage that the heat flux can be obtained directly from the temperature difference across the insulating layer, which does not require knowledge of the heat flow into the test part. This measurement is valid even for time scales for which lateral conduction in the metal layer or backwall heating effects would invalidate the semi-infinite assumption. The use of double-sided thin film gauges had previously been restricted because of manufacturing issues, but with the improvement of gauge technology they have become widespread (see for example (Anthony et al., 2011) and (Kahveci et al., 2013)).

The third issue regards the determination of non-dimensional heat transfer parameters. To understand the performance of a cooling film, distributions of film cooling effectiveness and heat

transfer coefficient are required. The film cooling effectiveness follows from a measurement of the adiabatic wall temperature, which again is obtained from the extrapolation of a regression of the convective heat flux as a function of the wall temperature. In order to increase the accuracy of the measurements (or to be able to separate the adiabatic wall temperature and heat transfer coefficient at all when there is insufficient change in temperature for the regression), different options to vary the wall temperature and increase the range for the regression have been introduced. These will be reviewed together with other heated configurations below. The procedure for taking heat transfer measurements on a film-cooled aerofoil is discussed further in chapter 4.

Improvements in data acquisition

An early method to process the signal from a thin film gauge was to use a transmission line as an electronic analogue for heat conduction into a semi-infinite wall (Oldfield et al., 1984). This approach allowed to convert a temperature signal into a signal proportional to the heat transfer rate without the need for time-consuming data processing. With advances in computing power, however, it has become more feasible to directly compute the heat flux from the measured temperature signal.

A crucial advance in this direction was the development of the impulse response processing technique by Oldfield (2008), which can also take into account a finite substrate thickness such as in two-layered gauges or double-sided gauges (see section 5.4). Similarly, one can apply a reverse transformation to obtain the temperature signal from a recorded heat flux signal (Chana and Jones, 2003).

To fully exploit the advantages of the impulse response method, new heat transfer amplifiers (HTAs) have been designed (Oldfield and Beard, 2014). A central challenge is that the typical thin film gauge frequency response leads to a strong attenuation of high-frequency information and therefore a low signal to noise ratio (Anthony, 2002). The new HTA design developed by Oldfield and Beard (2014) makes use of a two-breakpoint, gain-shaping differential amplifier to compensate for this effect and enhance the high-frequency response. A high-speed data acquisition with a sampling frequency of 2 MHz is then used to record the data, which can then

be processed further to recover the measured temperature signal and calculate the corresponding heat transfer rate. The data processing will be presented in section 5.4.

Heated configurations

The need to measure the heat flux at different wall temperatures to determine the adiabatic wall temperature was highlighted by Thorpe et al. (2004b) in their work on the over-tip region. In order to obtain Nusselt number distributions on the HP NGV casing it is necessary to measure the adiabatic wall temperature in a region of large temporal and spatial variations in the flow. Thin film gauges were mounted on a Macor block, which was instrumented with two Peltier heat pumps and a heat exchanger to heat or cool the block. By varying the excitation voltage a range of substrate temperature differences of up to 30 K was achieved. The experiments were carried out in the Oxford Rotor Facility and allowed to take time-resolved heat transfer measurements to better understand the flow flow field and interaction effects in the tip-gap (Thorpe et al., 2004c).

Collins et al. (2015b) continued the work on the casing heat transfer on the OTRF. An aluminium insert in the over-tip rotor casing was instrumented with thin film gauges. The wall temperature was controlled with a water circuit and an external Peltier heat exchanger was used to vary the water temperature between 8 °C and 60 °C. As the insulating substrate layer of the gauges was thicker than the penetration depth of the thermal pulse during the test duration, a semi-infinite assumption could be made. Given the variations in total temperature local to the rotor casing, Collins et al. (2015b) developed a floating regression which accounts for changes in the driving temperature difference and thus allows to extend the run time available for the regression. This regression method is detailed in section 5.4 and will also used in the current work.

Pinilla et al. (2012) described a method to experimentally determine the adiabatic wall temperature on the low-pressure NGV of a 1 1/2 turbine stage tested in the Compression Tube Facility at the von Karman Institute. The investigated (structural) vane was heated with electrical resistors on the tip and hub. The tests were carried out at five different substrate temperatures. By insulating the instrumented NGV from the turbine casing, uniform pre-run

temperatures were achieved. The temperature history on the surface was recorded with two-layered thin film gauges. The heat flux was obtained from the unsteady 2D heat conduction equation based on the temperature distribution on the aerofoil surface at the beginning of the run (see also (Solano and Paniagua, 2009)).

The discussion of heated total temperature probes is of particular interest, because of the similar geometry restrictions and conditions of use than those of thin film gauges on aerofoils. The first total temperature probe instrumented with thin film gauges consisted of two platinum thin film gauges painted onto the tip of two hemispherical quartz probes, one of which had a heater element embedded (Buttsworth and Jones, 1998a). The calculation of the total temperature relied on the assumption that the heated and the unheated films are exposed to an identical flow. Thus, in an attempt to increase the spatial resolution the two gauges were joined in one probe with a small heater underneath the hot gauge and with a certain separation between the two gauges (Buttsworth et al., 1998). Further developments of this probe included thin film heater elements and a slot between the two gauges (Ralph, 2000).

A higher resolution was achieved by Buttsworth and Jones (1998b) by removing the heater and heating one of the gauges with a short current pulse. In order to generate a substantial temperature difference (and to stop the cold film from heating up), the high current through was applied approximately 1 s before the run. However, this method required to correct for lateral conduction effects in the probe caused by induced convective heat flux gradients (Buttsworth and Jones, 1997). Buttsworth and Jones (1998b) concluded that it is possible to use the self-heating gauge to measure the convective heat transfer, as long as transient effects of the ohmic heating are accounted for.

The two heating methods for the total temperature probes have the disadvantage that the temperatures of hot and cold gauge converge during a test, i.e. they are not suitable methods for steady-state tests. An alternative method is to design a total temperature probe in which the temperature increase of the "hot" gauge is accelerated by better insulating one of the gauges. The gauge described by Chana (2004) has a small air cavity underneath one of the gauges, but alternative options such as changing the substrate material have also been considered (Passaro et al., 2003). These probes have been successfully used in engine tests (e.g. (Lubbock, 2014)).

Outlook

The aim of this work is to combine the latest gauge manufacturing technology with the developments in adiabatic wall temperature measurement using heated substrates to create novel double-sided thin film gauges. Two heated configurations will be discussed, which allow to use the gauges over a range of wall temperatures and thus improve the range of the regression. These gauges will be used to acquire heat transfer data in the OTRF.

2.3 The Oxford Turbine Research Facility

The heat transfer studies presented in this thesis were carried out in the OTRF. This section describes the experimental facility and gives an update on the latest developments. There is numerous literature available on the OTRF, thus the focus of this section is placed on the experimental hardware. The main aim of the OTRF is to provide high-quality heat transfer data which can be used to validate numerical predictions and further develop design methods.

The OTRF is a short-duration wind tunnel, capable of testing 1 1/2 engine size turbine stages at the correct non-dimensional parameters in order to perform aerodynamic and heat transfer measurements. Jones et al. (1973) describe the operating principle (see also section 2.1). The facility consists of a high-pressure reservoir, a piston tube, a plug valve which releases the air into the working section and a dump tank (see figures 2.1 and 2.2). An aerodynamic braking system is used to maintain constant turbine speed during the test run. Two separate systems have been used in the past to generate an engine-realistic turbine inlet temperature profile – with hot streaks as a result of combustor exit flows – as well as inlet swirl.

The aim of these experiments is to provide data that can be scaled to the engine environment. The OTRF captures the radial pressure gradient of the flow-field and unsteady flow phenomena. To maintain aerodynamic similarity for a compressible viscous flow the following dimensionless groups need to be matched: Reynolds number, Mach number and ratio of specific heats. The parameters required to describe the film cooling are discussed in section 7.2. During a run, Mach number, Reynolds number, non-dimensional speed, gas-to-wall temperature ratio and turbulence intensity are engine-representative. The scaling from engine conditions and the

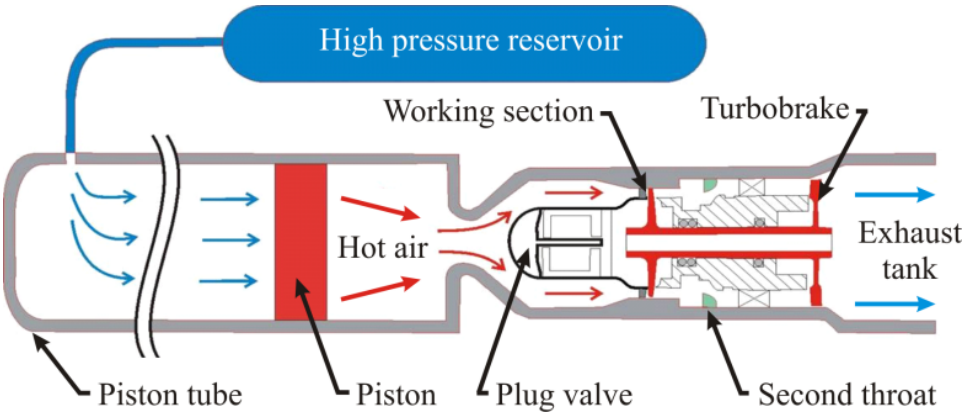

Figure 2.1: Schematic of the OTRF.

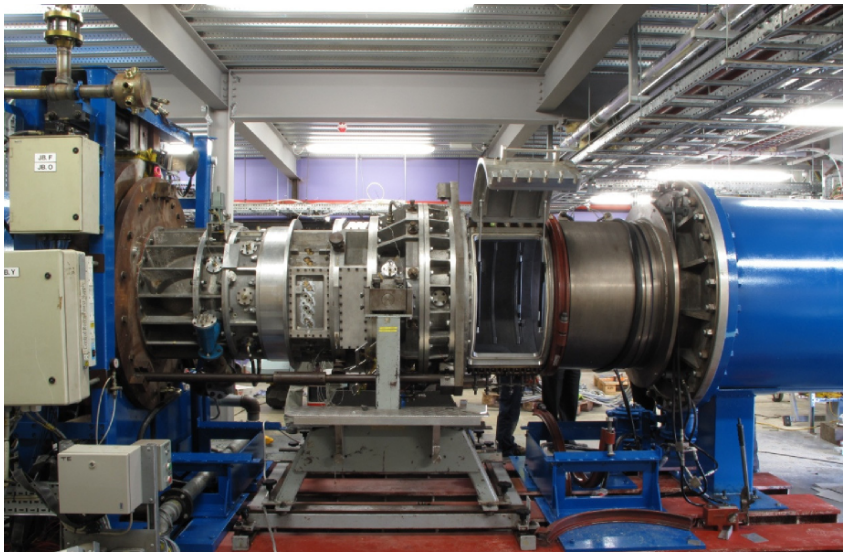

Figure 2.2: Photograph of the working section in the OTRF.

extent of the experimental simulation in the OTRF are discussed in section 3.1.

2.3.1 Historical overview

A review of the OTRF is given by Chana et al. (2013). The OTRF was originally called the Pyestock Isentropic Light Piston Facility, when it was built at the Royal Aircraft Establishment (RAE) in the late 1980s. In 2010 this facility was moved to the Osney Laboratory at the University of Oxford, where it replaced the Oxford Rotor Facility. It can be used to test up to 1 1/2 turbine stages. At the RAE a full-scale aero-engine high-pressure turbine stage working section was developed and fitted with the MT1 HP stage, which is a highly-loaded unshrouded

turbine stage (Hilditch et al., 1994). A significant new feature added was an aerodynamic turbobrake (Goodisman et al., 1992), which is placed on the same shaft as the turbine and is driven by the turbine exit flow. By matching the turbobrake power to that of the turbine, the shaft speed is kept constant during a test run.

The rotating module was installed at the RAE in order to investigate heat transfer and aerodynamics of unshrouded HP turbine stages on a high-pressure research turbine. During this time blade internal cooling passages were designed and a coolant delivery system was implemented. The OTRF has subsequently been used to investigate shrouded turbines within the High Performance High Reliability Shrouded Turbine Programme (Haller and Hilditch, 2007). Shroud cooling was also implemented, with a film cooling design that is representative of an engine configuration (Chana and Haller, 2009a,b).

The temperature at the exit of a combustion system is non-uniform due to an incomplete mixing of hot and cold gas streams. An inlet temperature distortion generator was first introduced by Chana et al. (2003a) using the existing inlet boundary layer bleed system, which allowed injecting cold air and therefore generated hot spots between the injection points. To reduce the mixing and direct the cold air, small tapering duct sections with internal vanes were added. The temperature distortion generator was upgraded by Povey and Qureshi (2009) in order to simulate an aggressive combustor temperature profile of a modern engine with a more pronounced maximum-to-minimum temperature ratio. In this design hot streaks were obtained by introducing cold gas into the hot mainstream flow through radial and circumferential slots upstream of the turbine stage. Finally, to study the impact of inlet swirl variations, an inlet swirl simulator was commissioned in the OTRF (Qureshi and Povey, 2011; Qureshi et al., 2012).

To quantify the performance of the OTRF, measurements of the turbine power were taken, accounting for the heat transferred from the fluid to the surrounding surfaces and rotor blades. Such measurements require the determination of the mass flow rate and the shaft torque (Beard et al., 2010). In order to accurately measure the latter, a strain gauge system was designed and implemented.

2.3.2 LEMCOTEC and SILOET upgrades

The OTRF is currently going through two major upgrades to be able to test a cooled turbine stage under engine-realistic inlet conditions of temperature and swirl. Two new turbine stages, LEMCOTEC (Lundbladh et al., 2016) and SILOET (Matthews et al., 2012), and a combined swirl and temperature distortion combustor simulator (Hall et al., 2014) have been designed. The aim is to study HP turbine aero-thermal performance and film cooling efficiency in the presence of cooling flows with non-uniform inlet flows.

The LEMCOTEC (Low Emissions Core-Engine Technologies) programme is a collaborative project co-funded by the European Commission and several industrial partners. The key objective is to reduce air-traffic emissions. The thermal efficiency of aero-engines is improved by increasing the overall pressure ratio (see section 1.1). To reduce the NO_x emissions, swirl stabilised lean premixed prevaporised combustors are used. The improvements required include compressor, combustor, turbine and structures technologies. The focus of the LEMCOTEC work on turbines is on the cooling efficiency of ultra high-pressure engines which have an increased turbine inlet temperature and are subjected to high levels of swirl and complex temperature profiles from the lean burn combustors. A 1 1/2 turbine stage has been designed. It has a film-cooled HP NGV (without TE slot) and an uncooled rotor.

The SILOET (Strategic Investment in Low-Carbon Engine Technology) programme is a Rolls-Royce programme directed at the study of a modern, shroudless cooled HP turbine module with NGV and blade film cooling and blade root seal leakage flow. It has been designed for lean-burn combustor exit flows with combined swirl and temperature distortion factor. The SILOET turbine is the most advanced of the two new turbine stages as it features a fully cooled HP NGV and rotor (including the TE slot). The design of the SILOET HP turbine stage is presented in chapter 3.

CHAPTER 3

Design of a Cooled High-Pressure Turbine Stage

This chapter details the design and manufacture of a new HP turbine stage for the OTRF within the SILOET programme. This turbine stage is the first fully cooled turbine stage to be developed for this facility. Section 3.1 describes the aerodynamic design and the scaling from engine to rig conditions. Section 3.2 discusses the cooling configuration of the HP NGV and HP rotor including film cooling holes and TE slots. The stresses in the stator without main flow (i.e. at the highest differential pressure) are analysed in section 3.3. The mechanical assessment of the rotor based on a finite element analysis (FEA) is given in section 3.4.

The design of the turbine stage was done in collaboration with the OTRF team, and the CAD was provided by Dr Paul Beard. The design of the cooling configuration and the mechanical assessment of the NGV and rotor are the author's own work.

3.1 Design of the SILOET cooled turbine stage

In this section the design of the new HP turbine stage for the OTRF is presented. The geometry and the cooling configuration are based on that of a modern civil engine. The rig running conditions match Rolls-Royce engine conditions, but have been adapted to the capability of the facility as well as to the experimental priorities.

3.1.1 Aerodynamic design

The annulus lines of the new cooled turbine stage are at 73% geometric scale of the design target. They were designed to minimise the hardware changes to the existing MT1 geometry.

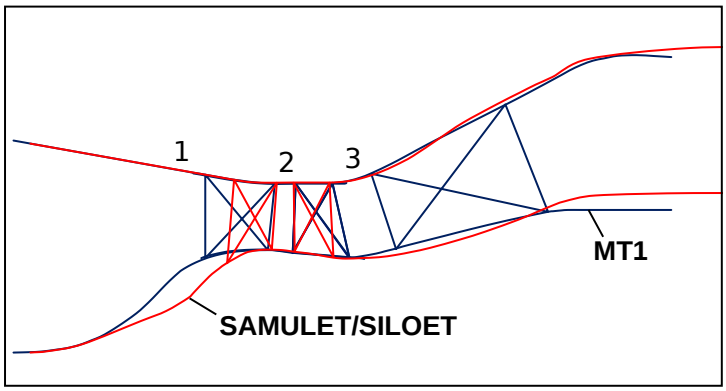

Figure 3.1: Schematic diagram of the OTRF annulus lines. The numbers mark axial stations in the turbine from the HP NGV inlet (1) to the HP rotor exit (3).

Even though the OTRF has the capacity to test up to 1 1/2 turbine stages, this project only investigates the HP NGV and rotor. Figure 3.1 shows the superimposed MT1 and SILOET annulus lines. As opposed to the engine target, the rotation direction of the OTRF is clockwise to retain the existing OTRF shaft and turbobrake.

The new turbine stage has 20 combustor burners, 40 HP NGVs and 60 HP rotor blades (see figure 3.2). This 1:2:3 ratio of burners, vanes and rotor blades reduces the computational cost of the CFD analysis. The 1:2 burner to HP NGV ratio is also relevant to modern and future turbine designs. Initially it was planned to use the MT1 disc for the SILOET turbine and the blade count was kept the same. The effect of the burners is modelled with a new combined inlet swirl and temperature profile generator, which has been developed in parallel in a separate Rolls-Royce programme. The existing MT1 disc design had to be modified to feed the coolant into the rotor blade and a new disc has been manufactured. The cooling delivery system has also been designed. New instrumentation cartridges have been manufactured, given the higher number of vanes compared to the MT1 turbine, which only has 32 vanes.

Figure 3.3 shows a cross section of the new turbine stage. The rotor coolant is fed from the front side of the disc through an inclined slot under the blade, which is in-line with the blade root. The radius of injection is as close as possible to the blade root to minimise radial pumping effects. A discussion of the cooling configuration follows in section 3.2. The coolant mass flow rate will be calculated from the metered feed pressure and temperature and known coolant

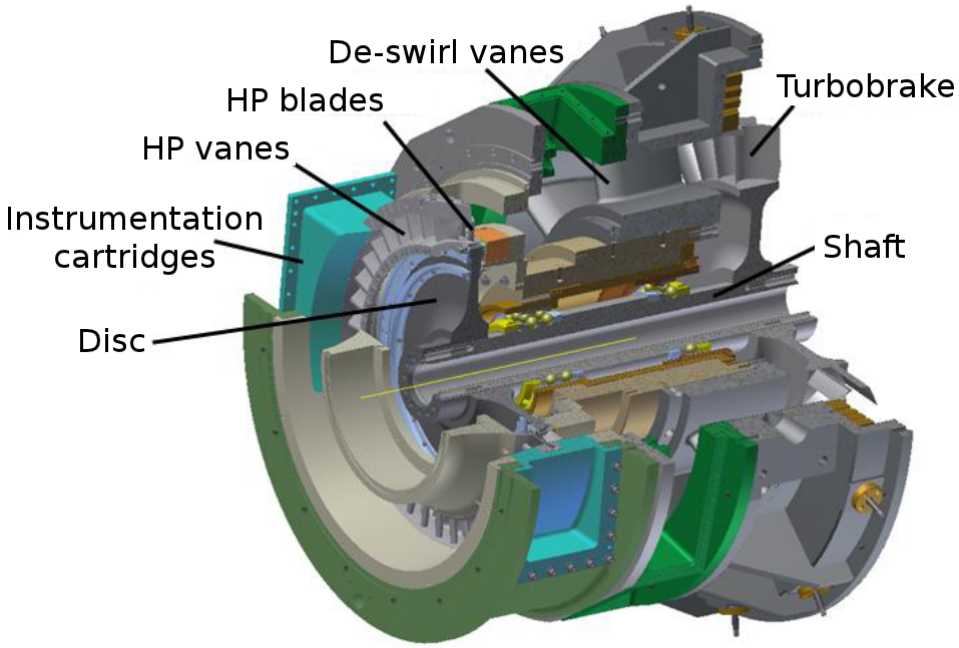

Figure 3.2: CAD layout of the OTRF with the new HP turbine stage.

capacity. Two new cover plates have been designed to hold the blade axially on the disc and for ease of sealing. The front cover plate has a three-step labyrinth seal, which controls the blade root seal flow. The coolant supply is sealed with O-rings on the inner side of the cover plates (not shown). Machined blocks of balsa wood will be inserted between the blade roots to avoid inter-platform leakage. The same lower labyrinth seals, which sealed the front and rear sides of the disc in the MT1 turbine, will be reused here.

The HP NGV and HP rotor blade aerofoil geometry was provided by Rolls-Royce and is based on a current civil engine. It is designed for lean-burn combustor interaction effects, i.e. simultaneous hot streaks and swirl. The rotor is shroudless with a flat tip. The platforms and the fixtures of the NGVs in the OTRF, are similar to those used in the previous turbine design. The blade hub engine geometry has been reproduced with a lip on the front face of the blade platform, which fits into a circular gap on the NGV hub and acts as a further control of the blade root seal leakage flow (see figure 3.3).

The axial chord of the new rotor blade is shorter than that of the MT1 geometry and the platform has been shortened to reduce aerodynamic losses and weight. Aside from these changes,

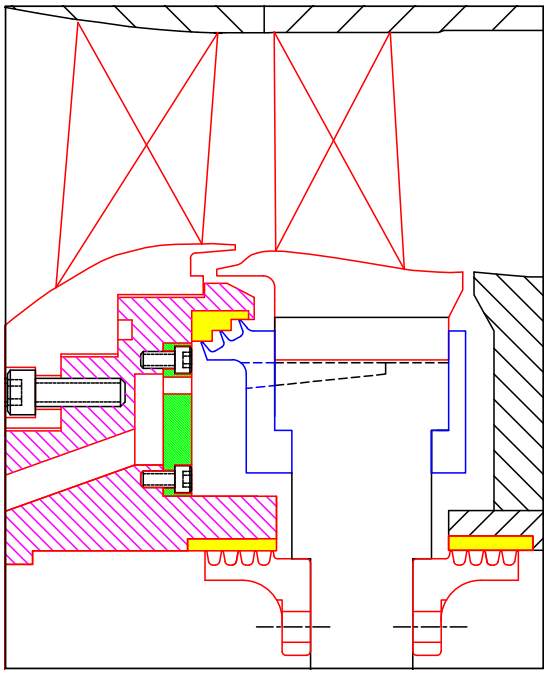

Figure 3.3: Schematic cross section of the new HP turbine stage.

the platform design – including the 20° angle of the blade root axis to the turbine axis – is the same as that of the MT1 turbine. The blade root geometry is identical to the former design and consists of a firtree with one lobe (see figure 3.13). However, the width of the blade shank was increased. A preliminary dynamic analysis of the bladed disc sector showed only little margin to resonance. This margin was extended by thickening and, hence, stiffening the shank. More information on the dynamic analysis is found in section 3.4.

The manufacture of the blades and vanes consists of three steps. First, the aerofoil geometry and the internal cavities are cast, because given their highly three-dimensional shape they cannot be machined. Second, the sides of the (NGV and blade) platforms, the blade root and the blade tip which require tighter tolerances are machined. The cooling holes are also machined. Finally, the TE slot cooling has to be spark eroded due to the complex geometry. More details are found in section 3.2.

The material of the disc is the same EN24T stainless steel (BS 970 817M40), also known as AISI 4340, used for the previous disc. The vanes and blades are made of an aluminium cast. The advantages of using aluminium instead of steel are the weight reduction and the

	EN24T Steel	**A357 Aluminium**	**EPIC A357 Aluminium**
σ_y, MPa	650	240	258
σ_{UTS}, MPa	850	300	353
ρ, $\mathrm{kg\,m^{-3}}$	7860	2670	2600
E, $\mathrm{N\,m^{-2}}$	$205.0 \cdot 10^9$	$72.4 \cdot 10^9$	$74.0 \cdot 10^9$
G, $\mathrm{N\,m^{-2}}$	$81.0 \cdot 10^9$	$26.8 \cdot 10^9$	$27.8 \cdot 10^9$
ν	0.30	0.33	0.33

Table 3.1: Properties of the materials of the disc (steel) and blades (aluminium). The tabulated properties are the yield strength σ_y, the ultimate tensile strength σ_{UTS}, the density ρ, the Young's modulus E, the modulus of rigidity G and the Poisson's ratio ν. Since the yield strength of the EPIC A357 aluminium cast is not known, it is approximated with the 0.2% elongation proof strength (from (Tritech)).

paramagnetic properties of aluminium. Thus aluminium blades, as opposed to steel blades, do not need to be costly demagnetised to remove magnetic fields which would induce voltages and influence the measuring equipment. Also, the high thermal conductivity of aluminium compared to steel allows to assume isothermal conditions on the rotor blade, which is very convenient for heat transfer measurements. The chosen A357 aluminium cast has high mechanical properties. Moreover, the supplier for the vanes and blades used a new investment casting process (Enhanced Property Investment Casting, EPIC), which improves the microstructure of the material and achieves higher strengths as well as an increase in the number of cycles to failure compared to conventional A357 aluminium casts. The material properties are summarised in table 3.1.

3.1.2 Scaling from engine conditions

This section describes restrictions of the test facility and instrumentation requirements to be taken into account when determining the running conditions of a scaled experiment. A turbine operates most efficiently at a design point, which is given by a certain Reynolds number Re and Mach number M or, equivalently, inlet total to exit static pressure ratio p_{01}/p_3 (if neglecting losses and differences in the ratio of specific heats γ). In an engine γ is given by the combustion products. Furthermore, the cooling of vanes and blades dictates a cooling configuration and

capacity. Two more parameters determine consequently the engine running conditions: the total coolant to total mainstream pressure and temperature ratios, p_{0c}/p_{01} and T_{0c}/T_{01}.

In the OTRF, Re can be changed independently of M by changing p_{01} and keeping T_{01} and p_{01}/p_3 constant. The inlet total pressure is given by the pressure in the piston tube. Thus, in the test facility Re is limited by the maximum operating pressure of 8.5 bar. The exit static pressure is determined by the downstream area of the second throat. In order to take direct loss measurements, Re needs to match the engine target. However, there are further constraints set by the instrumentation requirements, such as a minimum gas-to-wall temperature difference. For heat transfer measurements the Reynolds number to Nusselt number Nu, scaling rules are robust, which means that heat transfer measurements can be taken at different values of Re (as close as possible to the engine target) if a larger temperature difference can be achieved.

The OTRF cannot match the Maximum Take-Off (MTO) Re of the engine design on which the new turbine stage is based, but it can match Re at cruise. The Re in the rig is limited to about 64% of the engine MTO Re by the operating pressure. This is known as the "high Re" case. Since aerodynamically the HP turbine operates very similarly at cruise and MTO, aerodynamic and performance measurements will be taken at the cruise condition. The cooling design, on the contrary, is determined by the MTO conditions. Therefore, the heat transfer experiments will be conducted at cruise, at a lower Re than desired. Additional heat transfer measurements can be taken at higher Re to validate the Re to Nu scaling rules required to extrapolate the results to engine relevant conditions.

Table 3.2 shows the rig running conditions for the high Re case. The minimum mean inlet total temperature is set to 475 K in order to have a minimum temperature difference of around 40 K at the HP rotor exit, in case future programmes want to perform heat transfer measurements on an intermediate pressure vane. The rotational speed n is limited to 8525 rpm by vibrational considerations (see section 3.4). The current running conditions were designed to match the engine non-dimensional speed $n/\sqrt{T_{01}}$ and the gas-to-wall temperature ratio T_{01}/T_w. As for now, the Rolls-Royce through-flow code q263 has only been run at the high Re conditions to establish boundary conditions for CFD simulations of the stage.

Parameter	Value
Rotational speed n	$8525\,\mathrm{rpm}$
Inlet total temperature T_{01}	$475\,\mathrm{K}$
Inlet total pressure p_{01}	$8.5\,\mathrm{bar}$
Inlet mass flow rate $\dot{m}_1$	$23.97\,\mathrm{kg\,s^{-1}}$
Pressure ratio p_{01}/p_3	2.847
Gas-to-wall temperature ratio T_{01}/T_w	1.64
Capacity $\dot{m}_1\sqrt{T_{01}}/p_{01}$	$6.15 \cdot 10^{-4}\,\mathrm{kg\ s^{-1}\,K^{1/2}\,Pa^{-1}}$
Non-dimensional speed $n/\sqrt{T_{01}}$	$391.20\,\mathrm{rpm\,K^{-1/2}}$
Mach number at NGV exit	0.852
Reynolds number (based on NGV axial chord)	$3.10 \cdot 10^6$

Table 3.2: Operating point in the OTRF (high Re case). The values have been obtained from the Rolls-Royce through-flow code q263.

3.2 Cooling configuration

The cooling design of the new HP turbine stage was developed in collaboration with Rolls-Royce under the SILOET research programme. As explained in section 2.3, the aim of the SILOET project is to test an engine-realistic, fully cooled turbine design, which will include vane and rotor film cooling and TE slot cooling as well as the blade root seal leakage flow, and provide data for CFD validation. This data will contribute to gain a better understanding of the cooled stage performance and the CFD prediction capability. However, in order to allow access for surface instrumentation and make the interpretation of measurements easier, the cooling configuration is simplified. Only external cooling features are represented and only cylindrical film cooling holes are used. The internal geometry is kept as simple as possible without any internal cooling features.

Rolls-Royce in-house codes were employed for the modelling and the analysis of the new cooling system. The cooling configuration (including external positions and angles of the holes) was determined in the geometry creation programme gk07, based on that of a modern civil

engine. This information was then imported into the Rolls-Royce blade thermal analysis tool jb56. This code comprises an internal 1D flow cooling analysis (INCA) and a 3D boundary layer analysis (BLAY) software package, which performs external heat transfer calculations with the boundary conditions predicted by the through-flow code q263. Cooling systems in vanes and blades are modelled through 2D flow networks with given areas. A set of industry standard correlations are used to calculate the heat transfer, the pressure loss, the discharge coefficients and the film effectiveness.

The general cooling characteristics are obtained from the engine scaling and the rig limitations, as discussed in section 3.1. An important cooling parameter is the blade feed pressure ratio BFPR, which is defined as the ratio of total feed pressure $p_{0,\mathrm{feed}}$ to the total pressure of a mid-height stream $p_{0,\mathrm{str}}$ (for the blade in the relative frame). The BFPR is usually between 1.02 and 1.04. This definition allows an estimation of the total feed pressure from the flow total pressure, so that there is neither ingestion nor too much aerodynamic loss.

The BFPR is equivalent to the total coolant to total mainstream pressure ratio $p_{0\mathrm{c}}/p_{01}$. If the pressure ratio matches engine conditions (to establish the correct momentum flux ratio to first order) the test facility total coolant temperature $T_{0\mathrm{c}}$ determines the coolant mass flow rate. $T_{0\mathrm{c}}$ depends on the cooling delivery system and on the design of the heat transfer measurements. In this case it is $T_{0\mathrm{c}} = 290\,\mathrm{K}$.

For a given BFPR = 1.02 in the OTRF, the inlet total to exit static pressure ratio of the cooling holes, PR $= p_{0,\mathrm{inlet}}/p_{\mathrm{exit}}$, is set to match the engine target. The total coolant mass flow is 15.91% of the turbine stage inlet mass flow rate $\dot{m}_1 = 23.97\,\mathrm{kg\,s^{-1}}$ at the high Re condition (see table 3.2). It can be divided into the following cooling flows (from q263):

- HP NGV: 9.85% of $\dot{m}_1$ (of which 2.99% of $\dot{m}_1$ from the TE slot cooling)
- Blade root seal flow: 2.19% of $\dot{m}_1$
- HP rotor: 3.87% of $\dot{m}_1$ (of which 1.81% of $\dot{m}_1$ from the TE slot cooling)

In the next two sections the cooling configurations of the NGV and the rotor blade are described and the TE slot cooling design is detailed. The simulation of the cooling system in jb56 will be discussed and the results of the analysis presented.

Row	Diameter	#	Inner Rad	Pitch	Radial Angle	Planar Angle
SS5	0.59	22	254.19	1.98	0°	-70°
SS4	0.59	22	254.74	1.98	0°	-65°
SS3	0.59	23	253.39	1.98	0°	-55°
SS2	0.56	20	254.19	2.22	60° to -60°	-30°
SS1	0.56	20	252.91	2.22	60° to -60°	-10°
PS1	0.56	20	254.10	2.22	60° to -60°	25°
PS2	0.56	20	253.86	2.22	60° to -60°	70°
PS3	0.59	20	257.37	1.98	0°	110°
PS4	0.59	19	259.01	1.98	0°	105°
PS5	0.59	17	259.28	2.22	0°	105°

Table 3.3: Cooling configuration of the HP NGV. The diameters, inner radii and pitch are given in mm. The counting of the rows starts from the row closest to the stagnation line on the suction side (SS) and on the pressure side (PS). The radial angle is the angle in the radial direction. The planar angle determines the angle on a radial cross section.

3.2.1 High-pressure nozzle guide vane

The HP NGV has only two internal cavities (the Rolls-Royce engine target has three). The wall thickness is equivalent to the engine target, so that the rows of cooling holes have a similar length to diameter ratio to the real geometry. This parameter determines the discharge coefficient of a hole $C_\mathrm{d} = \dot{m}_\mathrm{actual}/\dot{m}_\mathrm{ideal}$ and thus its mass flow rate. The cavities are modelled in jb56 as a radial duct of known area, perimeter and centroid location. The cooling configuration consists of ten rows of film cooling holes, five of them on the pressure side and five on the suction side. The details are summarised in table 3.3. Figure 3.4 shows five cross sections through the aerofoil with the cooling hole geometry.

The diameters and pitch of the cooling holes are scaled down to 73% of the engine target. The rows have a radial extension from about 3% to about 97% of the blade height to maximise the coverage. At the leading edge (also known as shower head) the rows of cooling holes SS2, SS1, PS1 and PS2 have been staggered to protect against inlet swirl. Their radial inclination

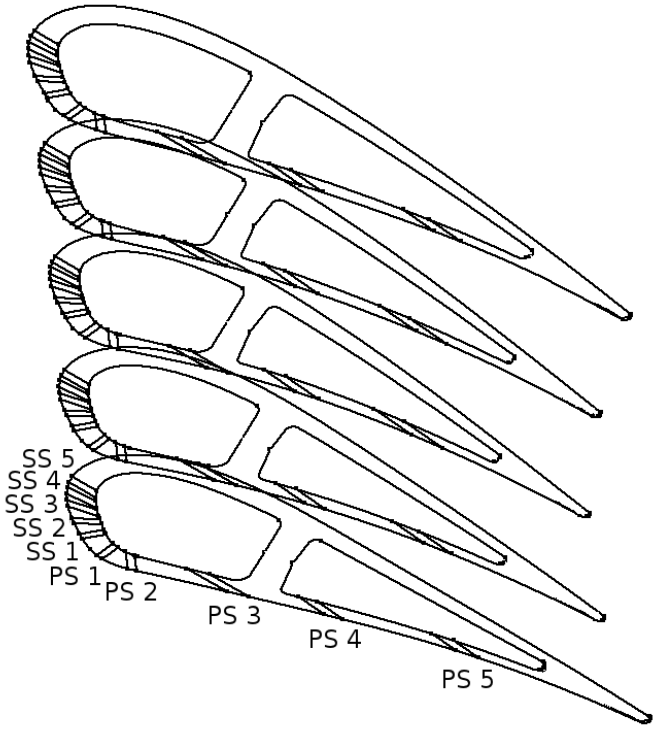

Figure 3.4: Cross sections through the HP NGV (without TE slot cooling). The shape of the two internal cavities does not correspond to the real geometry.

changes stepwise from 60° at the hub to 35°, -35° and to -60° at the casing with a varying transition height in order to improve the cooling effectiveness. For ease of manufacture, the planar angles are constant over the blade height. The rows PS4 and PS5 are fed from the rear cavity. The discharge coefficients of the film cooling holes were calculated using the correlations implemented by Rowbury (1998). C_d is a function of the known geometry, i.e. the length and the diameter of the cooling holes, and of the hole Re.

The TE cooling consists of five slots extending from 4% to 96% of the blade height. Each slot is 6.8 mm long, 3.0 mm wide and 0.33 mm high. The cutback geometry is sketched in figure 3.5. The TE slots have a race-track shape and are fed through a single race-track shaped hole, which defines a flow-controlling area of 2.22 mm^2. For the preliminary calculations, they were modelled in jb56 with $C_\mathrm{d} = 0.93$, which is based on Rolls-Royce experience. The correct C_d to Re curves for the slots can be determined experimentally when the parts are finished.

The coolant is introduced from the case of the vane in a cross feed and the same feed

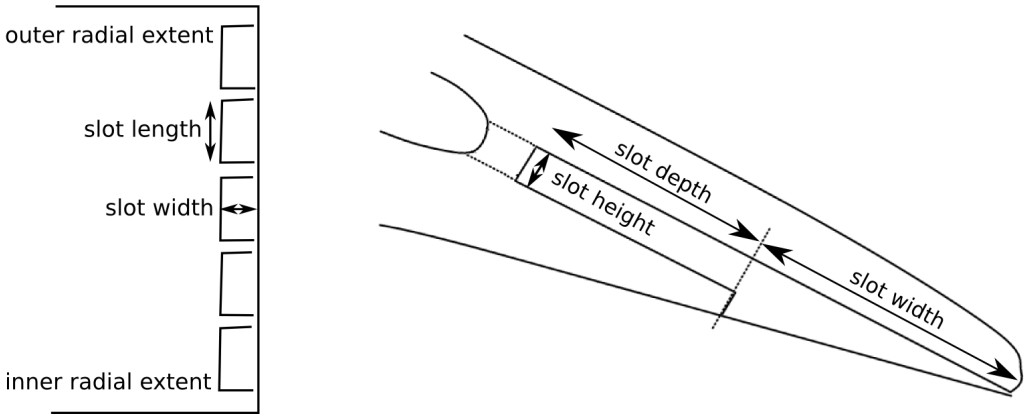

Figure 3.5: Sketch of the TE slot cutback geometry with 5 slots (NGV). The width of the feed holes is given by the slot height.

parameters are assumed for both internal cavities. The total feed temperature $T_{0,\text{feed}}$ is equal to $T_{0c} = 290\,\text{K}$. The total feed pressure is obtained from the BFPR and a known mid-height stream total pressure, which is taken from the q263 prediction. It is $p_{0,\text{feed}} = 8.67\,\text{bar}$. During the design process the results from the jb56 analysis were used to check that there is no ingestion (if PR > 1) and that the blowing ratio is acceptable. The blowing ratio BR is defined as the mass flux ratio

$$\text{BR} = \frac{\rho_{\text{inj}}\, u_{\text{inj}}}{\rho_{\infty}\, u_{\infty}} \tag{3.1}$$

where inj denotes a particular coolant jet and ∞ the local mainstream. It is desirable to have a low blowing ratio without ingestion to minimise lift-off. A typical value is a mass flux of the coolant jet $\rho_{\text{inj}}\, u_{\text{inj}}$ of 101% of the mainstream flow. Since at the current rig running conditions it is not possible to match the BFPR and cooling hole blowing ratios, while maintaning engine-realistic cooling film pressure margins, the experimental plan is to test at two different blowing ratios. The scaling of these results to engine relevant conditions will need to be further investigated.

With a pressure ratio between 1.02 and 1.15 for the cooling holes, the current NGV cooling configuration is predicted to have no ingestion. At the TE slot the pressure ratio goes from 1.21 to 1.55. On some of the leading edge holes on SS2 and SS1 the exit blowing ratio normal to the surface is bigger than 2 and film lift-off likely. This problem particularly affects the PS2 film.

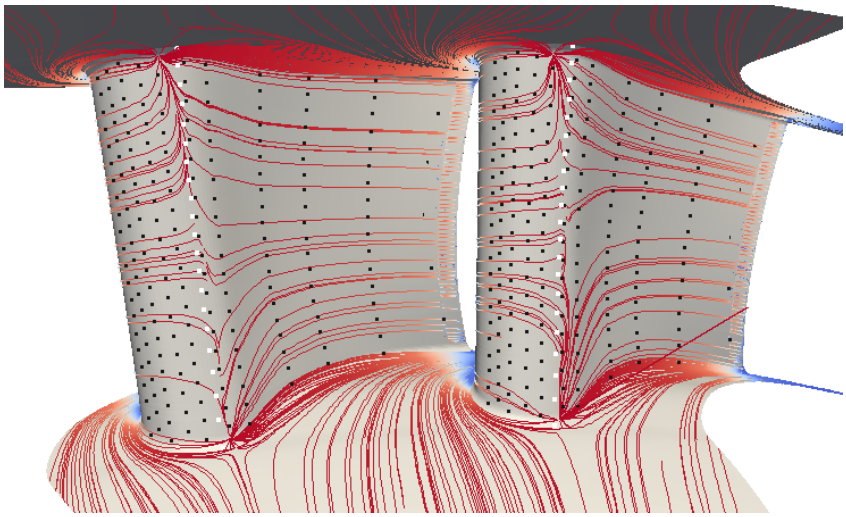

Figure 3.6: HP NGV cooling configuration with superimposed surface streamlines from the CFD calculation by Dr Paul Beard. The black dots mark the exit locations of the cooling holes. The 2D stagnation line is given by the white dots.

The blowing ratios are high close to the leading edge due to the low external velocities near the stagnation point. Until the parts are flow tested, however, this analysis is only based on a best-practice estimation of the C_d and will require updating.

The HP NGV cooling configuration is shown in figure 3.6 together with streamlines obtained from steady isothermal CFD calculations by Dr Paul Beard, which include film cooling and TE slot flows. The streamlines are coloured by static pressure. Despite the swirl and the temperature distortion at the vane inlet, the flow around the vane is very regular. There are no areas of separation and the film cooling offers good coverage. The 3D stagnation line runs between SS1 and PS1 and the films are expected to distribute evenly.

3.2.2 High-pressure rotor blade

The rotor blade also has two internal cavities, designed to reproduce the engine cooling configuration. There are three rows of film cooling holes each on the pressure and the suction side (see figure 3.7). PS2 and PS3 are fed from the rear cavity. The hole diameters and pitch and the inner radial extent of the rows have been scaled down to 73% of the engine target. The radial angle is constant over the blade height for all rows, but otherwise the design criteria and modelling in jb56 are the same as for the HP NGV. More details on the cooling configuration

Row	Diameter	#	Inner Rad	Pitch	Radial Angle	Planar Angle
SS3	0.28	20	267.21	1.22	30°	-50°
SS2	0.28	21	267.80	1.22	30°	-20°
SS1	0.33	22	258.95	1.70	65°	30°
PS1	0.33	22	258.00	1.70	55°	80°
PS2	0.28	25	264.94	1.22	-25°	110°
PS3	0.28	30	258.11	1.26	30°	95°

Table 3.4: Cooling configuration of the HP rotor blade.

are found in table 3.4. The discharge coefficients of the film cooling holes are calculated using the correlations by Rowbury (1998).

The TE cooling consists of seven race-track shaped slots. They extend from 7% to 93% of the blade height and are each 4.9 mm long, 3.0 mm wide and 0.3 mm high. The target flow-controlling area of 0.86 mm^2 per slot is smaller than the actual slot area. Therefore the flow is controlled by two 1.50 mm long, race-track shaped feed holes upstream of the slots with an estimated $C_\text{d} = 0.9$. The number of feed holes is limited by the minimal size of the electrodes used in the spark eroding process. To allow for a mixing out of the two jets before reaching the outer flow, the depth of the slot (see figure 3.5) has to be at least three times the gap between the two feed holes, i.e. 2.85 mm. The slot discharge coefficient is factored by the feed-holes-to-slot area ratio of 0.6 and is set to 0.54 in the jb56 software. It can be updated once experimental values are available.

The coolant feed in the rotor blade is modelled as two separate ducts with the same inlet parameters. Hence, the current model does not account for possible pressure losses in the bucket groove, which can be added once the flow test data is available. The relative total feed temperature $T_{0,\text{feed}}$ is set to 97% of the HP NGV total feed temperature of 290 K which corresponds to 281.30 K. This value will need to be confirmed by rig measurements. Given BFPR = 1.02 and the total relative pressure of a mid-height stream from the q263 results, the total relative feed pressure is $p_{0,\text{feed}} = 5.58$ bar. The outcome of the jb56 calculations shows that

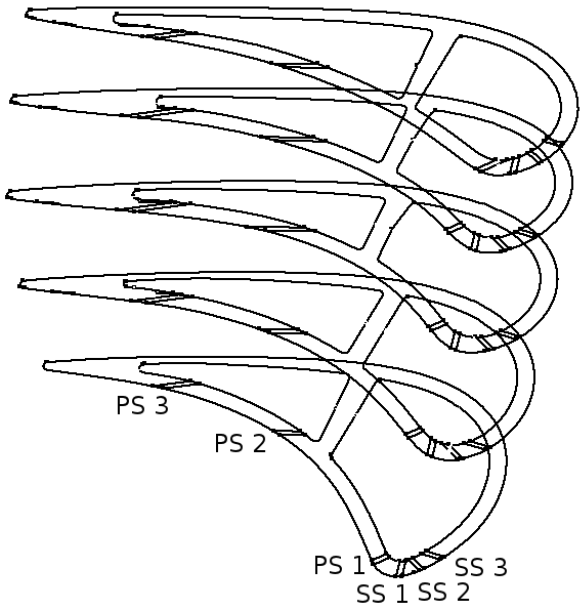

Figure 3.7: Cross sections through the HP rotor blade (without TE slot cooling). This image has been rotated in order to recognise the cooling configuration better.

there is no ingestion expected in the HP rotor blade with a pressure ratio of the cooling holes between 1.10 and 1.38 and little risk of film lift-off due to the low blowing ratios. The pressure ratio at the TE slot goes from 1.34 to 1.49.

In figure 3.8 the exit locations of the cooling holes are plotted together with the streamlines resulting from steady isothermal CFD calculations with cooling flows conducted by Dr Paul Beard. As in figure 3.6, the streamlines are coloured by static pressure. The leading edge films distribute evenly, offering good coverage of the blade and without any lift-off predicted. At the blade tip the blade tip leakage flow vortex is forming.

3.3 Stress analysis of the stator without main flow

The largest differential pressure across the aerofoils occurs at the beginning of a run when the rig is at nearly vacuum and the coolant is blowing at a constant mass flow rate. At this point all cooling holes are choked. The inner cavity pressure can be calculated from the coolant capacity under choked conditions. The coolant capacity Γ of the HP NGV under rig-running conditions

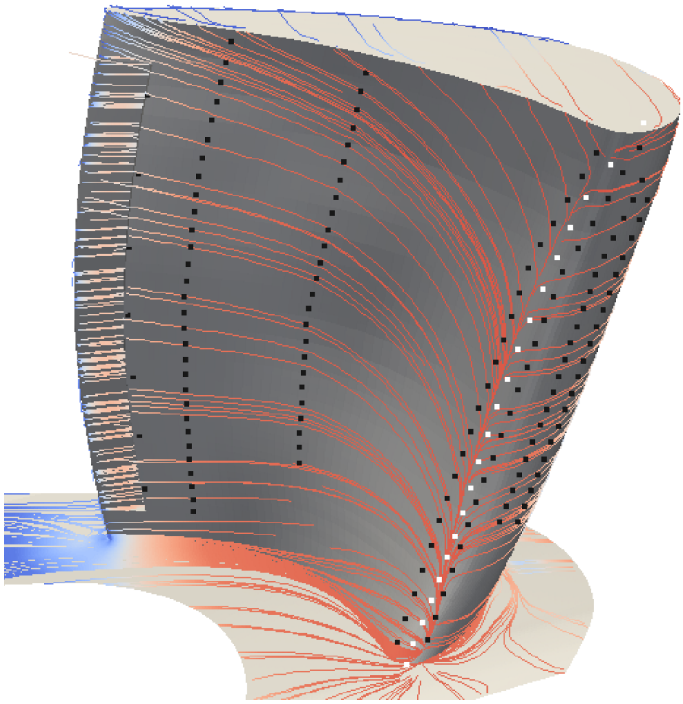

Figure 3.8: HP rotor blade cooling configuration with superimposed surface streamlines from the CFD calculation by Dr Paul Beard.

can be obtained from the results of the modelling of the cooling system in jb56:

$$\Gamma = \frac{\dot{m}\sqrt{T_{0c}}}{p_{0c}} \tag{3.2}$$

with the mass flow rate $\dot{m}$, the total coolant temperature T_{0c} and the averaged coolant total pressure p_{0c} for each row of film cooling holes. The coolant parameters of the HP NGV are summarised in table 3.5.

The 1D isentropic capacity through a given area depends on the area A, the ratio of specific heats γ and the gas constant R, as well as on the pressure ratio p_{0c}/p_{exit} if the flow is not choked. For $M_{exit} < 1$ it is (Luque Martínez, 2011)

$$\Gamma = A\sqrt{\frac{\gamma}{R}}\left(\frac{p_{0c}}{p_{exit}}\right)^{\frac{1-\gamma}{2\gamma}}\sqrt{\frac{2}{\gamma-1}\left[\left(\frac{p_{0c}}{p_{exit}}\right)^{\frac{\gamma-1}{\gamma}}-1\right]}\,. \tag{3.3}$$

This equation can be used to calculate a best-fit capacity curve from the pairs of values of coolant capacity and pressure ratio for each row of film cooling holes. The results are shown in figure 3.9 for the full range of pressure ratios and for the engine-realistic range. The cumulative

Row	Mass flow rate	T_{01}	p_{0c}	Capacity	PR
	$10^{-3}\,\mathrm{kg\,s^{-1}}$	K	bar	$(\times 10^{-8})$	
SS5	5.65	290	8.668	11.10	1.13
SS4	4.87	290	8.347	9.94	1.08
SS3	4.27	290	8.668	8.39	1.05
SS2	3.42	290	8.668	6.72	1.03
SS1	3.21	290	8.668	6.30	1.02
PS1	3.04	290	8.668	5.97	1.02
PS2	3.14	290	8.668	6.16	1.02
PS3	3.57	290	8.668	7.02	1.03
PS4	3.87	290	8.663	7.61	1.04
PS5	6.02	290	8.663	11.83	1.10
PS6 (TE)	17.93	290	8.664	35.24	1.31

Table 3.5: Coolant parameters for each row of cooling holes of the HP NGV.

capacity at choked conditions is the sum of the row-by-row cooling capacities at the nominal choking pressure ratio for 1D compressible flow (1.8929 for a value of $\gamma = 1.4$), which is plotted as a black dashed line. The choked coolant capacity is $2.34 \cdot 10^{-6}\,\mathrm{kg\,K^{1/2}\,s^{-1}\,Pa^{-1}}$ and the coolant total pressure in the inner cavity at the beginning of the run is 4.29 bar. Note that during a run the cavity pressure is 8.67 bar (for a rig operating pressure of 8.5 bar and a BFPR of 1.02) and that the differential pressure is as low as 0.17 bar.

An FEA of the HP NGV was conducted using the Autodesk Simulation Multiphysics Suite to calculate the von Mises stresses on the aerofoil. The two internal cavities of the NGV aerofoil were included in the FE model, but the film cooling holes and TE slots were not modelled. A constant pressure of 4.5 bar was applied on the inner cavity walls. The model had two fixed boundary conditions on the hub and casing surfaces of the aerofoil. The results for the safety factor based on the 0.2% proof strength of 258 MPa for aluminium A357 are shown in figure 3.10.

The highest stresses are observed on the late pressure side, where the rear plenum wall is thinnest. A maximum von Mises stress of 66 MPa was measured in the rear plenum on the TE

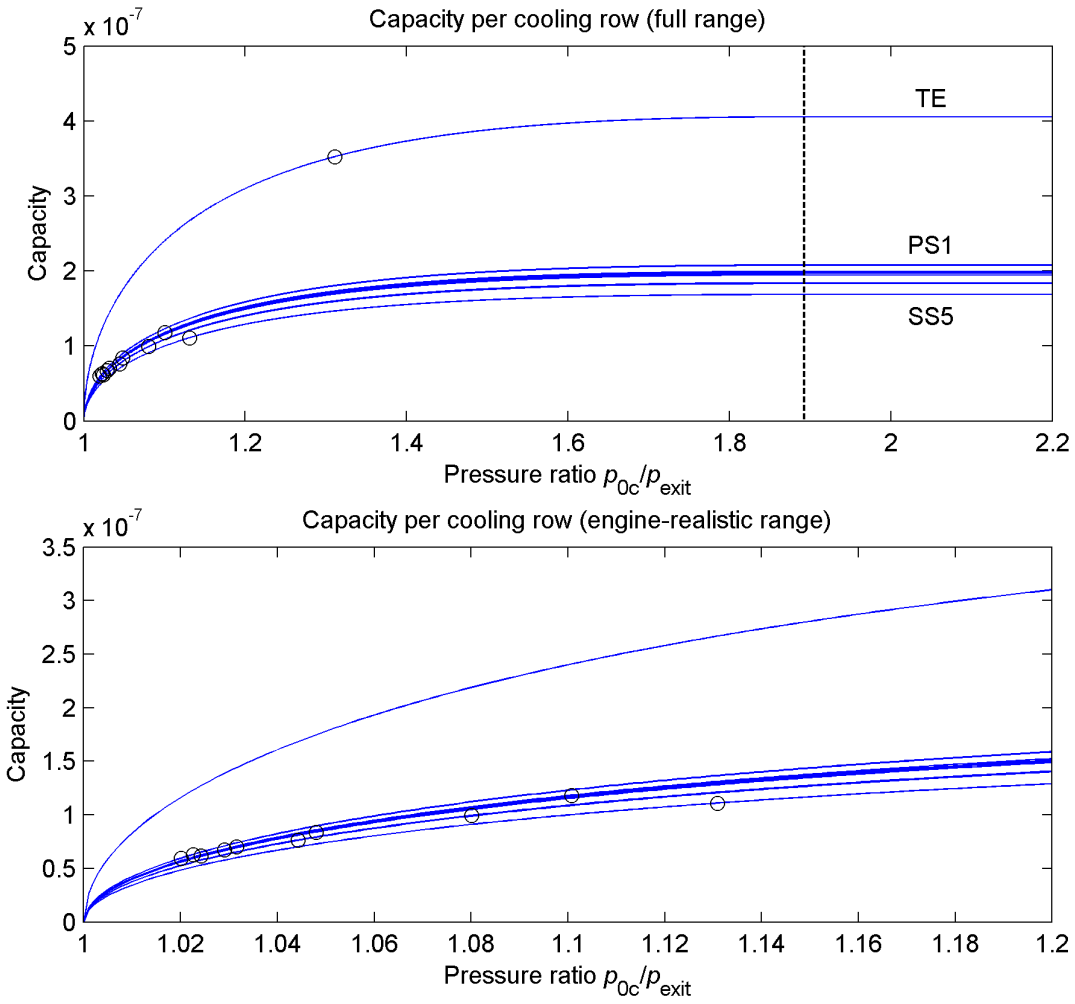

Figure 3.9: Row-by-row cooling capacity curves and rig operating points for each row.

radius, which accounts for the minimal safety factor of 3.90. On the aerofoil walls the stresses will be higher than the modelling results by a factor of 3 because of the stress concentration factor of the cooling holes. There are no cooling holes in the area of highest stress, but PS5 is relatively close. The safety factor is consequently reduced by a factor of 3 when taking into account the cooling holes on the aerofoil.

Currently, the highest pressure the HP NGV can be subjected to in a worst case scenario is 9 bar (set by the safety valve relief pressure). The FEA was also conducted with a constant pressure of 9 bar on the inner cavity walls. The boundary conditions were the same as before. Figure 3.11 shows the results for the safety factor in this high pressure case. The stress pattern

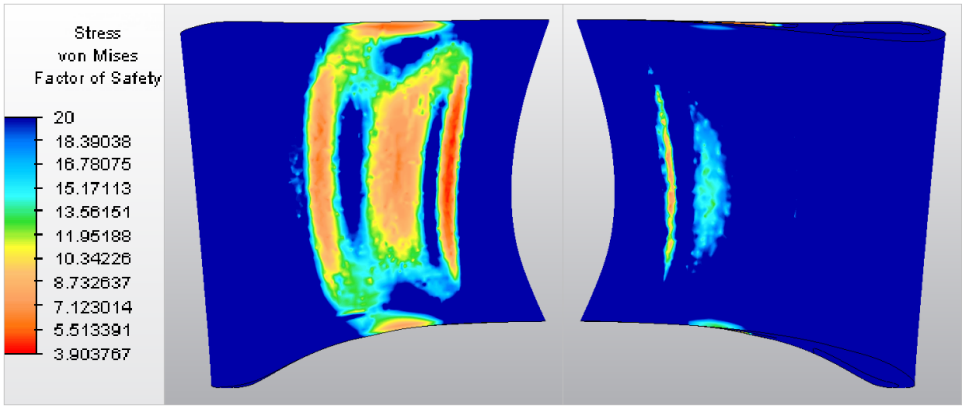

Figure 3.10: Stress von Mises factor of safety at 4.5 bar (left: pressure side, right: suction side).

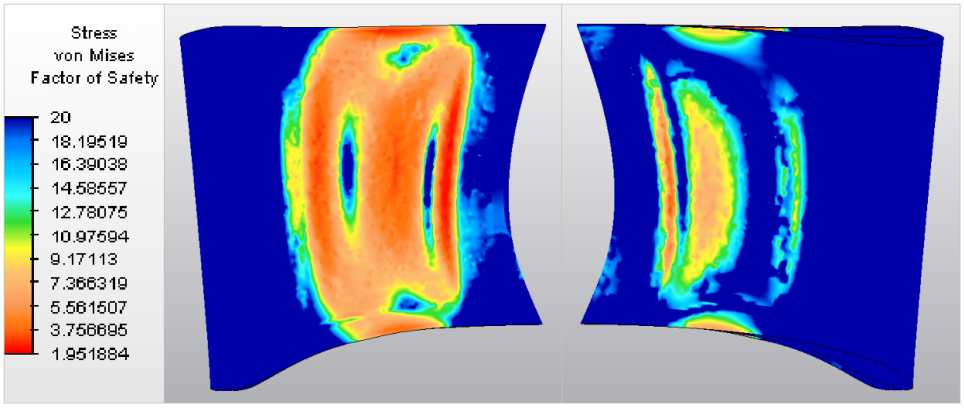

Figure 3.11: Stress von Mises factor of safety at 9 bar (left: pressure side, right: suction side).

is the same, but the maximum von Mises stress has gone up to 132 MPa. The minimum safety factor is 1.95 on the rear plenum TE radius. Given the safety factor of just above 3 on the aerofoil walls, the NGV is likely to yield on the pressure side by the cooling holes (stress concentration factor of 3). The NGVs would not survive a pressurisation to 9 bar undamaged and measures to reduce the maximum differential pressure will need to be investigated before installing the NGVs.

3.4 Mechanical assessment of the rotor blade

The stress analysis of the HP turbine blade was performed using the Rolls-Royce FEA software sc03. This in-house code was developed to carry out 2D and 3D mechanical and thermal assessments of turbine components. It is also a platform for several other Rolls-Royce programmes,

such as jb56. The aim of sc03 is to calculate temperatures, deflections, strains and stresses in a body with applied mechanical and/or thermal loads. Given that the OTRF has a relatively low inlet total temperature of less than 500 K and a run time of only 0.7 s it can be assumed that the aluminium blade maintains a constant wall temperature of $T_w = 290\,\mathrm{K}$. Therefore a thermal analysis of the blade was not required.

There are three main assumptions made by sc03 (sc03 Manual, 1999). Firstly, it is assumed that the application of the loads is sufficiently slow, so that the mechanical response is quasi-static. Secondly, an additive strain decomposition is accepted as valid, because the strains are expected to be sufficiently small[1] and, thirdly, the effect of load stiffening on the normal modes is assumed to be negligible apart from that of the centrifugal loads.

In this chapter the elastic modelling of the stresses on the blade and the disc is presented and the results are discussed. The high-stress regions on the blade root and the disc post have been carefully analysed taking into account the effect of the notches. Finally, a stress based assessment of the fatigue life follows. A vibrational analysis of the bladed disc gives insight into the dynamic characteristics of the system and provides the natural frequencies, which determine the margin between the design speed and critical resonances.

3.4.1 Modelling of the steady-state stresses

The rotor design described in section 3.1 was assessed on an axisymmetric 6° bladed disc sector to reduce the computational cost. It included the two lower labyrinth seals and the two upper cover plates (see figure 3.12) as well as the two internal cavities and the TE slot cooling, but not the cooling holes. The mesh for the FEA was created using the automatic mesh generator implemented in the programme on a solid model of the geometry. Even though sc03 is often used as an automatic analysis tool in which the programme meshes, analyses and if necessary refines the mesh until a previously defined accuracy is achieved, it can also perform non-adaptive analyses on separately specified meshes, as was done here. The refinement of the mesh depends on the application (static or dynamic calculation). In this case – again to reduce calculating

[1] Note, this does not preclude geometric non-linearity, inelastic strain – as with creep and plasticity – or surface contact non-linearity (sc03 Manual, 1999).

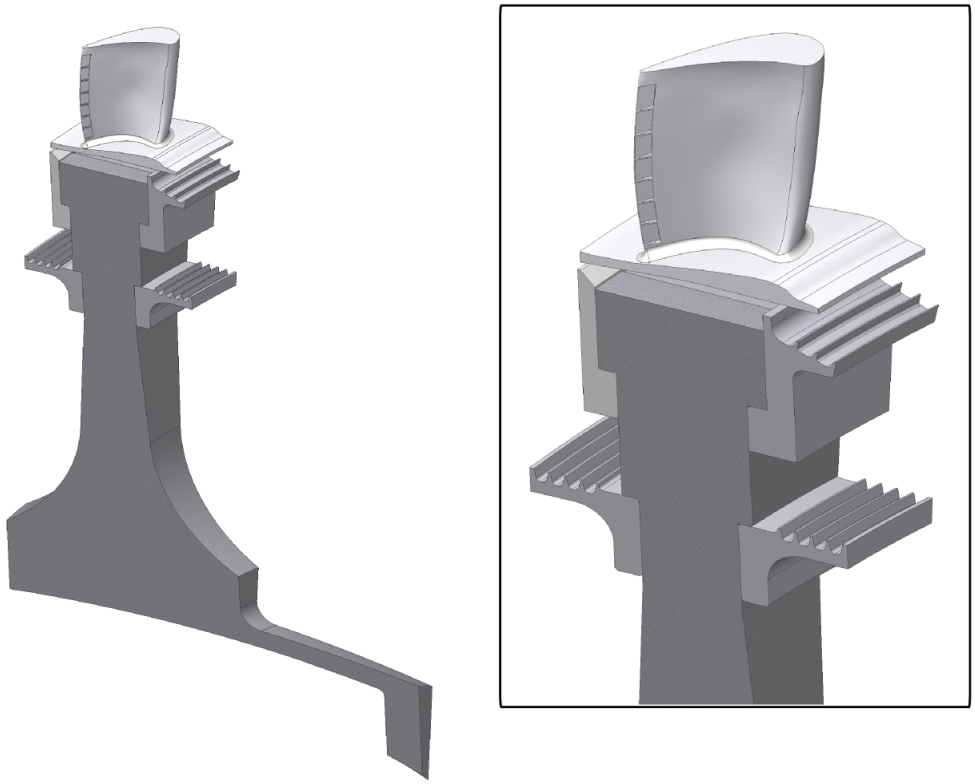

Figure 3.12: Bladed disc sector for the mechanical analysis. In order to avoid cutting through the blade, the disc is split along the 20° axis of the blade root.

time and in result increase the flexibility of the analysis – two different unstructured meshes were generated. One mesh had a very fine local resolution of the disc and a coarsely resolved blade and vice versa. Both meshes are shown in figure 3.13.

In regions where high stresses are expected, such as the blade root or the bucket groove, it is important to manually include a certain number of internal nodes. Otherwise, sc03 will deliver a very low-quality internal mesh and it will not be possible to accurately assess the stress decay. The present model was meshed with a minimum of one internal node layer and up to four internal node layers in the regions mentioned above. The mesh characteristics of the steady-state stress analysis are summarised in table 3.6.

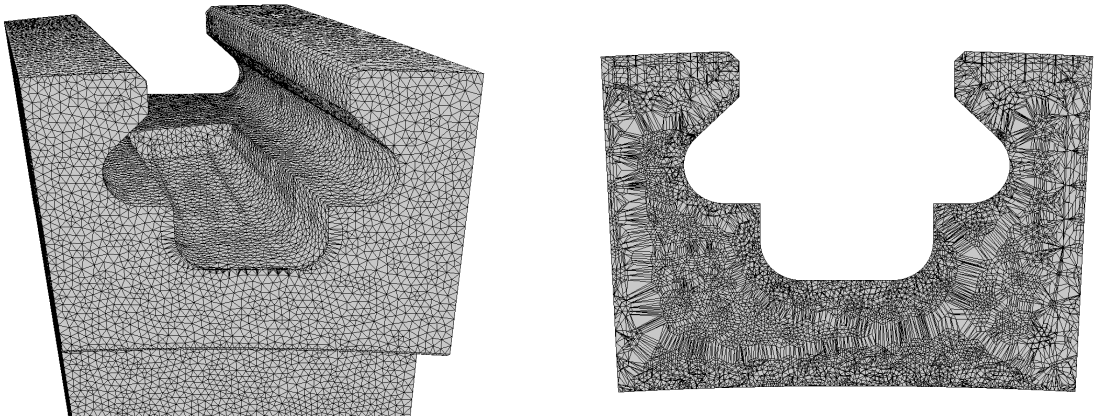

(a) Disc Mesh

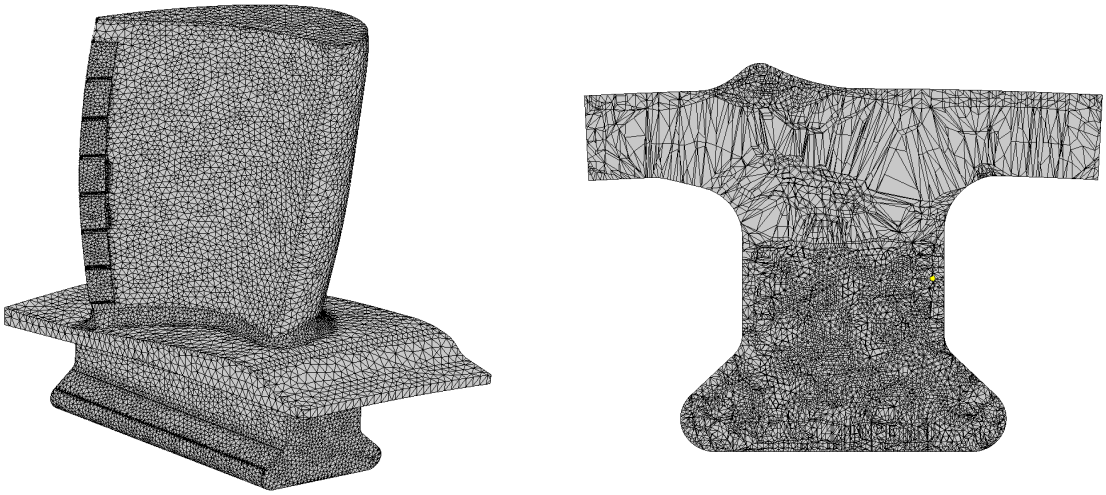

(b) Blade Mesh

Figure 3.13: Mesh for the steady-state stress analysis showing internal node layers at notch features of interest.

	Disc Mesh	**Blade Mesh**
Type of elements	Tetrahedra	Tetrahedra
Number of elements	420 294	224 291
Average edge length	1.26 mm	1.55 mm

Table 3.6: Mesh characteristics of the disc and blade for the FEA.

Boundary conditions

The boundary conditions defined for the bladed disc sector are depicted in figure 3.14. Cyclic joints were applied on the sides of the disc and of the seals to represent the whole rotor, while circumferential restraints stopped the bodies from moving in the circumferential direction. The inclined contact surfaces (pressure flanks) between the blade and the disc were modelled with sliding joints. These joints restrain the movement of the faces in the normal direction, while allowing them to slide in the other two directions. The same restraint was used on the ledges between the seals and the disc to model the radial contact. The disc was axially fixed by defining a zero normal displacement on the front face of the disc (see figure 3.12).

Sliding joints were also set on the axial contact faces between the seals and the disc, where the cover plates and the labyrinth seals are respectively clamped onto the disc. In order to avoid having internal threads on the rotor disc, the front rings are bolted into their rear counterparts with 16 M5 bolts, which cause a clamping pressure between the contact faces of only about 0.3 MPa.[1] The clearance of the holes on the disc is large enough not to put a circumferential load on the bolts.

Finally, the blade was axially fixed onto the rear cover plate with a sliding joint. The front side of the blade, however, was modelled as an open joint, in which the faces can move independently from each other. This restraint accounted for the fact that given the machining tolerances and the blade set-up it is likely to have a clearance which, from a stress point of view, is a more conservative modelling, since higher stresses are expected.

The finished model was used to run two isothermal analyses with $T_w = 290\,K$ on both meshes: one at the design speed of 8525 rpm and one at an overspeed of 12000 rpm. This value corresponds to the maximum rotational speed that the OTRF can achieve, which is around 10000 rpm, plus a 20% safety margin. When commissioning a new turbine stage it is necessary to carry out an overspeed test in a spin-test facility. Therefore, this stress analysis not only has to prove the durability of the new rotor at the operating point, but also show that it can withstand the spin-up to 12000 rpm. The pressure load applied on the aerofoil was obtained

[1] Following advice from the Rotatives department at Rolls-Royce the number of bolts for the cover plates was later reduced from 16 to 6, which increased the clamping pressure to 0.8 MPa.

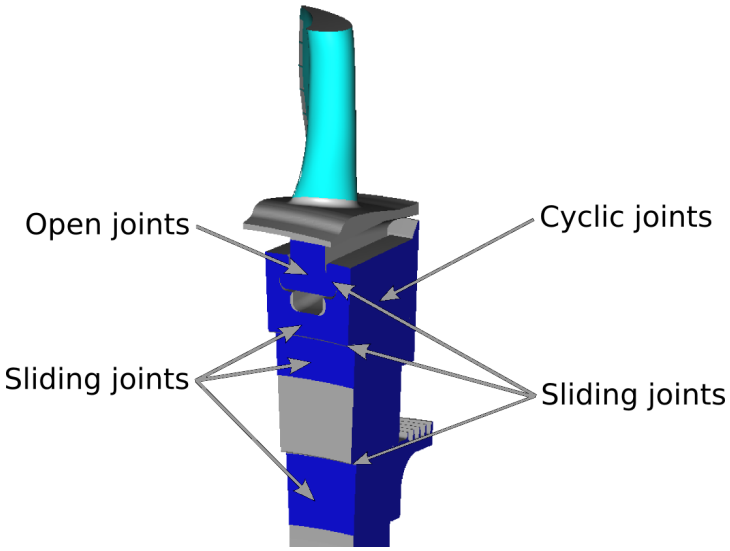

Figure 3.14: Boundary conditions for the steady-state stress analysis.

from CFD calculations and mapped on the pressure and suction sides, but it had a very small effect compared to the centrifugal loads, as the next section will show.

Evaluation of life-limiting features

For a mechanical analysis of a bladed disc sector various criteria need to be studied. First of all, an assessment of the dovetail root is performed. Therefore, the crushing load on the contact faces between the blade and the disc is calculated. The crushing load results from the centrifugal load of the blade and is a function of the shaft speed. The corresponding crushing stresses are compressive stresses, which are generated between the contact faces – also known as bedding area – and can be calculated from the reaction forces on the contact faces. The Rolls-Royce design criteria currently limits the allowable crushing load to 60% of the minimum of 0.1% elongation proof strength of the weaker of the blade and disc materials (RR Stress Criteria, 2011).

At 12000 rpm the crushing stresses of the current design are approximately 73 MPa on the contact face at the pressure side of the blade and approximately 83 MPa on the contact face at the suction side. Even at the higher rotational speed, the crushing load is less than 40% of the minimal 0.2% proof strength $\sigma_y = 258$ MPa of the blade material, which as an aluminium cast

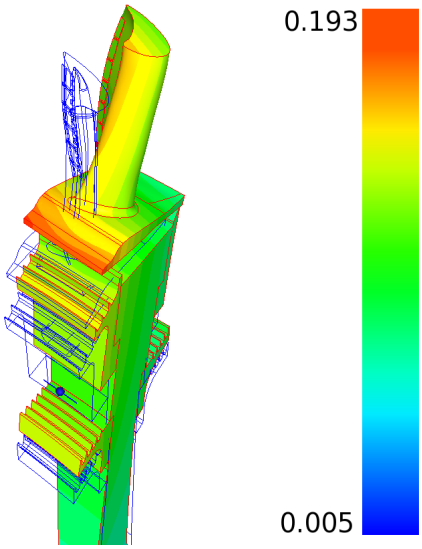

Figure 3.15: Deflection of the bladed disc sector under a centrifugal load of 8525 rpm (not to scale). The radial displacement is plotted in mm. It is minimal at the fixture of the disc on the shaft.

is weaker than the stainless steel used for the disc. The crushing stresses are consequently well within the margins established by Rolls-Royce.

The difference between the load on the pressure and suction sides of the blade root has several reasons. Note that the design process ensured that the centre of gravity of the aerofoil is centred on the blade shank and hence a circumferential unbalance of the blade can be excluded. The displacement of the centre of gravity caused by the centrifugal and gas loads leads to a torque on the blade root (see deflection in figure 3.15), resulting in a higher load on the suction side of the dovetail. The gas bending moment alone accounts for about 8 MPa difference. If a perfect balancing was necessary, it would require a further iteration in the design process to locate the optimal axial position of the aerofoil on the blade platform. The deformation is simultaneously influenced by restoring moments and non-linear effects on the contact faces, which are very difficult to estimate. Ultimately, if the difference between the load on the pressure and suction sides is smaller than 15%, as it is here the case, it is considered unimportant.

From a lifing point of view, the decisive factor are the stresses at the operating point, but as previously explained a safe operation of the overspeed test has to be demonstrated. The steady-state stresses of the blade at 12000 rpm are displayed in figure 3.16 with the areas of

highest stresses – the life limiting features – clearly recognisable on the blade root fillet. The fatigue notch factor or strength reduction ratio K_f can be used to evaluate the stresses and the endurance of the part. K_f describes the ratio of the fatigue strength of a smooth, unnotched specimen S_f to the fatigue strength of a specimen with a notch:

$$K_\mathrm{f} = \frac{S_\mathrm{f}}{S_\mathrm{f,notched}} > 1 \,. \tag{3.4}$$

To accurately apply this empirical factor to a real geometry is only possible if the notch sensitivity of the material is closely characterised (Grote and Feldhusen, 2007). Instead, the stress concentration factor (also generally known as notch factor)

$$K_\mathrm{t} = \frac{\sigma_\mathrm{max}}{\sigma_\mathrm{n}} > 1 \tag{3.5}$$

with the greatest elastic stress in the area of a notch σ_max and the corresponding nominal stress σ_n is often used. The stress concentration factor is a theoretical indication of the effect of a notch on the mechanical behaviour. It is usually higher than the fatigue notch factor, because it does not take stress relief due to local plastic deformation into account. Accordingly, using K_t rather than K_f is easier and quicker to calculate and the plasticity effects are inherently included in the specimen fatigue curves. Therefore, the K_t based method is as realistic as the K_f based approach if a fatigue curve with a representative K_t value is used. For the present study only elastic calculations were performed, as the computing cost of including plastic effects is very high in comparison.

The highest stresses are observed in highly-notched features. At the dovetail they can reach up to $\sigma_\mathrm{max} = 450\,\mathrm{MPa}$ (see figure 3.16). A calculation of the stress concentration factor from the stress decay assuming isotropic material properties, gives $K_\mathrm{t} = 2.26$ and $\sigma_\mathrm{n} \approx 200\,\mathrm{MPa}$. The nominal stresses at the blade root are therefore smaller than the proof strength of the blade material. As notch factors are often tabulated, it is common practice to round them down to the next smaller value in the tables. If the same notch factor is interpolated from the stress decay one obtains $K_\mathrm{t} \approx 3.58$, which indicates that the first calculation was rather pessimistic. In the following section the fatigue life of this particular feature will be predicted.

This information is, however, not enough to determine whether the blade will be able to

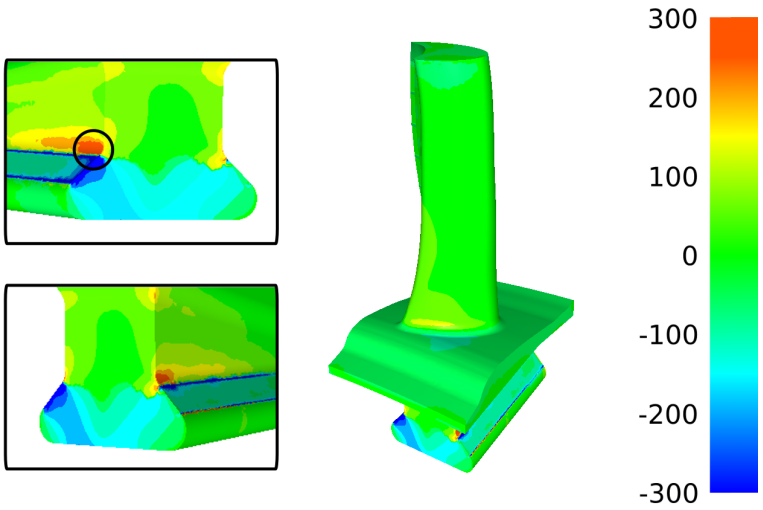

Figure 3.16: Worst principal stresses of the blade at 12000 rpm in MPa. The worst principal stresses are the numerically highest principal stresses. The circle marks the region of highest stress with $\sigma_{\max} = 450\,\text{MPa}$.

withstand the applied load. A more accurate prediction is given by an estimate of the terminal speed. The terminal speed is the shaft speed at which a fatal failure is expected. Instead of looking at the peak stress, the mean principal stress in radial direction σ_{yy} on a circumferential cross section is calculated. This value is then compared to the yield strength of the material (which is a more conservative approach than using the ultimate tensile strength). The factor between the two can be used to extrapolate the speed at which the cross section will reach the yield strength under the assumption that σ_{yy} is proportional to n^2. The lowest terminal speed of the blade is obtained at the fillet on the blade shank, but at approximately 27000 rpm it is still far above the maximum rotational speed.

The rest of the blade was investigated especially with regard to the cooling holes which were not modelled. In the areas of the aerofoil with cooling holes the stresses are expected to go up by a factor of three (corresponding to the stress concentration factor of a cylindrical hole), but even then the stress level is lower than at the shank. This statement also applies to perforations that will to have to be drilled for instrumentation purposes on the platform or on the aerofoil. Regarding possible cracks or pores in the turbine parts, these parts are cast according to a high quality casting specification based on aerospace material standards (SAE, 2010), which ensures that only parts that meet the standard are used on the rig. Furthermore, dye penetration tests

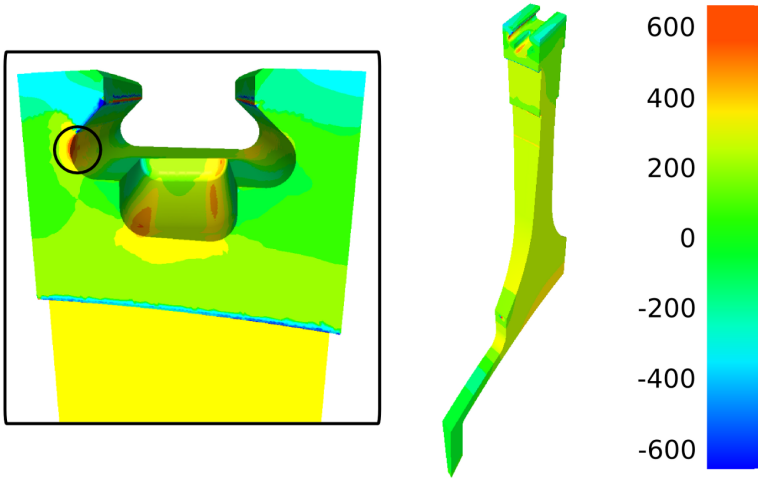

Figure 3.17: Worst principal stresses of the disc at 12000 rpm in MPa. The circle marks the region of highest stress at the disc post with $\sigma_{\max} = 733$ MPa.

are performed routinely in order to detect possible surface cracks that may appear during use. For this reason it was not necessary to perform a fracture mechanics analysis of possible cracks or pores in the turbine castings.

When running the OTRF it is very important to have an accurate estimate of the blade tip clearance. The design tip gap for the test turbine is 0.25 mm, which is typical of engine clearance. In order to ensure this target is met, the radial growth of the blade during the spinning has to be taken into account. At the operating speed of 8525 rpm the maximum radial displacement of the blade tip is 0.170 mm (see figure 3.15). The blade root was displaced by this value when designing the rig at static conditions.

The steady-state stresses of the disc at 12000 rpm are shown in figure 3.17. The highest stresses were predicted in the region of the disc post and on the inner radii of the ledges for the cover plates and labyrinth seals. The contours of the disc stresses look similar to those calculated by Goodisman (1991) and Fowler (1994) when the previous disc used in the facility was developed. Both disc designs show a characteristic radial distribution of the stresses (see figure 3.18).

The highest stresses at the disc post, $\sigma_{\max} = 733$ MPa at 12000 rpm, are on the curve next to the contact faces (see figure 3.17). It is $K_t = 1.66$ and $\sigma_n \approx 440$ MPa, which means that the

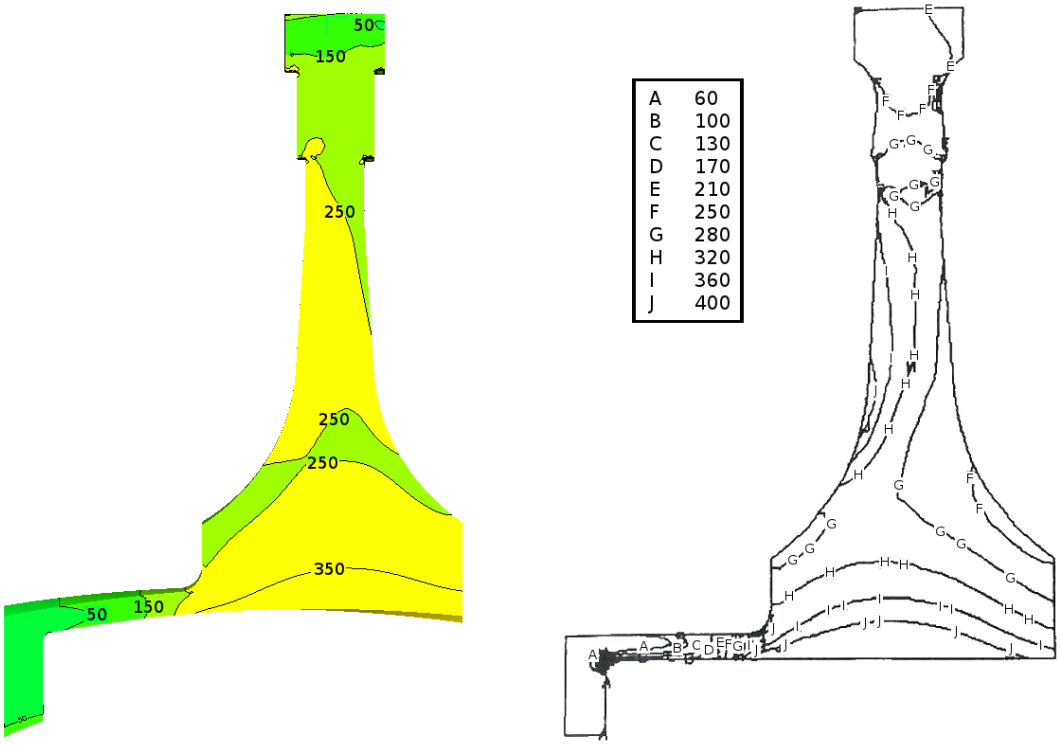

Figure 3.18: Comparison of disc stresses at 12000 rpm with results from (Fowler, 1994) on the right. The lines mark regions of constant von Mises stresses (in MPa). The labyrinth seals are not shown.

nominal stress at the notch root is below the yield strength $\sigma_y = 650\,\text{MPa}$ of the stainless steel used for the disc (EN24T). In the rest of the bucket groove the stresses are below the yield, even at the higher shaft speed. Any instrumentation that is needed to monitor the air going into the blade cavities – such as pressure transducers or thermocouples – can be embedded in the base area of the slot that feeds the coolant. The terminal speed of the disc can be estimated following the explanation above as 31000 rpm at the position of highest stress of the disc post. This means that in the case of a failure the blade would break first. From a design point of view this succession is very important, because a blade release is less dangerous than a bursting of the disc. In the next section the actual life expectancy will be assessed.

sc03 is known to overpredict the stresses at the edge of the bedding. The stress concentration that appears on the disc post along the edge of the contact faces in figure 3.17 is unrealistic in both its position and magnitude and can be disregarded. However, these false stresses might

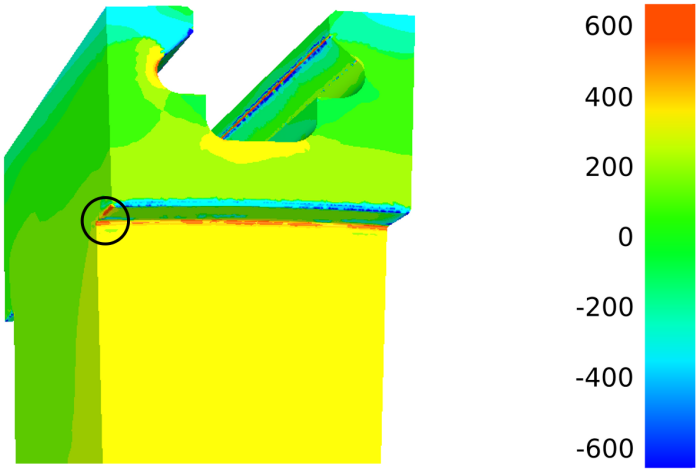

Figure 3.19: Worst principal stresses at the front ledge of the disc at 12000 rpm in MPa. The circle marks the region of highest stress in the fillet with $\sigma_{max} = 960$ MPa. The stresses on the lateral edge are not real.

have had an influence on the crushing stresses calculated earlier. It is possible that a peaking stress value at the edge of the bedding has intensified the asymmetry between the pressure and suction side of the blade root.

The highest stresses of the disc were actually predicted at the ledges designed to hold the cover plates and the labyrinth seals. At 12000 rpm the front side of the disc experiences stresses up to $\sigma_{max} = 960$ MPa on the inner radius with $K_t = 2.26$, as shown in figure 3.19. The nominal stress in the notch base is $\sigma_n \approx 425$ MPa and hence lower than at the disc post. In order to reduce these stresses the radius will be increased from 0.2 mm to 0.5 mm. Given that the crushing stresses on the contact face are very small, it is not a problem to slightly reduce the area. The stresses at the downstream side of the disc are – as expected – much lower, because the weight of the seals is smaller. The stresses are all below the yield strength.

The labyrinth seals are only spun-up to maximally 10000 rpm during the overspeed test. The highest stress at the lower ledge is $\sigma_{max} = 900$ MPa with $K_t = 3.62$ and a resulting nominal stress $\sigma_n \approx 250$ MPa. For the mechanical assessment of the new rotor the cover plates and the labyrinth seals have been evaluated, too. They are made of the same stainless steel as the disc and at 12000 rpm their maximum stresses stay below the yield strength of 650 MPa.

In order to assess the general quality of the calculation, sc03 incorporates an estimation of the

discretisation error in the FE results. For the local stresses sc03 uses a residual based method, which involves substituting the discrete solution into the underlying differential equation and measuring the discrepancy to the exact solution (sc03 Manual, 1999). This stress error can then be plotted as a percentage of the worst principal stresses. Due to the poor internal meshing of sc03 it is unavoidable to have local regions of high mesh distortion and consequently high stress error. This is not a concern, as long as the areas of high stress are finely resolved and the stress error is kept below 10%. The overall quality of the two meshes was considered good with stress errors within an acceptable range in the critical regions.

Stress based fatigue lifing

In the chosen lifing approach the life of the rotating parts is limited by the areas of highest stress. Since at the design speed the stresses of the blades and disc are below the corresponding yield strengths it is not required to assess their life. The following lifing estimations are based on the stresses at 12000 rpm of the life-limiting features presented above. To obtain the expected life empirical S-N curves are used, which show the relationship between a stress S and the number of cycles to failure N. It is important to be consistent in the definition of the stresses. Since only elastic stresses have been modelled, they have to be used to determine the life. Plastic effects are taken into account by the location of the S-N curves.

The S-N curve of the EPIC A357 aluminium cast is shown in figure 3.20 together with the S-N curve of a conventional A357 aluminium cast. They are, however, only valid for smooth specimens with $K_\mathrm{t} = 1$ and not for the notched features, where the highest stresses are observed. Using this S-N curve for a part with $K_\mathrm{t} > 1$ is either a too pessimistic approach, because if the maximal stress σ_max is used, it assumes that stress over the whole cross section or a too optimistic approach if the nominal stress at the notch σ_n is used. For $K_\mathrm{t} > 1$ the curve is displaced to the left, so that at the same stress the number of cycles to failure is reduced.

Since the fatigue curve for $K_\mathrm{t} = 1$ is not sufficient to assess the life of the blades, it is supplemented with notched fatigue data from literature (see table 3.7), which corresponds to a conventional A357 aluminium cast comparable to the A357 baseline of the supplier. The values in the table show that a smooth specimen has the same life expectancy as a notched

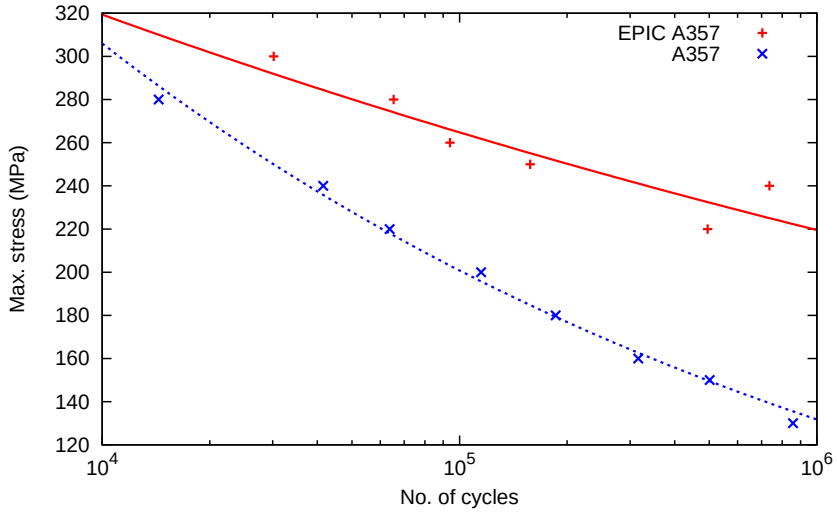

Figure 3.20: S-N curve for conventionally cast A357 aluminium and for EPIC A357 at room temperature with $K_t = 1$ (from (Tritech)).

Specimen	Maximal Stress	Cycles to Failure
$\mathbf{K_t = 1}$	24	148 000
	24	198 000
	24	205 000
	24	167 000
	24	269 000
	24	299 000
$\mathbf{K_t = 3}$	14	83 000
	14	236 000
	14	215 000
	14	307 000
	14	373 000
	14	214 000

Table 3.7: Fatigue data for smooth and notched A357 cast plates (from (Gunther, 1979)). The maximal stresses are given in ksi with 1 ksi = 6.895 MPa.

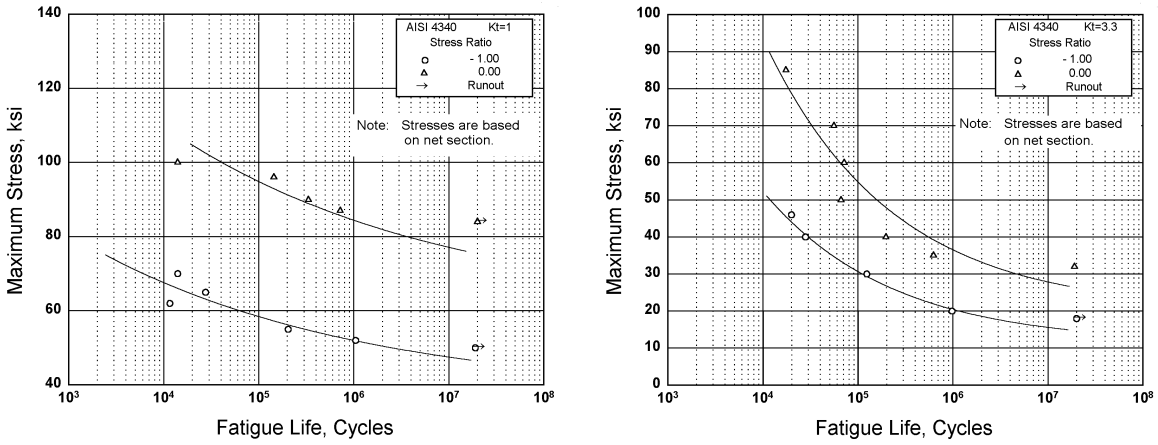

Figure 3.21: S-N curves for EN24T at room temperature (from (MIL-HDBK-5H, 1998)).

specimen with a stress concentration factor $K_\mathrm{t} = 3$ at around 50% of the stress. If this stress concentration factor is assumed for the life-limiting feature at the blade root, a nominal stress $\sigma_\mathrm{n} \approx 150\,\mathrm{MPa}$ is obtained. Following the ratio of notched to unnotched stress from table 3.7, the number of cycles to failure for the notched feature can be read off figure 3.20 for a maximal stress of 300 MPa. For the EPIC A357 aluminium cast the expected life is about 10^4 cycles corresponding to 40 years at 250 runs of the OTRF a year.

The company that manufactured the disc billet does not supply any fatigue data, but EN24T is a widely used steel and literature is commonly available. In figure 3.21 the S-N curves for a smooth and a notched specimen ($K_\mathrm{t} = 3.3$) are displayed. The highest stresses at the disc are measured at the disc post. However, the local stress concentration factor is $K_\mathrm{t} = 1.66$ and thus considerably smaller than that of the fatigue curve in figure 3.21. A conservative estimate of the life is achieved if the assessment uses the nominal stress at the notch root $\sigma_\mathrm{n} \approx 440\,\mathrm{MPa}$, which corresponds to the smaller notch factor, on the curve of the larger notch factor. In this case the stress ratio $R = \sigma_\mathrm{min}/\sigma_\mathrm{max}$ is 0 and a life in the order of 10^4 is obtained.

3.4.2 Vibrational analysis

The model with internal cavities shown in figure 3.12 was also used for the dynamic analysis of the bladed disc sector. The cooling holes are not expected to have any influence on the stiffness of the blade and thus on its dynamic properties. The aim of a modal analysis is to determine the

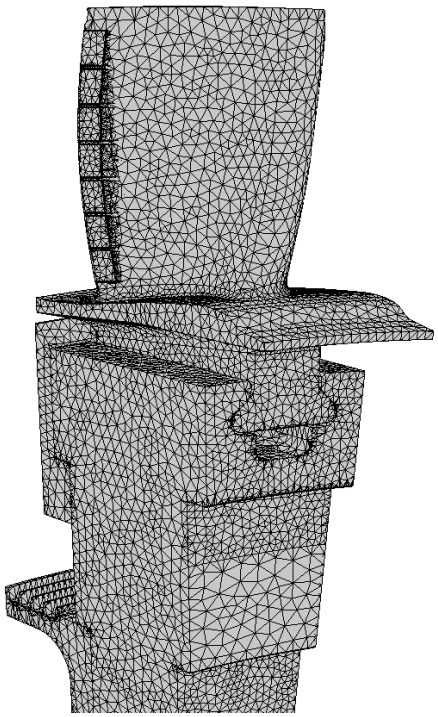

Figure 3.22: Mesh for the dynamic analysis.

eigen frequencies of a system. How likely resonance is to occur depends on the margin between these natural frequencies and the excitation frequencies. Information on how sc03 calculates the natural frequencies and the modes is found in the sc03 manual (sc03 Manual, 1999). There is no need for internal nodes and the overall mesh size can be reduced (see figure 3.22). This new mesh has a total of 90 019 elements and an average edge length of 2.73 mm.

In a bladed disc the dynamic properties of the blades and the disc merge and become more complex. The frequency of the blade modes is reduced by the disc flexibility, depending on the vibration of the disc itself. The disc has a sinusoidal vibration shape, which creates radial lines of zero displacement named nodal diameters. The higher the number of nodal diameters, the stiffer the disc is. When external cyclic forces are applied to the system, the vibration response will have the same frequency as that of the excitation source. The magnitude of the response depends on the damping properties of the component and on how close the excited frequency is to one of the eigen frequencies of the system.

The excitation forces affecting turbine blades in an engine usually come from (upstream or

downstream) modifications of the gas flow. They are commonly referred to as engine order (EO) excitations and their frequencies are proportional to the shaft speed. Geometry differences due to manufacturing tolerances or an out of balance rotor can cause asymmetric flow perturbations, which are captured by low engine orders (1 to 10 EO). The frequency associated with a certain EO at a given rotational speed n can be calculated as

$$f\ [\mathrm{Hz}] = \frac{n\ [\mathrm{rpm}] \cdot \mathrm{EO}}{60}\ . \tag{3.6}$$

The most common method to identify critical combinations of excitation and vibration frequencies for rotating components is to plot them together in a Campbell diagram. This diagram shows periodic excitation sources (engine orders) and the natural frequencies – hence, accounting for stiffening and softening effects.

It is expected that the stiffness of the bladed disc sector is strongly influenced by how the cover plates and lower labyrinth seals are attached to the rotor. Therefore, the definition of the boundary conditions needs to be revised. From a stress point of view the realistic boundary conditions are those defined at the beginning of this section. For the dynamic analysis a distinction between the "clamped" case, in which the seals are fully attached to the rotor, and the "open" case, in which the seals interact as little as possible with the rotor, is introduced.

In the open case cyclic joints were still used to model the whole rotor, but all the axial contacts between the cover plates or the seals and the disc were reduced to open joints, which meant that the surfaces did not restrain each other and could move independently. The cover plates and the seals were only fixed to the disc with sliding joints at the ledges. This model corresponds to the case in which there is an axial gap between the parts.

Once the disc is spun up, the dynamic forces are too small (compared to the centrifugal loads) to cause a relative sliding of the inclined contact faces between the blade and the disc. Therefore, fixed joints were applied on these faces for the dynamic analysis, which means that the surfaces acted as if they were attached to each other. In addition, the blade was axially restricted to the disc by point-tying of a node at the blade root to the closest node on the disc.

The results for the open case are summarised in the Campbell diagram on figure 3.23. The most interesting excitation source is the 40 EO, because it corresponds to the number of NGVs.

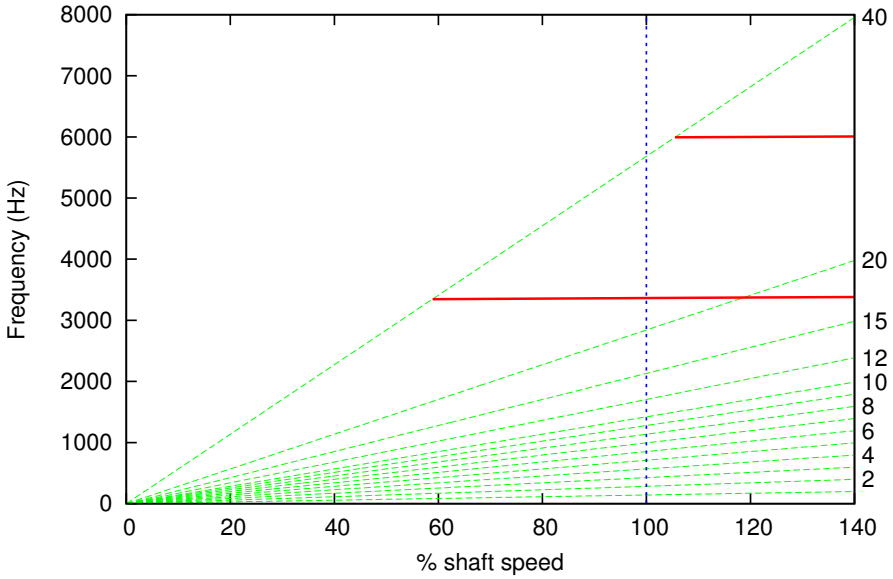

Figure 3.23: Campbell diagram for the open case. The first and second mode are shown in red. The green lines correspond to the EO excitation. 100% shaft speed is the current design speed of 8525 rpm.

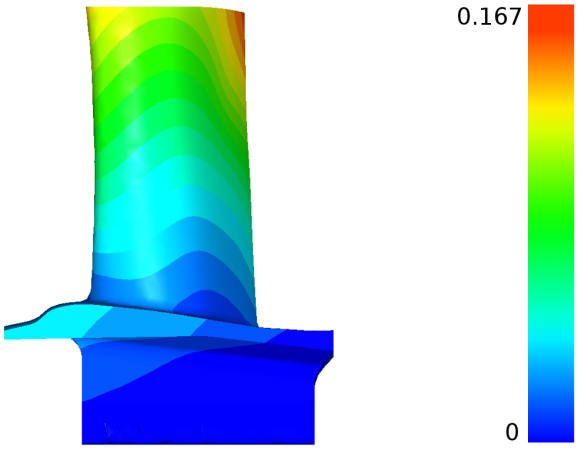

Figure 3.24: Displacement contours of the second edgewise mode for the open case. The resulting displacement is plotted in mm.

It excites the second mode with 40 nodal diameters of the disc at 105.5% of the operating speed with a frequency of 5993.1 Hz. The mode shape of the blades is edgewise and the expected displacement is shown in figure 3.24. As the margin to the resonance speed is bigger than 3% it is considered safe by the European Aviation Safety Agency certifications (CS-E, 2010) and there is no need for further resonance work to assess the alternating stresses.

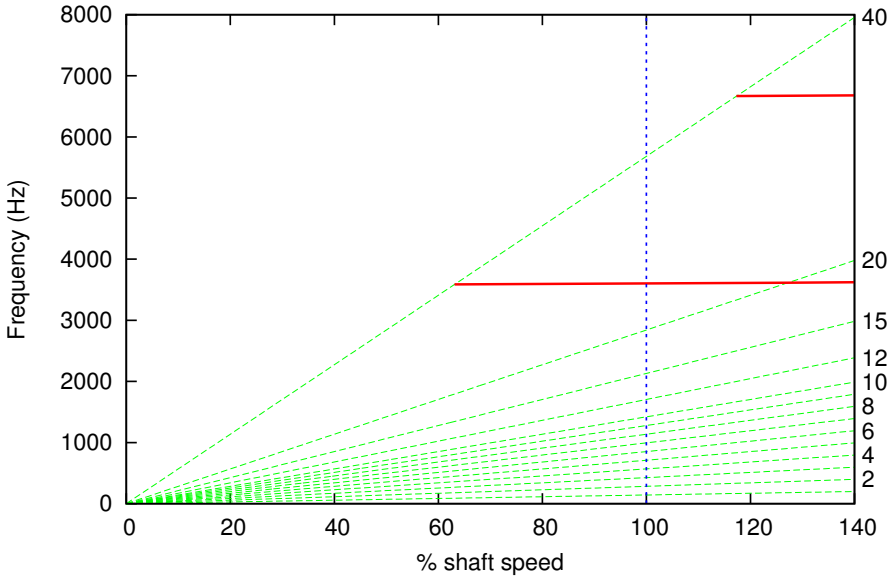

Figure 3.25: Campbell diagram for the clamped case.

The first mode is excited by the 40 EO and the 20 EO (the number of swirl and temperature distortion generators), but well outside the operating range at 58.9% and at 118.6% design speed. The lower EOs do not pose a problem. Moreover, this simulation is a worst case scenario, because if the stiffness of the system is increased by modelling the clamping of the cover plates and the seals onto the disc the eigen frequencies rise. It can be assumed that in reality there will be some friction between the seals and the disc or the blades and therefore the margin to the resonance speed is likely to be larger.

For the clamped case all the contacts between the cover plates, the labyrinth seals and the disc were set as fixed joints. This means that all the contact faces behave as if they were permanently attached to each other. The results are shown in figure 3.25. As expected, the natural frequencies of the second mode increased considerably – the 40 EO excites the second mode at a frequency of 6662.7 Hz. The margin to the resonance speed has increased by 11.8% to 117.3% of the design speed.

The stiffening of the axial fixation has a significant impact because it restricts the motion along the blade root, which strongly affects the edgewise mode. The first mode frequencies have only increased by between 4.2% and 8.6% and are still not a source of concern. The vibration frequency of the finished parts will be between the two calculated limit cases and will have to

be determined before the test runs and compared to these results. The different manufacturing methods used for the blades – casting, CNC machining and spark eroding – also have an effect on the mistuning of the blades, which will need to be investigated.

3.5 Summary turbine design

A new fully cooled turbine stage has been developed for the OTRF. It is based on a modern civil engine with a lean-burn combustor. The NGV and rotor have surface film cooling as well as TE slots and the blade root seal leakage flow is also represented. The cooling configuration has been modelled with Rolls-Royce software to calculate the cooling capacities and predict the behaviour of the cooling films.

A mechanical assessment of the NGV and rotor has been performed. At the beginning of the run the stresses in the stator are highest when the rig is at vacuum and the cooling air is blowing. The results of the FEA show that additional measures will be required to reduce the maximum pressure the vanes are exposed to. The steady-state stresses of the rotor have been determined at the operating speed and at a required overspeed. The life-limiting features have been identified and their fatigue life has been estimated. Finally, a vibrational analysis of the rotor has been conducted to obtain the natural frequencies of the system and ensure a safe operation at the design speed for the expected excitation frequencies.

The manufacture of the turbine stage has been a long and complicated process. The casting of the vanes and rotor blades from aluminium proved to be very challenging because of the intricate internal geometries, which had to be further simplified for ease of core removal. The cooling holes and platforms then had to be machined on complicated 3D geometries with restricted access. Finally, the spark eroding of the TE slots also required improvements of the manufacturing technique, as the aluminium cast is not the material of choice for this process and there was little prior experience. All in all, the manufacture of the turbine stage has been a significant effort in order to produce a state-of-the-art turbine stage for testing in a transient facility, which is sure to yield many exciting results.

CHAPTER 4

Development of Double-Sided Thin Film Gauges for Heat Transfer Measurement

This chapter describes the instrumentation required to obtain accurate and reliable heat transfer data of a fully cooled HP turbine stage. The thin film gauges and procedure for heat transfer measurements on a film-cooled aerofoil are discussed in section 4.1. In section 4.2 a review of thin film gauge theory is given and an analytical model to account for lateral conduction effects in the substrate is introduced. A 1D FE model for the investigation of the thermal pulse through a gauge is presented and validated in section 4.3. This model is used to compare and evaluate different gauge configurations in section 4.4.

4.1 Heat transfer measurements

Thin film surface resistance gauges are used to measure the surface temperature and calculate the heat flux. The heat flux is determined from Fourier's law of thermal conduction

$$\dot{\vec{q}} = -k\vec{\nabla}T \ , \tag{4.1}$$

where k is the thermal conductivity. Consequently, the local heat flux can be obtained by measuring the temperature difference across a thin layer material of known thermal properties. Thin film gauges have been developed for many years at the Osney Laboratory and are extensively used in rotating turbine test rigs, where instrumentation is otherwise difficult (Doorly and Oldfield, 1987). They are particularly suited for short-duration experiments as they have a high frequency response (see section 2.2). Given the restricted access to the working section, optical

methods cannot be used, and commercial calorimeters, which are usually cylindrical, are very difficult to get flush with the curved surface in order to minimise flow disturbance. Current thin film technology offers a high gauge density and, hence, a high resolution of the discrete measurements (e.g. (Collins et al., 2015a)).

For two-layer, single-sided thin film gauges (as shown in figure 4.1a) it is necessary to either assume a semi-infinite substrate when taking heat transfer measurements or to separately determine the driving temperature difference across the insulating layer to obtain the heat flux. On a cooled aerofoil the thickness of the wall and with it that of the insulating layer (generally Kapton) is restricted and the assumption of the semi-infinite substrate is usually not valid (see section 4.2). The temperature under the insulating layer can be measured for instance with a thermocouple, but then nearly isothermal conditions have to be assumed, meaning that the temperature changes in the vane are small compared to ΔT across the insulating layer and do not depend on time.

For these reasons, and to simplify processing, double-sided thin film gauges are increasingly used (for example by (Anthony et al., 2011)). They consist of two thin film temperature gauges mounted on either side of an insulating layer (see figure 4.1b). The bottom (innermost) gauge is electrically insulated from the metal surface by an additional insulating layer.

For changes with low frequency the temperature drop across the insulator is directly proportional to the heat flux to the wall and the double-sided gauges can be used as conduction

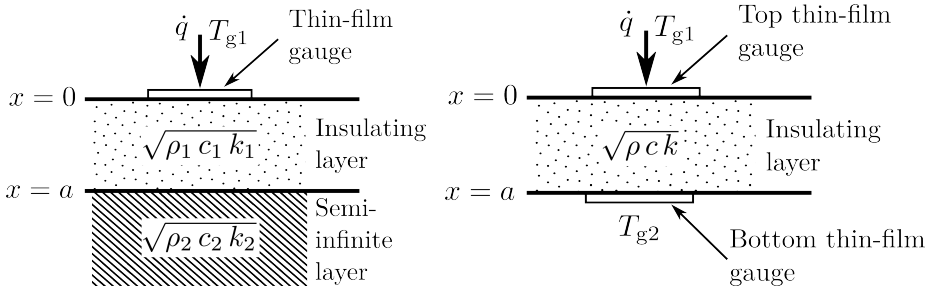

(a) Single-sided TFG (b) Double-sided TFG

Figure 4.1: Thin film gauge geometry (based on (Oldfield, 2012)).

gauges. The heat transfer rate is then given by

$$\dot{q} = \frac{k}{a}(T_{\mathrm{g1}} - T_{\mathrm{g2}}) \ , \tag{4.2}$$

where a is the thickness of the top insulating layer. Above a certain frequency, however, the insulator appears to the top surface to be infinitely thick and a semi-infinite analysis can be performed. The main advantage of double-sided thin film gauges is that the temperature difference can be determined directly at a point of interest without the need for additional thermocouples.

4.1.1 Measuring procedure

This section focuses on the determination of the adiabatic wall temperature T_{aw} from heat transfer measurements. This quantity can be obtained from a linear interpolation of the heat flux $\dot{q}$ as a function of the wall temperature T_{w} with the slope equal to the heat transfer coefficient, by determining the temperature for which $\dot{q} = 0$.[1] A higher accuracy of the interpolation can be achieved by either heating the aerofoil wall or the gauge itself and performing tests at different substrate temperatures, so that the range of values for the regression is increased. This approach is illustrated schematically in figure 4.2.

If the temperature of the aerofoil was higher than that of the coolant, their time-dependencies

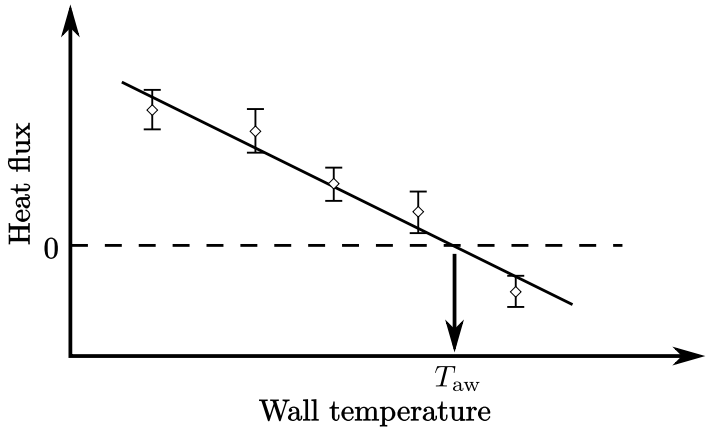

Figure 4.2: Wall heat transfer rates for different values of the wall temperature.

[1] The use of a linear regression calls for an adiabatic wall temperature, which stays constant at the measurement location for the duration of one test run.

would have to be known to correctly interpret the unsteady heat transfer measurements. During a test run the temperature of the coolant flowing through the internal cavities of the blade would increase, as the temperature of the preheated inner wall would decrease.

At the same time, the outer wall temperature is heated up by the hot gas. The adiabatic wall temperature T_{aw} depends on the film cooling effectiveness

$$\eta_{\mathrm{f}} = \frac{T_{0\mathrm{h}} - T_{\mathrm{aw}}}{T_{0\mathrm{h}} - T_{0\mathrm{c}}} \,, \tag{4.3}$$

where $T_{0\mathrm{h}}$ is the total hot gas temperature and $T_{0\mathrm{c}}$ is the total coolant temperature. Larger values of η_{f} (i.e. higher film cooling effectiveness) correspond to a lower adiabatic wall temperature. Neglecting the heating of the cooling film (the so-called heat pick-up), the adiabatic wall temperature stays constant for the test duration, but in a more realistic description it is expected to increase.

Changing aerofoil temperatures between runs in the OTRF by employing e.g. cartridge or PTC heaters is challenging, because of spatial limitations. Moreover, it is difficult to achieve the uniform initial surface temperature required to carry out heat transfer measurements, given the losses to the ambient and casing due to insulation difficulties. For these reasons the option to heat the aerofoil was dismissed in favour of heating only the substrate. Two arrangements of heated gauges have been developed namely: double-sided gauges with an underside thin film heater and self-heating double-sided gauges. An improved regression can be obtained with such gauges without the need for complex heating systems. The heater concepts are presented in section 5.2.

4.1.2 Measuring a film-cooled turbine stage

The coolant delivery system is designed to minimise internal heat transfer by avoiding dead volumes. If the coolant temperature is set to be equal to the wall temperature at ambient conditions ($T_{0\mathrm{c}} = T_{\mathrm{w}} = 290\,\mathrm{K}$) there is no heat pick-up before the run. Because of their large thermal mass, the aluminium parts are likely to stay isothermal and are thus largely insensitive to compression effects.

One central objective is to determine the Nusselt number

$$\mathrm{Nu} = \frac{hL}{k} = \frac{\dot{q}L}{(T_{\mathrm{aw}} - T_{\mathrm{w}})k} \tag{4.4}$$

where h is the heat transfer coefficient and L the characteristic length. If the film effectiveness is very high (i.e. close to unity), it becomes difficult to take accurate heat transfer measurements, because $\dot{q}$ is very small and T_{aw} is very close to $T_{0\mathrm{c}}$ (and therefore to T_{w}). An accurate determination of Nu is then only possible if the coolant temperature is different from the wall temperature. In that case the heat pick-up in the internal channels would lead to a significant uncertainty in $T_{0\mathrm{c}}$ making it necessary to assess the internal heat transfer. Nevertheless, one can argue that areas where the film effectiveness is very high, in particular near the cooling rows, do not pose a problem for the part and therefore do not need to be investigated in detail.

4.2 Theoretical considerations

The theory of thin film surface resistance gauges for heat transfer measurements is well documented (see (Schultz and Jones, 1973) and (Doorly and Oldfield, 1987)). The basic principles of thin film gauges on a semi-infinite layer and on a two-layer substrate are reviewed here.

The resistance of a thin film gauge increases linearly with temperature:

$$R(T) = R_0(1 + \alpha \Delta T) \,, \tag{4.5}$$

where R_0 is the resistance at a reference temperature T_0 and α is the temperature coefficient of resistance. Defining the change in surface temperature $\Delta T = T - T_0$ and the change in the resistance of the thin film gauge $\Delta R = R(T) - R_0$ one obtains

$$\Delta T = \frac{\Delta R}{\alpha \, R_0} \tag{4.6}$$

If the gauge current I is constant, the voltage across the gauge is given by $V(T) = I\,R(T)$ and hence the change in resistance is proportional to a change in voltage ΔV:

$$\Delta V = V(T) - V_0 = I\,(R(T) - R_0) = I\,\Delta R \,. \tag{4.7}$$

It then follows

$$\Delta T = \frac{\Delta V}{\alpha V_0} \, . \tag{4.8}$$

Since it is relatively easy to obtain a constant current from a power supply unit, the temperature history of a surface in an experiment can be obtained by recording ΔV across the gauge.

4.2.1 One-dimensional heat conduction equation

In a short-duration test the penetration depth of the thermal pulse into the insulating layer is small compared to other dimensions and hence the insulating layer can be taken to be homogenous and isotropic in the lateral directions. In particular, the heat flux into the wall is much larger than any lateral heat flux. Assuming furthermore that the effect of the gauge is negligible, i.e. that it has negligible thermal resistance, the equation governing the temperature distribution in the insulating layer is the one-dimensional Fourier equation:

$$\frac{\partial^2 T}{\partial x^2} = \frac{1}{\alpha} \frac{\partial T}{\partial t} \tag{4.9}$$

with the thermal diffusivity

$$\alpha = \frac{k}{\rho c} \, , \tag{4.10}$$

the density ρ and the specific heat capacity c.

As long as the penetration depth of the thermal pulse is sufficiently small that a semi-infinite analysis can be performed, equation 4.9 can be used to infer the surface heat flux $\dot{q}_\mathrm{s}$ from the surface temperature $T_\mathrm{s}(t) = T(x = 0, t)$. Assuming uniform initial temperature conditions it can be shown that the Laplace transforms for surface heat flux and surface temperature for a single-layer substrate thin film gauge are related by (Schultz and Jones, 1973):

$$\overline{\dot{q}}_\mathrm{s} = \sqrt{\rho c k} \sqrt{s} \, \overline{T}_\mathrm{s} \, , \tag{4.11}$$

where over-line represents the Laplace transform and s is the Laplace transform variable.

If the heat flux at the surface is constant Q, then $\overline{\dot{q}}_\mathrm{s} = Q/s$ and it follows

$$\overline{T}_\mathrm{s} = \frac{Q}{\mathrm{s}^{3/2} \sqrt{\rho c k}} \tag{4.12}$$

$$\Rightarrow T_{\mathrm{s}}(t) = \frac{2Q}{\sqrt{\rho c k}}\sqrt{\frac{t}{\pi}}\,. \tag{4.13}$$

The resulting surface temperature rise is parabolic for constant heat flux. If the surface heat flux is time-dependent, the temperature rise will deviate from this simple form. For general time-dependence equation 4.11 can be solved to give the time-dependent heat flux (Oldfield et al., 1978):

$$\dot{q}(t) = \sqrt{\frac{\rho c k}{\pi}}\left(\frac{T(t)}{\sqrt{t}} + \frac{1}{2}\int_0^t \frac{T(t)-T(\tau)}{(t-\tau)^{3/2}}\,\mathrm{d}\tau\right)\,. \tag{4.14}$$

In order to estimate the validity of the semi-infinite analysis, one can once again assume a constant heat flux at the surface and determine the temperature at a general depth x in the insulating layer. The Laplace transform of this quantity is given by

$$\overline{T}(x,t) = \frac{1}{\sqrt{\rho c k}}\frac{Q}{\sqrt{s}}e^{-x\sqrt{s/\alpha}}\,. \tag{4.15}$$

One then obtains

$$T(x,t) = \frac{Q}{\sqrt{\rho c k}}\left[2\sqrt{\frac{t}{\pi}}e^{-\frac{x^2}{4\alpha t}} - \frac{x}{\sqrt{\alpha}}\operatorname{erfc}\frac{x^2}{2\sqrt{\alpha t}}\right]\,, \tag{4.16}$$

where erfc is the complementary error function. The heat flux at depth x is then given by

$$\dot{q}(x) = -k\frac{\partial T}{\partial x} = \dot{q}_s \operatorname{erfc}\frac{x}{2\sqrt{\alpha t}}\,. \tag{4.17}$$

The typical penetration depth of a thermal pulse after time t is therefore given by $2\sqrt{\alpha\, t}$. For a typical insulating layer with thickness $a = 100\,\mu\mathrm{m}$ and $\alpha = 7.75\cdot 10^{-8}\,\mathrm{m^2\,s^{-1}}$, the approximation of a semi-infinite substrate hence breaks down after about 0.04 s.

To extend the validity of the semi-infinite analysis, one can consider a two-layer substrate thin film gauge (as shown in figure 4.1a) with an insulating layer of thickness a followed by a semi-infinite metal substrate. For this set-up, equation 4.11 becomes (Doorly and Oldfield, 1987):

$$\overline{\dot{q}}_{\mathrm{s}} = \sqrt{\rho_1 c_1 k_1}\sqrt{s}\,\frac{1 - A\exp(-2a\sqrt{s/\alpha_1})}{1 + A\exp(-2a\sqrt{s/\alpha_1})}\,\overline{T}_{\mathrm{s}} \tag{4.18}$$

with

$$A = \frac{\sqrt{\rho_1 c_1 k_1} - \sqrt{\rho_2 c_2 k_2}}{\sqrt{\rho_1 c_1 k_1} + \sqrt{\rho_2 c_2 k_2}}\,, \tag{4.19}$$

where 1 denotes the insulating layer and 2 the semi-infinite metal substrate.

While it is difficult to solve this equation analytically, the surface temperature signals can be processed into heat transfer rates by the use of analogue electronic circuits, as detailed by (Oldfield et al., 1984). More recently, impulse response processing of temperature signals has been introduced (Oldfield, 2008). The data processing used for this approach will be discussed in section 5.4.

4.2.2 Lateral conduction effects of heated gauges

So far only one-dimensional heating conduction has been considered, based on the argument that for very short periods of time, such as the given test window, the lateral conduction effects can be neglected. Specifically, for a given thermal diffusivity α (see equation 4.10), the lateral conduction is considered negligible if the test time t is sufficiently short that $\alpha\, t \ll l^2$, where l is the lateral length over which significant variations in temperature occur. As explained in section 4.1, the advantage of double-sided thin film gauges in comparison to single-sided thin film gauges is that the heat flux to the wall can be calculated for longer time scales. This is particularly important when considering local heating of the gauge substrate, because in this case lateral conduction effects become more important.

The simplest way to estimate the lateral conduction effects in the insulating layer is to consider the thin film heater or gauge as a 1D, 2D or 3D point heating source and calculate the analytical steady-state temperature distribution. The corresponding geometries are a cube, a cylinder and a sphere (as depicted in figure 4.3). The model thickness x equals the thickness of the insulating layer, which is either the distance of the heater from the wall or the total thickness of a double-sided thin film gauge (for self-heating gauges). The heating power is obtained from the current through the heater or through the gauge and the respective heater or gauge resistance. The resulting heat flux is then calculated based on the heated surface. At the wall the temperature is set to ambient. In this simple model the effect of the copper or the

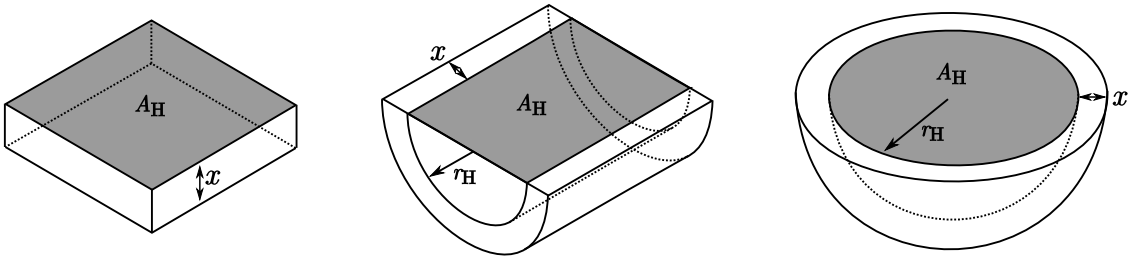

Figure 4.3: Heating source geometries.

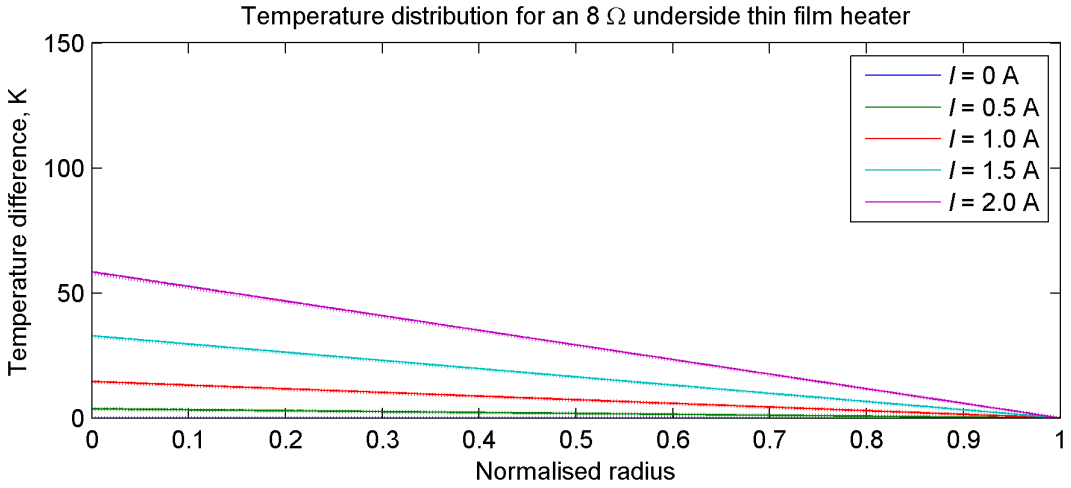

Figure 4.4: Overlapping 1D (continuous line), 2D (dashed line) and 3D (dotted line) temperature distribution across the insulating layer of an underside thin film heater element.

platinum layer (for self-heating gauges) is neglected. Typical geometries of a thin film heater element and a self-heating double-sided gauge will be given in chapter 5.

The temperature distribution in the insulating layer of an 8 Ω thin film heater, which covers at least five times the gauge area on an aerofoil side, is calculated assuming an adiabatic outer surface. The results are shown in figure 4.4. The normalised radius is the distance from the heating source. The 0 normalised radius corresponds to the location of the heating source (the heater). The radius is 1 at the wall. Higher temperatures are achieved with increasing current through the heater. As expected from the heater geometry, the temperature distribution is very one-dimensional and 2D and 3D effects can be neglected. Moreover, it is important to note that for this calculation the total area of the heater was used and not of the copper tracks alone, which already accounts for certain 2D and 3D heating effects.

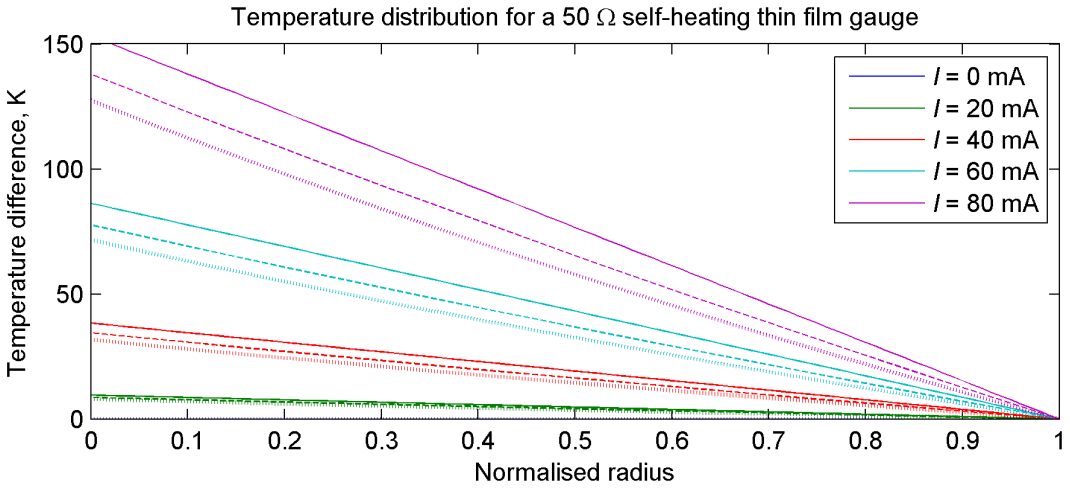

Figure 4.5: 1D (continuous line), 2D (dashed line) and 3D (dotted line) temperature distribution across a heated gauge.

The temperature distribution over the gauge thickness for a self-heating gauge is shown in figure 4.5 for a range of heating currents. The 0 normalised radius corresponds to the location of the top gauge. The 1D problem shows a linear temperature decay, the 2D problem a logarithmic decay and the 3D problem a hyperbolic decay. At the location of the heating source the temperatures differ considerably and the effect is still noticeable at a normalised radius of 0.5, which corresponds to the location of the bottom gauge. This analytical solution can be used to calculate the temperature of the top/bottom gauge based on the known temperature of the bottom/top gauge (see also section 5.5).

4.3 Modelling of the thermal pulse through a multi-layer system

The previous section focused on various simplified geometries, which allow for an analytical calculation of the steady-state temperature distributions. To calculate the transient behaviour of a realistic geometry numerical methods are necessary, as will be discussed next.

A 1D FE code was implemented in Matlab to model the thermal pulse across a double-sided thin film gauge. In this code a double-sided thin film gauge is modelled as a three-layer system of unlimited lateral extent. The system consists of two Kapton layers of variable thickness (the insulating layers) and a 1 mm aluminium layer, representing the aerofoil wall. The copper tracks

can be neglected in the model, because their thermal resistance is several orders of magnitude smaller than that of the Kapton layers. The platinum films are sufficiently thin to appear thermally transparent to the applied heat flux and are not included either. The current through the gauges is chosen low enough, so that ohmic heating does not have an effect. A similar model was investigated by Epstein et al. (1986).

The time-dependent temperatures are computed through an iterative process from a known, spatially uniform heat flux on the outer and inner surfaces over the run time. The heat flux between adjacent cells is obtained from Fourier's law of thermal conduction (equation 4.1) and the temperature of each cell is assumed to be uniform throughout the cell. It is also assumed that the three layers make perfect thermal contact. The thermal properties of the layer materials are summarised in table 4.1.

The aim of this model is to find an optimum gauge configuration which has a large enough temperature difference across the insulating layer to measure the heat flux accurately and that also offers a sufficient regression over the run time to calculate the adiabatic wall temperature and heat transfer coefficient. The first case considered is a step change in temperature, which serves as a validation of the model. The rig start-up characteristics are then used to get a realistic response.

4.3.1 Step temperature change and validation

The first model consists of two 115 µm Kapton layers and a 1 mm aluminium wall, subjected to a step temperature change. The geometry is typical for the substrate of a double-sided thin film gauge consisting of a 50 µm thick Kapton layer on a 65 µm glue layer. The initial temperature

Material	**Density** ρ, $\mathrm{kg\,m^{-3}}$	**Specific heat capacity** c, $\mathrm{J\,kg^{-1}\,K^{-1}}$	**Thermal conductivity** k, $\mathrm{W\,m^{-1}\,K^{-1}}$
Kapton	1420	1090	0.12
Aluminium	2700	880	207

Table 4.1: Thermal properties of the layer materials for the thin film gauge model.

is 290 K and the inlet total temperature of the hot stream is 444 K at the time $t = 0$ s. The temperature of the coolant stream on the inner side of the aluminium wall is constant 290 K. The external and internal heat transfer coefficients are set to 4000 $\mathrm{W\,m^{-2}\,K^{-1}}$. The surface temperatures are defined based on the local adiabatic effectiveness (on the outer wall $\eta_f = 0$ and on the inner wall $\eta_f = 1$). Each wall layer consists of 100 cells and the solution is reported at 1000 time steps, which are spaced evenly in $\sqrt{t}$.

Figure 4.6 shows the response in wall temperature and surface heat flux to a step change in temperature as a function of $\sqrt{t}$. The red lines correspond to the temperatures measured by the top and bottom gauge. The top wall temperature increases linearly with $\sqrt{t}$ at the beginning (when the semi-infinite assumption is valid) and then stagnates. The time response can be understood from the heat flux into the wall and the thermal properties of the layers. The inner wall temperature is the temperature of the cooling cavity wall.

Once the temperatures stabilise, the difference across the upper Kapton layer is around 60 K for the given boundary conditions. This temperature difference would be used in a run to determine the heat flux (see section 5.4). In the model the heat flux is known and can be plotted against the outer wall temperature, which would be measured by the top thin film gauge (see bottom plot on figure 4.6). The adiabatic wall temperature and heat transfer coefficient follow from a linear extrapolation of the heat flux as a function of the wall temperature for $\dot{q} = 0$. The OTRF tries to match this step change in temperature, but an exact match is not achieved. Realistic inlet conditions will be considered in the next section.

Validation case

The analytical solution was calculated for a transient system consisting of one Kapton layer with uniform initial temperature subjected to a step change in the temperature of the upper surface and isothermal conditions on the lower surface. Assuming an infinite plate with the thickness a and the thermal diffusivity α, the governing equation is the one-dimensional Fourier equation (see equation 4.9). The general solution of the Fourier equation for a plate of finite

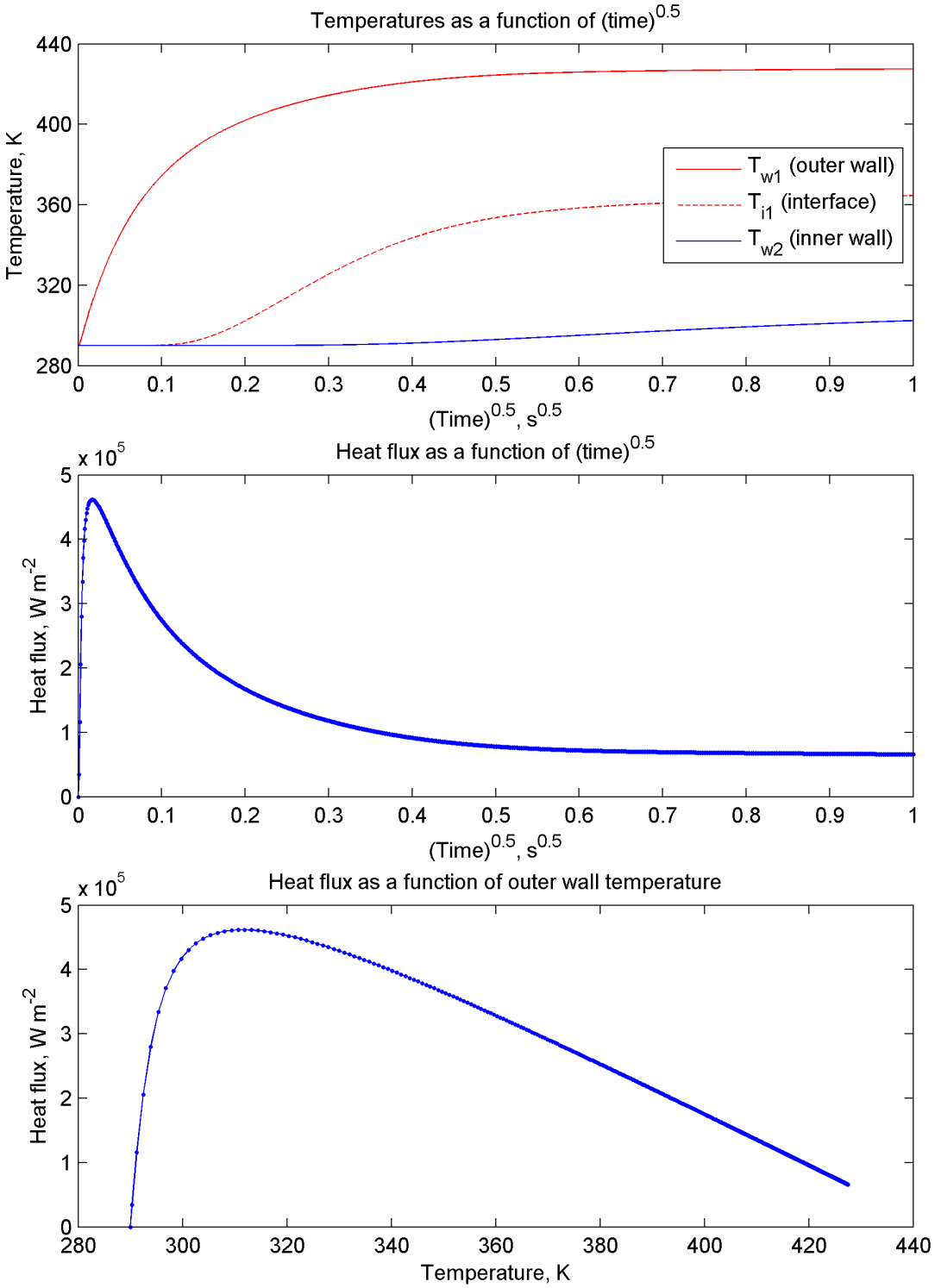

Figure 4.6: Ideal response to a step change in temperature: wall temperatures and heat flux.

thickness is given by

$$T = T_a - \frac{x}{a} T_b + \sum_{n=1}^{\infty} c_n \sin\frac{n\pi x}{a} \exp\left(-\left(\frac{n\pi}{a}\right)^2 \alpha t\right) . \tag{4.20}$$

If one surface is held constant at the temperature T_1 for $t > 0$ and the other surface stays at the uniform initial temperature T_0, the boundary conditions are satisfied by setting:

$$T_a = T_1 \, , T_b = T_1 - T_0 \, , c_n = \frac{2}{\pi n}(T_0 - T_1) \, . \tag{4.21}$$

Since the heat transfer coefficient of the analytical solution tends to infinity – i.e. the surface temperature is equal to the freestream and coolant temperatures respectively – a comparison with the FE model requires re-running the simulation with a very large heat transfer coefficient, which has been arbitrarily taken to be $h = 10^6\,\mathrm{W\,m^{-2}\,K^{-1}}$, in order to have identical constraints. The spatial temperature distribution for the 1D FE model is shown in figure 4.7 at various times and compared to the analytical solution. The agreement is excellent considering that the accuracy of the first point in the FE model is limited by the cell thickness.

4.3.2 Realistic inlet conditions

The response of a double-sided thin film gauge needs to be investigated under the conditions and with the start-up characteristics of the rig. Figure 4.8 shows uniform inlet temperature as well as uncooled and cooled pressure traces from experimental data. The pressure trace determines the behaviour of the heat transfer coefficient and the useful run time is limited by the stability of the heat transfer coefficient. The longer the stable time range is, the higher the quality of the regression used to determine the adiabatic wall temperature.

The input for the 1D FE model (temperature and heat transfer coefficient) is given in figure 4.9. A typical run lasts about 0.5 s. An inlet temperature profile has been derived from the experimental data. It has a plateau at 444 K. When taking experimental data, the regression will consider the varying inlet total temperature. The external heat transfer coefficient is set to $500\,\mathrm{W\,m^{-2}\,K^{-1}}$ before the run to account for natural and forced convection. The stable run value is set to $4000\,\mathrm{W\,m^{-2}\,K^{-1}}$.

In a cooled test the cooling air starts blowing about 1 s before the run (see figure 4.10). The

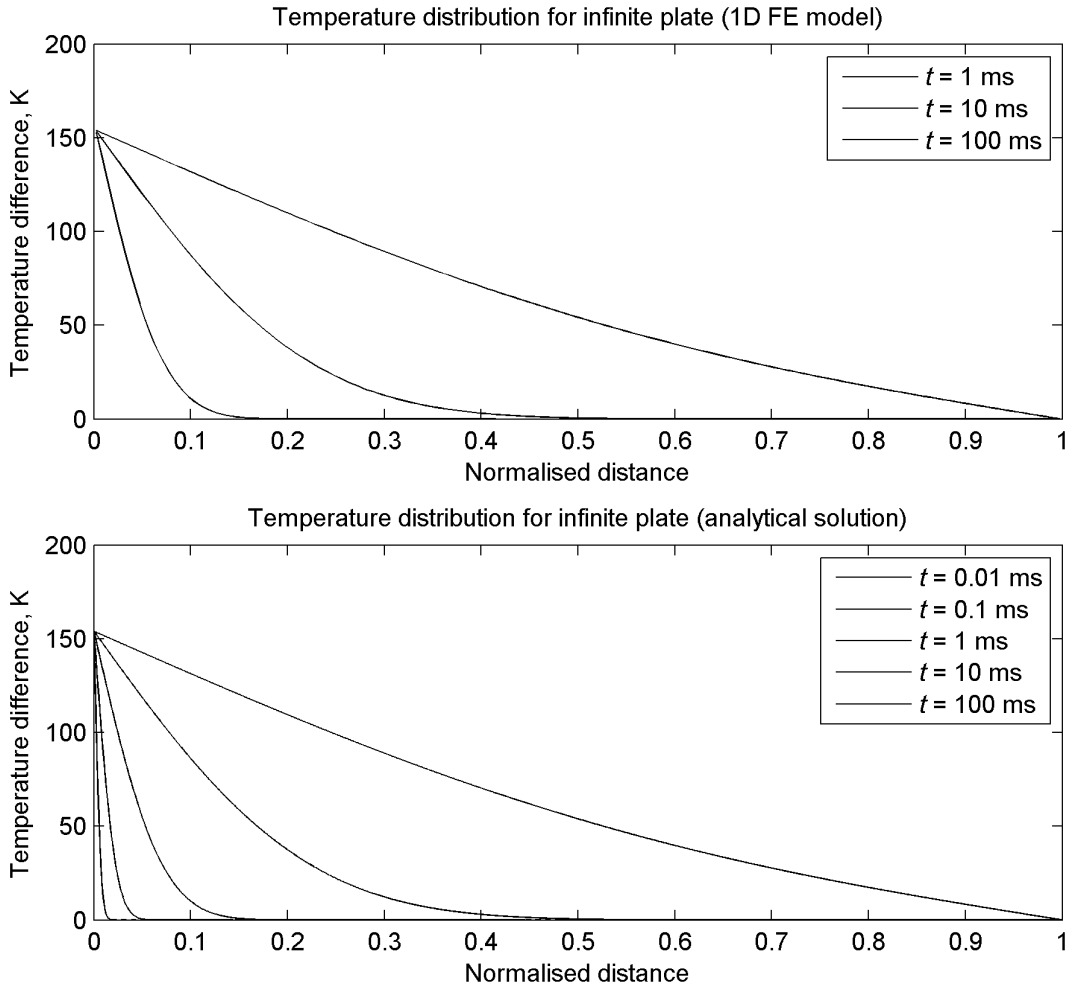

Figure 4.7: Comparison of the results for the temperature distribution of an infinite plate subjected to a step in top surface temperature: 1D FE model (top) and analytical solution (bottom). The plate thickness corresponds to that of a double-sided thin film gauge. The temperature in the plate increases with increasing time.

coolant leads to an increase of the inlet total pressure before the run, which can also be observed in figure 4.8. In the coolant cavity the pressure increases steadily to the coolant delivery pressure, as the cooling holes choke. The pressure increases slightly when the main flow starts blowing and the hole exit pressure rises. The trace of the internal heat transfer coefficient is given by the total pressure in the cavity. The internal heat transfer coefficient is set to $500\,\mathrm{W\,m^{-2}\,K^{-1}}$ before the run. The stable run value is set to $1500\,\mathrm{W\,m^{-2}\,K^{-1}}$. The coolant temperature is assumed to stay constant at 290 K (the spike in cavity temperature because of the compression of the air in the coolant supply system is not modelled).

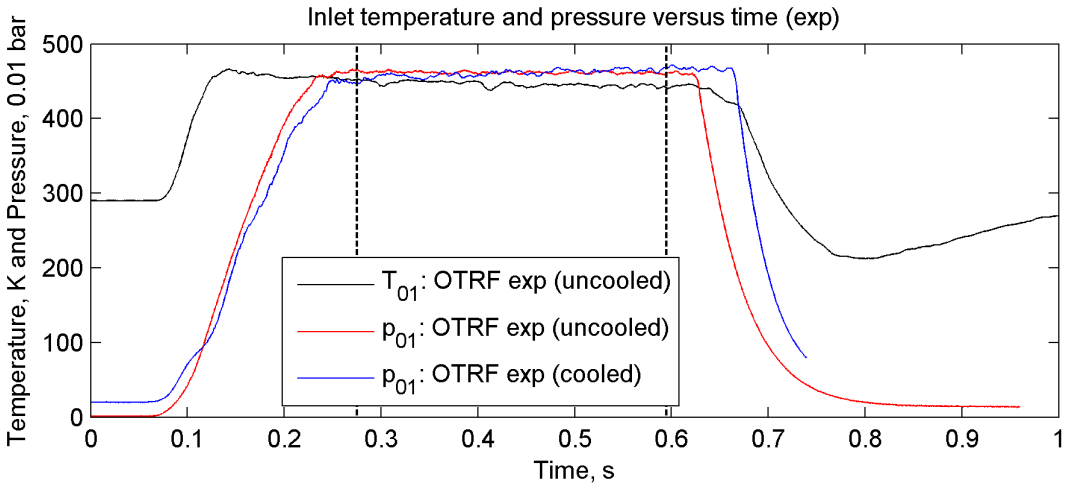

Figure 4.8: OTRF inlet total temperature and inlet total pressure for an uncooled and a cooled run. The run starts at about $t = 0.1\,\mathrm{s}$ and lasts about 0.5 s. The dashed vertical lines mark the stable run time limited by the inlet total pressure.

In this study the external film cooling effectiveness ranges from 0 to 1. The aim of this model is to compare different 1D gauge configurations. The importance of modelling 2D and 3D effects will be discussed in chapter 5. The limitations of the chosen boundary conditions for the 1D FE model will be investigated using experimental data in chapter 7.

The current model will be used to study the regression of the heat flux over the wall temperature for unheated gauges and compare it to the results from heated gauges. As a baseline for the further study of the quality of the regression, a semi-infinite case is discussed. The semi-infinite case consists of two layers of 115 µm Kapton each on a thick layer of Perspex (2 cm). The thermal properties of Perspex are very similar to those of Kapton. This configuration would offer the best possible regression if wall thickness (and wall material) was not a constraint, as the adiabatic inner wall results in the largest temperature increase during the stable run time.

A parametric study was carried out to determine the effect of varying the number N of cells per layer and the number of time steps. For $N = 400$ the error is limited to the time outside the stable run period. However, the maximum difference in outer wall temperature between $N = 100$ and $N = 400$ is only 0.7% at 0.9 s. In conclusion, $N = 100$ is accurate enough and it is much quicker to run. Concerning the number of reporting time steps, 100 time steps per second was determined to yield a sufficiently accurate solution. The reporting time steps are not spaced

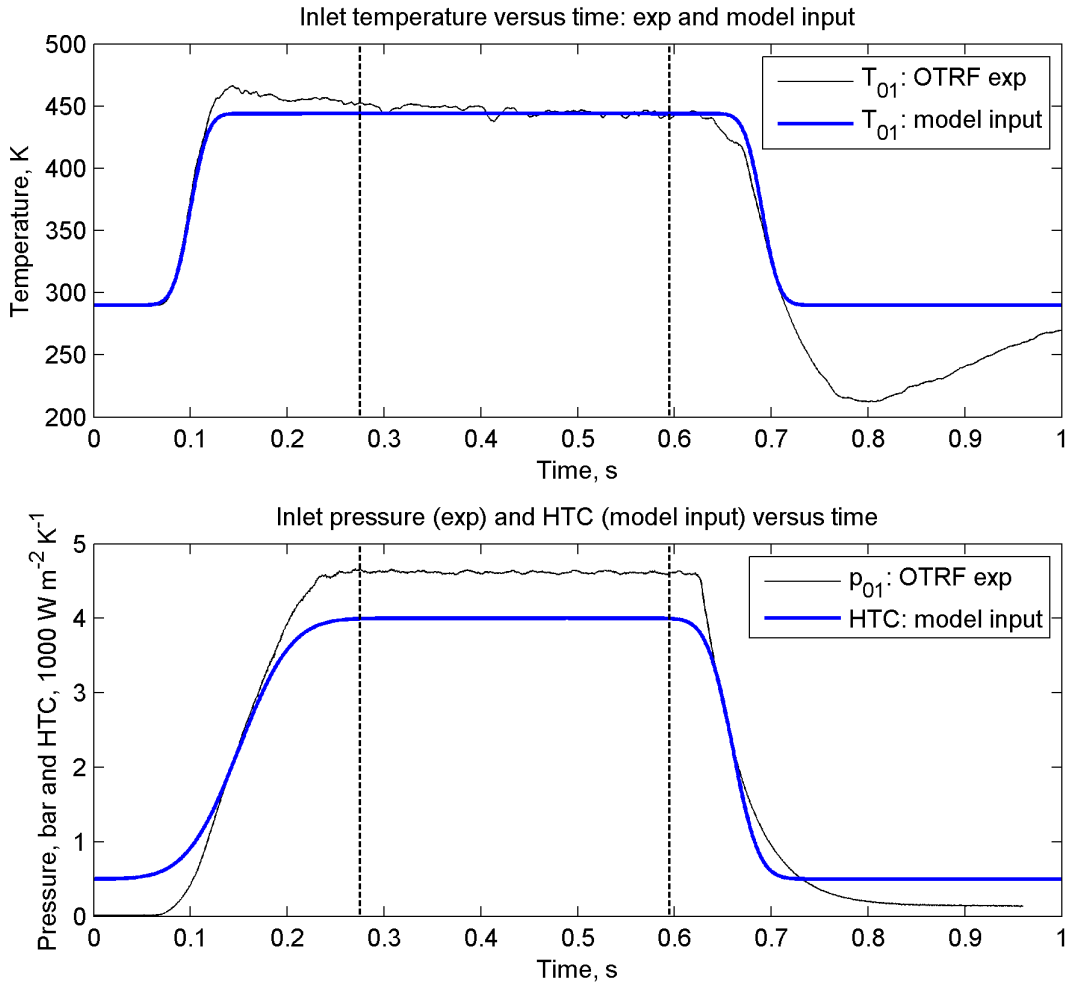

Figure 4.9: Temperature and external heat transfer coefficient for the 1D FE model. The thermal boundary conditions of the FE model are based on experimental data.

evenly in $\sqrt{t}$ anymore, because the focus is not on the start of the surface temperature rise, but on the temperature rise during the stable part of the run.

The results for the baseline (i.e. semi-infinite) case are shown in figure 4.11 for $\eta_f = 0$, so that the adiabatic wall temperature is equal to the temperature of the hot gas (see equation 4.3). The outer wall temperature increases quickly to just below the inlet total temperature. The inner wall temperature stays constant at 290 K. During the stable run time a temperature increase of 10 K is achieved on the external surface.[1] With increasing film effectiveness the temperature

[1] In chapter 5 the temperature change during the stable run time is used to calculate the heat flux. The semi-infinite baseline has the particularity that it can be processed both as a single-sided and as a double-sided gauge, which will be used to validate the post-processing.

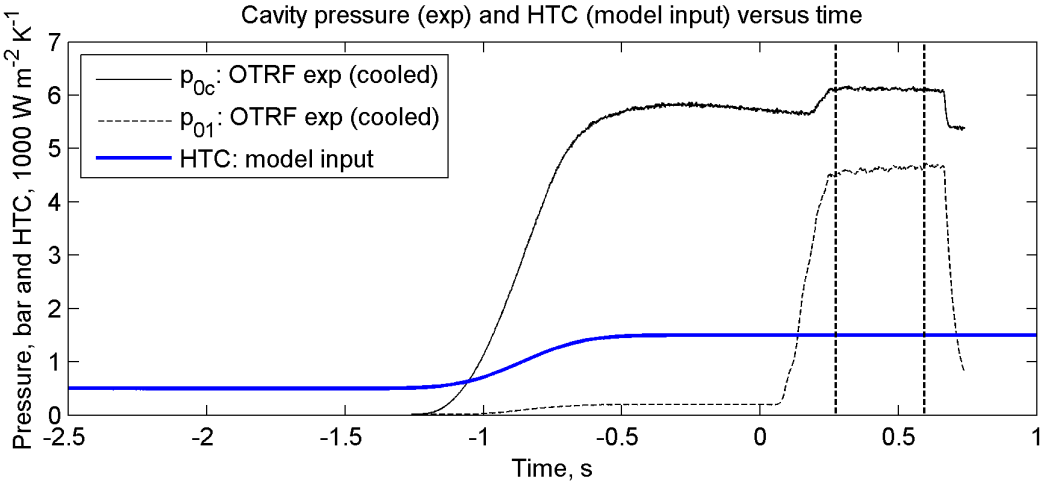

Figure 4.10: Cavity pressure and corresponding internal heat transfer coefficient.

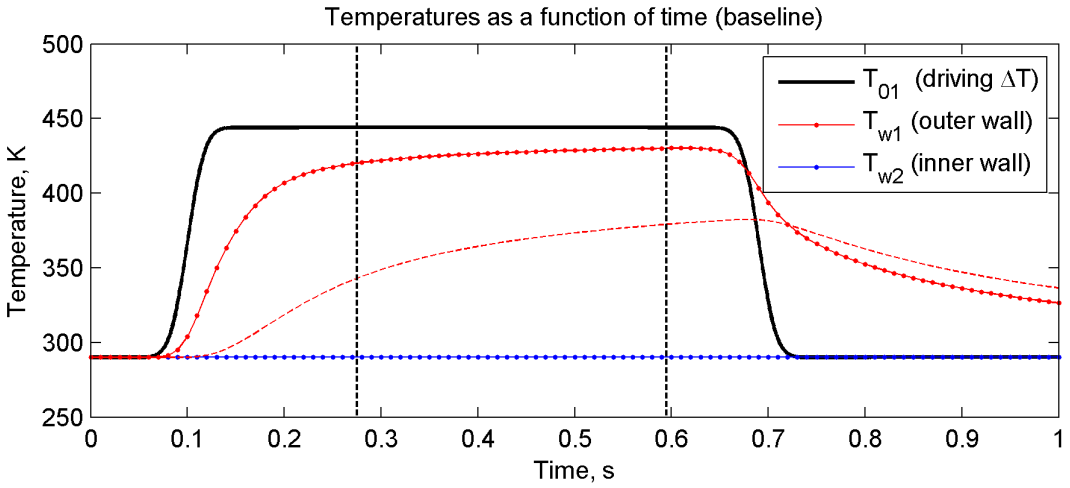

Figure 4.11: Wall temperatures for a double-sided thin film gauge on a thick layer of Perspex (2 cm) for $\eta_f = 0$. This semi-infinite case will be used as a baseline for the comparison of different gauge configurations.

reached by the outer wall is reduced and the adiabatic wall temperature decreases.

From now on the wall is again taken to be a 1 mm thick aluminium plate. The resulting temperature traces are shown in figure 4.12 for $\eta_f = 0$. For the unheated case (figure 4.12a), the temperature of the inner wall increases by about 10 K compared to the baseline case, because of the thinner metallic wall. At the beginning of the run the baseline case and the case with finite thickness show very similar temperature traces. However, during the stable part of the run the temperature of the substrate continues to increase for the semi-infinite case (as is best visible in

the temperature trace of the interface), whereas it stagnates for the thinner aluminium wall. In the latter case the temperature difference between the top and bottom gauge is around 75 K, which is large enough to determine the heat flux accurately.

An important observation is that the temperature of the outer wall changes by only about 7 K during the stable part of the run (for the baseline it was 10 K). Such a temperature rise is insufficient to obtain a reliable regression in order to determine the adiabatic wall temperature. As will be discussed in detail in section 4.4, heating the gauges offers the possibility to improve this regression. In the following, the results of unheated gauges are compared to those of gauges with a heated substrate.

Ohmic heating of the gauges can be used to generate a pre-run temperature distribution in the substrate without affecting the measurement of the heat flux due to convection, as long as any pre-run heat fluxes are corrected for (O'Brien, 1990). In chapter 5 two heating arrangements will be introduced and the necessary changes to the gauge configuration will be discussed. For ease of comparison, the gauge configuration will be left unchanged for now and the heating is just regarded as a heating source at the location of the top gauge. In the model the heating is added as a source term to the heat flux calculation on the top surface following the equation

$$\dot{q}_{\mathrm{H}} = \frac{I^2 R_0}{A_{\mathrm{g}}} \left(1 + \alpha(T - T_0)\right) \ , \tag{4.22}$$

where I is the constant current through the gauge, R_0 is the resistance of the gauge with area A_{g} at a nominal reference temperature T_0 and α is the temperature coefficient of resistance. Typical gauges have an R_0 value of 50 Ω and an area of 6 mm^2 with $\alpha = 1.5 \cdot 10^{-3}\,\mathrm{K}^{-1}$ ($T_0 = 290\,\mathrm{K}$). The heated results presented in figure 4.12b correspond to a current of 80 mA. For the modelling of heated gauges the run time was increased to 30 s to account for the time it takes the substrate temperature to stabilise. To simplify the comparison, the heat transfer coefficient on the inner wall is set constant at 1500 W/(m^{2}K).

The effect of the ohmic heating can be seen before the start of the run as the outer wall temperature increases to about 360 K for 80 mA. The amount of heat applied is arbitrary, but limited by the outgassing temperature of the glue, which occurs at about 390 K (3M, 2005). Note that the temperature of the glue is given by the temperature of the interface which is

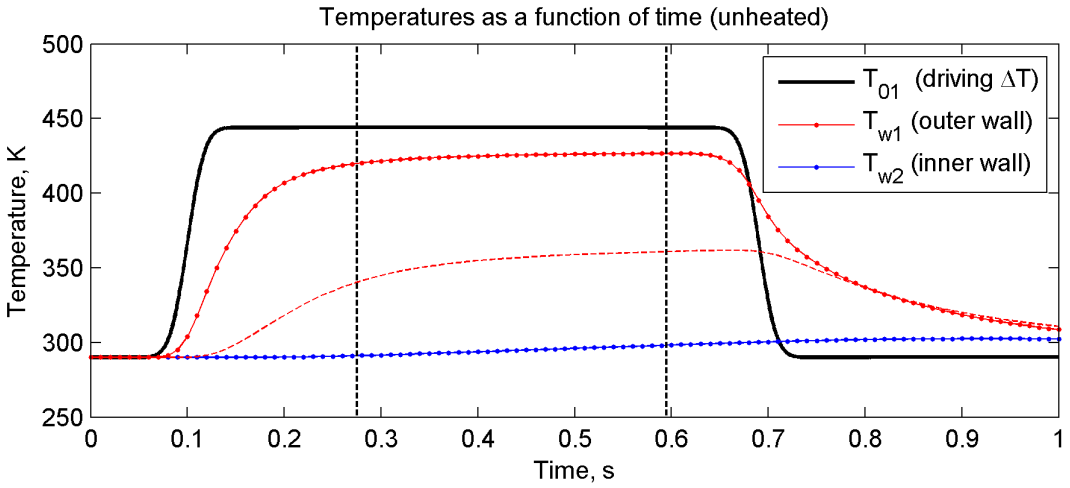

(a) Unheated gauge ($\eta_f = 0$)

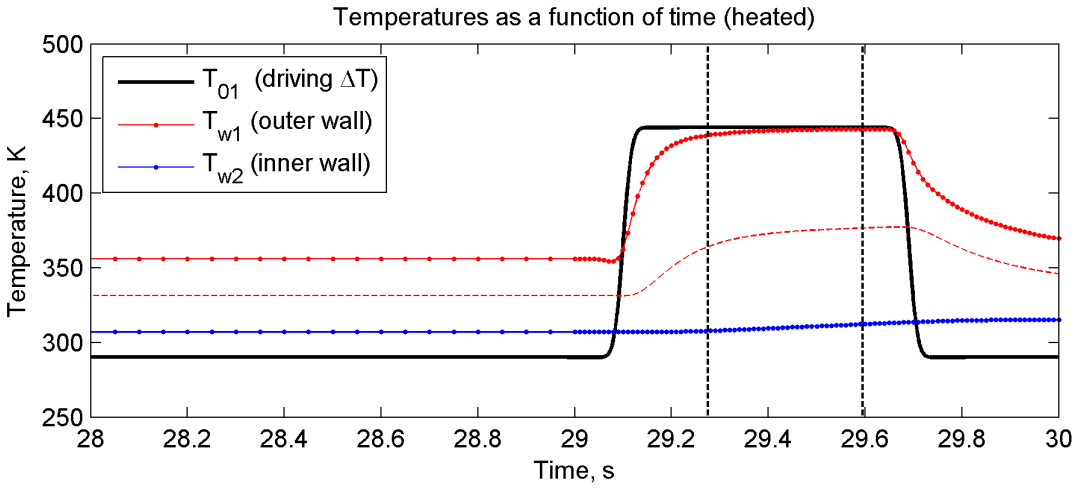

(b) Gauge with heated substrate at 80 mA ($\eta_f = 0$)

Figure 4.12: Wall temperatures for a double-sided thin film gauge on an aluminium wall of 1 mm thickness.

about 330 K for 80 mA. The preheating should not exceed this temperature. In section 5.5 a detailed analysis will be performed to establish the effect of the ohmic heating on the pre-run non-uniform local temperature distribution (see also the lateral conduction effects discussed in section 4.2).

The heat flux traces for three current settings are shown in figure 4.13a. The negative values of the heat flux at the beginning of the run for non-zero heating currents correspond to the heat transferred by the heated surface to the surroundings. With increased preheating the

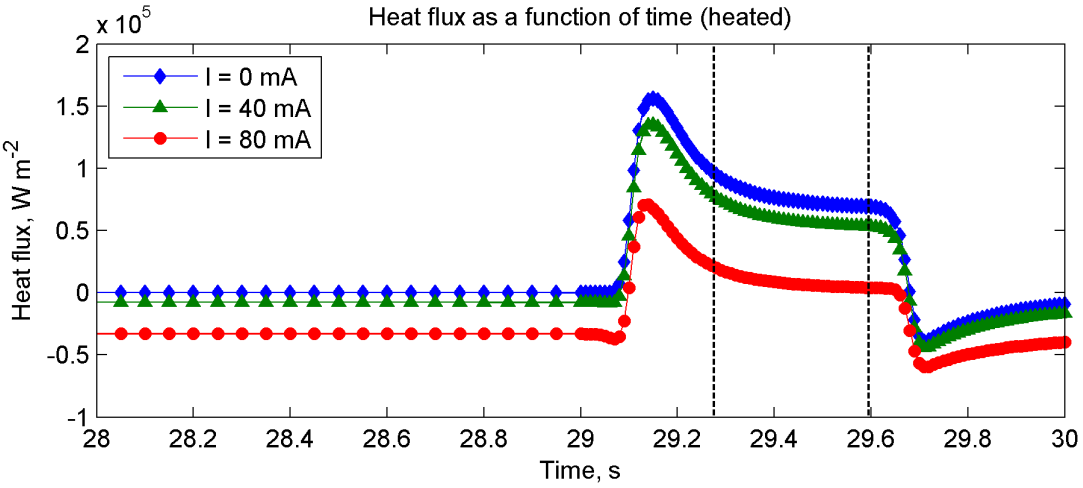

(a) Heat flux trace for three current settings

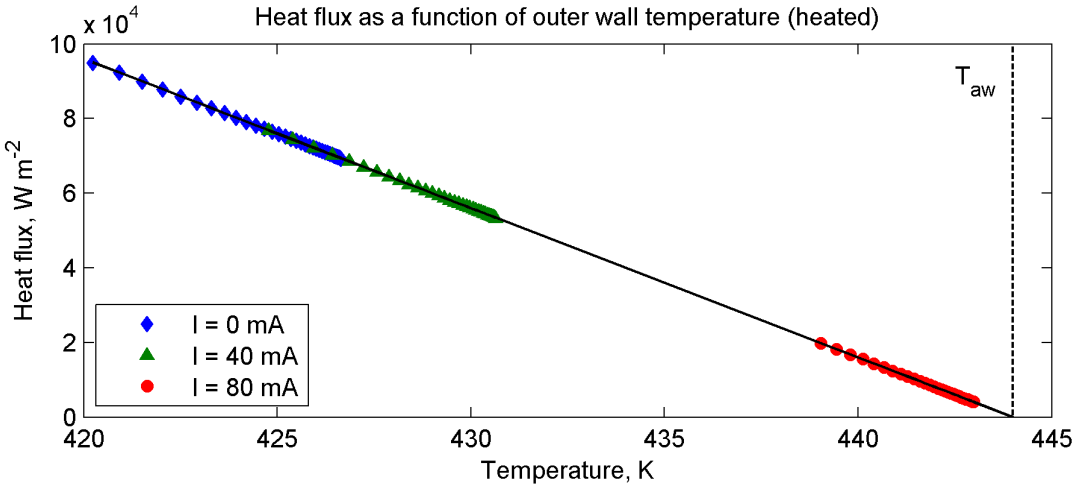

(b) Heat flux over wall temperature for three current settings and extrapolation to obtain T_{aw}

Figure 4.13: Heat flux as a function of time and wall temperature for three current settings: 0 mA, 40 mA and 80 mA. The results are shown for $\eta_{\mathrm{f}} = 0$. T_{aw} is obtained from a linear extrapolation of the heat flux in the stable range.

heat flux during the run becomes smaller. Figure 4.13b shows the extrapolation of the heat fluxes to obtain T_{aw}. By heating the substrate the range of data available for the extrapolation is extended. The design of the double-sided gauges has to ensure that the adiabatic wall temperature and the heat transfer coefficient can be measured accurately, while at the same time achieving a large enough temperature difference across the substrate layer (65 K for $\eta_{\mathrm{f}} = 0$ in figure 4.12b). A quantitative analysis of these requirements is performed below.

4.4 Analysis of different gauge configurations

The accuracy with which the adiabatic wall temperature can be determined depends on the ratio of the outer wall temperature difference during the stable part of the run $\Delta T_{\mathrm{w}} = T_{\mathrm{w2}} - T_{\mathrm{w1}}$ and the difference between the adiabatic wall temperature T_{aw} and the first (furthest) regression point T_{w1}. The stability criterion S is introduced, where

$$S = \frac{\Delta T_{\mathrm{w}}}{T_{\mathrm{aw}} - T_{\mathrm{w1}}} \; . \tag{4.23}$$

Table 4.2 summarises the value of S over a range of realistic (total) gauge thicknesses. For ease of manufacture only symmetrical gauge configurations have been considered. For all cases the ratio increases with increasing gauge thickness, corresponding to an improved quality of the regression. For the baseline case, S is always close to 0.4. In contrast, the unheated case yields a value of S that is significantly smaller and depends more strongly on the total gauge thickness. For gauge thicknesses between 180 µm and 280 µm, the stability criterion varies between 0.18 and 0.35. The heated case, on the other hand, achieves significantly larger values for the stability criterion, which can even exceed unity for sufficiently thick substrates.

For the baseline case and the unheated case, the ratio of the surface temperature range for the extrapolation and the distance to the adiabatic wall temperature (equation 4.23) is independent of the film effectiveness. For the heated case, the ohmic heating increases the wall temperature and therefore the stability criterion changes as a function of the film effectiveness (table 4.2 shows the results for $\eta_{\mathrm{f}} = 0$). Figure 4.14 shows how the temperature achieved by the outer wall decreases with increasing film cooling effectiveness as the driving temperature difference

Total gauge thickness	180 µm	230 µm	280 µm
Baseline	0.39	0.41	0.42
Unheated case	0.18	0.27	0.35
Heated case at 80 mA ($\eta_{\mathrm{f}} = 0$)	0.40	0.81	1.29

Table 4.2: Quality of the regression in terms of the stability criterion S (equation 4.23) over a range of gauge thicknesses.

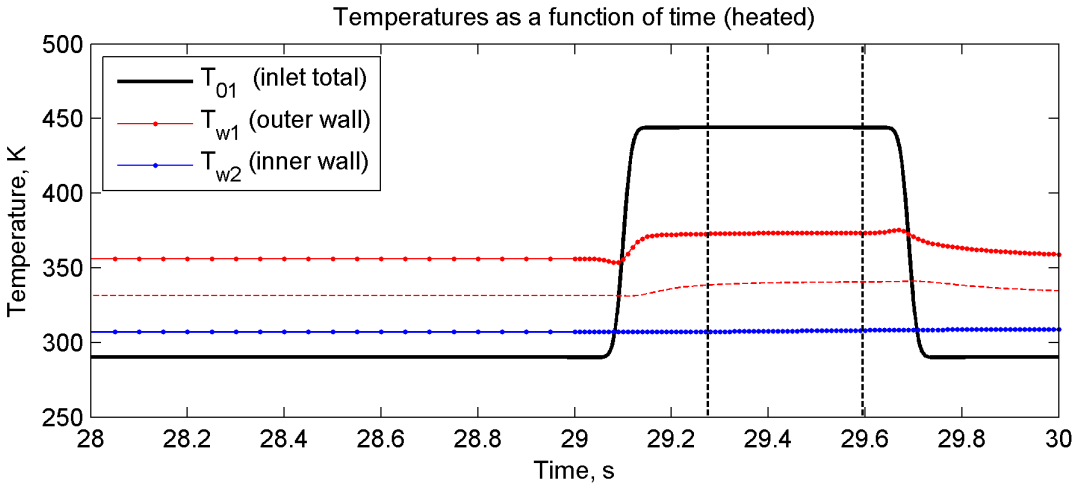

(a) Local adiabatic effectiveness $\eta_f = 0.5$

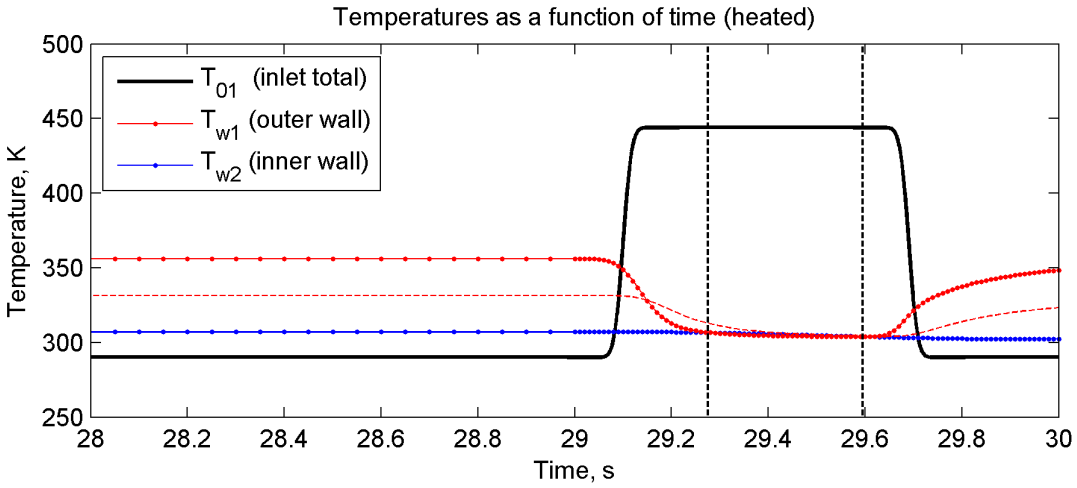

(b) Local adiabatic effectiveness $\eta_f = 1.0$

Figure 4.14: Wall temperatures for a double-sided thin film gauge with heated substrate at 80 mA on 1 mm aluminium wall for two different values of η_f.

decreases (for a heating current of 80 mA). For a sufficiently large film effectiveness the wall temperature achieved during the preheating is larger than the driving temperature during the run, which results in the outer wall being cooled during the run. The dependence of the resulting temperature range for the regression on the film effectiveness is depicted in figure 4.15 for a 230 µm thick gauge.

The dependence of the stability criterion on the film effectiveness is summarised in table 4.3.[1]

[1]The value of S cannot be computed for $\eta_f = 1$ in the unheated case as both the numerator and the denominator vanish.

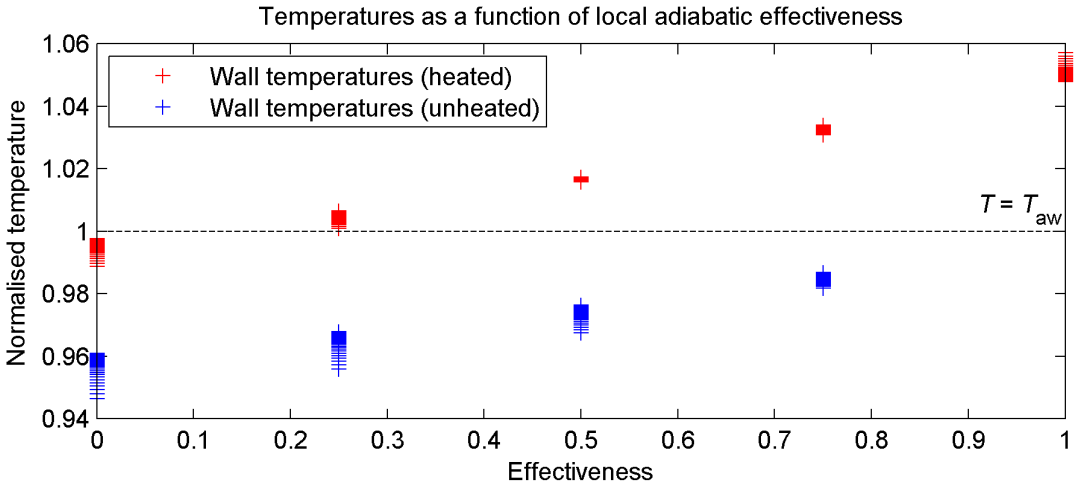

Figure 4.15: Surface temperature range for the extrapolation of the heat flux to obtain T_{aw} as a function of the effectiveness. The temperatures are normalised by T_{aw}. The unheated results (in blue) are compared to the heated results at 80 mA (in red).

Local adiabatic effectiveness	0	0.25	0.5	0.75	1.0
Unheated case	0.27	0.27	0.27	0.27	–
Heated case at 80 mA	0.81	0.94	0.11	0.10	0.18
Combination	0.96	1.15	1.54	1.53	1

Table 4.3: Variation of the stability criterion S (equation 4.23) as a function of the effectiveness and results for the combination of unheated and heated case.

The heated case has an optimum in which the surface temperature range is almost equal to the temperature difference to the adiabatic wall (and where $\dot{q} = 0$ might be achieved). However, this maximum in S does not necessarily correspond to a very accurate determination of the heat transfer coefficient, as the surface temperature range is very small. The maximum is followed by a minimum, where the temperature range is much smaller than the distance to the adiabatic wall temperature. At larger values of η_f the temperature range and S increase again. Note that a film cooling effectiveness close to unity drastically reduces the temperature difference between top and bottom gauges. For $\eta_f = 0.5$ this difference is still around 30 K, whereas for $\eta_f = 1.0$ the substrate is nearly isothermal (see figure 4.14). In this case it becomes very difficult to determine the heat flux.

The best results are achieved by a combination of unheated and heated tests. When the results from the unheated case are joined with the results from the heated case at 80 mA, the values for the stability criterion S range from 0.96 to 1.53 (see table 4.3). This means that the temperature range for the regression is similar to or larger than the difference between the adiabatic wall temperature and the first regression point, resulting in a very accurate extrapolation.

4.5 Summary

A measuring procedure to obtain distributions of Nusselt number and film cooling effectiveness on a film-cooled turbine stage has been discussed. By measuring the heat transfer rate for different wall temperatures, the heat transfer coefficient and the adiabatic wall temperature can be determined more accurately. The use of double-sided thin film gauges to measure the heat flux has been proposed and the underlying thin film gauge theory has been reviewed. An analytical model to account for lateral conduction effects has been presented. The transient behaviour of the double-sided thin film gauges has been investigated with a 1D FE multi-layer model. Finally, the improvement in the regression quality achieved by heated double-sided thin film gauges has been quantified with a stability criterion.

This chapter has provided the theoretical background for the use of heated double-sided gauges on a cooled turbine stage in a transient facility. In the following chapter a concrete gauge design will be developed based on the findings from this chapter.

CHAPTER 5

Modelling and Testing of Double-Sided Thin Film Gauges

This chapter presents the realisation of the thin film gauge concept developed and modelled in chapter 4. This new gauge concept consists of a double-sided thin film gauge with two different heating configurations. The final design of the gauges and the heating configurations are discussed in sections 5.1 and 5.2.

The focus of this chapter is on the process of obtaining heat transfer rates, which includes the calibration of the temperature coefficients of resistance (section 5.3) and the data analysis (section 5.4). In section 5.5 the problem of determining the initial gauge temperature is addressed and two analytical models are introduced to describe the thermal conduction in the gauge substrate for the two heating configurations. The thin film heaters are tested on the bench to validate the model prediction. Finally, in section 5.6 the experimental uncertainties associated with heat transfer measurements using heated gauges are assessed.

5.1 Thin film gauge design and manufacture

The design of the thin film gauges used in this study is based on the work by Collins et al. (2015a). When designing resistance gauges the aim is to maximise the gauge signal for a certain change in temperature. Gauge sensitivity is proportional to the resistance (and the temperature coefficient of resistance) of the gauge as well as to the current through the gauge. The larger the temperature coefficient of resistance of the gauge, the higher the temperature sensitivity (see also section 5.3).

For a platinum thin film gauge[1] the gauge resistance R_g is given by the resistivity of platinum ρ_{Pt} and the geometry of the gauge:

$$R_g = \frac{\rho_{Pt}\, l}{A}\,, \tag{5.1}$$

where l is the gauge length and A the cross sectional area. Typical resistivity of platinum is $\rho_{Pt} = 10.5 \cdot 10^{-8}\,\Omega\,\mathrm{m}$. For conventional thin film gauges the gauge current is chosen so as to minimise the ohmic heating of the gauges. The gauge sensitivity can then be maximised by maximising the l/d ratio, where d is the width of the gauge (the thickness of the gauge is determined by the manufacturing process, as discussed below).[2]

Previous designs of thin film gauges used at the Osney Laboratory had l/d ratios of around 10 (see section 2.2). These designs can be traced back to the beginning of the thin film gauge development, when sensors were hand-painted on glass-ceramic substrates (Schultz and Jones, 1973). The ratio can be increased through the use of long thin films in serpentine patterns in order to increase spatial resolution. The final gauge design and the manufactured result are presented in figure 5.1. For the chosen gauge dimension an MT1 NGV can be instrumented with 30 gauges over the aerofoil surface at constant span.

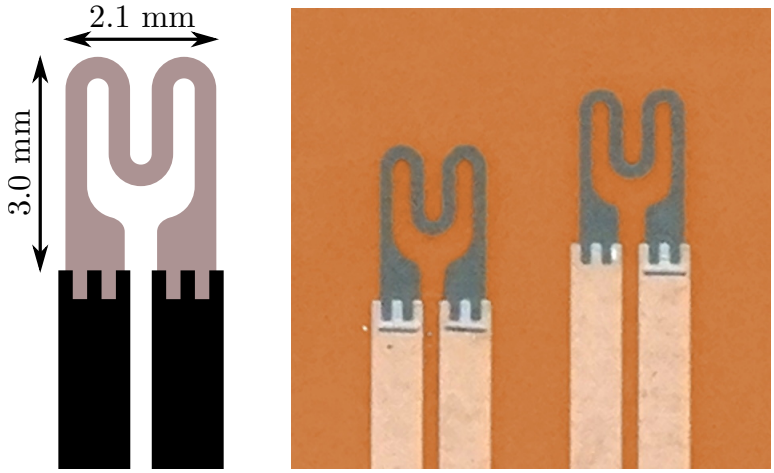

Figure 5.1: Thin film gauge design based on the work of Collins et al. (2015a): gauge dimensions and photograph.

[1] Platinum is commonly used as the material for the film, because of its high temperature sensitivity and its stable resistance-temperature relationship over a wide range of temperatures.

[2] For these observations the effect of the resistance of the copper tracks connecting the gauge to the current source is considered negligible.

The gauges are manufactured using a newly developed two-step manufacturing process (Collins et al., 2015a). The base material is a single-sided or double-sided polyimide film (Kapton) bonded to copper foil (see for example (DuPont^{TM}, 2012)). In the first step the geometry of the copper tracks is etched on the copper layer after exposure to UV light, which hardens the photoresist applied on the surface and protects the copper tracks (dry film photoresist lift off technique). The platinum film is deposited over the copper tracks in the second step. For this purpose, the gauge geometry is projected on the copper tracks and the entire surface is sputtered with a thin layer of platinum ($< 0.04\,\mu$m) . The unwanted platinum is removed together with the developed photoresist. The gauge resistance is metered during the sputtering. In order to achieve a good copper-platinum bond, the contact surface is maximised (see figure 5.1). However, the joint has proven to be very sensitive to manufacturing issues.

The simplest way to manufacture a double-sided thin film gauge is to manufacture a pair of single-sided thin film gauges as described above and then glue them together. The Kapton and glue layers have been found to have very similar thermal properties and will be regarded as one layer in the following. An alternative way of manufacturing double-sided gauges, which was investigated but has not been used for the current work, would be to use a double-sided substrate and sputter the platinum gauges on both sides of the insulating layer (see figure 5.2). The main advantage of the second manufacturing process is the elimination of the added uncertainties related to the thickness and the material properties of the glue. Also, it ensures a better alignment of the two platinum gauges on curved surfaces. This process has been used for the

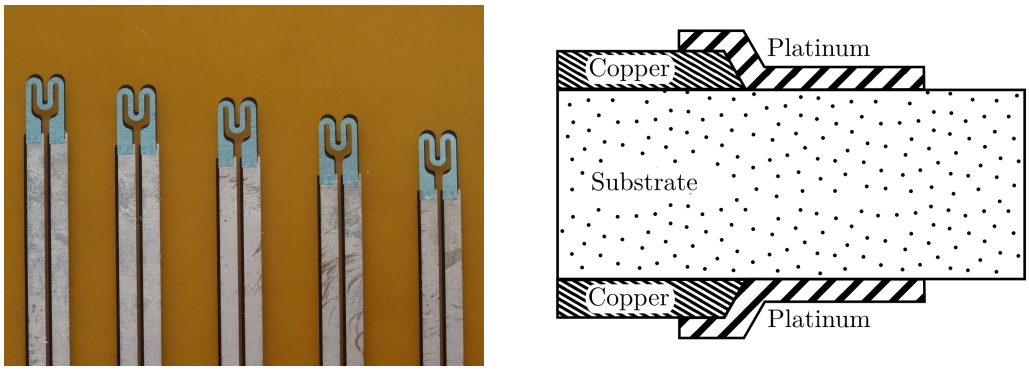

Figure 5.2: Double-sided thin film gauges fabricated using new manufacturing process.

first time to manufacture double-sided thin film gauges out of double-sided material. The accuracy achieved in the manufacture of double-sided thin film gauges was very good and the alignment between top and bottom gauge was within 0.1 mm.

The optimum thickness of the insulating layer between the top and bottom gauges has been determined as approximately 100 µm based on the modelling of the thermal pulse through the double-sided gauge, as explained in sections 4.3 and 4.4. The final gauge configuration also depends on the heating scheme, which will be described next.

5.2 Heating of double-sided thin film gauges

As explained in section 4.1, the basic idea of heated thin film gauges is to heat the gauge substrate in order to increase the temperature range over which the extrapolation to obtain T_{aw} and h is performed. Two heating concepts are presented: a thin film heater and self-heating gauges.

5.2.1 Thin film heater element

The simplest way to heat the gauge substrate is a thin film heater element placed underneath the thin film gauge on the surface of the part to be measured. The heater element has the advantage that it does not require space in the wall (as a cartridge heater would) and thus it does not affect the structural stability, which makes it an obvious choice for a heavily cooled vane. However, an additional insulating layer is required. The gauge configuration with an underside thin film heater is shown in figure 5.3a.

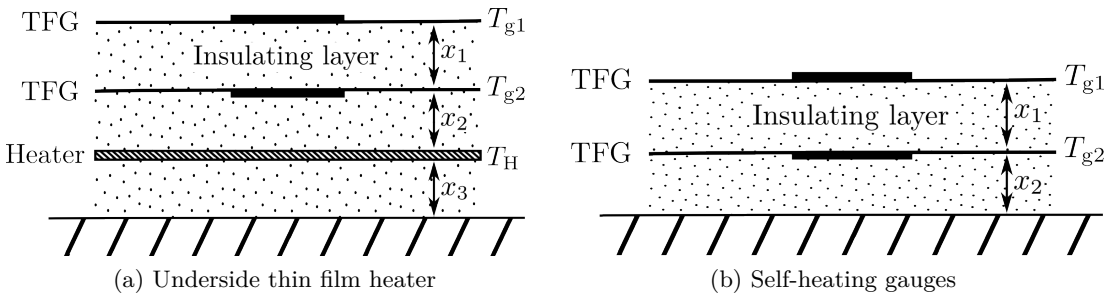

(a) Underside thin film heater (b) Self-heating gauges

Figure 5.3: Two heated thin film gauge arrangements.

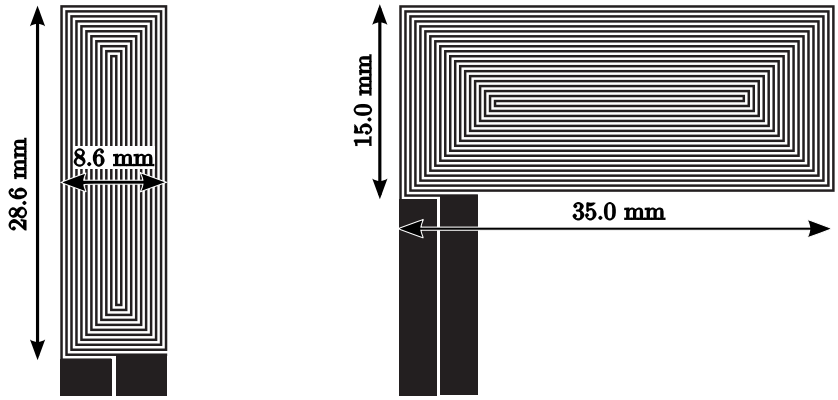

Figure 5.4: Different heater designs for different applications – including testing on uncooled and cooled aerofoil surfaces.

The heater is a copper spiral. The thickness and spacing of the tracks is limited by the accuracy of the etching process to 0.2 mm. Different heater designs developed for this study are shown in figure 5.4. Depending on the length of the heater tracks and the thickness of the copper, a wide range of resistances can be achieved. The heating power is limited by the outgassing temperature of the glue, which implies $\dot{q}_{\mathrm{H}} < 100\,\mathrm{kW\,m^{-2}}$ for a typical gauge configuration and a maximum preheating temperature difference of 100 K. The thicker the insulating layer between the heater and the wall, the less heating power is required. The thinner the insulating layer between the heater and the bottom gauge, the hotter the gauge substrate gets. For ease of manufacture all substrate layers investigated here have the same thickness of 100 µm.

5.2.2 Self-heating gauges

The idea for self-heating gauges originates from Jones (2013), who suggested using an array of heat transfer gauges as heaters in order to achieve a uniform heating of the test surface prior to the run.[1] Although in such a set-up the surface temperature will peak at the position of the heaters (i.e. the thin film gauges), the variation of the temperature on the surface is expected to be small compared to the average temperature difference between gas and surface (see figure 5.5). Nevertheless, the size of the temperature non-uniformity needs to be assessed carefully.

[1] Any surface temperature state could be chosen and the heat transfer coefficient defined for similar temperature distributions. However, a uniform surface temperature is not too far from the engine state.

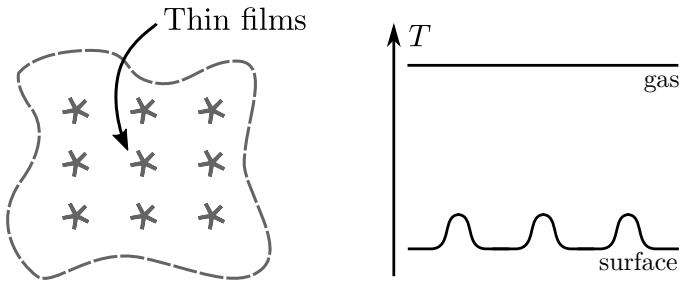

Figure 5.5: Steady-state temperature with individual film currents being adjusted to regulate the surface temperature.

At the beginning of the run the surface is in thermal equilibrium, i.e. the electrical power converted into heat by the thin film gauges equals the heat losses via conduction and convection. The electrical power is stable. Since the conduction field after the beginning of the run is expected to remain nearly constant, it is possible to infer the change in convective surface heat flux during the run by measuring the surface temperature with the thin film gauges. Provided the convective heat flux does not vary significantly between different points on the preheated surface, the local heat flux into the surface can be calculated using a conventional 1D conduction analysis. The measured heat transfer rate is equal to the surface heat flux minus the known pre-run heat flux.

If the double-sided gauges act as heaters by using the ohmic heating of the film at higher currents, the gauge configuration is identical to that of a conventional double-sided thin film gauge (see figure 5.3b). In comparison to the double-sided thin film gauges with an underside thin film heater, the total thickness of the package is reduced by the thickness of one additional insulating layer, which constitutes about one third of the package.

The heating of the gauges depends on the current through the gauge and the resistance and area of the gauge. The change in gauge resistance with temperature can be accounted for using the temperature coefficient of resistance following equation 4.22. As with the heater element, the heating power should not surpass $100\,\mathrm{kW\,m^{-2}}$.

5.3 Calibration of the temperature coefficient of resistance

The thin film gauges are calibrated in a water bath, in which the resistance of the gauges at different temperatures is recorded to obtain the temperature coefficient of resistance α (Collins et al., 2015a). The present gauges were calibrated in a temperature range from 5 °C to 35 °C. The gauges can be calibrated at lower temperatures than those experienced during a test, because the temperature coefficient of platinum is nearly constant over a wide range of temperatures. The resistance is recorded at each temperature step, once isothermal conditions (within 0.3 K) are achieved between the water and the test part with the thin film gauges on it. This section gives an analytical definition of the temperature coefficient of resistance and its application in the experiments.

For a conductor

$$\frac{\mathrm{d}R}{\mathrm{d}T} \propto R \text{ (independent of } T\text{).} \tag{5.2}$$

Calling the constant of proportionality α, we obtain

$$\frac{\mathrm{d}R}{R} = \alpha\,\mathrm{d}T \quad \Rightarrow \quad \ln\frac{R}{R_0} = \alpha(T - T_0) \tag{5.3}$$

$$\Rightarrow \quad R(T) = R_0\, e^{\alpha(T-T_0)}\,, \tag{5.4}$$

where $R_0 = R(T_0)$. The choice of T_0 is arbitrary, since we could equivalently write

$$R(T) = R(T_1)e^{\alpha(T-T_1)} \quad \text{with} \quad R(T_1) = R_0\, e^{\alpha(T_1-T_0)} \tag{5.5}$$

$$\Rightarrow R(T) = R_0\, e^{\alpha(T_1-T_0)}e^{\alpha(T-T_1)} \tag{5.6}$$

$$= R_0\, e^{\alpha(T_1-T_0)+\alpha(T-T_1)} \tag{5.7}$$

$$= R_0\, e^{\alpha(T-T_0)}\,. \tag{5.8}$$

For $\alpha(T - T_0) \ll 1$, we can use $e^x \approx 1 + x$ to write

$$R(T) \approx R_0\,[1 + \alpha(T - T_0)]\,. \tag{5.9}$$

This will hold for $T \approx T_0$. Defining $m = \alpha R_0$ this can be written as

$$R(T) \approx R_0 + m(T - T_0) \; . \tag{5.10}$$

In contrast to α, m depends on R_0 (i.e. on T_0).

Extracting α from calibration data

If calibration data is available over a wide range of temperatures, a linear approximation will give a bad fit. Instead α and R_0 can be determined by fitting an exponential of the form

$$R(T) = R_0 \, e^{\alpha(T - T_0)} \; . \tag{5.11}$$

If there is only calibration data for a small range $T \approx T_1$, it is sufficient to fit a linear function

$$R(T) = R_0 + m(T - T_0) \tag{5.12}$$

where T_0 is arbitrary (and m does not depend on this choice). From this form, we can then determine α as

$$\alpha = \frac{m}{R(T_1)} \quad \Rightarrow \quad R(T) = R(T_1) \left[1 + \alpha(T - T_1)\right] \; . \tag{5.13}$$

Note that while T_0 is arbitrary, the resistance in the denominator must be evaluated at $T = T_1$, which is the temperature where calibration data is available (α is then independent of T_0). The linear approximation will then be valid for as long as T is not too different from T_1.

The temperature coefficient of resistance follows from the linear relationship between the resistance and the temperature and is calculated using a least-squares fit. Typical calibration data is shown in figure 5.6. The temperature coefficient achieved is usually around $1 \cdot 10^{-3}\,\mathrm{K}^{-1}$ for the thin film gauges. This value is lower than the value of $3.93 \cdot 10^{-3}\,\mathrm{K}^{-1}$ reported for the bulk material platinum, because of thin film effects, which result from a reduced mean free path of the electrons in the film.

Calculating α for the experimental set-up

After calibration the gauge sensitivity can be affected by two possible alterations:

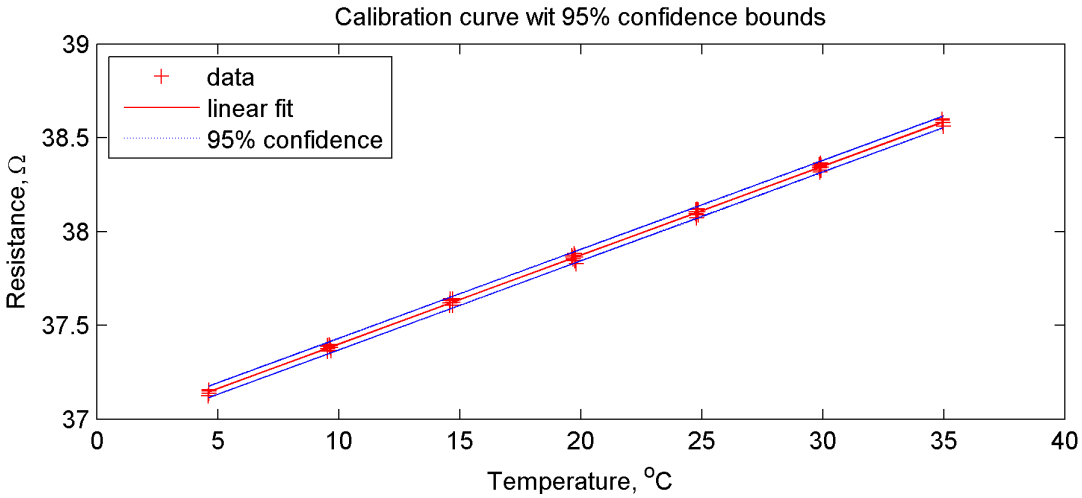

Figure 5.6: Typical calibration data with 95% confidence bounds.

- Due to a change in the wiring (e.g. soldering joints) a resistance is added in series to the gauge. This change will not affect the $\mathrm{d}R/\mathrm{d}T$ of the gauge, thus the slope m should be used for any further calculations.

- Stress changes in the substrate cause a change in absolute resistance of the gauge. The relative change $R^{-1}\,\mathrm{d}R/\mathrm{d}T$ should stay constant, thus α should be used for any further calculations.

During calibration gauges are attached to the part they will be used on whenever possible. When calibrating the gauges on an NGV, the NGV is also submerged in the water bath. Since the gauges are not manipulated after the calibration, changes in the substrate before the test are unlikely. Any change in resistance is therefore attributed to additional resistance added in series (lead resistance). Assuming a constant $\mathrm{d}R/\mathrm{d}T$ of the gauge, the α value can be recalculated from known pairs of gauge resistance and temperature in the final experimental set-up:

$$\alpha_{\mathrm{exp}} = \frac{\alpha_{\mathrm{cal}} R_{\mathrm{cal}}}{R_{\mathrm{g}} - \alpha_{\mathrm{cal}} R_{\mathrm{cal}} (T_{\mathrm{g}} - T_{\mathrm{cal}})} \,. \tag{5.14}$$

This equation accounts for changes in the lead resistance, which are however expected to be very small (a typical $1\,\Omega$ change in resistance corresponds to a change in α of around 2%).

The new design of thin film gauges has an l/d ratio of 26 compared to previous designs with an l/d ratio of around 10. Thus, it is to be expected that for the same platinum thickness the

resistance of the new gauges is larger by a factor of 2.6 (see equation 5.1). Previous experience has shown that gauges with resistances around 120 Ω do not calibrate well, as large drifts in R_0 are observed. These drifts are suspected to be caused by stress relaxation in the platinum film and/or at the copper joint. A thicker platinum film and the annealing of the gauges at 80 °C has been shown to reduce this effect. When reducing the resistance of the gauges to between 50 Ω and 60 Ω by depositing a thicker platinum layer the calibration stability improves significantly.

The resistances of the gauges were monitored during the test campaign. The low pressures at the start of the run and the high temperatures achieved with the heated gauges can both potentially lead to an outgassing of the glue. The formation of bubbles in the substrate could then cause a change in the gauge resistance and in the thickness of the substrate layer. Gauges with too large a change in resistance are dismissed.

5.4 Data analysis

This section describes the process of recording the gauge voltage and turning it into a temperature trace, which is used to calculate the heat flux and obtain the heat transfer coefficient and the adiabatic wall temperature from a regression of the heat flux over the wall temperature.

5.4.1 Measurement strategy for thin film gauges with or without underside heater

For the heat transfer measurements the initial voltage V_i across each gauge is recorded at the beginning of the run together with the temperature T_wi of the instrumented cassette, which is measured using up to four thermocouples. Given the 45 min time passing between each two runs, isothermal conditions can be assumed. The voltage across a gauge is then recorded during the run time. It is assumed that the current I stays constant, i.e. $I \approx I_\mathrm{i}$. The change in temperature follows from the change in resistance according to

$$\Delta T = T - T_\mathrm{wi} = \frac{(R - R_\mathrm{i})\,[1 + \alpha(T_\mathrm{wi} - T_\mathrm{cal})]}{\alpha R_\mathrm{i}} \tag{5.15}$$

where T_{cal} corresponds to the temperature at which the temperature coefficient of resistance α was determined. Since $I \approx I_{\mathrm{i}}$ the temperature difference can be expressed as a change in voltage

$$\Delta T = \frac{(V - V_{\mathrm{i}})\,[1 + \alpha(T_{\mathrm{wi}} - T_{\mathrm{cal}})]}{\alpha V_{\mathrm{i}}} \tag{5.16}$$

and no knowledge of the exact current is required. This calculation is valid for the single-sided as well as the double-sided thin film gauges.

When taking heat transfer measurements with double-sided thin film gauges on a heater element, the temperature of the cassette is recorded before the heater is switched on, thus ensuring that the measurement is taken under isothermal conditions. The heating of the gauge substrate is captured by the increase in voltage from the initial voltage to the voltage recorded just before the test starts. The post-processing is the same as described above.

5.4.2 Measurement strategy for self-heating thin film gauges

For double-sided thin film gauges with variable heating current through the top gauge, equation 5.16 cannot be used because both the current and the gauge temperature change during preheating. Heat transfer measurements then require additional information on the initial gauge temperature T_{gi}. This temperature cannot be measured in rig conditions, but it can be inferred from external information such as bench test data or thermal models. Once T_{gi} is known and the corresponding voltage V_{gi} has been measured, one can calculate any subsequent change in temperature:

$$\Delta T = T - T_{\mathrm{gi}} = \frac{(V - V_{\mathrm{gi}})\,[1 + \alpha(T_{\mathrm{gi}} - T_{\mathrm{cal}})]}{\alpha V_{\mathrm{gi}}}\,. \tag{5.17}$$

In this work the current through the bottom gauge is always kept constant. The temperature increase of the bottom gauges can therefore be calculated using equation 5.16, where the initial temperature of the cassette is recorded under isothermal conditions before increasing the current through the top gauge. Using an accurate model of the heat conduction between the two gauges, it is then possible to derive the temperature of the top gauge from the bottom gauge temperature, provided the two gauges are very well aligned.

An alternative option would be to obtain the initial top gauge temperature from a direct

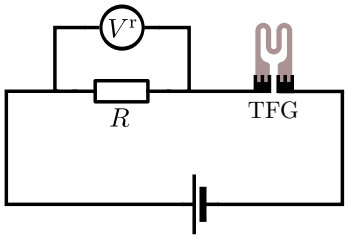

Figure 5.7: Circuit used to monitor the current through a thin film gauge with a constant resistor in series.

current measurement, i.e. to measure both V and I and then calculate $R(T)$ and hence determine T. In this case, equation 5.15 becomes

$$\Delta T = T - T_{\mathrm{wi}} = \frac{(V/I - V_{\mathrm{i}}/I_{\mathrm{i}})\,[1 + \alpha(T_{\mathrm{wi}} - T_{\mathrm{cal}})]}{\alpha V_{\mathrm{i}}/I_{\mathrm{i}}} \tag{5.18}$$

$$= \frac{(V\ I_{\mathrm{i}}/I - V_{\mathrm{i}})\,[1 + \alpha(T_{\mathrm{wi}} - T_{\mathrm{cal}})]}{\alpha V_{\mathrm{i}}} \tag{5.19}$$

with the current through the top gauge $I > I_{\mathrm{i}}$ set after the reference measurement. However, the quantity $V\,I_{\mathrm{i}}/I$ is much more difficult to measure accurately than V (which enters in equation 5.16).

For example, if the change in current is monitored with a constant resistor in series – using the circuit sketched in figure 5.7 – it follows that

$$\Delta T = \frac{(V^{\mathrm{g}}\ V_{\mathrm{i}}^{\mathrm{r}}/V^{\mathrm{r}} - V_{\mathrm{i}}^{\mathrm{g}})\,[1 + \alpha(T_{\mathrm{wi}} - T_{\mathrm{cal}})]}{\alpha V_{\mathrm{i}}^{\mathrm{g}}} \tag{5.20}$$

where g and r stand for gauge and resistor respectively and V_{i} is the reference voltage at isothermal conditions. In order to determine ΔT with a precision of 1 K it is necessary to measure the product $V^{\mathrm{g}}/V_{\mathrm{i}}^{\mathrm{g}}$ and $V^{\mathrm{r}}/V_{\mathrm{i}}^{\mathrm{r}}$ with an error of less than 0.1%. The problem is that in the case of large heating currents, $V^{\mathrm{g}}/V_{\mathrm{i}}^{\mathrm{g}}$ and $V^{\mathrm{r}}/V_{\mathrm{i}}^{\mathrm{r}}$ will be very large, typically of order 10–20. This is in contrast to the unheated case, where V/V_{i} is always very close to unity. Given the wide range of voltages, it is very challenging to measure both voltage ratios in the heated case to the required level of accuracy. Because of these larger uncertainties in the temperature measurements, the option of inferring gauge temperatures from current measurements has been discarded.

To summarise, the principle of operation for measuring the surface temperature using both

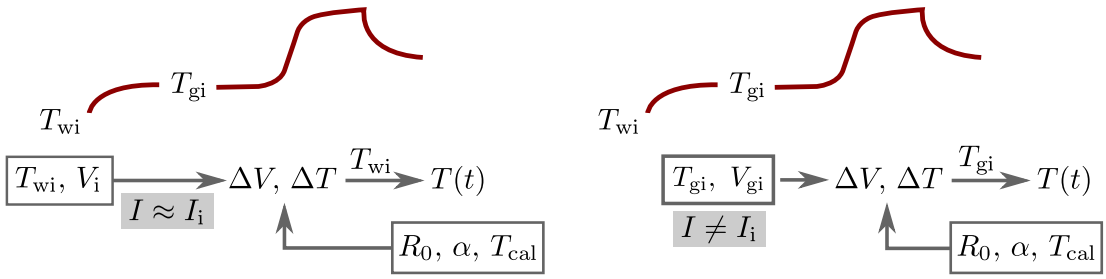

(a) Thin film gauges with underside heater.

(b) Self-heating thin film gauges.

Figure 5.8: Principle of operation of two heated thin film gauge arrangements to measure the surface temperature history.

heated thin film gauge arrangements is illustrated in figure 5.8. For gauges with an underside heater (left panel), the initial temperature and voltage can be used directly to infer the temperature trace for the top and bottom gauges from the change in voltage. For the self-heating gauges the top and bottom temperatures are calculated in two different ways. The bottom gauge temperature trace follows from the initial temperature and the corresponding change in voltage, as for a gauge with an underside heater. However, the current through the top gauge is increased after the reference measurement is taken and knowledge of the initial gauge temperature is required to obtain the temperature trace (right panel). The problem of determining the initial gauge temperature will be further discussed in section 5.5.

5.4.3 Use of HTA3 amplifier and modification for higher currents

The HTA3 thin film signal conditioning amplifier is used as a current source for the thin film gauges and to record the heat transfer signal. A description and a user guide is given in (Oldfield and Beard, 2014). The HTA3 amplifier uses an SSM2019 chip from Analog Devices, which was designed as an audio preamplifier. The characteristics of this amplifier are low noise, wide bandwidth and high gain. The HTA3 circuit diagram can be found in appendix A.1.

The DC output is used to set and monitor the thin film voltage. The cut off frequency is 407 Hz and the gain is approximately 4.7. A higher gain can be achieved with the AC output low speed, which has the same cut-off frequency but a gain of approximately 47.0. Higher frequencies can be studied with the AC output high speed, which has a high frequency boost to

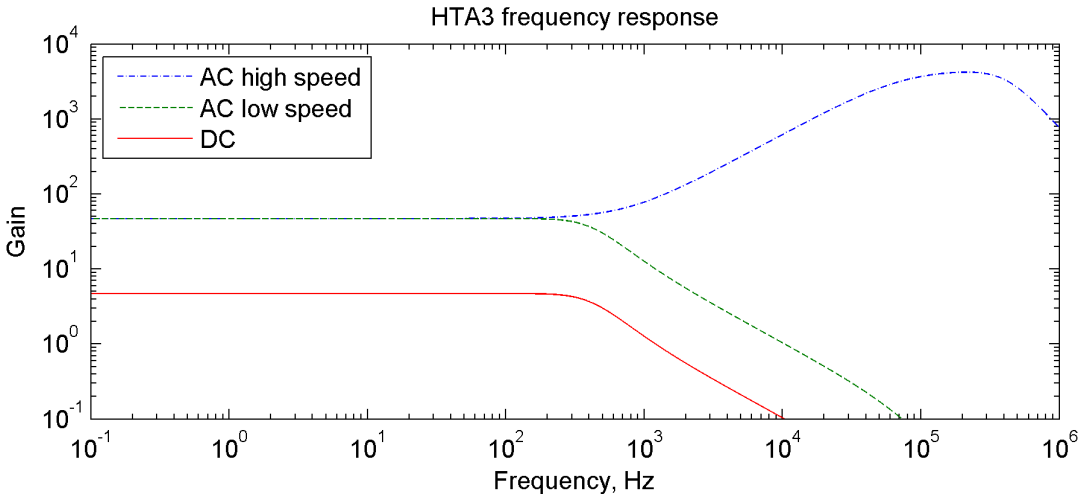

Figure 5.9: HTA3 frequency response.

counteract the decreasing thin film gauge frequency response (Oldfield and Beard, 2014). The resulting frequency response is shown in figure 5.9. The high frequency boost has to be removed by digital post-processing.

The HTA3 amplifier has been calibrated in order to determine the frequency response for each channel. For this purpose the input from a signal generator and the output on separate channels was measured. To remove the instrument error, the calibration was repeated with switched channels and the geometric mean of the gain was calculated. The frequency of the input was increased stepwise from 10 Hz to 1 MHz (for the high frequency response). This calibration can be performed by the manufacturer, who employs a calibrated inverse circuit, i.e. a passive circuit which has a frequency response which is the inverse of that of the ideal HTA3 frequency response. This circuit allows a voltage signal to be supplied and measured at all frequencies resulting in a better calibration accuracy.

High constant current source modification

In order to achieve the higher currents necessary for using the HTA3 amplifier with self-heating gauges, the original maximum current of 20 mA had to be increased. This change required a modification of the high constant current supply to allow for currents up to 150 mA. The modification is detailed in (Oldfield and Beard, 2014) and shown in appendix A.1.

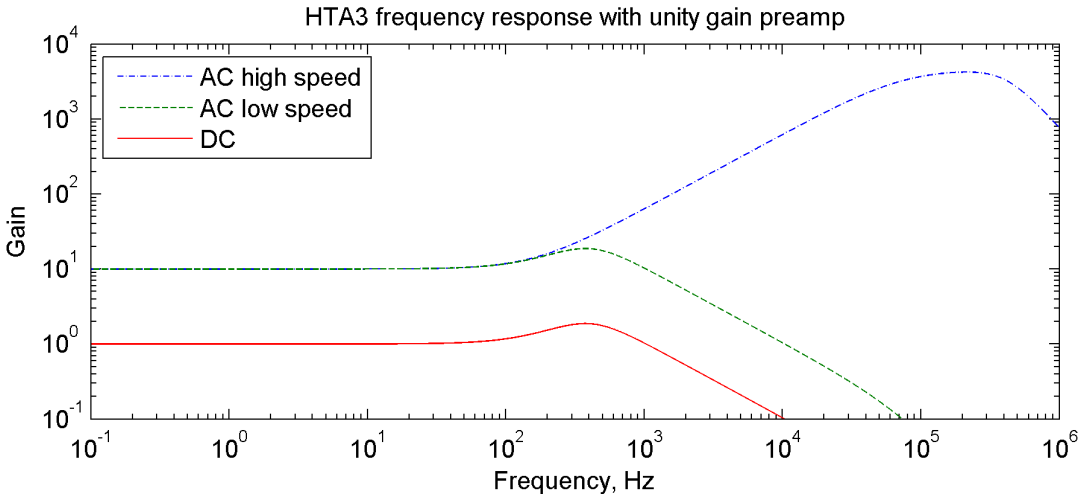

Figure 5.10: HTA3 frequency response with unity gain preamp (modified circuit).

Connecting a 150 mA current source to a 50 Ω thin film gauge would produce a 7.5 V DC voltage on the input, which would saturate the DC output for the original gain of 4.7. The increase in the maximum achievable current therefore required a reduction of the gain to unity in order to prevent the stage from saturating. A further modification of the circuit was required to reduce the gain. This change caused a hump in the frequency response of the DC output as can be seen in figure 5.10. The hump in the DC and AC low speed response can be removed in post-processing, in a similar way as for the original high frequency response. The modified HTA3 required recalibration as discussed above. This recalibration was performed in-house.

5.4.4 Impulse response processing of transient heat transfer signals

Historically, the experimental heat transfer rate was obtained from the surface temperature signal using numerical approximations to the solutions of the linear differential equations relating the two (see section 4.2). The impulse response method, in contrast, only uses known pairs of exact solutions, such as the temperature response to a step in heat flux, to derive a sampled approximation of the impulse response of the gauge system (Oldfield, 2008). This impulse response is then used as a finite impulse response digital filter to convert the surface temperature signal into a heat transfer rate.

Since the differential equations describing a thin film gauge are linear and time invariant, the

response $q(t)$ to a temperature trace $T(t)$ can be calculated from the impulse response $h(t)$ of the system from the convolution integral

$$q(t) = h(t) * T(t) = \int_{-\infty}^{\infty} h(\tau)T(t-\tau)\,\mathrm{d}\tau\ . \tag{5.21}$$

Taking τ as a continuous variable this integral can be difficult to evaluate and $h(t)$ often has singularities at the origin.

In the discrete-time domain (with the sampling period t_s or sampling frequency $f_\mathrm{s} = 1/t_\mathrm{s}$) the continuous signal $T(t)$ is replaced by the discrete sequence

$$T[n] = T(nt_\mathrm{s}) \text{ for } n = \ldots -3, -2, -1, 0, 1, 2, 3 \ldots \tag{5.22}$$

and the convolution integral becomes the convolution sum

$$q[n] = h[n] * T[n] = \sum_{k=-\infty}^{\infty} h[k]T[n-k] = \sum_{k=-\infty}^{\infty} h[n-k]T[k]\ . \tag{5.23}$$

If all the signals are assumed to be 0 for $n \leq 0$ and of a finite length N the convolution sum can be reduced to

$$q[n] = h[n] * T[n] = \sum_{k=1}^{N} h[k]T[n-k] = \sum_{k=1}^{N} h[n-k]T[k]\ . \tag{5.24}$$

This discrete convolution can be calculated using a Matlab function.

The impulse response function sequence $h[n]$ can be obtained from a pair of non-singular solutions $q_1(t)$ and $T_1(t)$ for the heat transfer equations in the gauge substrate (e.g. a step in heat flux and the corresponding "parabolic" rise in temperature for a semi-infinite substrate), as follows:

$$q_1[n] = h[n] * T_1[n] \tag{5.25}$$

and $h[n]$ can be found by deconvolution. Taking z-transforms, the convolution is replaced by a multiplication, which can be inverted:

$$Q_1(z) = H(z)T_1(z) \rightarrow H(z) = \frac{Q_1(z)}{T_1(z)}\ . \tag{5.26}$$

Convoluting the impulse response with an impulse function

$$\delta[n] = \begin{cases} 1 & n = 0 \\ 0 & \text{otherwise} \end{cases} \tag{5.27}$$

will by definition give back the impulse response:

$$H(z) = H(z)\Delta(z) = \frac{Q_1(z)}{T_1(z)}\Delta(z) \,, \tag{5.28}$$

where $\Delta(z)$ is the z-transform of $\delta[n]$. Thus, the required impulse response can be obtained by digitally filtering the impulse function $\delta[n]$ using an IIR (infinite impulse response) filter with coefficients $Q_1(z)/T_1(z)$, which has been implemented in Matlab. It is enough to calculate the impulse response once for each set of gauge parameters, making this processing of surface temperature signals computationally very efficient.

This method and the corresponding filter routines have been extended to two-layer substrate gauges and double-sided gauges (Oldfield, 2008). The central idea is that any double-sided thin film gauge can be modelled as the superposition of two single-sided thin film gauges. If a is the thickness of the double-sided thin film gauge and T_{g1} and T_{g2} are the temperatures of the top and bottom gauge (see figure 4.1b) this method proceeds as follows. The first single-sided gauge has a surface temperature of $(T_{g1} - T_{g2})/2$, a thickness of $a/2$ and an infinitely conducting lower surface with $T = 0$, while the second single-sided gauge has a surface temperature of $(T_{g1} + T_{g2})/2$, a thickness of $a/2$ and an insulating lower substrate ($\dot{q} = 0$). It is straightforward to calculate the corresponding response functions h_d and h_c for these simple cases. The heat flux for the double sided thin film gauge is then given by

$$q_1 = h_1 * T_{g1} + h_2 * T_{g2} \tag{5.29}$$

with

$$h_1 = \frac{h_d + h_c}{2} \quad \text{and} \quad h_2 = \frac{h_c - h_d}{2} \,. \tag{5.30}$$

Validation of the data processing

There are two methods of post-processing data from double-sided thin film gauges if a semi-infinite substrate can be assumed. The temperature signals of the top and bottom sensors of a double-sided gauge can be used to obtain the heat flux as described above (double-sided processing). Alternatively, the temperature signal of the top gauge is enough to calculate the heat flux (two-layer processing). The two methods can be compared using the 1D multi-layer model introduced in section 4.2 and used to validate the post-processing.

Figure 5.11 shows the temperature trace of the top and bottom sensors of a double-sided gauge (230 µm Kapton) on a 1 cm aluminium wall for the unheated case. The inner wall temperature is set constant at 290 K. The results are reported at 1000 time steps. These temperature signals are used to obtain the heat flux from the impulse response method for a two-layer substrate gauge and for a double-sided gauge. The results are compared in figure 5.12 with the true heat transfer rate, which can be directly obtained from the multi-layer model. The difference between the two-layer and double-sided post-processing is shown in figure 5.13. Note that the error in heat flux also depends on the accuracy of the 1D diffusion equation model (which in this case consists of 1000 cells per Kapton layer and 100 cells in the aluminium wall). In both cases the discrepancy is largest at the transients and reaches a maximum of 3.6%.

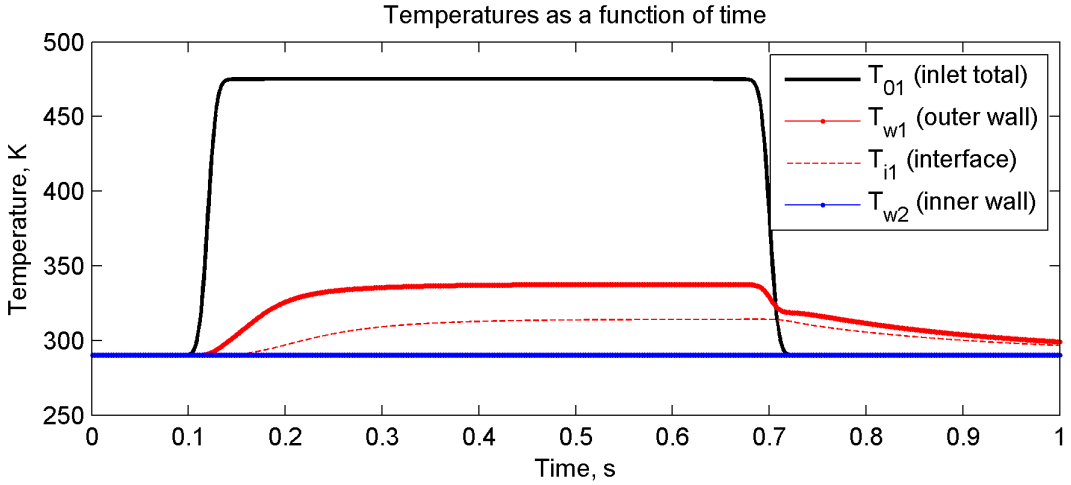

Figure 5.11: Model of the wall temperatures of a double-sided gauge using the 1D diffusion equation (as introduced in section 4.2).

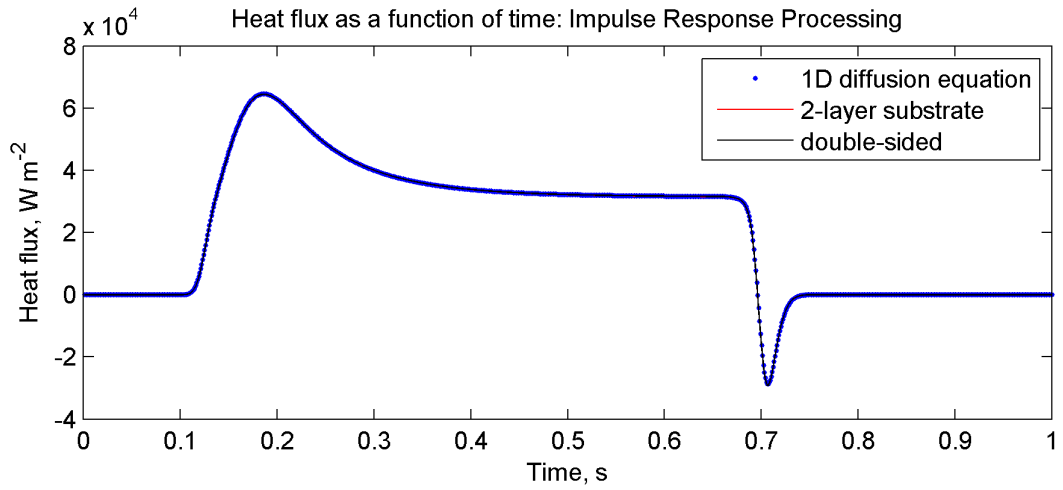

Figure 5.12: Heat flux trace for two-layer and double-sided processing. The temperatures in figure 5.11 are given as an input to the impulse response method. The results are compared to the 1D diffusion equation. The red and black lines are indistinguishable.

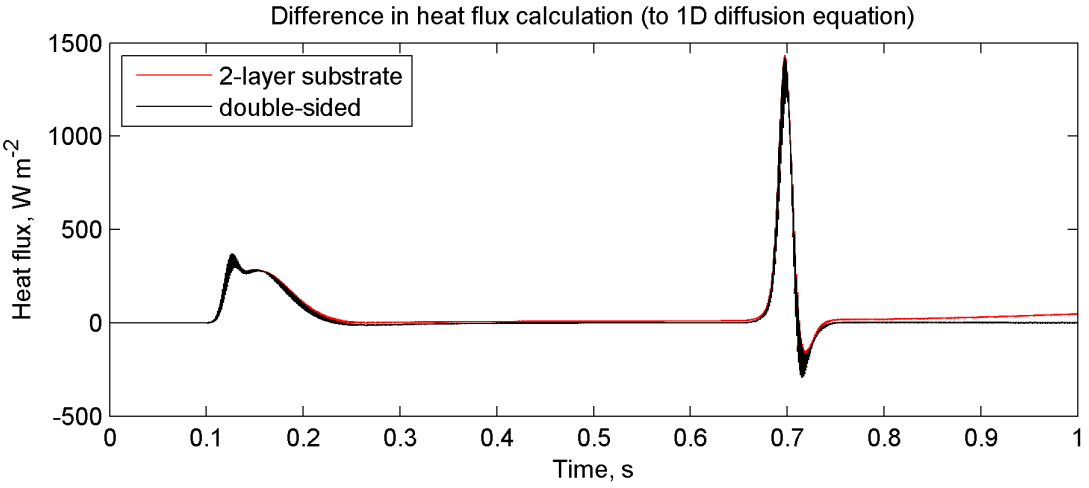

Figure 5.13: Comparison of the discrepancy between two-layer and double-sided post-processing of the temperature signals of a double-sided gauge.

In addition to the numerical study, the impulse response method was validated experimentally using a shutter rig, which provides a step change in heat flux. The resulting surface temperature history was recorded with single-sided and double-sided thin film gauges. The underlying heat flux was then reconstructed using the impulse response method for both types of gauges. The step change as well as the magnitude of the heat transfer rate during the run were well captured qualitatively, although it is difficult to quantify the agreement due to the variability of the heat

flux provided by the hot air gun.

5.4.5 Regression of heat flux over wall temperature

Once the heat flux into the wall has been obtained from the temperature history of the gauges using the impulse response processing described above, the adiabatic wall temperature and heat transfer coefficient follow from a regression of the heat flux data over the wall temperature (see figure 4.2). The quality of the regression can be improved by performing the regression on data from multiple runs. In this case more accurate results are obtained if the regression accounts for changes in the inlet total temperature. This so-called floating regression was developed for over-tip heat transfer measurements, where the local total temperature is strongly influenced by work extraction from the fluid by the rotor. For the stator tests presented in chapters 6 and 7 the effect is less important but should nevertheless be included. The magnitude of the correction is estimated below.

If the total temperature at the heat transfer measurement location $T_{0,x}$ is different from the temperature measured at the inlet plane T_{01}, the resulting change in driving temperature during the run duration must be taken into account for the linear regression (Collins et al., 2015b). Assuming the change in temperature can be described by a polytropic expansion, it follows:

$$\frac{T_{0,x}}{T_{01}} = \left(\frac{p_{0,x}}{p_{01}}\right)^{(n-1)/n} . \tag{5.31}$$

For an aerodynamically stable run the ratio of local and inlet pressure remains constant. Thus, if the effects of the polytropic process are assumed to be larger than those caused by flow stagnation, the adiabatic wall temperature T_{aw} can be expressed as a linear function of the time varying inlet total temperature:

$$T_{\mathrm{aw}} = k\, T_{01} . \tag{5.32}$$

The convective heat flux equation can then be expressed with the heat transfer coefficient h as

$$\dot{q} = h(T_{\mathrm{w}} - kT_{01}) . \tag{5.33}$$

Collins et al. (2015b) introduce a corrected wall temperature T'_{w}, which can be plotted against

$\dot{q}$ for the purposes of a regression:

$$T'_{\mathrm{w}} = T_{\mathrm{w}} - k(T_{01} - \overline{T_{01}}) \ , \tag{5.34}$$

where $\overline{T_{01}}$ is the time averaged inlet total temperature. The corrected wall temperature accounts for the effect of the time-dependent change in inlet total temperature on the wall temperature. T'_{aw} is defined as $k\overline{T_{01}}$ and is given by the intercept with the corrected temperature axis. For typical OTRF data the difference between the time averaged inlet total temperature and the instantaneous temperature is maximally 10 K (see also section 7.1). For a value of k close to 1, this difference corresponds to the contribution to the corrected wall temperature.

The fitting parameters of the straight line are calculated iteratively from this first estimate of T_{aw}. The updated value of k for each iteration is given by

$$k_{(i)} = T'_{\mathrm{aw}(i-1)}/\overline{T_{01}} \ . \tag{5.35}$$

For the regression the $\dot{q}$ data is resampled at regular intervals of T'_{w}. This resampling removes the bias of the regression towards the region of smaller change in temperature and gives equal weighting to the entire temperature rise.

5.5 Gauge preheating and problem of determining initial temperature

This section discusses the preheating of the gauge substrate using an underside thin film heater and the ohmic heating of the gauges. The aim is to introduce models to describe the gauge temperatures, which can be demonstrated experimentally.

5.5.1 Thin film heater element

A bench test was performed to study how the substrate of a double-sided thin film gauge can be heated using a heater element. The tested heater designs correspond to those presented in section 5.2. The experimental configuration consisted of a set of double-sided gauges placed on each type of thin film heater on an aluminium plate (see figure 5.14). A thermocouple was used to record the temperature on top of each heater. These thermocouples were separated from the heater by two Kapton layers with a combined thickness of 210 µm, which equals the thickness

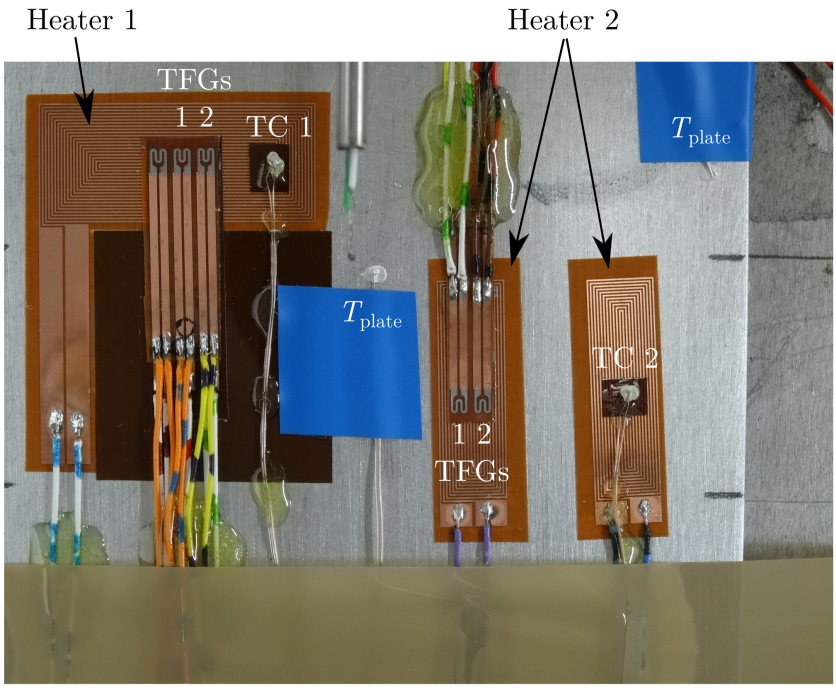

Figure 5.14: Experimental set-up to test gauge preheating with underside thin film heaters. Heater 1 is the big horizontal heater. Heater 2 is the small vertical heater. There are no results for the leftmost thin film gauge on heater 1, as it did not calibrate.

of the gauge substrate. The temperature of the plate was also measured with thermocouples.

The three heaters were connected in series and tested simultaneously on the bench. The two identical vertical heaters were used to measure the surface temperature under identical conditions using thin film gauges and a thermocouple. The current through the heaters was kept constant for the duration of each test and then increased stepwise from 0 A to 1.6 A. Two consecutive tests were carried out at each current setting. The results as measured by the two top gauges and the corresponding thermocouple are compared in figure 5.15 for each type of heater. This figure shows the temperature difference relative to the wall temperature measured by two thermocouples on the aluminium plate. The preheating temperatures were time-averaged for at least 2 s. The agreement between the two consecutive tests is excellent. There is however a small systematic difference between the temperatures measured by the two thin film gauges above each heater. The temperature measured by the first (left) thin film gauge of heater 1 and the second (right) thin film gauge of heater 2 is consistently higher. The difference between the two thin film gauges is proportional to the total preheating temperature difference and is at

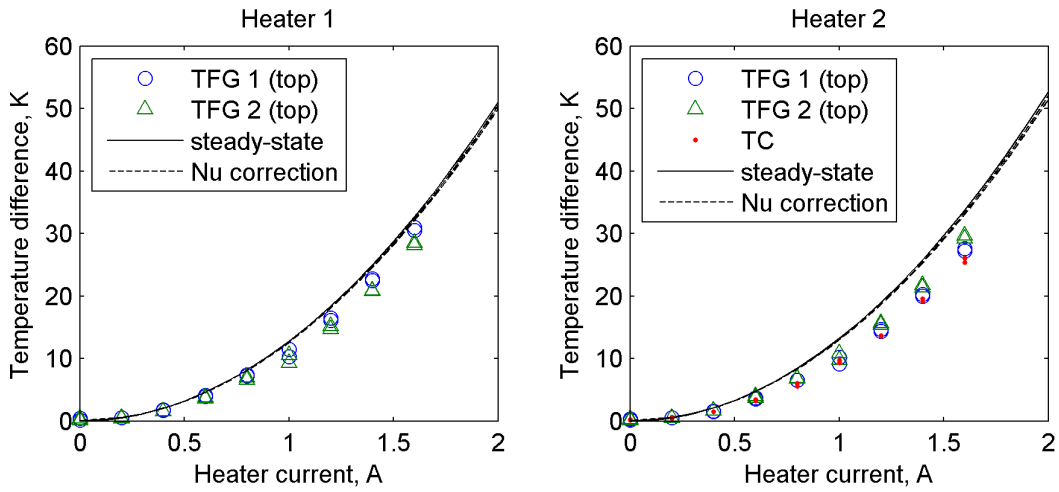

Figure 5.15: Preheating top gauge temperatures over increasing heater current for 18 consecutive tests. The temperatures measured by the two thin film gauges are compared to analytical results. For heater 2 the surface temperature measured by a thermocouple is also shown.

most 2 K. While this temperature difference lies within the expected temperature uncertainty it could also point to slightly uneven heating, because in both cases the hotter thin film gauge is located more centrally on the heater. On heater 2 it can also be observed that both thin film gauges are consistently hotter than the thermocouple.

Heat transfer prediction and Nusselt number correction

In figure 5.15 the measured gauge temperatures are also compared to the temperatures obtained from a steady-state calculation (see equation 4.1). The analytical predictions agree well with the experimental results. To account for the heat dissipation into the environment a correlation for the Nusselt number for a surface in natural convection was used. The Nusselt number can be expressed as a function of Grashof number Gr and Prandtl number Pr (Howatson et al., 2009)

$$\mathrm{Nu} = C(\mathrm{Gr}\,\mathrm{Pr})^n \,, \tag{5.36}$$

where C and n are two empirical factors, which depend on the geometry and the flow conditions. For a heated horizontal plate facing up these factors are (Howatson et al., 2009)

$$C = 0.54 \text{ and } n = \frac{1}{4} \text{ for } \mathrm{Gr}\,\mathrm{Pr} = 10^5 - 10^7 \,, \tag{5.37}$$

$$C = 0.14 \text{ and } n = \frac{1}{3} \text{ for } \mathrm{Gr}\,\mathrm{Pr} = 10^7 - 10^{11} \; . \tag{5.38}$$

The Grashof number is a non-dimensional parameter that describes the ratio of buoyancy to viscous force acting on a fluid:

$$\mathrm{Gr} = \frac{g\beta(T_\mathrm{s} - T_\infty)L^3}{\nu^2} \tag{5.39}$$

with the acceleration of gravity g, the coefficient of volume thermal expansion β, the difference between surface and freestream temperature $T_\mathrm{s} - T_\infty$, the characteristic length L and the kinematic viscosity $\nu = \mu/\rho$, where μ is the dynamic viscosity. The Prandtl number

$$\mathrm{Pr} = \frac{\nu}{\alpha} = \frac{\mu\, c_p}{k} \tag{5.40}$$

is the ratio of viscosity (responsible for viscous dissipation) to thermal diffusivity (responsible for the conduction of heat within the boundary layer).

The Grashof and Nusselt numbers can be calculated for a given range of surface temperatures to obtain the convective heat transfer coefficient h. The temperature at the heater T_H and thus the heater power $\dot{q}_\mathrm{H}$ follow from the heat transfer into the wall and conductive heat transfer through three layers of conductivity k and thicknesses x_1, x_2 and x_3 (see figure 5.3a.):

$$\dot{q}_\mathrm{conv} = h(T_\mathrm{g1} - T_\infty) = k\frac{T_\mathrm{g2} - T_\mathrm{g1}}{x_1} \; , \tag{5.41}$$

$$k\frac{T_\mathrm{g2} - T_\mathrm{g1}}{x_1} = k\frac{T_\mathrm{H} - T_\mathrm{g2}}{x_2} \; , \tag{5.42}$$

$$k\frac{T_\mathrm{H} - T_\mathrm{g2}}{x_2} = \dot{q}_\mathrm{H} - k\frac{T_\mathrm{H} - T_\mathrm{w}}{x_3} \; , \tag{5.43}$$

where T_g1 and T_g2 are the temperatures of the top and bottom gauges and T_w is the temperature of the wall. For this comparison radiative and lateral conduction effects have been neglected. One finds that there is almost no natural convection and the Nusselt numbers predicted are very low. Hence, the gauge substrate is nearly isothermal and the Nusselt number correction is very small. In particular, the surface temperatures are almost independent of which correlation is used to calculate the Nusselt number. This prediction is in agreement with the observation that the bottom gauge temperatures shown in figure 5.16 are very similar to the top gauge temperatures.

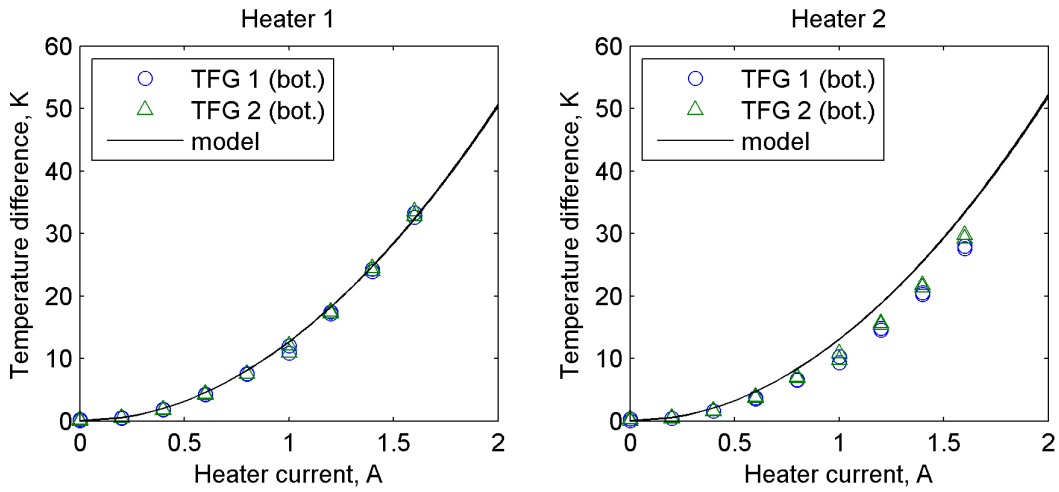

Figure 5.16: Preheating bottom gauge temperatures over increasing heater current for 18 consecutive tests. The temperatures measured by the two thin film gauges are compared to analytical results. The predicted top gauge temperatures are identical to the bottom gauge temperatures.

While the general agreement between model and data is very good, the model overpredicts the temperatures for both top and bottom gauges by up to 5 K for large heater currents. This disagreement is likely due to the difficulties of accurately measuring the wall temperature at the position of the gauges. Alternatively, the observed difference might suggest that the Kapton layer is thinner than expected (the implications of the uncertainty in the substrate thickness are discussed in section 6.1). Overall, this data gives good confidence in the achieved preheating. The substrate temperatures are compatible with the material restrictions and the test plan in the OTRF, where preheating temperature differences of less than 100 K are targeted. Furthermore, the data from separate test runs is consistent and repeatable. The temperatures measured by the double-sided thin film gauges also agree well with those obtained from thermocouple measurements on the heater surface.

IR thermography of thin film heater element

An FLIR A655sc camera (640x480 resolution) was also used to acquire qualitative IR images of a thin film heater element as it heated up with increasing heating current. Two aerofoil type heaters with a total resistance of 17.6 Ω were connected in series. The current through the

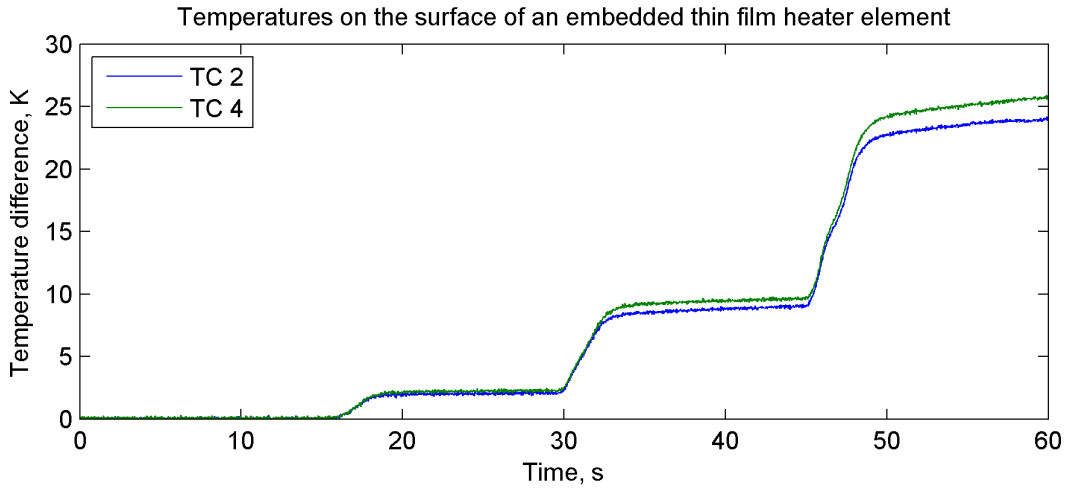

Figure 5.17: Temperatures measured on top of two layers of Kapton on the heater surface. The current through the heaters was stepwise increased from 0 A to 1.5 A and held constant for around 15 s at each step.

heaters was increased in 0.5 A steps from 0 A to 1.5 A and held constant for around 15 s at each step. The heaters were instrumented with thermocouples on top of the two layers of Kapton on the surface. The temperature traces are shown in figure 5.17.

When increasing the current through the heaters, the surface heated up quickly. At higher currents the surface temperature continued increasing at constant current until it reached steady-state. The IR record shows that the heating of the surface is very uniform over the heater extension (see figure 5.18). At the edge of the heater temperature gradients appear. The aluminium plate underneath stayed nearly isothermal, but the temperature of the Kapton surrounding the heater increased.

5.5.2 Self-heating gauges

As discussed in section 5.4, for the self-heating gauges it is necessary to determine the initial top gauge temperature, which is difficult to measure directly. If this temperature is to be inferred from another measured temperature such as the bottom gauge temperature or the wall temperature, it is necessary to describe the conduction in the gauge substrate. The heating heat flux can be calculated from the known voltage and resistance of the top gauge $\dot{q}_{\mathrm{H}} = V^2/(R\,A_{\mathrm{g}})$, where A_{g} is the platinum surface. Since the preheating is expected to have reached steady-state

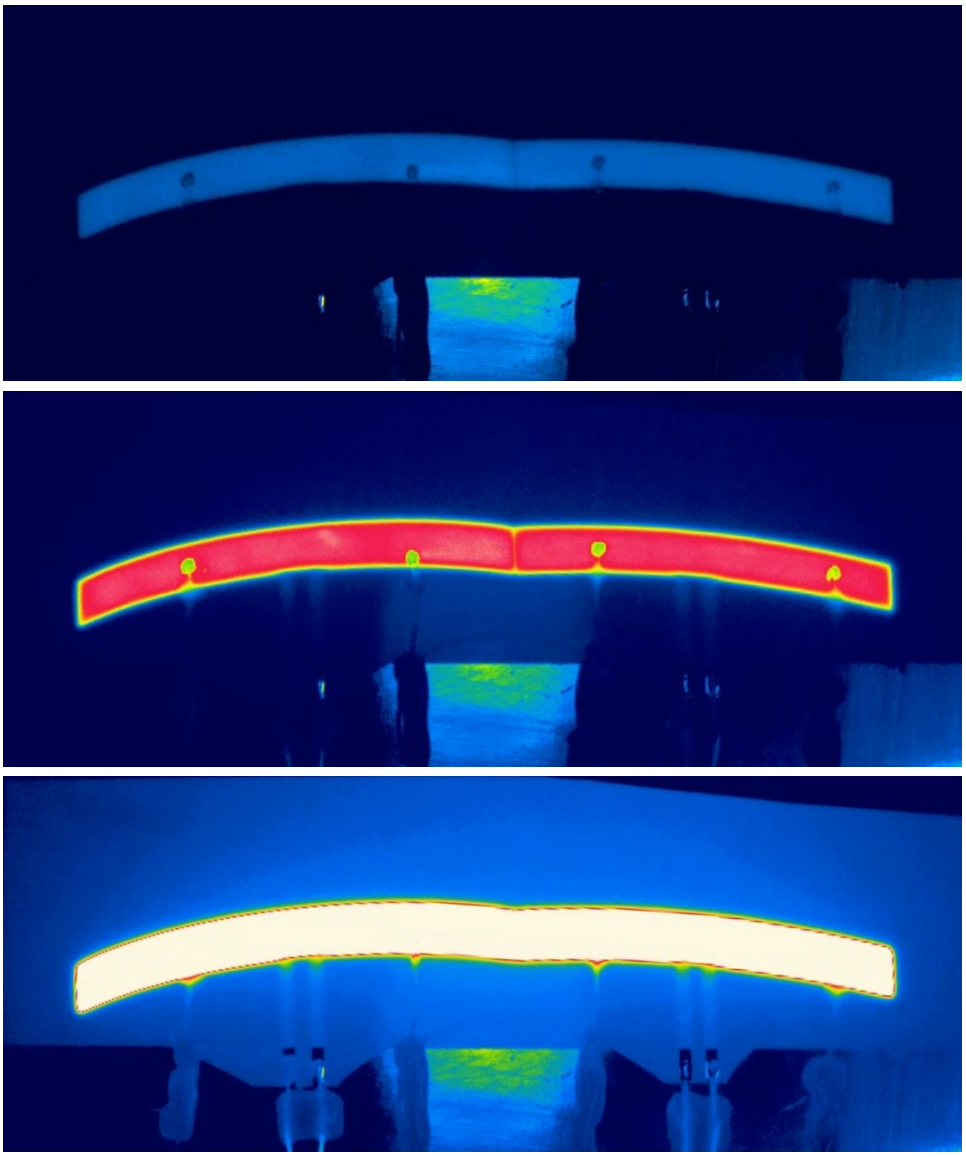

Figure 5.18: Qualitative IR images of heated thin film heater taken from IR record. The images show the surface temperature distribution at 0.5 A, 1.0 A and 1.5 A respectively. The cold spots are the thermocouples.

before the run (as shown by the transient modelling of the gauges in section 4.3), the temperature of the top gauge then follows from thermal conduction. For the following, the platinum thickness of less than 1 µm can be neglected, as it has negligible thermal resistance. Given the gauge track width of 0.3 mm which is about three times the thickness of around 100 µm of each insulating layer, there are two possible descriptions of this multi-layer system.

As the length of the platinum tracks is large in comparison to their width and to the thickness

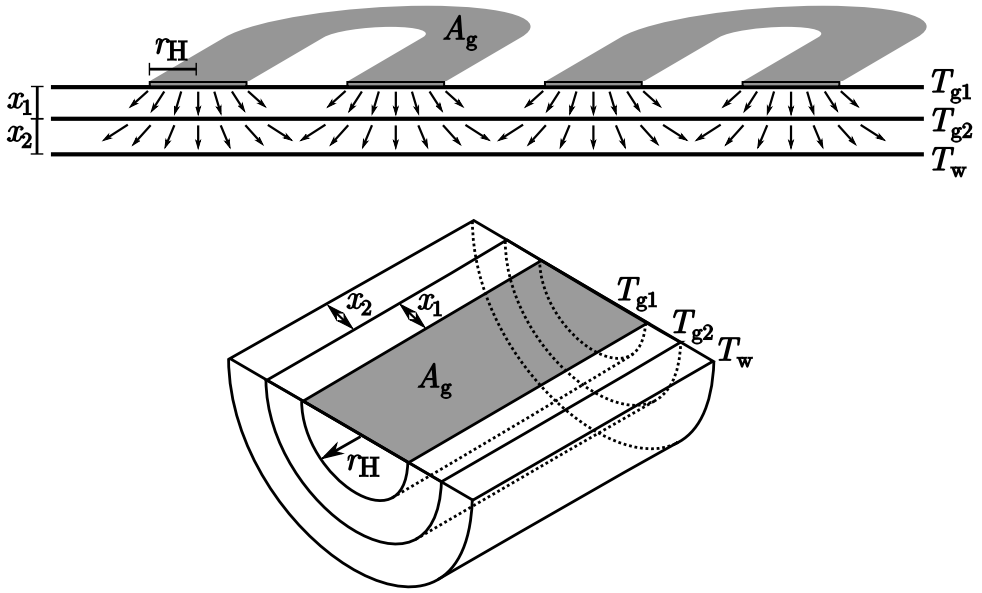

(a) 2D thermal conduction model.

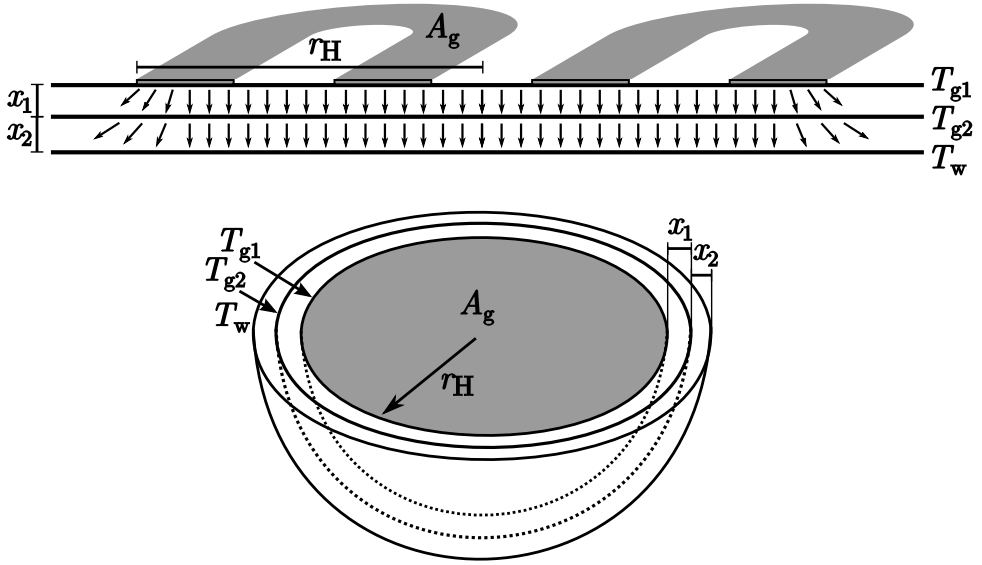

(b) 3D thermal conduction model.

Figure 5.19: Different representations of the gauge geometry (see figures 5.1 and 5.3b).

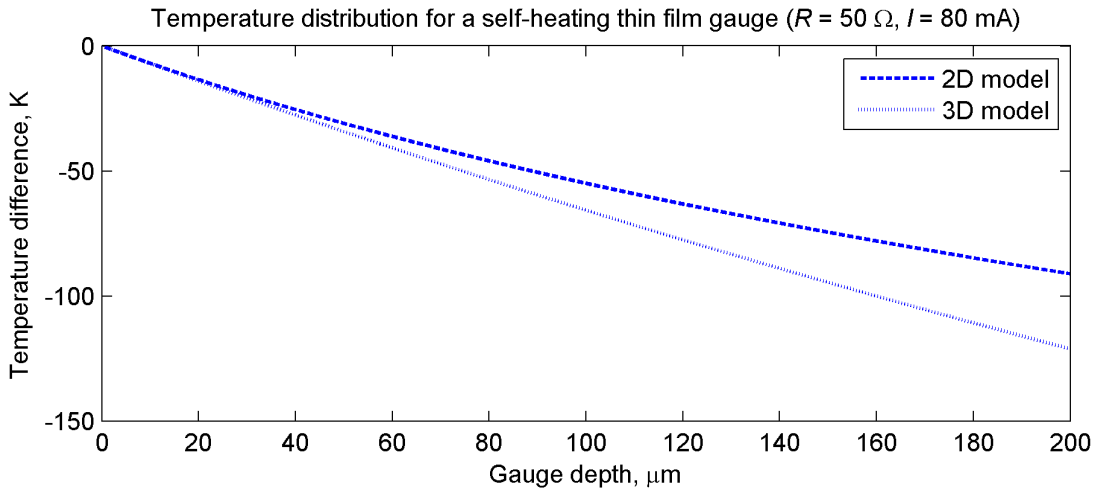

Figure 5.20: Comparison of predicted temperature differences by the 2D and by the 3D thermal conduction model. The temperature differences are calculated for a fixed top gauge temperature.

of the substrate layer, a good description is given by a 2D model (see also section 4.2). This case is represented in figure 5.19a. The radius of the heating source is half the track width, i.e. $r_H = 0.15\,\text{mm}$. An alternative description is obtained by neglecting the space between the tracks and taking the total gauge area $A_g = 3.72\,\text{mm}^2$ as a "point" heating source (see figure 5.19b). The radius for the resulting 3D model is then $r_H = 1.09\,\text{mm}$.

The predicted temperature profiles are shown in figure 5.20 for a fixed top gauge temperature and a typical gauge resistance and current of $50\,\Omega$ and $80\,\text{mA}$. As expected the differences between the two models grow with increasing depth into the substrate. Already at the position of the bottom gauges the predictions differ by as much as $15\,\text{K}$ for the given heating heat flux. Note that, in contrast to the model discussed in section 4.2, the decay here is larger at 3D, because a larger radius is assumed. In practice the temperature will be fixed by the measured bottom or wall temperature, which results in higher temperature predictions for the top gauge in the 3D case.

It would also be possible to define a combined conduction model, in which the conduction is different for the top and bottom substrate layers. For simplicity only full 2D or 3D models will be considered with the experimental results. At this stage the self-heating double-sided thin film gauges should be considered an experimental concept, the feasibility of which is to be proven.

As will be shown in chapter 6, the different model assumptions lead to noticeable variations in the heat transfer measurements. It is therefore important to validate these models against measurements using the predicted bottom gauge temperatures for a given wall temperature, as done in section 6.4. Alternatively, reliable model predictions could be obtained from a 3D FEA prediction of the thermal conduction in the gauge substrate, which is beyond the scope of this work. The impact of the experimental and modelling uncertainties are investigated in the following section.

5.6 Experimental uncertainties

The aim of this section is to describe the uncertainty associated with the heat transfer measurements in order to demonstrate that high-accuracy measurements can be taken in a rotating HP turbine environment. The quantities of interest in this context are the uncertainties of the fitting parameters of the linear regression (i.e. the slope h and the x-axis offset T_{aw} of the best-fit line), which ultimately determine the uncertainty of the Nusselt number Nu and the film cooling effectiveness η_{f}.

There are two classes of uncertainties: Statistical uncertainties, namely fluctuations during the duration of a run, which lead to uncertainties in the linear regression, and systematical uncertainties, which affect all measurements taken during a given run and therefore bias the regression. Statistical uncertainties differ from gauge to gauge, so that a general discussion is difficult. Nevertheless, these uncertainties can always be reduced by taking a larger number of measurements. The focus of this section will therefore be on systematic uncertainties, which cannot easily be reduced. The impact of these uncertainties on temperature and heat transfer measurements will be discussed for both the unheated and the heated case. Subsequently, a specific example will be introduced to illustrate how these uncertainties affect the determination of the heat transfer coefficient and the adiabatic wall temperature.

Unheated gauges

Systematical uncertainties typically result from quantities that are determined only once at the beginning of the run, such as the initial wall temperature T_{wi}, the voltage V_{i} and the temperature coefficient α of a given thin film gauge. In terms of these quantities, the wall temperature is given by (see equations 5.15 and 5.16):

$$T = T_{\mathrm{wi}} + \Delta T = T_{\mathrm{wi}} + \frac{\Delta V}{V_i\,\alpha}\,. \tag{5.44}$$

The temperature dependence of the gauge resistance, $\mathrm{d}R/\mathrm{d}T$, can be reliably determined from calibration data. As for example discussed in Pinilla et al. (2012), uncertainties in the resistance-temperature calibration slope lead to a relative error of less than 1%. The calculation of $\alpha = R_0^{-1}\,\mathrm{d}R/\mathrm{d}T$, on the other hand, requires knowledge of the reference resistance R_0. This quantity may exhibit a drift between the calibration and the experiment and may furthermore be affected by changes in the connecting wires (see section 5.3). In the absence of a precise measurement of the current through the gauges at the beginning of each run, the resistance of the gauges needs to be re-measured frequently. The resulting variations allow to estimate the uncertainty of R_0, and hence of α, to be of order 2%.[1]

The initial voltage V_{i} is typically of order 0.25 V, with a measurement resolution better than 1 mV, such that the relative error is at the sub-percent level. However, an additional source of error on the voltage V_{i} is given by the stability of the constant current source. For this reason a larger error of 1% will be used.

The absolute error $\sigma_{\Delta T}$ of ΔT can be written as

$$\sigma_{\Delta T} = \left[\left(\frac{\partial \Delta T}{\partial V_{\mathrm{i}}}\sigma_{V_{\mathrm{i}}}\right)^2 + \left(\frac{\partial \Delta T}{\partial R_0}\sigma_{R_0}\right)^2\right]^{1/2}\,, \tag{5.45}$$

where the uncertainties in ΔV and $\mathrm{d}R/\mathrm{d}T$ have been assumed to be negligible. It then follows for the relative error

$$\frac{\sigma_{\Delta T}}{\Delta T} = \left[\left(\frac{\sigma_{V_{\mathrm{i}}}}{V_{\mathrm{i}}}\right)^2 + \left(\frac{\sigma_{R_0}}{R_0}\right)^2\right]^{1/2}\,, \tag{5.46}$$

i.e. the relative errors of V_{i} and R_0 are simply added in quadrature. One then finds that the

[1] Gauges with a variation of more than 5% were removed from the analysis.

Quantity		Unheated	Underside heater ($\Delta T_\mathrm{H} = 80\,\mathrm{K}$)	Self-heating ($\Delta T_\mathrm{H} = 80\,\mathrm{K}$)
T_wi		0.3%	1%	4%
ΔT		2.2%	5.1%	5.1%
	V_i	1%	1%	1%
	R_0	2%	5%	5%
$\dot{q}$		5%	5%	5%
	a	5%	5%	5%
h		5.5%	7.2%	7.2%
	$\dot{q}$	5%	5%	5%
	ΔT	2.2%	5.1%	5.1%

Table 5.1: Systematical uncertainties affecting temperature and heat transfer measurements for unheated and heated configurations. Note that the determination of h from a single run is affected by large statistical uncertainties, which are not included in this table.

uncertainty in R_0 dominates the uncertainty in ΔT.

For unheated gauges T_wi is known with an accuracy of about 1 K (Povey, 2003). This error can be reduced by using several thermocouples in the test working section and by allowing for stabilising periods between runs. However, if the aerofoils are heated up between runs this error is likely to increase. Non-uniform heating is therefore an important source of uncertainty and lateral conduction terms within the Kapton layer need to be considered.

The main sources of uncertainty in the heat transfer rate are the thermal properties of the insulator and the thickness of the insulating layer (substrate and glue). Previous investigations (see for example (Povey, 2003)) agree that the principle source of uncertainty in $\dot{q}$ is the thickness of the insulating layer a. As discussed in section 6.1 (see figure 6.7), the resulting uncertainty is of order $\sigma_{\dot{q}}/\dot{q} \approx 5\%$. A summary of the systematical uncertainties discussed above is given in table 5.1.

Heated gauges

For heated gauges T_{gi} is more difficult to determine than for the unheated case and the corresponding uncertainties will therefore be larger. First of all, measurements of the temperature difference achieved by heating are affected by the same systematical uncertainties discussed above and are therefore of order 2%. For example, if heating leads to an initial temperature difference of 50 K, the resulting uncertainty will be about 1 K in addition to the uncertainty of the initial temperature before heating. Additional uncertainties may be introduced by the need to make model assumptions to relate the temperatures of top and bottom gauges (such as the ones discussed in section 5.5 for self-heating gauges). By comparing the predictions of different models (see section 6.4), this uncertainty can be estimated to be at most of order 15 K. Crucially, uncertainties in the initial temperature difference between top gauge and bottom gauge do not affect the measured convective heat flux, because the heat flux resulting from this temperature difference reflects the effect of heating and is therefore subtracted from all subsequent measurements.

The second source of uncertainty concerns the temperature differences ΔT, i.e. the determination of R_0 and V_{i}. The reference resistance R_0 is expected to increase slightly due to the higher temperatures at the beginning of the run. This effect is expected to be of order $\alpha \Delta T_{\mathrm{H}}$, where ΔT_{H} is the temperature difference achieved by heating. For $\Delta T_{\mathrm{H}} = 50\,\mathrm{K}$, the resulting change in R_0 may be of order 5%. Note that this effect can in principle be corrected for by using the known slope $\mathrm{d}R/\mathrm{d}T$ and the preheating temperature difference, so it is conservative to assume 5% uncertainty in R_0.

For the case of gauges with an underside thin film heater the value of V_{gi} is independent of the heating current. For self-heating gauges, on the other hand, larger V_{gi} is required for larger heating currents. While this should in principle make it easier to measure V_{gi} accurately, non-linearities (e.g. in the amplification) may become a concern. While difficult to quantify, it is possible that these effects become more important at larger values of V_{gi}, leading to larger uncertainties in ΔT. Nevertheless, a larger heating current implies that T_{gi} is closer to T_{aw} and consequently ΔT is smaller. Thus, even though the relative uncertainty in ΔT may grow in the

heated case, the absolute error may in fact decrease.

Finally, the heating heat flux $\dot{q}_\mathrm{H}$ is determined only once at the beginning of the run and then subtracted from all subsequent measurements of $\dot{q}$. It is therefore an important assumption that this heat flux remains constant over the duration of the run. While this is a good approximation for gauges with an underside heater, the situation is more complicated for self-heating gauges, because in this case the heater is in contact with the hot gas (and potentially the coolant), which may affect its performance. Also, the importance of 2D and 3D effects may be different before the run (when only the gauges are heated) and during the run (when the entire surface is in contact with the hot gas). It is assumed that these effects are small compared to the uncertainties in $\dot{q}$ resulting from the uncertainty in the thickness of the substrate layer (see above). Consequently, the uncertainty of $\dot{q}$ is comparable for heated and unheated case. All systematical uncertainties for the heated case are summarised in table 5.1.

Uncertainties in the linear regression

To estimate the uncertainty of the heat transfer coefficient, it is instructive to consider two discrete measurements of the wall temperature, T_1 and T_2, and the corresponding heat fluxes $\dot{q}_1$ and $\dot{q}_2$. The heat transfer coefficient is then given by

$$h = \frac{\dot{q}_2 - \dot{q}_1}{T_2 - T_1} \,. \tag{5.47}$$

If both measurements are taking during the same run, this expression can be simplified to

$$h = \frac{(\dot{q}_2 - \dot{q}_1)\, V_\mathrm{i}\, \alpha}{\Delta V_2 - \Delta V_1} \,, \tag{5.48}$$

which does not depend on T_wi. Adding the systematic uncertainties in α, V_i and $\dot{q}$ in quadrature, one finds the resulting uncertainty of h to be of order 5–7% (see table 5.1).

For a single run, the systematic uncertainties affecting h are all taken into account. However, the achievable temperature differences during a single run are rather small and statistical uncertainties are typically very large. It is therefore desirable to combine heated and unheated runs. While this approach leads to larger systematic uncertainties due to the need to compare runs with different initial wall temperatures, it significantly increases the range of T_w and hence

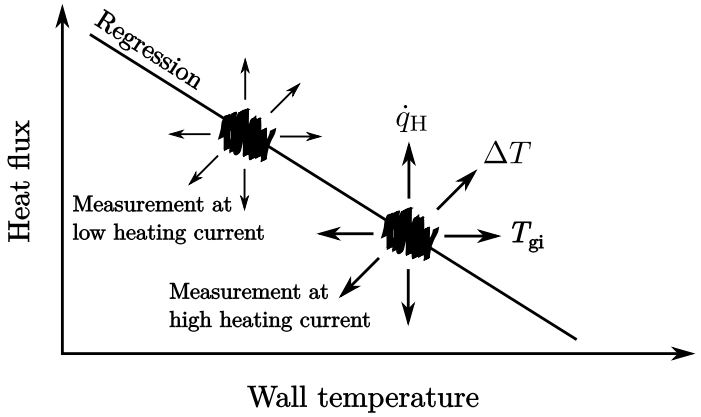

Figure 5.21: Illustration of the different sources of uncertainties affecting (self-)heated gauges.

improves the reliability of the linear regression.

Figure 5.21 illustrates the various sources of uncertainties affecting the regression. Note that, if the temperature difference ΔT of the top gauge is underestimated, this will lead to an underestimation of the wall temperature T_{w} as well as an underestimation of the temperature difference between top and bottom gauge, which in turn results in underestimating the heat flux. An uncertainty in ΔT therefore may shift measurements at different heating currents in the diagonal direction, roughly perpendicular to the direction of the regression. As discussed above, uncertainties in T_{gi} do not affect measurements of $\dot{q}$ and can only shift measurements at different heating currents in the horizontal direction.

The resulting uncertainties in h can be calculated for a specific example, which is presented in table 5.2. It is assumed that the measurements T_1 and $\dot{q}_1$ correspond to the unheated case, whereas T_2 and $\dot{q}_2$ result from one of the heated cases. The given temperatures and heat fluxes are representative of the measurements that will be discussed in the following chapters and the errors are derived from the uncertainties shown in table 5.1.

The uncertainty in h can be calculated from standard error propagation:

$$\sigma_h = \left[\left(\frac{\partial h}{\partial \dot{q}_1} \sigma_{\dot{q}_1} \right)^2 + \left(\frac{\partial h}{\partial \dot{q}_2} \sigma_{\dot{q}_2} \right)^2 + \left(\frac{\partial h}{\partial T_1} \sigma_{T_1} \right)^2 + \left(\frac{\partial h}{\partial T_2} \sigma_{T_2} \right)^2 \right]^{1/2} \tag{5.49}$$

$$= \left[\left(\frac{\sigma_{\dot{q}_1}}{T_2 - T_1} \right)^2 + \left(\frac{\sigma_{\dot{q}_2}}{T_2 - T_1} \right)^2 + \left(\frac{\sigma_{T_1}(\dot{q}_1 - \dot{q}_2)}{(T_2 - T_1)^2} \right)^2 + \left(\frac{\sigma_{T_2}(\dot{q}_1 - \dot{q}_2)}{(T_2 - T_1)^2} \right)^2 \right]^{1/2} . \tag{5.50}$$

Quantity		Unheated	Underside heater	Self-heating
T		$(360 \pm 1.8)\,\mathrm{K}$	$(420 \pm 4.5)\,\mathrm{K}$	$(420 \pm 15)\,\mathrm{K}$
	T_i	$(290 \pm 1)\,\mathrm{K}$	$(370 \pm 3.7)\,\mathrm{K}$	$(370 \pm 15)\,\mathrm{K}$
	ΔT	$(70 \pm 1.5)\,\mathrm{K}$	$(50 \pm 2.6)\,\mathrm{K}$	$(50 \pm 2.6)\,\mathrm{K}$
$\dot{q}$		$(6 \pm 0.3) \cdot 10^4\,\mathrm{W\,m^{-2}}$	$(1.5 \pm 0.1) \cdot 10^4\,\mathrm{W\,m^{-2}}$	$(1.5 \pm 0.1) \cdot 10^4\,\mathrm{W\,m^{-2}}$
h		–	$(750 \pm 80)\,\mathrm{W\,m^{-2}\,K^{-1}}$	$(750 \pm 196)\,\mathrm{W\,m^{-2}\,K^{-1}}$
T_aw		–	$(440 \pm 7)\,\mathrm{K}$	$(440 \pm 20)\,\mathrm{K}$

Table 5.2: A specific example to illustrate the effect of systematical uncertainties on the linear regression. For the determination of the heat transfer coefficient and the adiabatic wall temperature the unheated case is combined with the respective heated case.

The uncertainties in h are then found to be about 11% for the case with an underside heater and about 26% for self-heating gauges. These uncertainties can be reduced further by taking a number of different measurements at different heater settings. Comparing the results from gauges with an underside heater and self-heating gauges, it becomes clear that reducing the uncertainty in the initial gauge temperature for the self-heating gauges is key to obtaining accurate heat transfer data.

The adiabatic wall temperature is determined from a linear extrapolation of the heat flux results for a set of different values of T_w:

$$T_\mathrm{aw} = \frac{T_2\,\dot{q}_1 - T_1\,\dot{q}_2}{\dot{q}_1 - \dot{q}_2}\,. \tag{5.51}$$

Again, standard error propagation gives

$$\sigma_{T_\mathrm{aw}} = \left[\left(\frac{\dot{q}_2\,\sigma_{T_1}}{\dot{q}_1 - \dot{q}_2}\right)^2 + \left(\frac{\dot{q}_1\,\sigma_{T_2}}{\dot{q}_1 - \dot{q}_2}\right)^2 + \left(\frac{(T_2 - T_1)\,\dot{q}_1\,\sigma_{\dot{q}_2}}{(\dot{q}_1 - \dot{q}_2)^2}\right)^2 + \left(\frac{(T_2 - T_1)\,\dot{q}_2\,\sigma_{\dot{q}_1}}{(\dot{q}_1 - \dot{q}_2)^2}\right)^2\right]^{1/2}\,. \tag{5.52}$$

The uncertainties in T_aw are then found to be about 1.6% in the case with an underside heater and about 4.5% for self-heating gauges. If the gauges are preheated to a temperature close to the adiabatic wall temperature both $\dot{q}_2$ and ΔT_2 are very small. As a result, $\sigma_{\dot{q}_2}$ is also very small and $\sigma_{T_2} \approx \sigma_{T_\mathrm{gi}}$. In this case, equation 5.52 simplifies to

$$\sigma_{T_\mathrm{aw}} = \sigma_{T_\mathrm{gi}}\,, \tag{5.53}$$

i.e. the uncertainty in the adiabatic wall temperature is exclusively given by the uncertainty in the preheating temperature.

For known errors in T_{aw} and h, the errors in Nu and η_{f} follow from standard error propagation:

$$\frac{\sigma_{\mathrm{Nu}}}{\mathrm{Nu}} = \frac{\sigma_h}{h} \,, \tag{5.54}$$

$$\frac{\sigma_{\eta_{\mathrm{f}}}}{\eta_{\mathrm{f}}} = \frac{\sigma_{T_{\mathrm{aw}}}}{T_{01} - T_{\mathrm{aw}}} \,. \tag{5.55}$$

5.7 Summary

A design for double-sided thin film gauges has been developed based on the latest gauge manufacturing technology. These gauges are to be tested in two heating configurations, namely double-sided thin film gauges with an underside thin film heater and self-heating thin film gauges. The heating configurations allow varying the wall temperature and thus increase the range for the regression that yields the adiabatic wall temperature and the heat transfer coefficient. For each heating configuration the temperature trace can be calculated from the voltage signal and the calibrated temperature coefficient of resistance. The impulse response method is then used to calculate the convective heat flux from the temperature history. This approach has been validated with a numerical model. The adiabatic wall temperature and the heat transfer coefficient follow from a floating regression. A central problem of the heated configurations is the determination of the initial gauge temperature. This problem can be addressed with models for the thermal conduction in the substrate for each heated configuration. These models therefore form an essential part of the measurement strategy and need to be validated using experimental data. The resulting systematic errors have been included in a thorough discussion of the experimental uncertainties associated with the acquisition of heat transfer data.

In the following two chapters the gauges and methods introduced in this chapter will be used to obtain heat transfer data on the casing and the NGV of an HP turbine stage under engine-realistic conditions in the OTRF.

CHAPTER 6

Casing Tests and Model Validation

Four gauge configurations were tested in the OTRF during the noise test campaign.[1] The four configurations investigated were: single-sided thin film gauges, double-sided thin film gauges, double-sided thin film gauges with an underside heater and self-heating double-sided thin film gauges. The aim of these measurements was to compare the performance of the four gauge configurations. During the tests the OTRF was run without the turbine stage, i.e. with the HP NGV and rotor removed and replaced with a simple annular nozzle configuration. The gauges were placed on the casing endwall in an NGV cassette, just after what corresponds to the blade over-tip region, to measure the heat transfer into the endwall. Figure 6.1 shows the test cross section and the exact axial location of the gauges.

These tests were performed under uniform inlet conditions at two inlet total temperatures (412 K and 444 K). The back pressure was varied during the test campaign in order to achieve Mach numbers ranging from 0.8 to 1.1 at the throat. The distribution of the isentropic Mach number over the axial axis of the rig (as measured during the test campaign) is shown in figure 6.2. As the heat transfer is a function of the Reynolds number, the flow velocity needs to be corrected for when comparing runs at different Mach numbers. The test matrix is summarised in table 6.1.

Before the results for the four gauge configurations are presented in sections 6.1 to 6.4, a number of issues are discussed which are relevant to all runs. These are the gauge calibration and installation as well as the timing and stability of the data acquisition. The results from

[1] The aim of the noise project is to measure the indirect combustion noise caused by temperature field instabilities in the turbine (Ron, 2015).

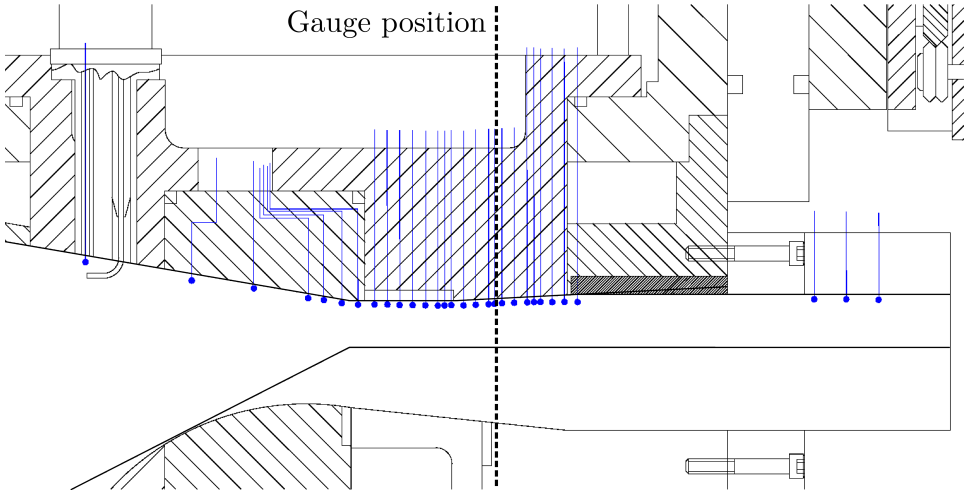

Figure 6.1: OTRF cross section for the noise test campaign showing pressure tappings and gauge location.

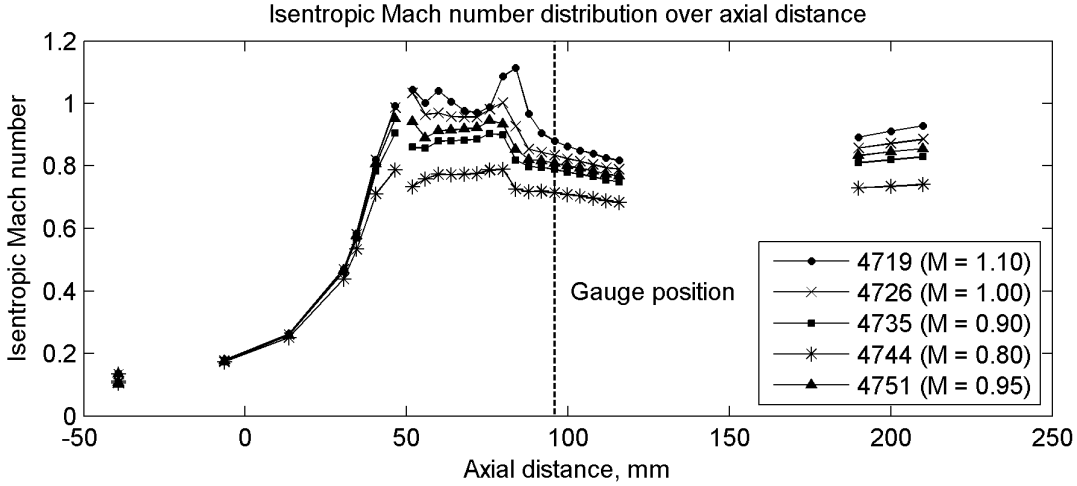

Figure 6.2: Isentropic Mach number distribution over the OTRF axial axis for different test conditions (experimental results). The Mach number is given at the throat.

the different configurations are summarised in section 6.5 and compared to predictions from a boundary layer code in section 6.6.

Calibration of the temperature coefficient of resistance

Since an NGV cassette is too large to fit into the calibration water bath, the gauges had to be calibrated on a separate aluminium plate before being attached to the surface of the casing. However, the change between the resistance as measured in the water bath and the resistance

Test	Run number	No. of runs	T_{01}, K	Target M
1	4712 to 4719	8	412	1.10
2	4720 to 4726	7	412	1.00
3	4727 to 4735	9	412	0.90
4	4736 to 4744	8	412	0.80
5	4745 to 4751	7	412	0.95
6	4752 to 4757	6	444	1.00

Table 6.1: Test conditions during the noise campaign.

measured on the rig after soldering the connection wires was negligible with a maximum difference of 0.1%. Overall, the gauges calibrated very well and achieved consistent temperature coefficients of resistance of approximately $1.3 \cdot 10^{-3}\,\mathrm{K}^{-1}$. The calibration data is shown in figure 6.3. The gauges were manufactured in two batches which explains the differences in resistance caused by different platinum thicknesses achieved during separate sputtering processes. The variation within each batch is less than 4%.

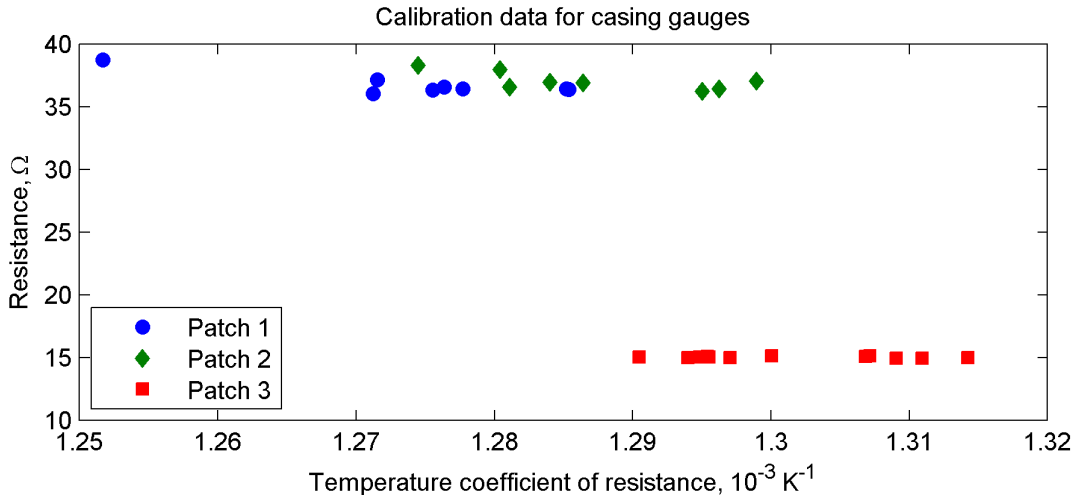

Figure 6.3: Resistance as a function of the temperature coefficient of resistance for the gauges used on the casing. Patches 1 and 2 were sputtered simultaneously and are used as top gauges and as double-sided gauges with an underside heater respectively. Patch 3 was sputtered separately and is used for the bottom gauges. During the same sputtering process very consistent gauges are achieved.

Gauge setting and inspection

The final gauge installation is shown by the photograph in figure 6.4. All insulating layers have a thickness of approximately 100 µm and were measured during the instrumentation process. The initial voltage for each gauge was set at 0.25 V using the HTA3 current supply. This voltage setting ensures a large enough gauge signal and at the same time the current is low enough that the ohmic heating generated by the gauge is much smaller than the heat flux to be measured. For the heated tests the current through the heater and self-heating gauges was stepwise increased and is detailed in the respective sections below. The isothermal gauge resistance was measured on every day of testing and variations were accounted for using equation 5.14. This measurement also helped to identify problematic gauges, which showed a large variation of resistance between measurements.

Unfortunately, the failure rate for double-sided thin film gauges is twice that of single-sided thin film gauges, as a failure of one of the two gauges will render the package useless. The bottom gauges were more frequently affected suggesting a problem in the manufacturing process, e.g. at the copper-platinum joints. Though most of the failures appeared at the beginning of testing, some gauges deteriorated during testing. A visual inspection at the end of the experimental campaign did not show any delamination of the gauges. The investigation of the failure modes will require additional inspection, which is not in the scope of this thesis. The good gauges showed very constant resistance values with variations of no more than 1% between measurements.

Time lag between measurement of inlet total temperature and casing gauges

During a run, the inlet total temperature is recorded at a temperature rake downstream of the plug valve before the start of the contraction into the test section. In this region the flow has a Mach number as low as M = 0.05. If this inlet total temperature is used to compute the adiabatic wall temperature at the location of the thin film gauges at the rotor exit, the time lag of the flow has to be considered.

At the NGV inlet plane the flow reaches a Mach number M = 0.2 (see figures 6.1 and 6.2).

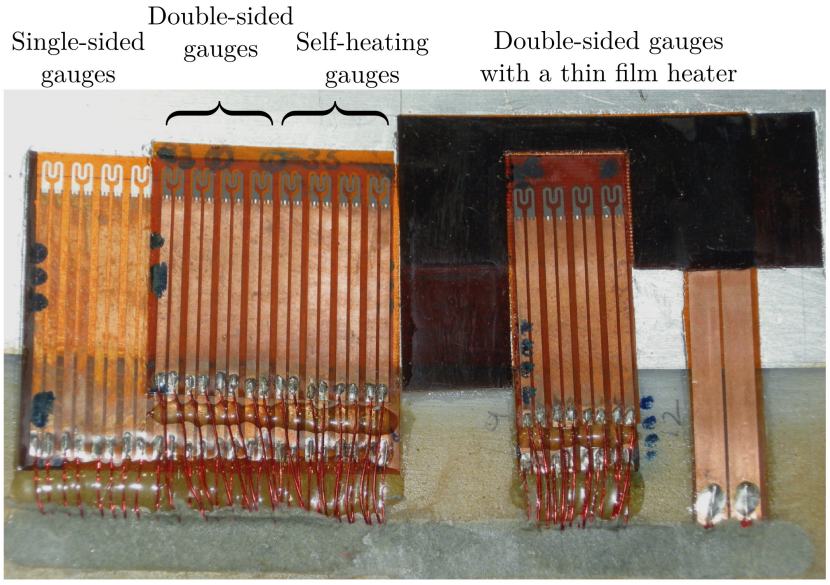

Figure 6.4: Photograph of the test section with thin film gauges. From left to right: single-sided thin film gauges, double-sided thin film gauges, self-heating double-sided thin film gauges and double-sided thin film gauges with an underside heater. In the following the gauges are numbered from 1 to 4 from left to right for each gauge type.

The flow is then significantly accelerated until it reaches transonic conditions at the throat. The last part of the contraction after the NGV inlet plane contributes very little to the time shift and will be disregarded. The temperature rake is 390 mm upstream of the NGV inlet plane. Using the continuity equation and assuming a linear increase in velocity between both axial points, a time shift of 11 ms between the temperature rake and the gauges is obtained.

This time shift explains an observed phase lag where the trace of the temperature difference precedes that of the heat flux. The corrected time difference has to be taken into account when performing the regression of heat flux over wall temperature. It is important to note, however, that even after the correction the temperature trace is expected to peak before the heat flux trace, depending on the time it takes for the thermal pulse to reach the aluminium wall.

Reference measurement and HTA3 stability

A reference voltage across the gauges is recorded prior to the run. At this point the rig is considered isothermal as a long enough time has passed since the previous run (typically over one hour). Between this measurement and the start of the data acquisition there is a time

lapse of less than 5 min, although this time can be longer in some rare cases. The stability of the measured pre-run temperature from the reference measurement to the start of the run is therefore an important issue also for unheated gauges. Figure 6.5 shows the temperature variation of eight thin film gauges connected to eight channels of one HTA3 box. For all but one channel, the temperature measurement is very stable with differences smaller than 0.1 K. One channel shows larger deviations. By measuring the stability of the HTA3 output, an instability of the current supply can be disregarded, so the issue must be caused by a drifting gauge.

The stability of the HTA3 signal over a long period of time is important, because it validates three assumptions. First, it confirms that the HTA3 is fit to be used for recording a short-duration experiment (in the range of 5 s). Second, it shows that the HTA3 current is stable enough to measure the heating up of the gauges prior to the run which takes around 10 s (as discussed below) and third, it eliminates the HTA3 signal amplifier as the cause for any temperature variations occurring in the time between the reference measurement and the start of the run.

Other physical effects that can cause a rise in temperature in the rig after the reference measurement are for example radiation sources in the rig. Windage effects can be neglected, because there is no rotor spinning up in this set-up. The gauge temperature could be reduced by

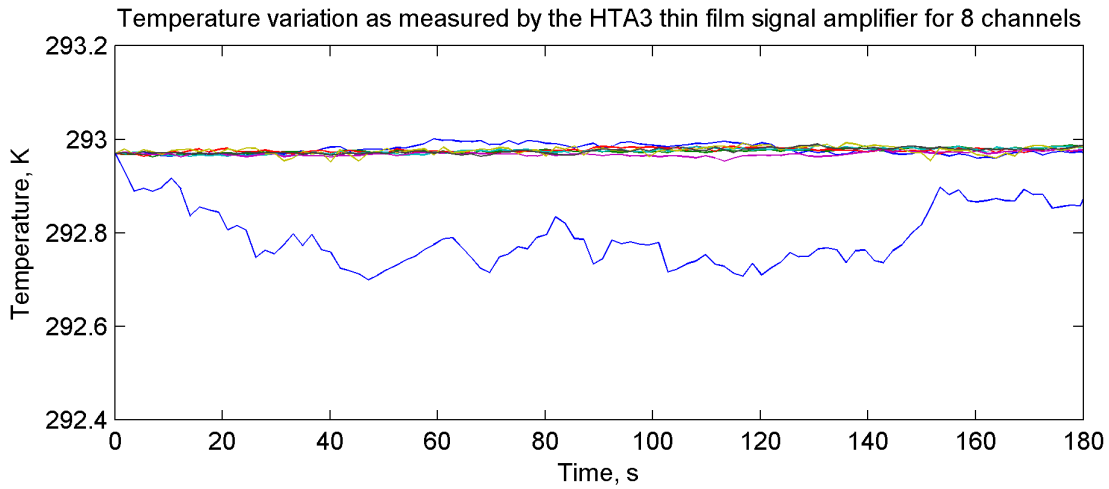

Figure 6.5: Temperature variation over a long time period as a stability check of the HTA3 thin film signal conditioning amplifier.

evaporation of bearing oil remains on the test surface at low pressures. However, this possibility can be disregarded as the reference measurement is taken when the rig is already at vacuum. Moreover, Ralph (2000) investigated the effect of pre-run natural convection by altering the pressure in the working section before the run. No significant effect was observed for pressures ranging from near vacuum to one atmosphere. After consideration of all these effects it is justified to make the assumption that the rig is still at isothermal conditions just prior to the run, i.e. the thermocouple measurement of the cassette temperature accurately reflects the temperature of all gauges.

6.1 Single-sided thin film gauges

The single-sided thin film gauges were sputtered onto an insulating layer, which was glued onto the casing surface (see figure 4.1a). The principle of operation of the single-sided gauges has been described in section 5.4 (see also figure 5.8). Figure 6.6 shows typical temperature traces for single-sided thin film gauges. The temperature differences were set to zero at the start of the run.[1] Each gauge has a good run-to-run agreement with a maximum variation of 5 K. These gauges achieve a considerable temperature increase of up to 70 K, but due to the limited thickness of the insulating layer they reach a steady-state condition very quickly. The two neighbouring gauges in the middle of the patch see very similar temperatures. The first and fourth gauge record higher and lower temperatures respectively. This pattern was repeatable for all tests at all conditions, even though the gauges were positioned at the same axial location and no circumferential variation in the flow was expected.

There are two possible explanations: either the temperature coefficient of the gauges changed since the calibration or there was a difference in the gauge substrate. The first possibility was eliminated as the measurement of the resistance of the gauges on the rig after the calibration showed negligible variation, leading to the conclusion that the temperature coefficient of the gauges was not altered between the calibration and the runs in the rig. If on the other hand, the substrate was poorly controlled in thickness (for example because an uneven pressure was

[1] In the following plots 0 s correspond to the moment at which stable pressure conditions are achieved, but the data acquisition starts about 2.5 s earlier.

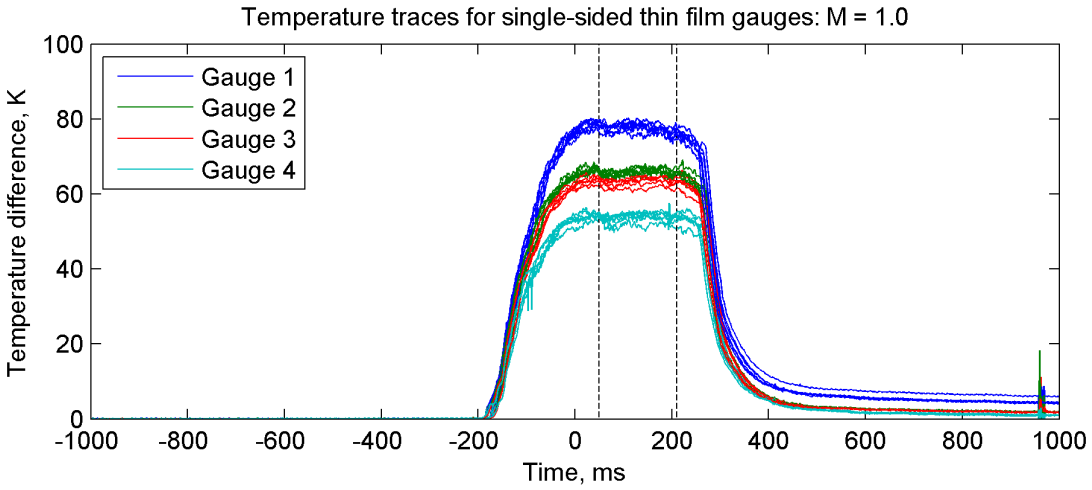

Figure 6.6: Temperature traces for four single-sided thin film gauges. The results for six tests are overlapped in this plot. The dashed lines mark a typical stable period used for the regression of one run and one gauge.

applied during manufacture), it should be possible to improve the agreement between the gauges by determining the individual substrate thicknesses using data from many runs. This approach will also serve as a consistency check over a range of flow Mach numbers.

To find the individual gauge thickness that collapses the data for many runs, the regression is performed defining the adiabatic wall temperature as the recovery temperature (i.e. fixing the x-axis intercept). The recovery temperature can be described as the temperature reached by a moving fluid when brought to rest through an adiabatic process (Kays et al., 2005):

$$T_\mathrm{r} = T + r\,\frac{u_\infty^2}{2c_p} = T\left(1 + r\,\frac{\gamma-1}{2}\,\mathrm{M}_\infty^2\right)\ . \tag{6.1}$$

where r is the recovery factor which is equal to $\mathrm{Pr}^{1/2}$ for a laminar boundary layer and equal to $\mathrm{Pr}^{1/3}$ for a turbulent boundary layer. In this case the recovery factor is set to $\mathrm{Pr}^{1/3} = 0.88$. The recovery temperature can be calculated for each Mach number condition from the known M_∞ (see figure 6.2) and the temperature T_{01} measured at the inlet.

In a first iteration the heat transfer coefficient is calculated for each gauge and each run for the nominal gauge thickness of 110 µm. An average heat transfer coefficient is obtained from all the runs at the same flow conditions. The results are shown in figure 6.7 (left plot). As expected from the temperature traces presented in figure 6.6, gauges 3 and 4 have a similar heat transfer.

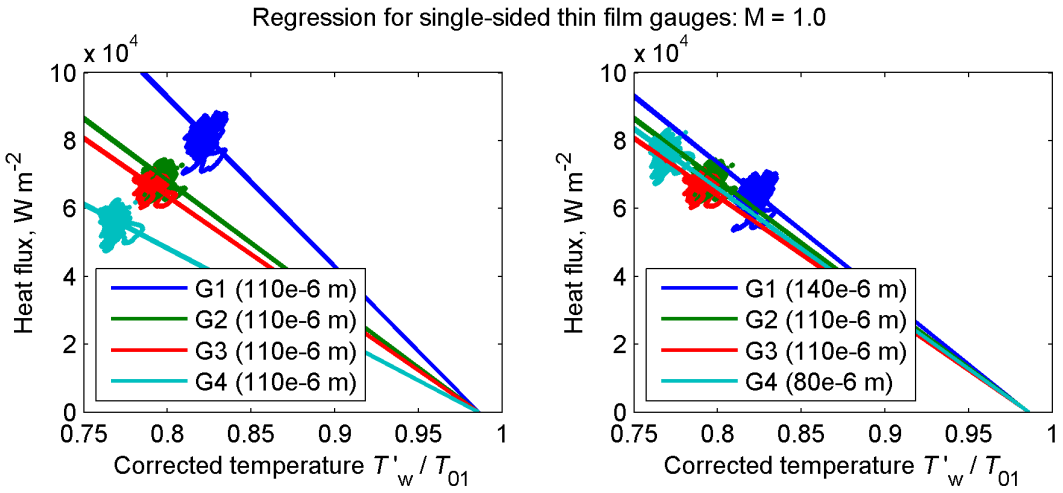

Figure 6.7: Regression data for four single-sided thin film gauges (G1 to G4). The regression is performed on data from the stable run period.

For the same gauge thickness the heat transfer coefficient of gauge 1 is larger and the heat transfer coefficient of gauge 4 is smaller than that of the middle gauges. By increasing the gauge thickness of gauge 4 to 140 µm and decreasing the gauge thickness of gauge 1 to 80 µm a better gauge-to-gauge agreement can be achieved over the whole range of Mach numbers, as illustrated in figure 6.7 (right plot). This thickness variation ties in with the manufacturing process and the type of glue used with the gauges. However, this also means that special care has to be put into the manufacture of the gauges and that a manufacturing process which eliminates the uncertainty in the glue thickness would be preferable (see section 5.1). The corrected heat flux traces are shown in figure 6.8 for M = 1 and $T_{01} = 444\,\mathrm{K}$.[1]

As expected, the nearly constant wall temperature during the stable part of the run makes it very difficult to achieve a good regression. A possible way to extend the range of the regression would be to include data points from the beginning and the end of the run. These measurements, however, would need to be corrected for the varying Reynolds number caused by the varying inlet total pressure and temperature.

The heat transfer results can be summarised for all conditions in a plot of heat transfer

[1]The difference in corrected temperature compared to figure 6.7 is caused by a different definition of the mean inlet total temperature.

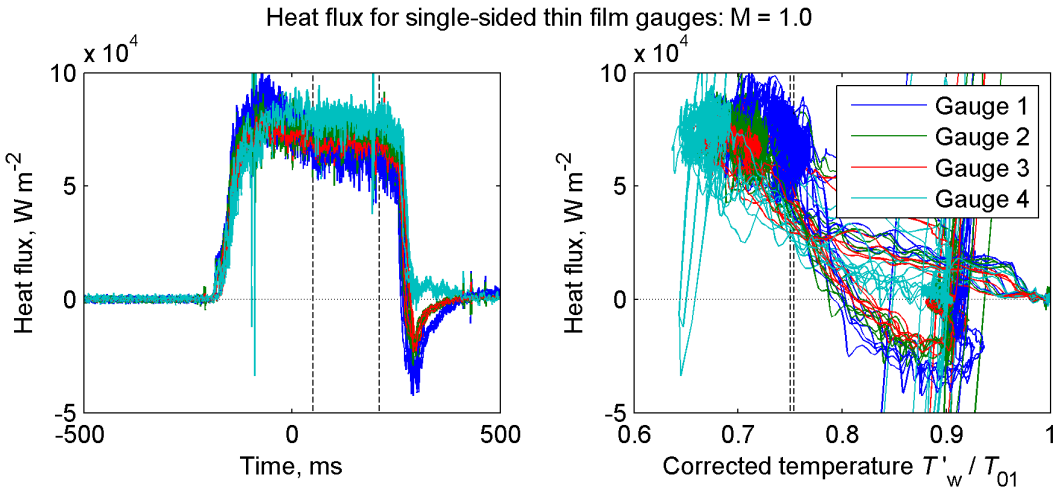

Figure 6.8: Heat flux for four single-sided thin film gauges after fitting the gauge thickness. The results for six tests are overlapped in this plot. The dashed lines mark a typical stable period used for the regression of one run and one gauge.

coefficient over Reynolds number. The local Reynolds number

$$\mathrm{Re}_x = \frac{u\,L}{\nu} \tag{6.2}$$

is computed from the flow velocity u, the characteristic length L (namely the length of the boundary layer at the position of the gauges x) and the kinematic viscosity ν. The flow velocity is obtained from the freestream Mach number and the inlet total temperature. The kinematic viscosity follows from the dynamic viscosity divided by the density, which are computed at the corresponding inlet total temperature and pressure (Oldfield and Guo, 1997). The local Reynolds number is given for each flow condition in table 6.2

These results can be compared to the heat transfer values predicted by Reynolds number correlations for external boundary layers in laminar or turbulent flow (Kays et al., 2005):

$$\mathrm{Nu} = 0.664\,\mathrm{Pr}^{1/3}\,\mathrm{Re}_x^{1/2} \text{ for laminar flow,} \tag{6.3}$$

$$\mathrm{Nu} = 0.0287\,\mathrm{Pr}^{3/5}\,\mathrm{Re}_x^{4/5} \text{ for turbulent flow.} \tag{6.4}$$

As the flow decelerates quickly from the throat to the location of the gauges (see figure 6.2), the flow is expected to be turbulent.

The results for the heat transfer coefficient as a function of the Reynolds number are shown

Test	T_{01}, K	Target M	Local Re ($\times 10^6$)
1	412	1.10	8.99
2	412	1.00	8.77
3	412	0.90	8.57
4	412	0.80	8.09
5	412	0.95	8.67
6	444	1.00	8.00

Table 6.2: Resulting Reynolds number for each test condition.

in figure 6.9a for the nominal gauge thickness. The spread in the values for the heat transfer coefficient gives an indication of the run-to-run variability and the uncertainty of the substrate thickness. A much better gauge-to-gauge agreement is achieved when individual gauge thicknesses are used to process the temperature traces (see figure 6.9b). Given the difficulties to measure a complex flow region with possible shock waves and boundary layer interaction effects, the results are very consistent. It is not possible to capture the increase in heat transfer coefficient with increase in Reynolds number, because the difference in heat transfer coefficient over the range of Reynolds numbers is very small and within the uncertainties of the experiment. These results also show that gauge 1 gave a better agreement with the correlation before fitting the gauge thickness. It would be necessary to further analyse the gauges to assess which gauge thickness is correct.

6.2 Double-sided thin film gauges

The configuration of the double-sided thin film gauges is depicted in figure 4.1b. When unheated, the principle of operation of the double-sided gauges is the same as that of the single-sided gauges. The same assumptions regarding the pre-run conditions (HTA3 stability, no temperature changes in the rig prior to the run, and constant temperature coefficient of resistance) can be made. The temperature traces for two of the double-sided gauges are shown in figure 6.10. The results demonstrate a high repeatability of the rig conditions and good consistency in the

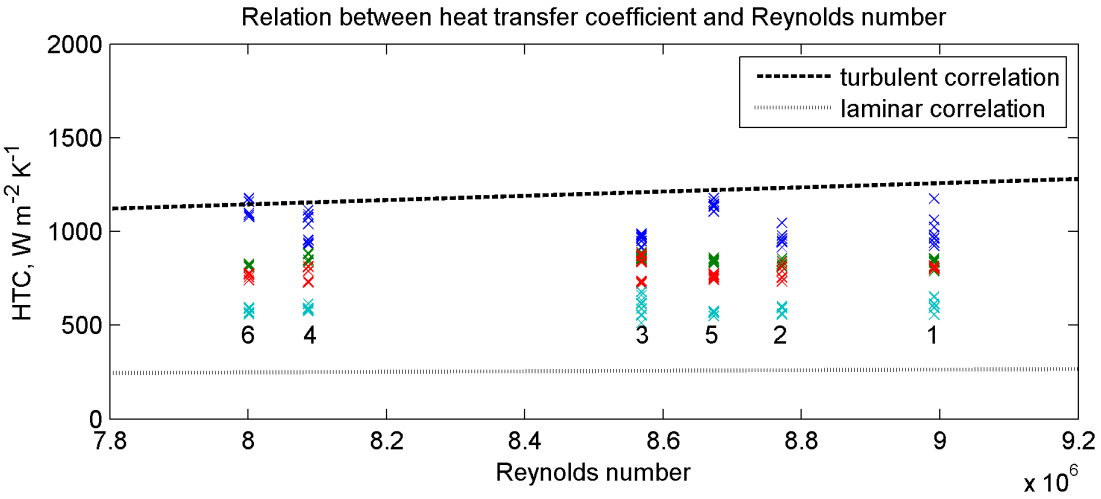

(a) Results based on nominal gauge thickness.

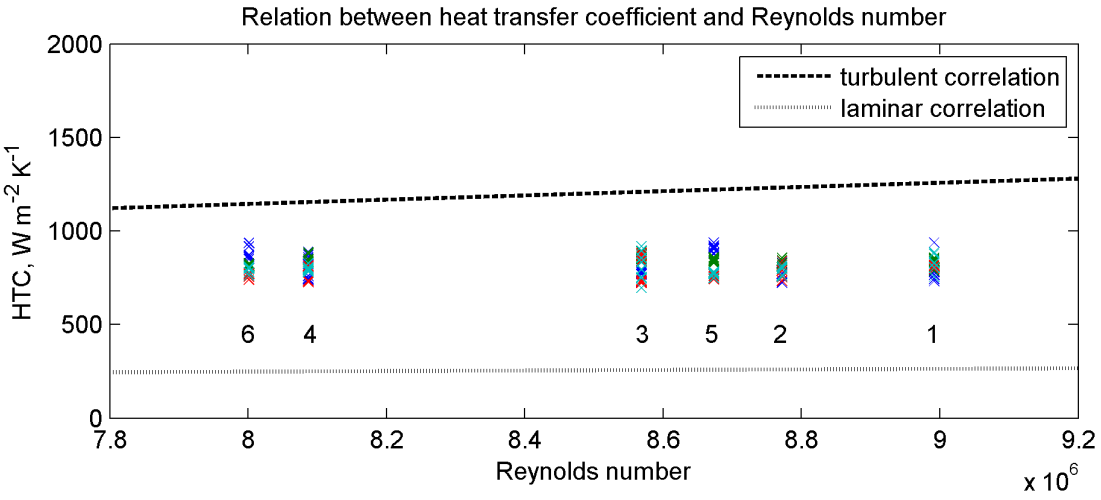

(b) Results for individually fitted gauge thickness.

Figure 6.9: Heat transfer coefficient plotted against Reynolds number from experimental data from single-sided thin film gauges compared to results from Reynolds number correlations. The numbers 1 to 6 correspond to the flow conditions described in table 6.2.

measured heat transfer. In comparison to the single-sided gauges (see figure 6.6), the top gauges see higher temperatures, with the top gauge temperature increasing by about 90 K during a run and the bottom gauge temperature by half this value. The double-sided gauges have a slower thermal penetration, which is caused by the thicker insulating layer.

Figure 6.11 shows the results for the heat flux for M = 1 and T_{01} = 444 K. Again the agreement between the two gauges is very good. Although the temperature range for the

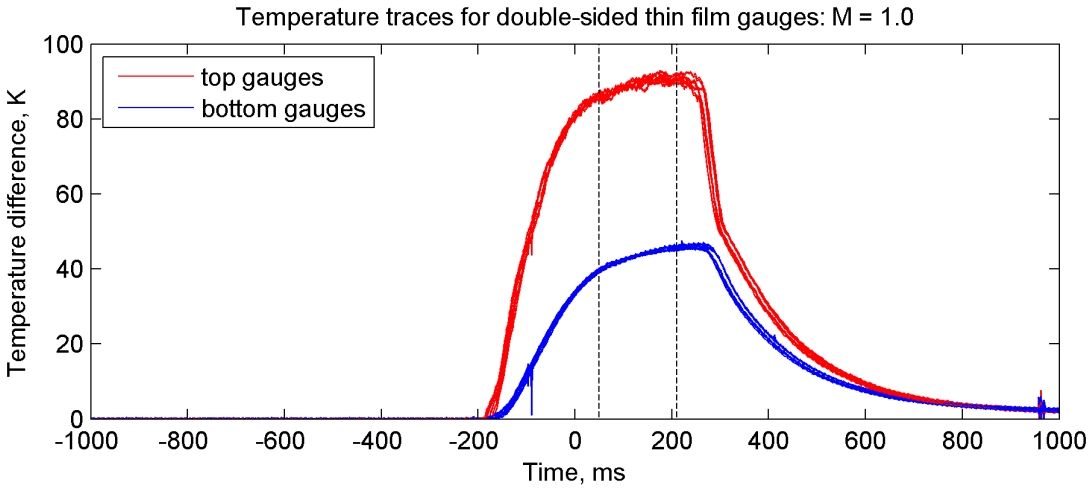

Figure 6.10: Temperature traces for two double-sided thin film gauges. The results for six tests are overlapped in this plot. The dashed lines mark a typical stable period used for the regression of one run and one gauge.

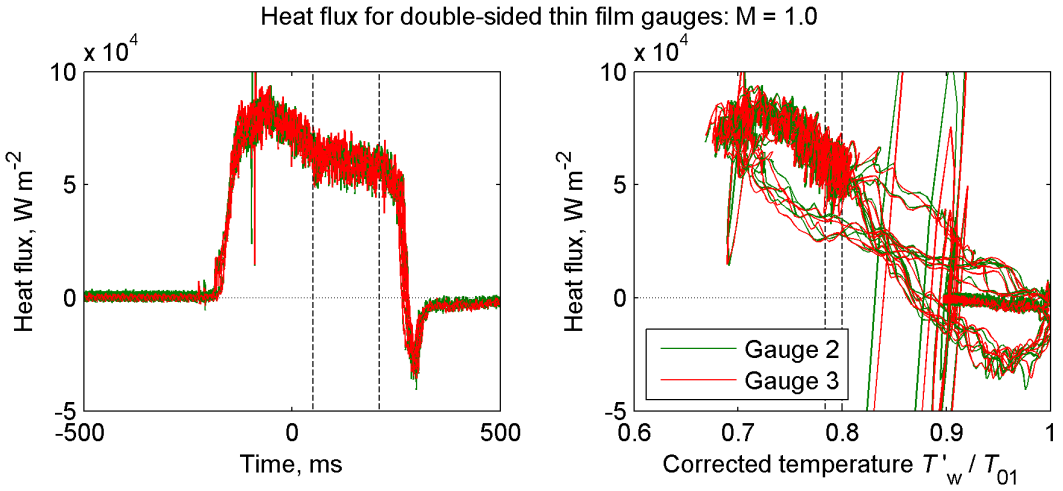

Figure 6.11: Heat flux for two double-sided thin film gauges. The results for six tests are overlapped in this plot. The dashed lines mark a typical stable period used for the regression of one run and one gauge.

regression is much larger (for the same stable run period) than for the single-sided thin film gauges, the regression does not converge for any flow condition. As for the single-sided gauges, the regression is then performed by setting the recovery temperature (equation 6.1) as the intercept for $\dot{q} = 0$. The results are summarised in figure 6.12. A quantitative comparison of the different thin film gauge configurations follows at the end of this chapter (see table 6.5).

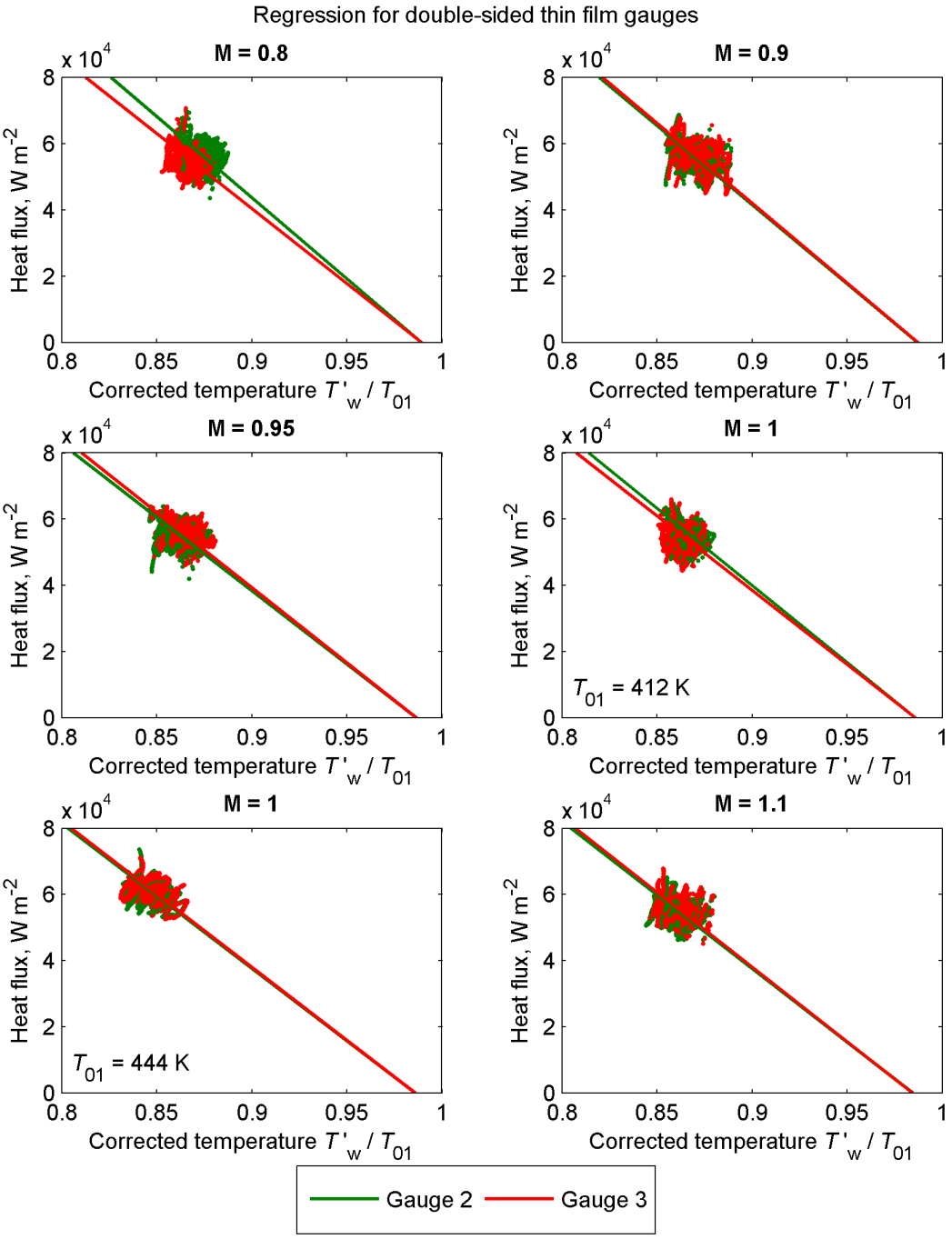

Figure 6.12: Regression data for two double-sided thin film gauges. The regression is performed on data from the stable run period. The inlet total temperature is given for the M = 1 case, which was run at two different inlet total temperatures.

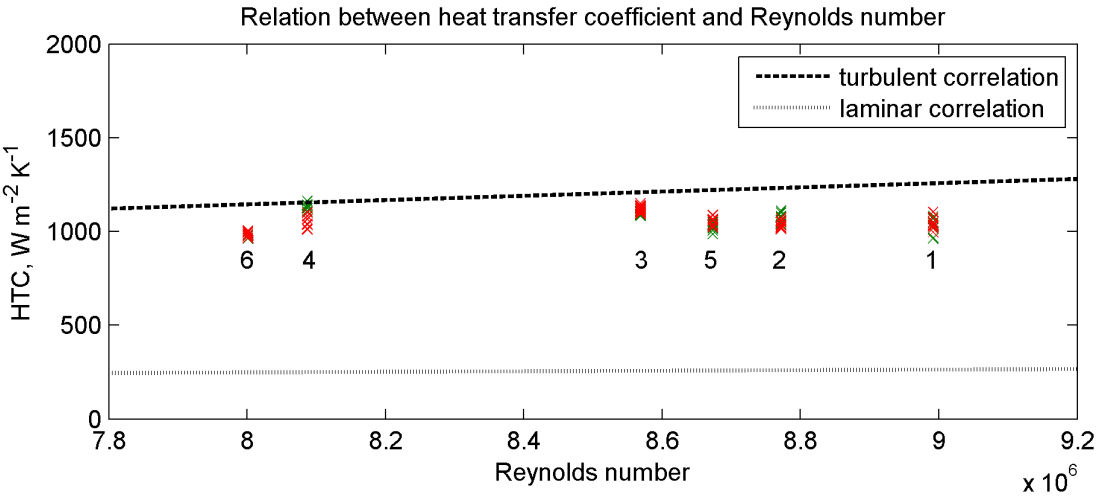

Figure 6.13: Heat transfer coefficient plotted against Reynolds number from experimental data from double-sided thin film gauges compared to results from Reynolds number correlations. The numbers 1 to 6 correspond to the flow conditions described in table 6.2.

The heat transfer results are plotted in figure 6.13 as a function of the local Reynolds number. The correlations shown for comparison are equation 6.3 for laminar flow and equation 6.4 for turbulent flow. The heat transfer coefficients measured with double-sided thin film gauges agree better with the turbulent flow prediction than those measured with single-sided gauges. In agreement with the predictions there is no strong dependence on the Reynolds number.

6.3 Double-sided thin film gauges with an underside thin film heater

The configuration of the double-sided thin film gauges with an underside thin film heater is shown in figure 5.3a. The horizontal heater design presented in section 5.2 was used to heat the substrate for these tests. The heater had a resistance of 8.1 Ω and an area of 525 mm^2. The heater was run at different current settings with the aim to cover a range of power densities up to 100 $\mathrm{kW\,m^{-2}}$ in order to achieve a wide range of substrate temperatures for the test run. Each of the six flow conditions discussed above was tested at a range of heater settings, as summarised in table 6.3. The table includes unheated tests and repetitions.

The principle of operation of the double-sided thin film gauges with a heater is depicted in figure 5.8. The heater is switched on a few minutes before the run after taking the measurement

Test	No. of runs	T_{01}, K	Target M	Heater current, A
1	8	412	1.10	0.8–1.6
2	7	412	1.00	1.4–2.2
3	9	412	0.90	1.4–2.6
4	8	412	0.80	1.7–2.1
5	7	412	0.95	0–2.1
6	6	444	1.00	unheated

Table 6.3: Test conditions and heater settings for double-sided thin film gauges with an underside thin film heater.

of the reference voltage at isothermal conditions. This voltage is used to compute the preheating temperature difference (see equation 5.16), as the temperature of the surface increases when the heater is switched on. Note also that the heater was not switched off until the end of the test. The temperature traces for one gauge are shown in figure 6.14 for the six investigated flow conditions. The temperature achieved by the gauges before the run depends on the amount of preheating. A maximum preheating surface temperature difference of 80 K was achieved. At identical heater settings repeatable results are achieved. The surface temperature drops just before the run when cold air accumulated in the rig is blown out.

The achieved preheating temperature differences as measured between the isothermal reference point and the start of the run are plotted in figure 6.15 against heater current. Since the conditions in the rig prior to the run are identical for all flow conditions, the preheating temperature differences from different runs can be directly compared. The measurements agree very well with the model within expected uncertainties (see section 5.5) and consistent preheating temperatures are achieved.

At each flow condition, i.e. for each Mach number and total inlet temperature, all runs at different heater settings are used for the regression employing the method described in section 5.4. For some conditions there are no unheated runs available. In contrast to the unheated cases both T_{aw} and h can be extracted from the regression, so it is not necessary to fix the adiabatic

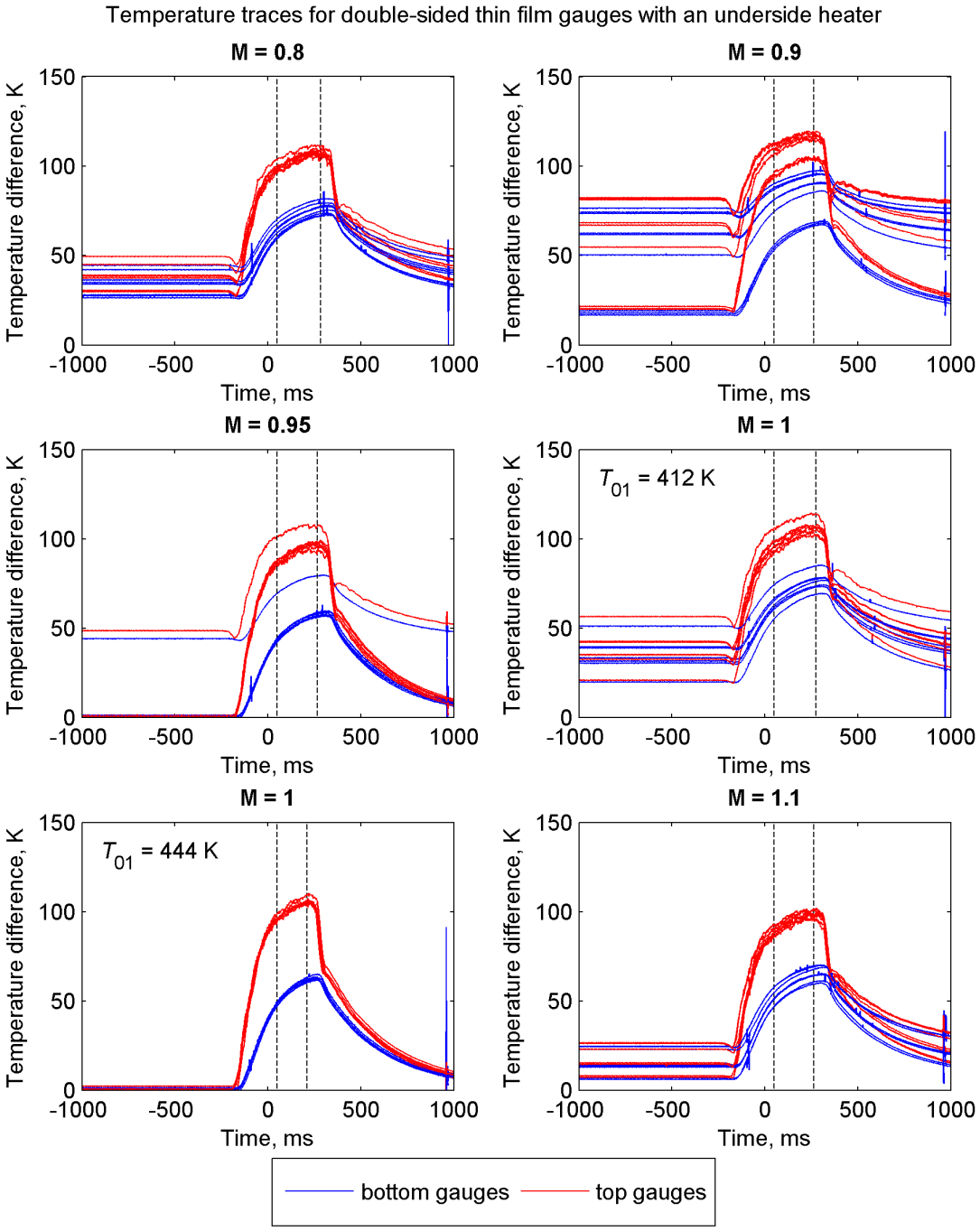

Figure 6.14: Temperature traces for one double-sided thin film gauge with an underside thin film heater. The results for a number of tests at different heater settings are shown for each flow condition (see table 6.3). The dashed lines mark a typical stable period used for the regression of one run. The inlet total temperature is given for the M = 1 case, which was run at two different inlet total temperatures.

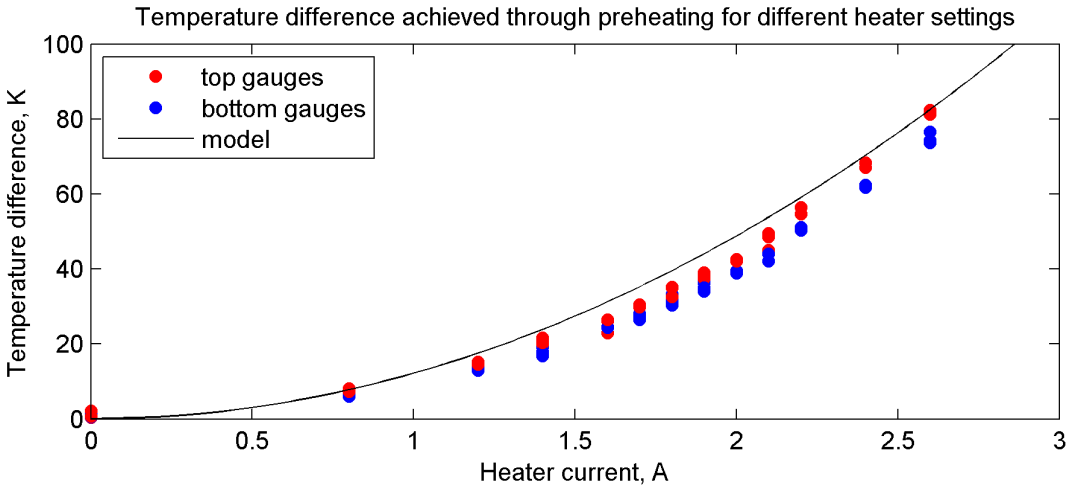

Figure 6.15: Preheating temperature difference from the isothermal reference point plotted against a range of heater currents.

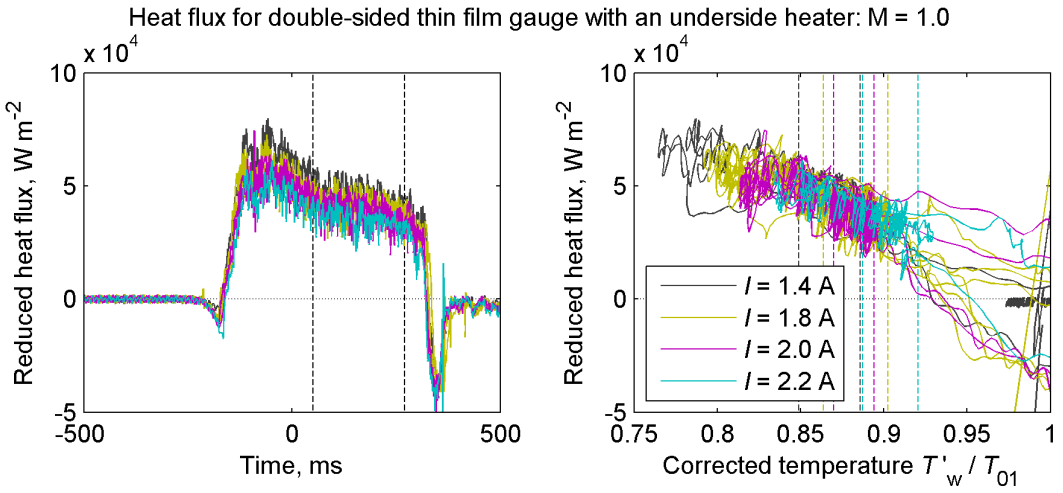

Figure 6.16: Heat flux for one double-sided thin film gauge with an underside heater. The results for seven tests are overlapped in this plot ($T_{01} = 412\,\mathrm{K}$). The dashed lines mark a typical stable period used for the regression of one run.

wall temperature to the recovery temperature. The convective heat flux is obtained from the temperature history using the impulse response method. Therefore, the preheating temperature difference and thus the heat flux are set to zero at the start of the run. This "reduced" heat flux and the corresponding regression results are shown in figure 6.16 for M = 1 and $T_{01} = 412\,\mathrm{K}$. At higher preheating temperatures the heat flux during the run decreases and thus the range for the regression is increased in comparison to the unheated double-sided gauges. The regression

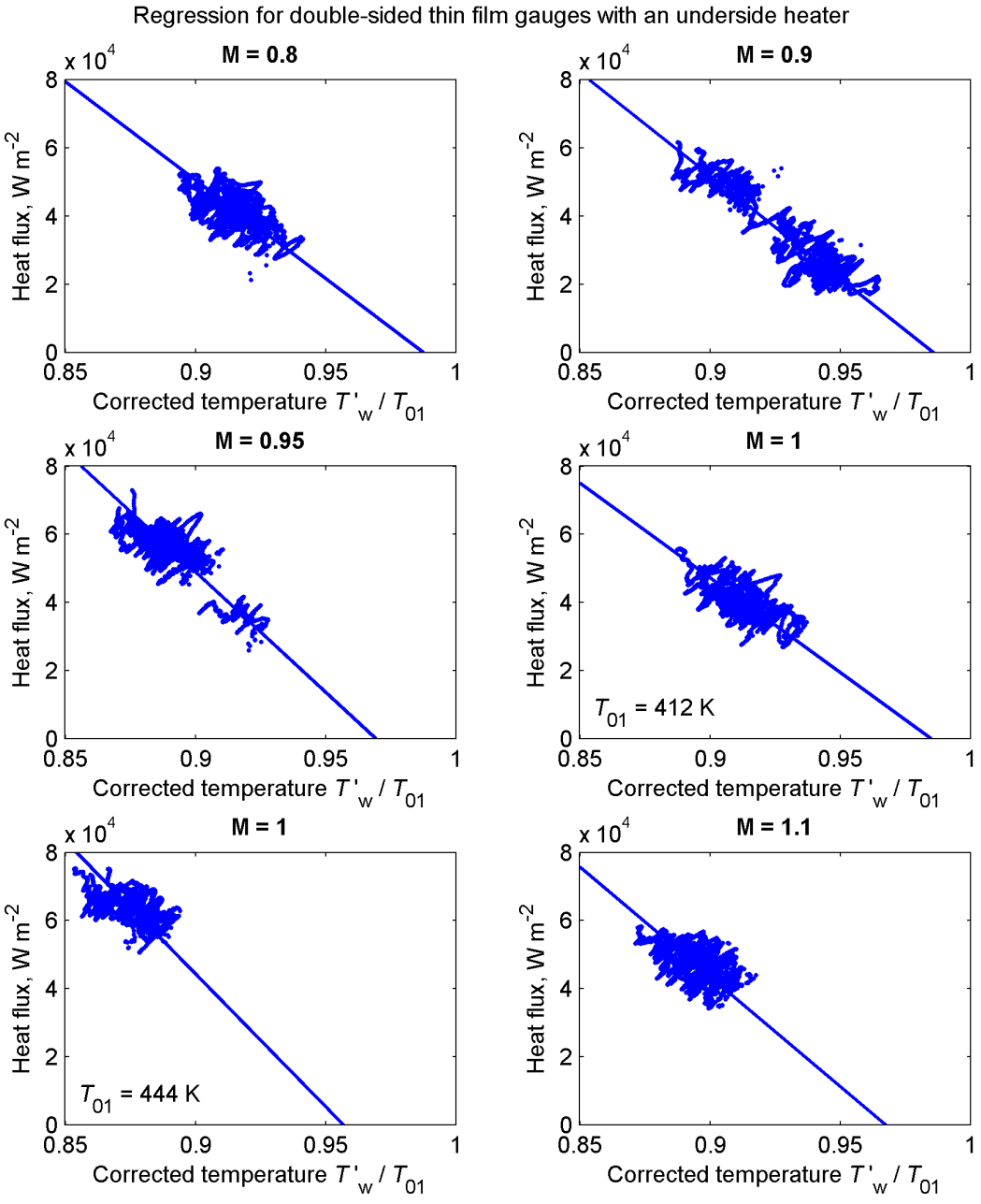

Figure 6.17: Regression data for one double-sided thin film gauge with an underside thin film heater element. The regression is performed on data from the stable run period.

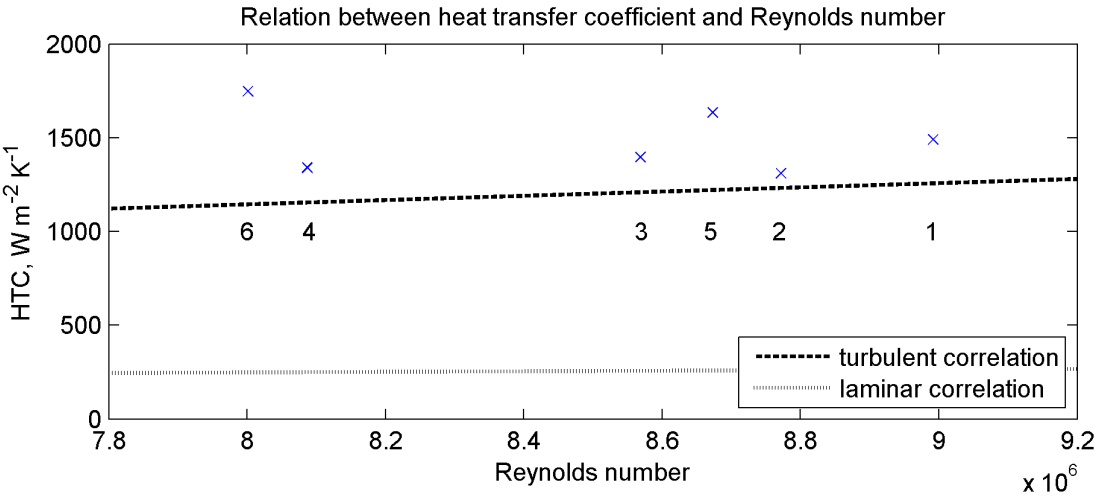

Figure 6.18: Heat transfer coefficient plotted against Reynolds number from experimental data from double-sided thin film gauges with an underside heater compared to results from Reynolds number correlations. The numbers 1 to 6 correspond to the flow conditions described in table 6.2.

results for all runs are shown in figure 6.17 and summarised in table 6.5 at the end of this chapter.

Figure 6.18 shows the heat transfer coefficient plotted against the Reynolds number. As all runs at one flow condition were combined in a multiple regression to obtain the heat transfer coefficient there is only one value for each condition. The results agree well – within the difficulties to model such a complex flow – with the correlation for turbulent flow (equation 6.4). The tests 5 and 6 (M = 0.95 and M = 1 with $T_{01} = 444\,\mathrm{K}$) had almost no heated runs and the results do not match the general trend. Noticeably, the separation of the adiabatic wall temperature and the heat transfer coefficient results in an overprediction of the latter when there is no heated data available. With exception of these two flow conditions, the double-sided thin film gauges with an underside thin film heater match the trend predicted by the correlation much better than the single-sided and the double-sided gauges. The quality of the regression could be further improved by including unheated and heated runs and thus extending the range of the regression for all flow conditions.

6.4 Double-sided thin film gauges with variable heating current

The configuration of the self-heating double-sided thin film gauges is identical to that of the unheated double-sided gauges (see figure 5.3b). In comparison to the double-sided thin film gauges with an underside thin film heater, the package thickness is reduced by about one third. The principle of operation has been discussed in section 5.4 (see figure 5.8). The current through the top gauges is set to a higher value using the modified HTA3 box in order to heat the gauge substrate over a range of temperatures, as detailed in table 6.4. The table includes unheated tests and repetitions.

A reference voltage measurement is taken before the run under isothermal conditions. For the bottom gauges, this voltage is used to calculate the temperature increase during preheating from equation 5.16. For the top gauges, the reference measurement is taken at a nominal gauge current of 5 mA, which is sufficiently small that no ohmic heating is expected. The current through the top gauge is set individually for each gauge. However, the reference voltage cannot be used to obtain the temperature increase of the top gauge, because of the subsequent change in gauge current relative to the reference measurement. Moreover, the current measurement is not accurate enough to use it to infer the top gauge temperature (see section 5.4). The aim is instead to determine the top gauge temperature from the heating heat flux and the bottom gauge temperature.

Test	No. of runs	T_{01}, K	Target M	Gauge current, mA
1	8	412	1.10	30–40
2	7	412	1.00	45–60
3	9	412	0.90	60–90
4	8	412	0.80	55–75
5	7	412	0.95	0–75
6	6	444	1.00	unheated

Table 6.4: Test conditions and top gauge current settings for self-heating double-sided thin film gauges.

Since the self-heating double-sided thin film gauges have the same configuration (i.e. thickness) as the unheated double-sided thin film gauges and the gauges are placed on the same axial location, it is expected that they will see the same temperature rise if the self-heating gauges are employed at a low enough current so that they are effectively unheated. This expectation could however not be confirmed due to issues with the reference voltage measurements, which are discussed in detail in appendix A.2. While these issues could not be resolved for the unheated self-heating gauges, they are not expected to affect any of the heated tests, where a separate measurement of the current was taken, which can be used to obtain an independent measurement of the reference voltage for a known gauge resistance. For now only the results for the heated tests will be presented.

6.4.1 Calculating the top gauge temperature

The temperature change of the top gauge after the start of data acquisition can be calculated using equation 5.16 from the measured initial voltage V_{gi} and the voltage difference ΔV. As explained in section 5.4, however, the actual temperature of the gauges at this point, which is higher than the temperature of the cassette, cannot be measured directly. An initial gauge temperature T_{gi} is nevertheless required to calculate the heat transfer coefficient. As discussed in section 5.5, the initial top gauge temperature can be calculated for a given heating heat flux provided that there are no heat losses into the rig prior to the run – as is the case for the single-sided and unheated double-sided gauges.[1]

In section 5.5 two models were introduced, which describe the 2D and 3D thermal conduction effects in a self-heating gauge. These models can now be validated against experimental data. Figure 6.19 shows the bottom gauge preheating temperature difference as measured in the rig for a range of top gauge voltages. The agreement between the four self-heating gauges is very good. The experimental results are compared to the predictions from the 2D and 3D models. The 3D model predicts a much steeper increase of temperature difference with increasing voltage because of the more concentrated equivalent 3D gauge geometry. The prediction of the 2D model, on the other hand, is much more in line with the observed bottom gauge temperature. Up to 2.5 V the

[1] An estimate of the effect of natural convection and radiation is given in chapter 7.

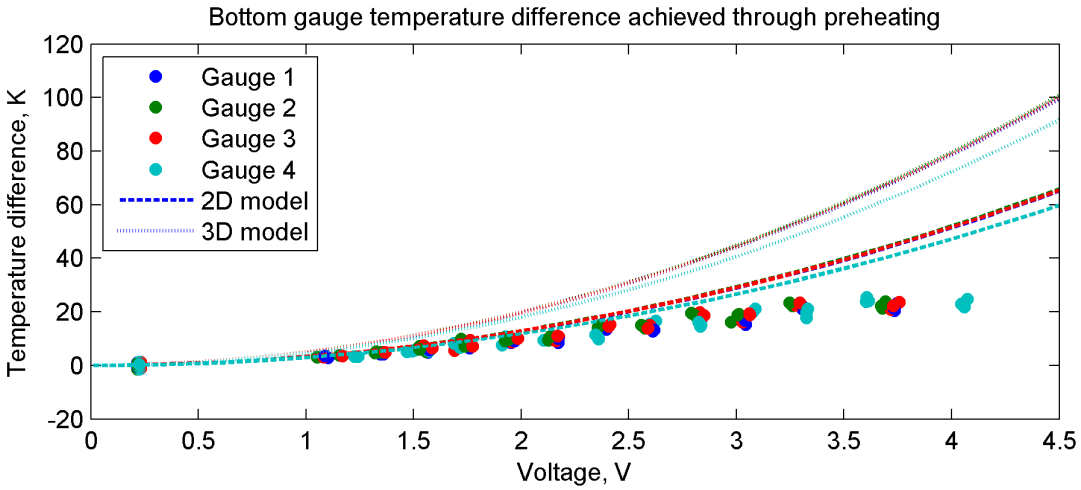

Figure 6.19: The bottom gauge temperature difference achieved for different gauge settings is plotted over the voltage across the top gauge and superimposed to the 2D (dashed line) and 3D (dotted line) model results.

agreement between the 2D model prediction and the experimental bottom gauge temperature differences is excellent (within experimental uncertainties). At higher voltages the bottom gauge temperature does not increase proportionally to V^2 and a flattening of the temperature curve is observed. This effect can be partially explained by the increase in gauge resistance with increasing gauge temperature, which leads to a decrease in the heating heat flux. By using the bottom gauge temperature to obtain the top gauge temperature this decrease in temperature has been taken into account for the post-processing. Given the greater discrepancy of the 3D prediction, in the following the results for the 2D calculation of the top gauge temperatures are presented.

6.4.2 Results

The temperature traces obtained from this calculation are shown in figure 6.20. For clarity only the results for one gauge have been plotted. There is no point in comparing the temperatures of one gauge at "one" heater setting as the current setting cannot ensure repeatability. Likewise, it is unnecessary to compare the results of several gauges at the same nominal heating power. The consistent temperature measurements from gauges of the same manufacture and configuration has been demonstrated for single-sided and double-sided thin film gauges. The same drop in

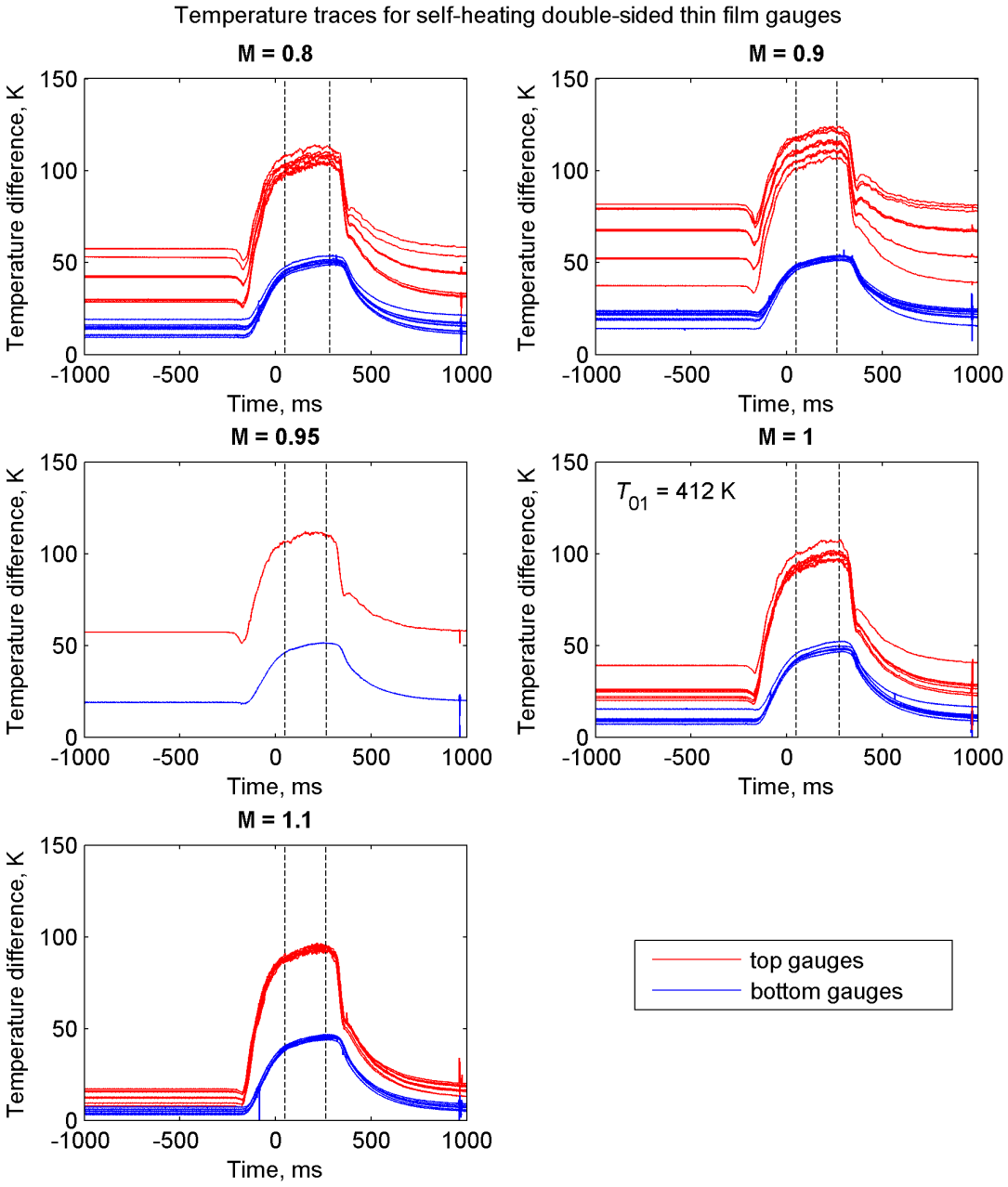

Figure 6.20: Temperature traces for one self-heating double-sided thin film gauge. The results for a number of tests at different heater settings are shown for each flow condition (see table 6.4). The dashed lines mark a typical stable period used for the regression of one run. The inlet total temperature is given to differentiate the M = 1 case.

temperature that was observed for the double-sided gauges with a heater at the start of the run can be seen here. Preheating surface temperature differences of up to 80 K are achieved. In comparison to the double-sided gauges with a heater the temperature difference between the top and bottom gauges at the start of the run is much larger, which is a result of heating the top gauge instead of the substrate (but if it was required a thin film heater with higher resistance could be designed).

As for the double-sided thin film gauges with an underside heater, the heat flux is obtained using the impulse response method with the temperature difference set to zero at the start of the run. The resulting reduced heat flux is equal to the convective heat flux alone, i.e. the surface heat flux minus the pre-run heat flux (see figure 6.21). With increasing gauge current, the surface temperature increases and the heat flux decreases. A wide temperature range is covered and a very good regression is achieved.

The heat transfer results from the four self-heating double-sided thin film gauges are presented in figure 6.22. For completeness a comparison with the results from the unheated double-sided thin film gauges is shown. For conditions 1, 2 and 5 (which correspond to M = 0.95, M = 1 and M = 1.1) the regression does not converge and it is necessary to separate the adiabatic wall temperature and the heat transfer coefficient by defining a recovery temperature (equation 6.1).

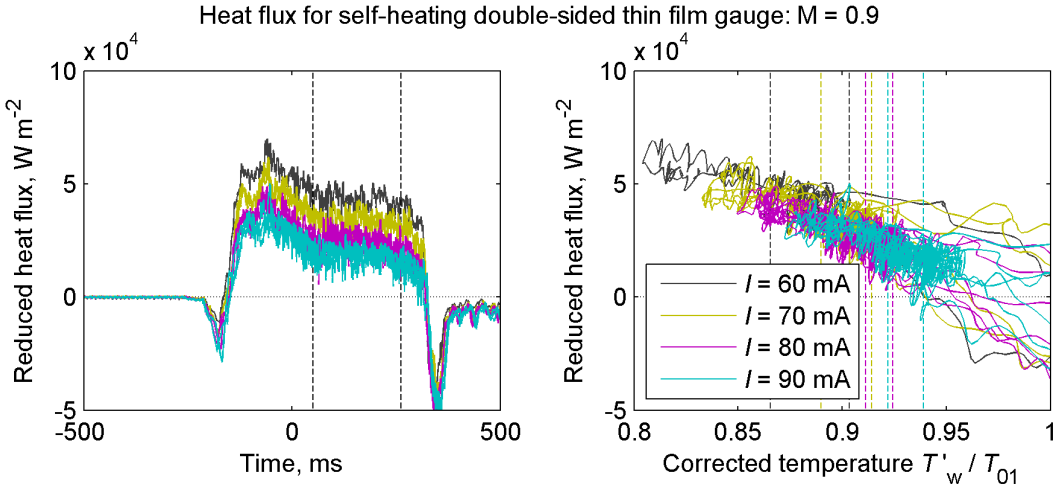

Figure 6.21: Heat flux for one self-heating double-sided thin film gauge. The results for nine tests are overlapped in this plot. The dashed lines mark a typical stable period used for the regression of one run.

The tests at conditions 3 and 4 (M = 0.8 and M = 0.9) were carried out over a wider range of gauge currents and achieve convergence.

Generally, the results agree well with those of the unheated double-sided thin film gauges. For the fixed regression (i.e. set recovery temperature) the results match the unheated gauges very well.[1] However, for the multiple regression the wall temperatures at higher heating power are lower than expected, which results in a lower adiabatic wall temperature and a higher heat transfer coefficient. If the wall temperatures were higher, the match with the unheated double-sided gauges would be better. It is thus necessary to question the chosen thermal conduction model to calculate the top gauge temperature from the bottom gauge temperature. As discussed in section 5.5, the 3D model predicts a larger temperature decay in the gauge substrate (see figure 5.20). Figure 6.23 shows the regression results if instead of the 2D model, the 3D model is used to obtain the top gauge temperature. For the fixed regression the differences between the two models are very small – if anything the 2D model can be considered to give the better match. The largest mismatch in heat transfer coefficient is observed for the M = 0.95 case. As the data from the one run at M = 0.95 is very close to the x-axis intercept due to the high gauge current setting, the slope is very sensitive to changes in temperature. For the multiple regression at M = 0.8 and M = 0.9 the 3D model gives a better match with the unheated double-sided gauges, despite its poor prediction of the bottom gauge temperatures.

In conclusion, the differences in the regression results between the 2D and 3D models are a measure of the modelling uncertainties. For the two chosen models these uncertainties are as high as 15 K. The effect of these uncertainties on the overall experimental uncertainties was discussed in section 5.6. In theory it is possible to find a simple thermal model, which better reproduces the bottom gauge temperature. However, as long as the temperature difference between the top and bottom gauge is proportional to V^2, a lower bottom gauge temperature will automatically lead to a further decrease in surface temperature, which contradicts expectation of the regression results. In order to reduce the model uncertainties a 3D FEA prediction of the

[1] These results also seem to imply a variation in the gauge thickness as studied for the single-sided thin film gauges. A better gauge-to-gauge agreement would be achieved if the substrate of gauge 1 was indeed thicker than the determined nominal gauge thickness. These differences will not be further studied for these gauges.

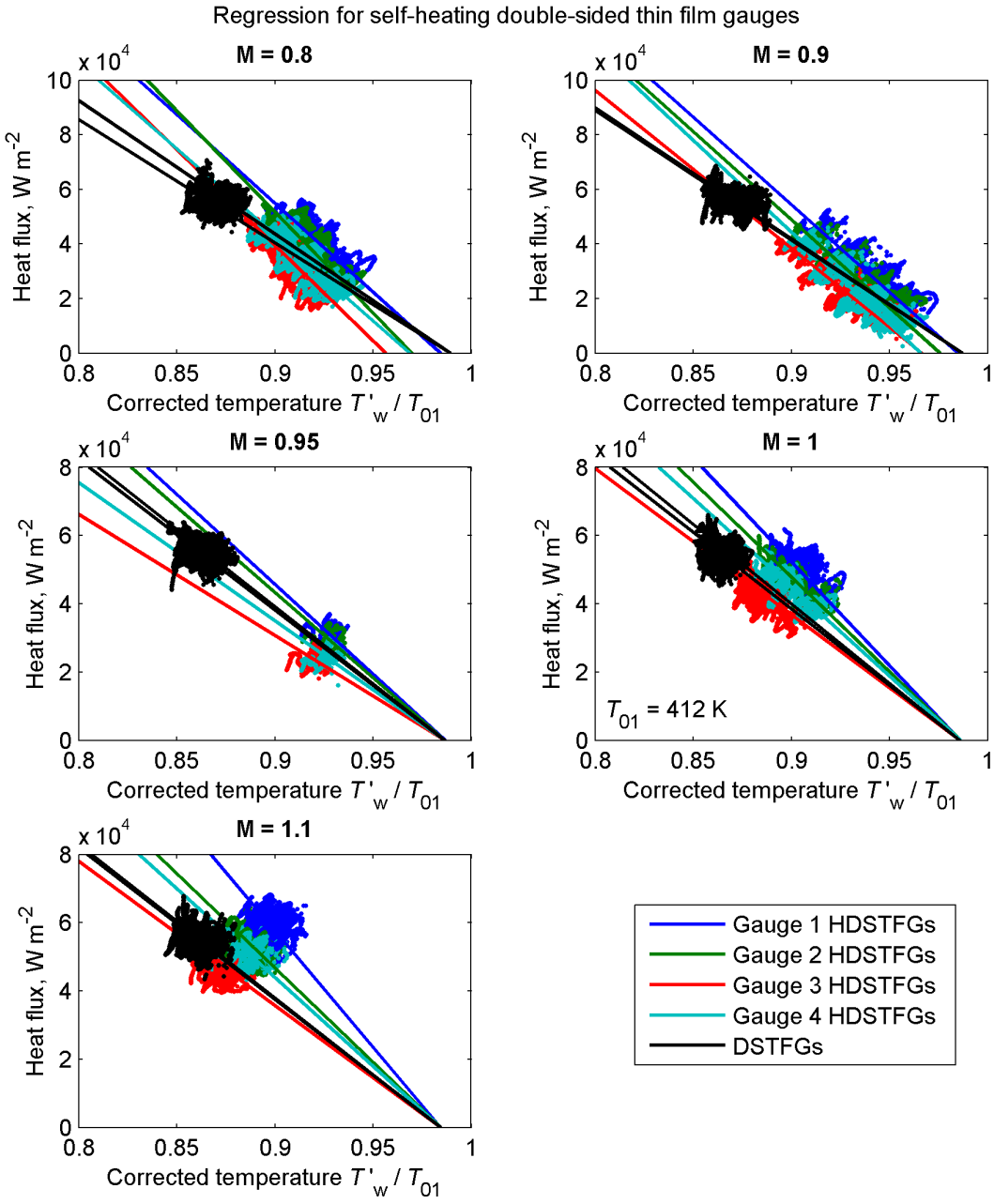

Figure 6.22: Regression data for four self-heating double-sided thin film gauges (HDSTFGs) compared to results from two double-sided thin film gauges (DSTFGs). The regression is performed on data from the stable run period.

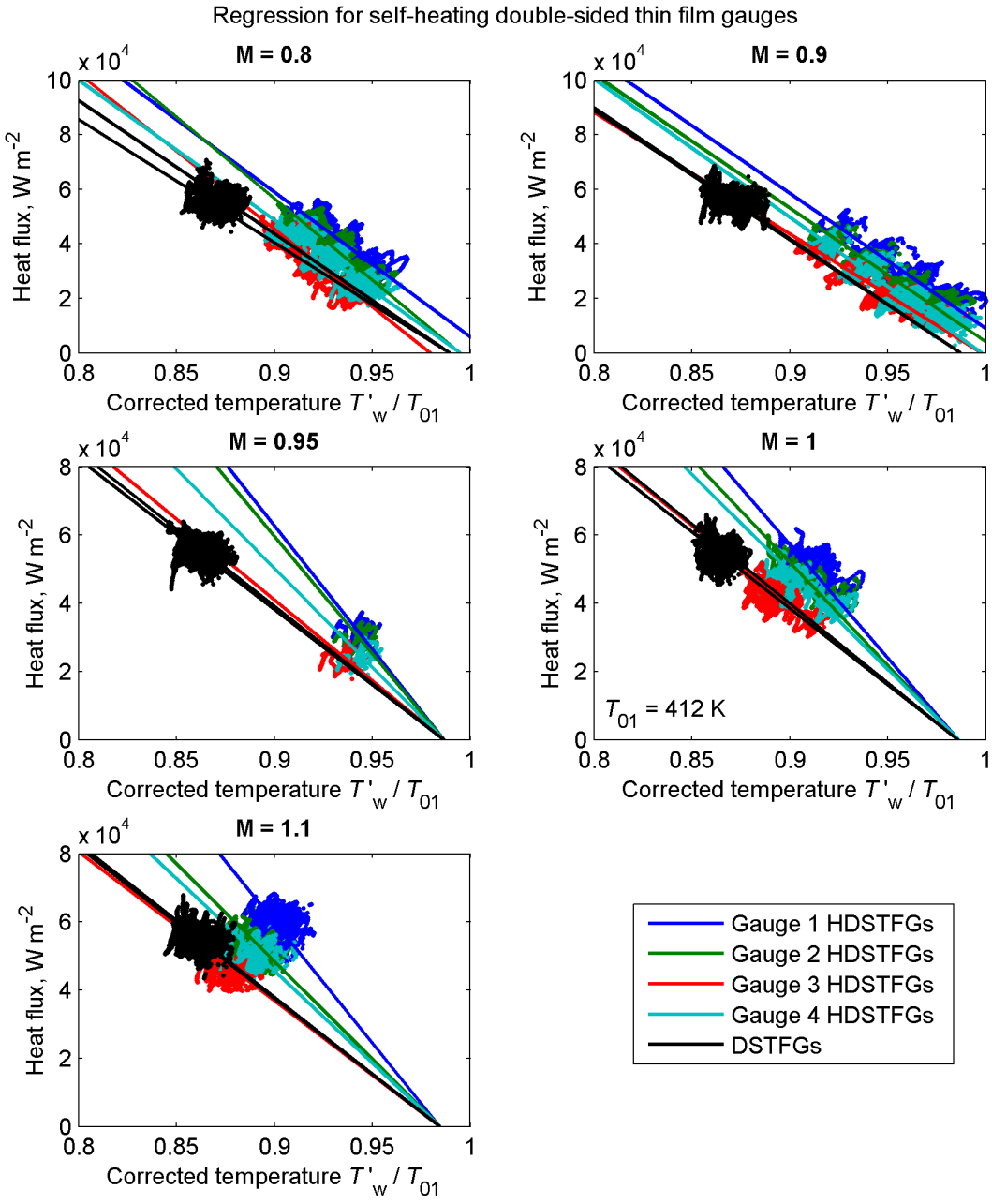

Figure 6.23: Regression data for four self-heating double-sided thin film gauges using the 3D thermal conduction model to obtain the top gauge temperature.

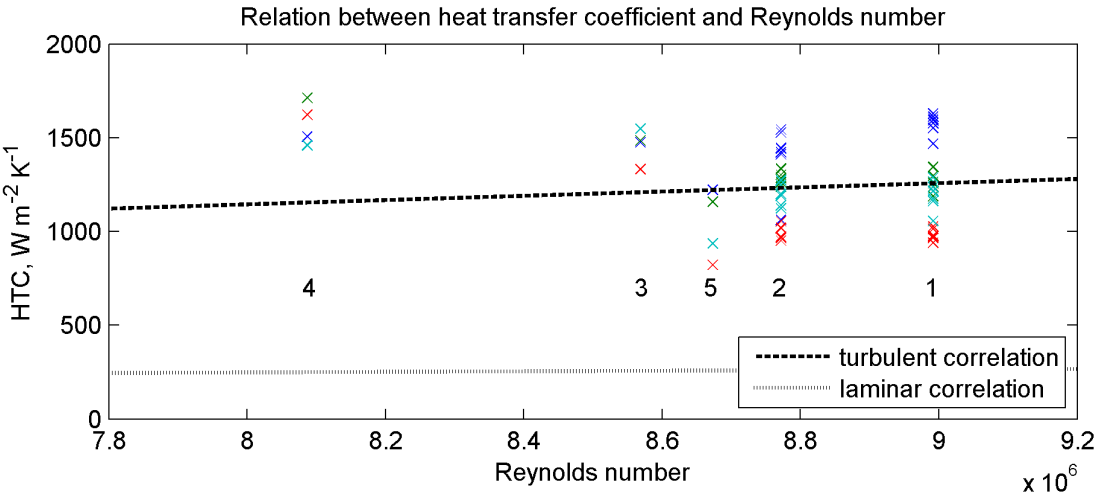

Figure 6.24: Heat transfer coefficient plotted against Reynolds number from experimental data from self-heating double-sided thin film gauges compared to results from Reynolds number correlations. The numbers 1 to 6 correspond to the flow conditions described in table 6.2.

thermal conduction in the gauge substrate will be necessary, as suggested in section 8.2. Ideally this model would be complemented by an accurate measurement of the gauge temperatures on the bench, by instrumenting the layers with thermocouples and using IR thermography to determine the top gauge temperature.

Figure 6.24 shows the heat transfer coefficient plotted against the Reynolds number and compared to the correlations from literature. For M = 0.8 and M = 0.9 (tests 4 and 3) the heat transfer coefficient is overpredicted, as is expected from an underprediction of the surface temperature and convective heat flux. The agreement with the correlations from literature is better for M = 1 and M = 1.1 (tests 2 and 1) which were run at lower gauge current settings. The regression results for each single run are shown. The spread in heat transfer coefficient is consistent with that observed in figure 6.9a for the single-sided gauges. The heat transfer coefficient values for M = 0.95 (test 5) are included for completeness, but they are not expected to follow any trend as they are the result from one high-current run, which required to set the recovery temperature for the regression. More consistent results may be obtained by heating the gauges over a wide temperature range for all flow conditions and by improving the modelling of the top gauge temperature.

6.5 Comparison of thin film gauge configurations

The results for the four investigated thin film gauge configurations are summarised in table 6.5. The heat transfer coefficient and adiabatic wall temperature are given for each flow condition (characterised by the corresponding Reynolds number from table 6.2). Where data from several gauges was available the mean value is taken. In the case of the single-sided gauges the results for the individually fitted gauge thicknesses are shown. The adiabatic wall temperature is given as a fraction of the mean inlet total temperature (see equation 5.32). The single-sided and double-sided gauges have identical adiabatic wall temperatures, which were defined as the recovery temperature (see equation 6.1). The two flow conditions with a Mach number $M = 1$ have the same adiabatic wall temperature. The variability in the adiabatic wall temperature is small, with differences of maximally 12 K.

There is no strong dependence of the heat transfer coefficient on the Reynolds number, but the magnitude of the measured heat transfer varies for the different gauge types. The lowest heat transfer was obtained for the fitted single-sided gauges and the highest for the heated double-sided thin film gauges. The differences between the unheated and heated thin film gauges result partially from the need to set a recovery temperature for the former, whereas it was possible to separate the adiabatic wall temperature and the heat transfer coefficient for the latter. Additional reasons for the observed differences have been discussed for each gauge type.

The last column in table 6.5 gives the value of the stability criterion defined in section 4.4 to evaluate different gauge configurations (see equation 4.23). The larger the stability criterion, the higher the quality of the regression. The stability criterion is thus also a good measure for the uncertainty of a regression. For the single-sided gauges the stability criterion is around 0.1. A higher stability criterion of around 0.2 is achieved with the double-sided gauges. The reason for this increase is the thicker total thickness of the double-sided thin film gauges in comparison to the single-sided gauges. Nevertheless, even for the double-sided thin film gauges the stability of the regression is insufficient to perform a multiple regression and it is necessary to make an assumption on the adiabatic wall temperature.

The highest stability criterion obtained with the double-sided thin film gauges with an

	Re ($\times 10^6$)	**HTC, W m^{-2} K^{-1}**	$\mathbf{T_{aw}/\overline{T_{01}}}$	**Stability crit.**
Single-sided TFGs	8.00	815	0.9859	0.09
	8.09	808	0.9893	0.10
	8.57	813	0.9871	0.08
	8.67	820	0.9865	0.19
	8.77	790	0.9859	0.10
	8.99	816	0.9844	0.09
Double-sided TFGs	8.00	982	0.9859	0.17
	8.09	1091	0.9893	0.17
	8.57	1112	0.9871	0.17
	8.67	1039	0.9865	0.20
	8.77	1058	0.9859	0.16
	8.99	1034	0.9844	0.13
DSTFGs with heater	8.00	1747	0.9566	0.39
	8.09	1341	0.9872	0.51
	8.57	1397	0.9855	0.79
	8.67	1634	0.9689	0.59
	8.77	1309	0.9846	0.51
	8.99	1491	0.9674	0.48
Self-heating DSTFGs	8.00	–	–	–
	8.09	1578	0.9698	0.74
	8.57	1461	0.9732	1.05
	8.67	1035	0.9865	0.33
	8.77	1223	0.9859	0.28
	8.99	1258	0.9844	0.21

Table 6.5: Comparison of the results for four different gauge configurations.

underside heater is just below 0.8. While the stability criterion varies with the flow condition because of the different range of heater settings, it is always possible to perform a multiple regression. The self-heating double-sided gauges have similar values of the stability criterion. For $\mathrm{Re} = 8.57 \cdot 10^6$ a peak value of 1.05 is achieved. Nearly adiabatic conditions were attained during this test.

6.6 Texstan modelling

There is no previous experimental data available to compare to the results of the heat transfer measurements on the casing in this particular set-up without a turbine stage. The heat transfer on the casing can be compared to the results predicted by the 2D boundary layer code Texstan. Texstan was developed from the STAN5 code which is documented in (Crawford and Kays, 1976). The description of Texstan is taken from (Kays et al., 2005).

Texstan is a finite-difference partial differential equation solver programmed in Fortran. The equations solved are the transport of momentum and a number of diffusion equations such as the stagnation enthalpy equation, the turbulence kinetic energy and the turbulence dissipation equation or the mass concentration. All equations are given as a diffusion term and a source term. The equations are formulated as Reynolds-averaged equations, which require turbulence models for closure. The Reynolds stresses are modelled based on the eddy viscosity model. Texstan contains three classes of models for the turbulent viscosity: mixing-length models, one-equation models and two-equation models. Texstan can be used to investigate a large number of geometries from external flows (e.g. flat plates and aerofoil shapes) to internal flows (e.g. pipe flows and annular ducts) for varying boundary conditions. The Texstan version used in this study was optimised by Chana et al. (2003b) for the modelling of flows in the OTRF.

Model inputs

The analysed geometry was a boundary layer flow without transverse curvature. The initial velocity profile was that of a turbulent turbine blade flow. The momentum equation and three diffusion equations were solved using a two-equation k-ϵ model from (Lam and Bremhorst, 1981),

where the turbulent kinetic energy k and the turbulent dissipation ϵ are the two additional transported variables to describe the turbulent flow. A turbulent Prandtl number of 0.9 was specified to solve the energy equation and to calculate the turbulent heat flux. The momentum equation only had a pressure gradient as a source term and the viscous dissipation was included. The fluid was defined as dry air and the effect of pressure on all properties except for density was ignored. The grid spacing, integration step size as well as the entrainment variables were set based on OTRF best practice (Chana et al., 2003b).

The inlet total pressure was 4.6 bar and the inlet total temperature was 444 K. The inlet turbulence intensity was varied between 3.5% and 6.0% and the turbulence dissipation was set to 10^4. The boundary conditions were of the Dirichlet type, i.e. a velocity distribution was defined at the wall surface and at the free stream. The velocity at the surface was set to zero (no-slip condition). The velocity profile at the free stream was obtained from a CFD calculation for M = 1 at the throat from (Ron, 2015). The wall temperature was 300 K.

The heat transfer predictions for three levels of turbulence intensity are shown in figure 6.25. The high heat transfer at the inlet is an effect of the definition of a zero boundary layer, but the boundary layer thickness rapidly increases. The model results confirm that at the location of the gauges the results are not affected by varying inlet turbulence intensity levels. These results

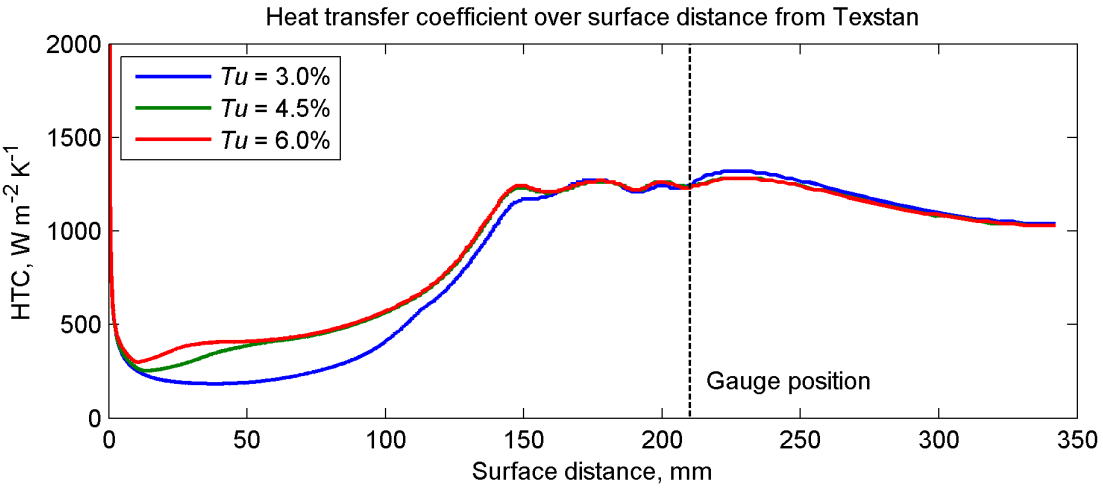

Figure 6.25: Heat transfer coefficient for different inlet turbulence intensity levels plotted against surface distance from the start of the flow.

agree well with those of Chana and Haller (2010), who predicted a steep increase of the Nusselt number from 3% to 5% inlet turbulence intensity followed by a a flattening of the Nusselt number profile at larger levels of turbulence intensity. At the axial distance corresponding to the gauge position, the heat transfer coefficient is relatively flat. The boundary layer code predicts a heat transfer coefficient around $1200\,\mathrm{W\,m^{-2}\,K^{-1}}$, which is in good agreement with the values measured by the heated gauge configurations for this flow condition.

6.7 Summary casing tests

This chapter has presented the first tests of the new double-sided gauges under engine-realistic conditions in the OTRF. The turbine casing of an annular nozzle configuration has been instrumented with single-sided gauges, double-sided gauges, double-sided gauges with an underside thin film heater and self-heating double-sided gauges. The heat transfer has been measured over a range of flow conditions. These experiments have served to demonstrate the measurement strategies described in section 5.4 as well as highlight the particularities of the current experimental set-up (for example regarding the stability of the reference measurements) in preparation for the heat transfer measurements on the aerofoils in chapter 7.

The results from these tests prove that heated arrangements of double-sided thin film gauges can be used to increase the range of the regression and obtain accurate heat transfer data. Whereas for the single-sided gauges and the double-sided gauges it was necessary to define the recovery temperature, the heated gauges allowed to separately determine the adiabatic wall temperature and the heat transfer coefficient. Furthermore, the preheating data acquired at the start of the run has provided validation of the models for thermal conduction in the heated substrate introduced in section 5.5. In the case of the self-heating gauges this investigation favoured the use of the 2D model for subsequent tests. The results from the different types of gauges haven been compared to correlations from literature and to the prediction from a boundary layer code. Finally, the improvement in the regression quality achieved through heated gauge configurations has been quantified using the stability criterion proposed in section 4.4.

CHAPTER 7

Heat Transfer Measurements on Uncooled and Cooled Aerofoils

The performance of different heated gauge configurations on HP NGV aerofoils is investigated in this chapter. The tests were carried out in the OTRF on the MT1 turbine. Four different types of thin film gauges have been tested: single-sided thin film gauges, double-sided thin film gauges, double-sided thin film gauges with heater elements and self-heating double-sided thin film gauges. The last two types of thin film gauges have also been tested on cooled NGVs. A fully instrumented cassette is shown in figure 7.1. The tests have been conducted under uniform inlet conditions (i.e. without inlet temperature distortion or swirl) at a range of heater settings (see section 7.1). The cooling hole geometry will be discussed together with the coolant delivery

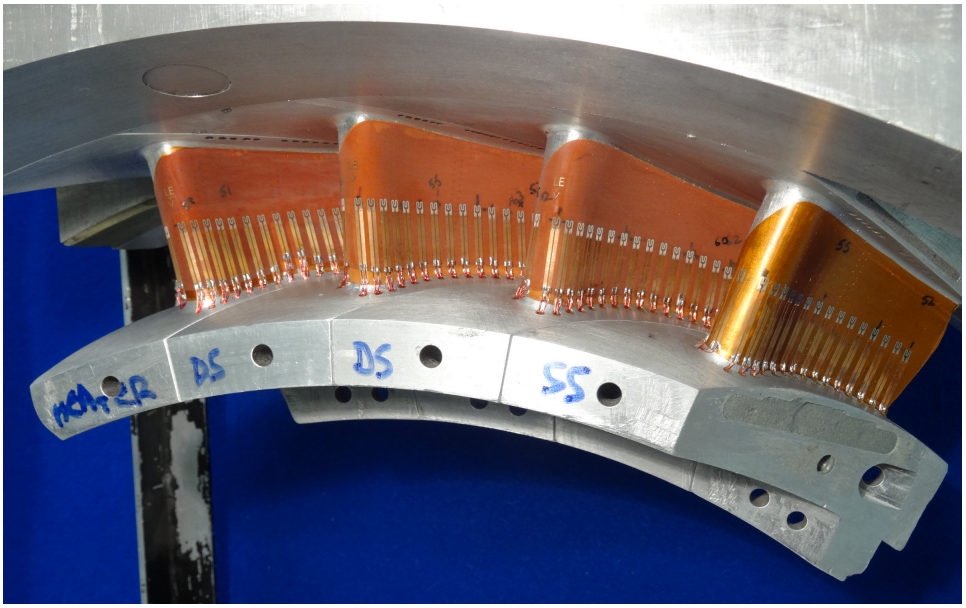

Figure 7.1: Fully instrumented cassette showing NGVs A to D (from right to left).

in section 7.2. Details on the instrumentation for this test campaign are given in section 7.3. The uncooled and cooled results are presented for each vane separately in sections 7.4 and 7.5.

The aim of these experiments is to demonstrate two measurement techniques to obtain the adiabatic wall temperature and the heat transfer coefficient on a cooled aerofoil in a short-duration wind tunnel under engine-realistic conditions. It is very difficult to separate these two parameters under these conditions and their accurate determination is of great interest for the engine design and optimisation.

7.1 Test conditions

The test conditions were those of the MT1 test turbine (see section 2.3). They are summarised in table 7.1. A typical inlet total temperature and total pressure trace is shown in figure 7.2. The stable run period is limited by the duration of constant inlet total pressure. During this period the Reynolds number is constant and the flow is considered aerodynamically stable, so that heat transfer measurements can be taken. By adjusting the opening of the plug valve a very flat inlet temperature profile is achieved (especially in comparison to older data from the OTRF, see for example (Qureshi, 2010)). A total of 49 runs were carried out and data recorded on a maximum of 160 channels at a time.

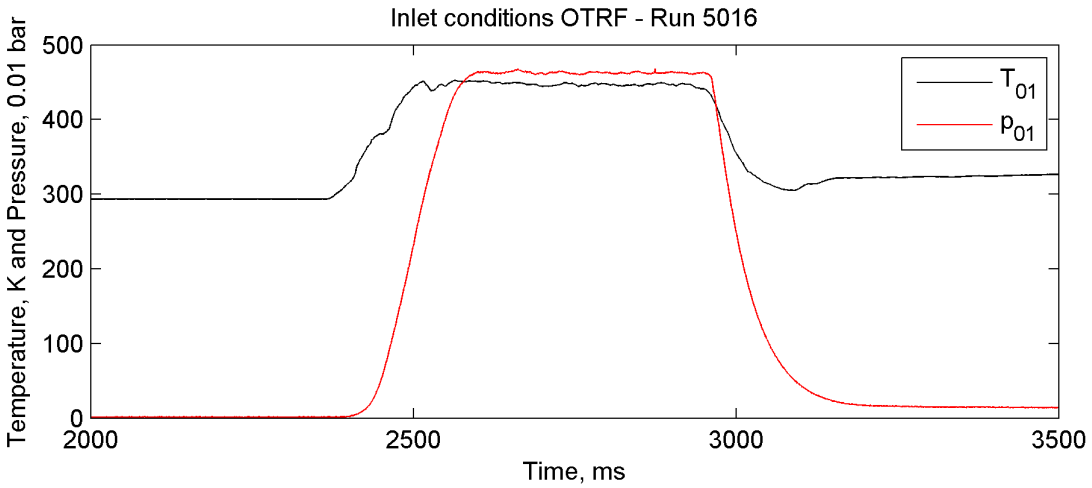

Figure 7.2: Inlet total temperature and total pressure for a typical OTRF run. Data is recorded from about 2.5 s prior to the run during spin-up.

Parameter	**Target**
Rotational speed n	$9500\,\mathrm{rpm}$
Inlet total temperature T_{01}	$444\,\mathrm{K}$
Inlet total pressure p_{01}	$4.6\,\mathrm{bar}$
Inlet mass flow rate $\dot{m}_1$	$17.4\,\mathrm{kg\,s^{-1}}$
Pressure ratio p_{01}/p_3	3.2
Gas-to-wall temperature ratio T_{01}/T_w	1.53
Capacity $\dot{m}_1\sqrt{T_{01}}/p_{01}$	$7.97 \cdot 10^{-4}\,\mathrm{kg\ s^{-1}\,K^{1/2}\,Pa^{-1}}$
Non-dimensional speed $n/\sqrt{T_{01}}$	$450.85\,\mathrm{rpm\,K^{-1/2}}$
Mach number at NGV exit	0.912
Reynolds number (based on NGV axial chord)	$1.61 \cdot 10^6$

Table 7.1: Operating point achieved in the OTRF.

The tests with cooled NGVs were conducted at the same conditions. The effect on the turbine work and capacity of two (partially) cooled NGVs in an annulus of 32 NGVs is considered negligible and a comparison of the stage pressures confirmed this (see figure 7.10).

7.2 Cooling configuration and coolant delivery

When performing a cooled experiment in a short-duration facility it is critical to deliver the coolant at the precise time at the required conditions. The cooling air has to start blowing before the main flow is released through the working section to achieve steady-state conditions during the run. For these tests, the coolant fluid was air, which was delivered from high-pressure bottles to the rig. A schematic of the cooling supply circuit is shown in figure 7.3. In order to avoid transients, the final section of the coolant delivery system was built very close to the rig and had a small dead volume.

An NGV pair is cross-fed and the coolant mass flow rate is monitored by a choked orifice in the coolant delivery system just upstream of the vanes. There are two separate feeds for the front and rear cavities, but in this set of experiments only the front cavity was blown.

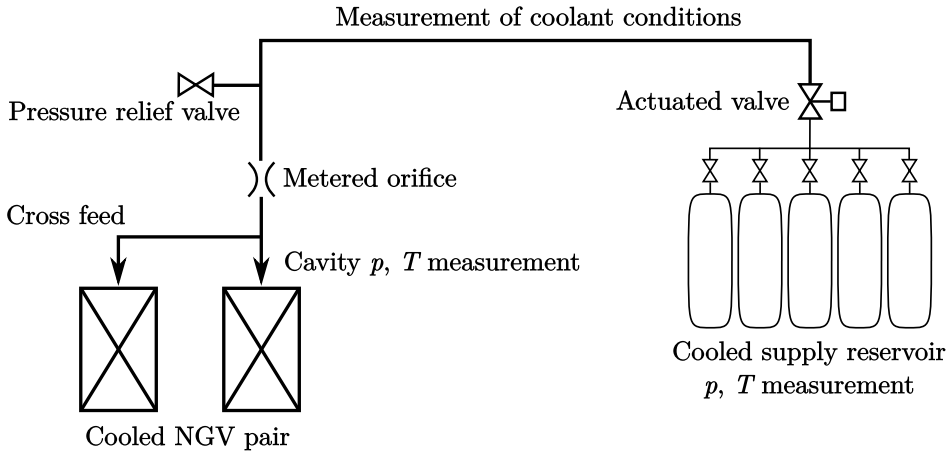

Figure 7.3: Schematic of the cooling supply circuit.

The cooling geometry was designed for the TATEF I Programme (Turbine Aero-Thermal External Flows) by SNECMA. The cooling configuration has engine-realistic hole geometries and operating conditions. The cooled NGVs have three rows of film cooling holes at the shower head. The actual design was limited by a set of manufacturing constraints, such as using cylindrical holes with realistic cooling hole inclination (50°), diameter (0.6 mm) and pitch (1.8 mm). The cooling holes were drilled on an iso-Mach line of the main flow, so that spanwise uniformity of the injected mass flow rate is achieved. No internal cooling elements have been included and due to manufacture limitations there are only two cylindrical cooling cavities. More information on the cooling geometry design is given in (Chana and Mole, 2000).

The mid-span cross section of a cooled NGV is depicted in figure 7.4. The front cavity feeds two rows of film cooling holes on the pressure side and a single row of film cooling holes on the suction side. The double rows on the pressure side are staggered with an axial separation of 1.56 mm. A photograph of an instrumented cooled NGV is shown in figure 7.5. The gauges were sputtered onto a Kapton sheet which was glued to the test surface. As it is not possible to wrap the Kapton around the cooled aerofoil, there will be a surface step on the cooled NGV just after the row of film cooling holes. For the double-sided gauges the size and thus the impact of the surface step on the cooling jet can be minimised by staggering the Kapton layers that make up the gauge (up to three layers for the double-sided gauges with an underside thin film heater). Future cooled NGVs will have a pocket machined in the surface to fit the gauges.

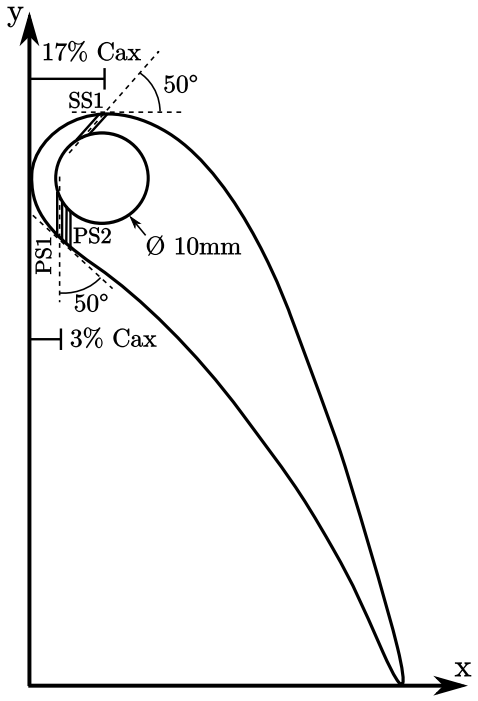

Figure 7.4: Mid-span cross section of a cooled NGV.

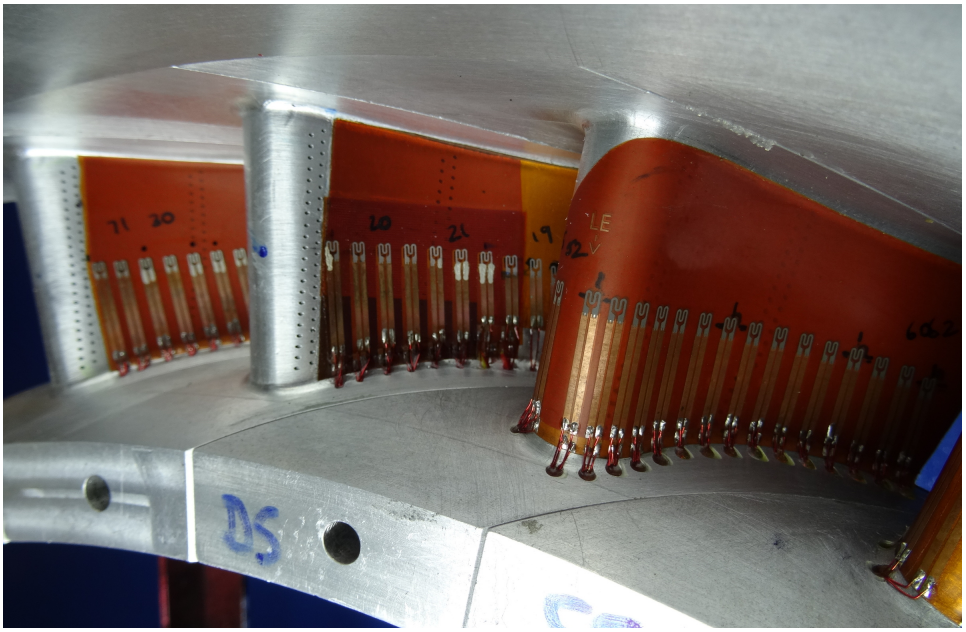

Figure 7.5: Fully instrumented cassette with two cooled HP NGVs instrumented with double-sided thin film gauges.

The film cooling can be described by three parameters:

$$\text{Density ratio DR} = \frac{\rho_{\text{inj}}}{\rho_\infty} \,, \tag{7.1}$$

$$\text{Blowing ratio BR} = \frac{\rho_{\text{inj}}\, u_{\text{inj}}}{\rho_\infty\, u_\infty} \,, \tag{7.2}$$

$$\text{Momentum flux ratio MFR} = \frac{\rho_{\text{inj}}\, u_{\text{inj}}^2}{\rho_\infty\, u_\infty^2} \,, \tag{7.3}$$

where ρ_{inj}, u_{inj} are the density and velocity of the coolant jet at the point of injection and ρ_∞, u_∞ correspond to the local mainstream. The experiments were run at one blowing rate.

The mass flow rate is metered by a choked nozzle and can be calculated as

$$\dot{m} = A\, C_{\text{d}}\, p_0 \sqrt{\frac{\gamma}{R\, T_0}} \left(\frac{2}{\gamma+1}\right)^{\frac{\gamma+1}{2(\gamma-1)}} \tag{7.4}$$

from the throat area A, the inlet pressure and temperature p_0 and T_0 and the discharge coefficient of the nozzle C_{d}, which had previously been calibrated.

The coolant conditions are summarised in table 7.2. The coolant is delivered at a pressure of 30 bar. To calculate the flow variables at the hole exit location the isentropic flow equations have been used. Figure 7.6 shows the isentropic Mach number distribution for an MT1 HP NGV. The mainstream has an isentropic Mach number of about 0.07 at the hole exit location on the pressure side. At the location of the suction side cooling holes, the isentropic Mach number is approximately 0.52. The total coolant pressure at the cavity inlet is obtained from a static pressure measurement in the coolant feed with an estimation of the head loss using Darcy's equation (Howatson et al., 2009).

In the OTRF, the coolant fluid is air at ambient temperature, which gives a density ratio of 1.7. In real engines the film cooling flows are cooler and density ratios of 2.0 are achieved (Han et al., 2012). The coolant-to-mainstream temperature ratio cannot be matched unless the coolant is refrigerated.[1] Similarly, an engine realistic density ratio can only be achieved using a foreign gas with a greater density as a coolant, but the same ratio of specific heats as air. Both options cannot be easily implemented in the OTRF and the focus was set on achieving engine-realistic blowing and momentum flux ratios.

[1] The temperature of the mainstream could be increased, but then the run time would be reduced.

Parameter	Current test campaign	TATEF I Programme
Pressure, bar	5.99	6.28
Mass flow rate, g s^{-1}	26.6	20.0
Temperature ratio	1.53	1.55
Density ratio	1.68	1.75
Blowing ratio	11.8 (PS) and 2.07 (SS)	9.20 (PS) and 2.04 (SS)
Momentum flux ratio	82.4 (PS) and 2.55 (SS)	48.0 (PS) and 2.35 (SS)

Table 7.2: Comparison of coolant conditions in the current test campaign with those of the TATEF I Programme (Chana and Mole, 2000).

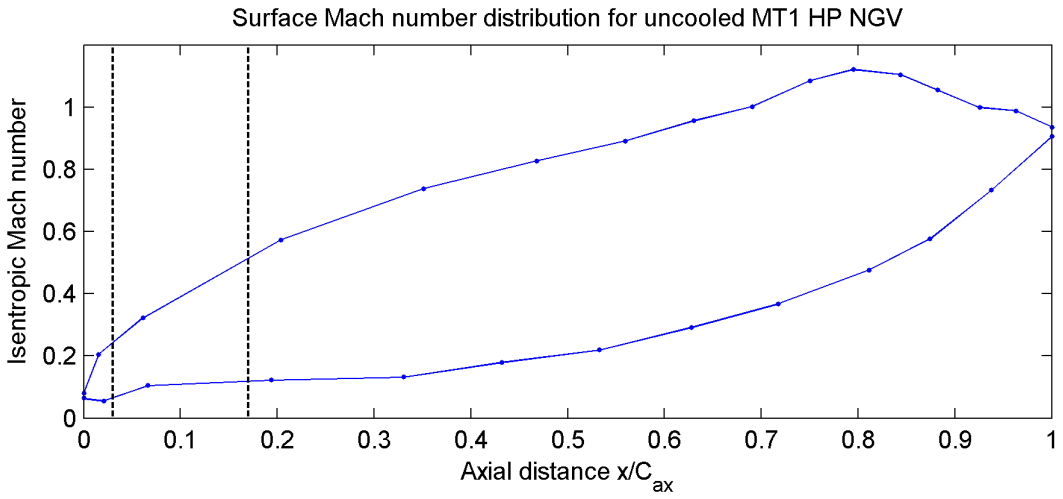

Figure 7.6: Isentropic Mach number distribution over axial distance at 50% span. The dashed lines mark the location of the cooling holes at 3% C_{ax} on the pressure side and at 17% C_{ax} on the suction side.

The aim of this set of experiments was to match the conditions of the original test campaign within the TATEF I programme. There is good agreement in the coolant delivery conditions as well as in the temperature and density ratios. The differences in the blowing and momentum flux ratio on the pressure side are due to the use of an averaged isentropic Mach number between the two film cooling rows on the pressure side in the present work. Furthermore, the values are well within the limits defined for this vane geometry (see (Hilditch et al., 1996)). On the suction side the blowing and momentum flux ratio agree very well.

7.3 Instrumentation

Six NGVs were instrumented with up to 30 gauges at 50% span. There were a total of 296 gauges across the six vanes. NGVs A and B were uncooled. They were instrumented with single-sided and double-sided thin film gauges respectively. NGVs C and D were tested first uncooled and then cooled. They were instrumented with double-sided gauges with an underside thin film heater and with self-heating double-sided gauges. All insulating layers had a thickness of approximately 100 µm and were measured during the instrumentation process. The design of the heater element and an instrumented (uncooled) NGV with a heater are shown in figures 7.7 and 7.8. The total area of the heater on the pressure side was 500 mm^2. The heater on the suction side had an area of 580 mm^2. Their respective resistances were 7.9 Ω and 9.2 Ω. The location and numbering of the thin film gauges on an uncooled HP NGV aerofoil are depicted in figure 7.9. The number of gauges was reduced slightly for the cooled aerofoils.

The gauges were manufactured in different batches and had resistances ranging from 25 Ω to 65 Ω. The gauge resistance in one batch usually varied around 5 Ω, but in some cases the differences within one batch were higher. The gauge resistance was recorded on each day of testing and served to exclude gauges which had a difference greater than 5% from the previous measurement. The temperature coefficient of resistance ranged between $1–1.25 \cdot 10^{-3}\,\mathrm{K}^{-1}$ and had a variation within each batch again of around 4%.

The heat transfer measurements on the NGV aerofoils were complemented with a set of pressure and temperature measurements to monitor the run conditions.

7.3.1 Tunnel and stage monitoring

The inlet and exit static pressures, NGV and rotor exit (casing and hub) static pressures as well as the NGV static pressure at 50% span and rotor casing static pressures were monitored with absolute pressure transducers (Sensor Technics CTE8000). Figure 7.10 shows typical results for an uncooled and a cooled run. A thermocouple rake is used to measure the temperature at the inlet to the turbine stage. The temperature of the cassette with instrumented NGVs was recorded with four thermocouples.

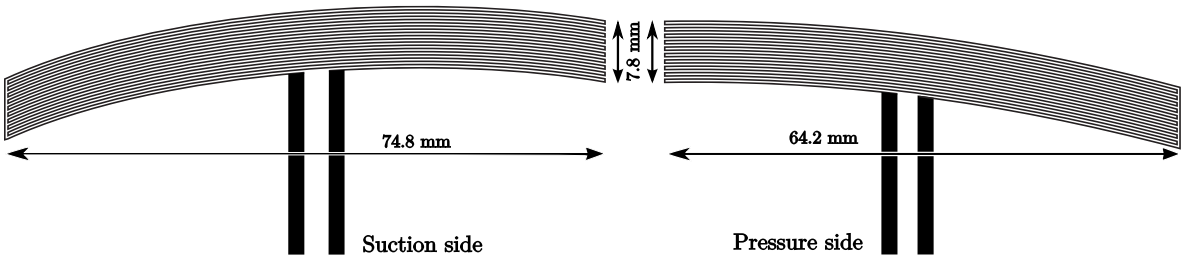

Figure 7.7: The heater design for the suction and pressure sides of the uncooled HP NGV is aligned with the gauge location at 50% span (see section 5.2 for details).

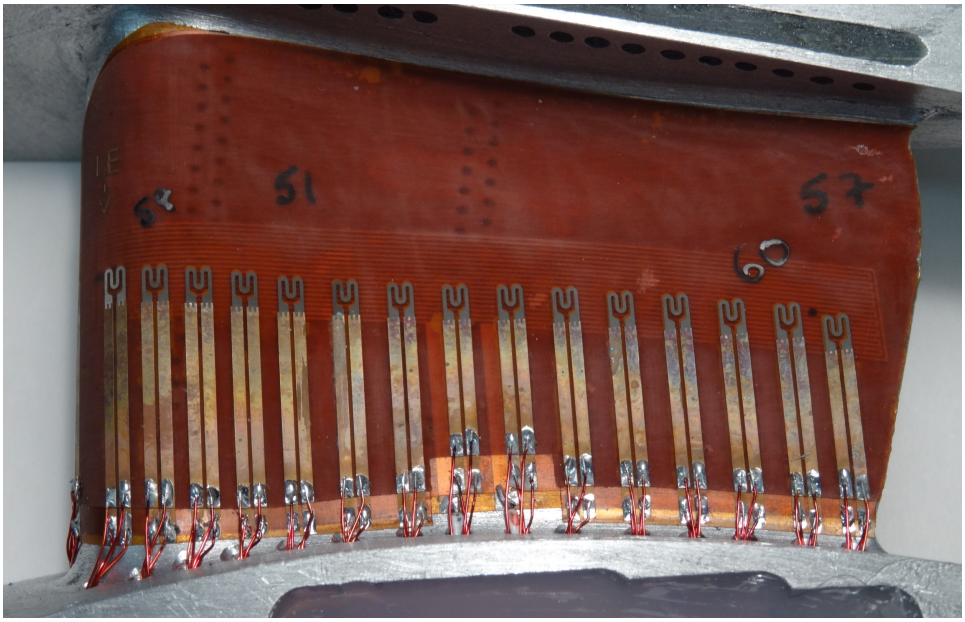

Figure 7.8: Uncooled HP NGV instrumented with double-sided thin film gauges with an underside thin film heater.

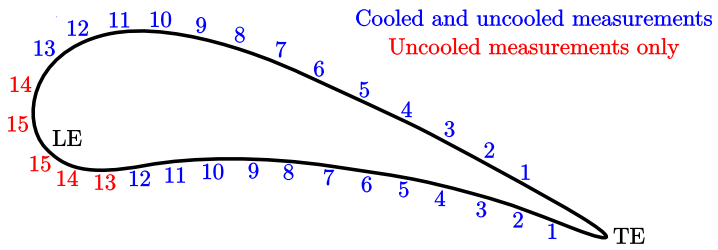

Figure 7.9: Location and numbering of thin film gauges on an uncooled HP NGV.

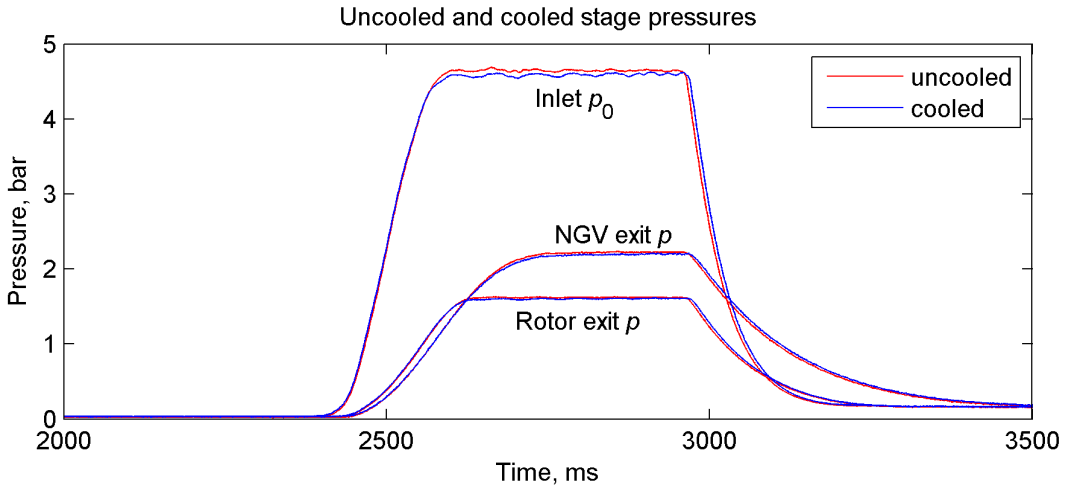

Figure 7.10: Pressures through the MT1 turbine stage.

7.3.2 Coolant supply conditions

The instrumentation of the coolant delivery system consisted of a measurement of the pressure of the coolant gas at the reservoir (at the high-pressure bottles and after the actuated valve, see figure 7.3), two temperature measurements upstream of the metered orifice and one pressure tapping and two temperature measurements at the front cavity inlet. As the velocity downstream of the orifice is low ($M < 0.3$), the losses in the cross-feed are low, and it can be assumed that the coolant delivery conditions are the same for both NGVs.

Typical coolant pressure and temperature traces are shown in figure 7.11. In the following plots 0 s correspond to the moment at which stable pressure conditions are achieved. The coolant starts blowing approximately 1 s before the run. The compression of the air in the coolant supply system causes a spike in cavity temperature, but the heat quickly dissipates and the coolant is delivered at constant temperature during the run. The two upstream thermocouples agree very well. The K-type thermocouple downstream of the orifice (TC 1) shows good response, but there is pickup which could be caused by the bead being intermittently earthed or partially earthed. This measurement is complemented by a shielded thermocouple (TC 2), which is very damped, but drifts down to the TC 1 measurement during the stable part of the run to a very good level of accuracy (within 2.3 K).

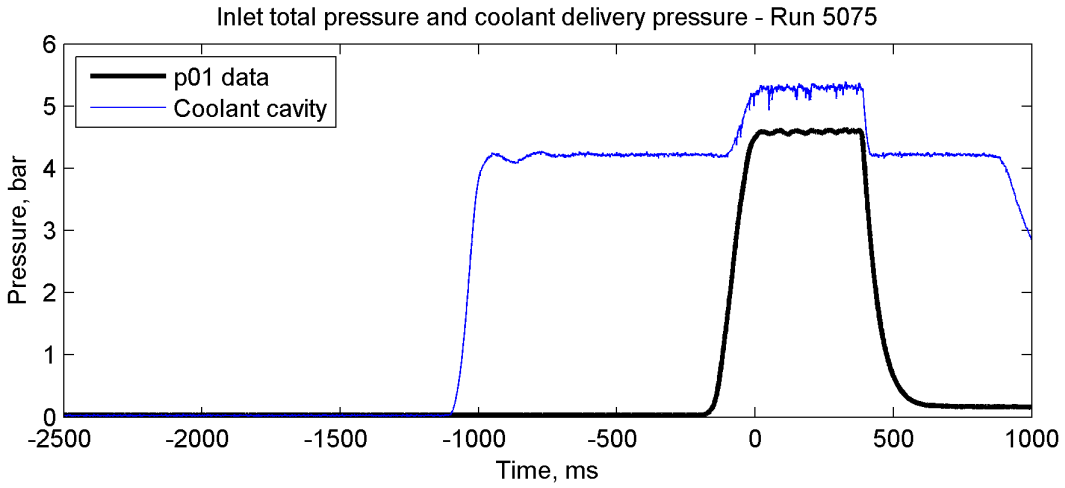

(a) Static pressure measured in the coolant feed cavity.

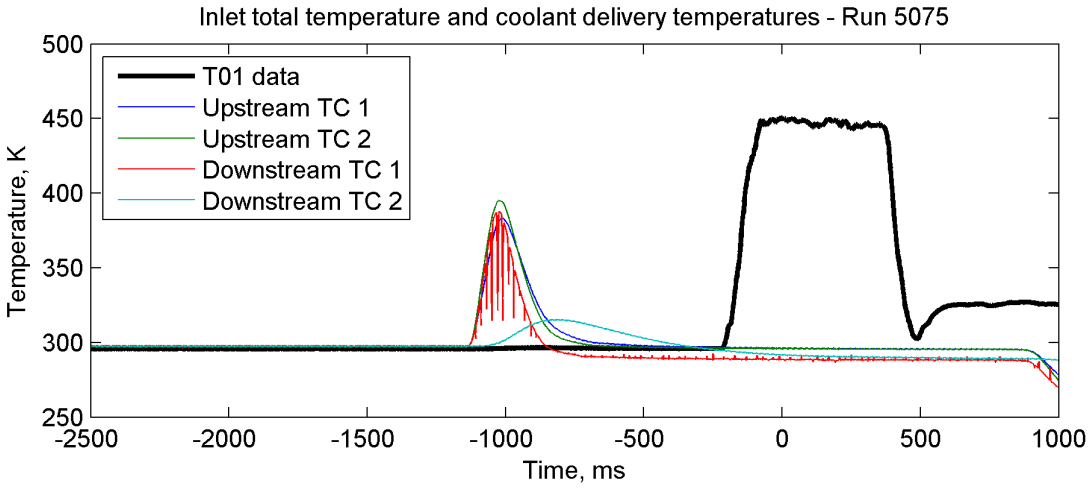

(b) The coolant delivery temperatures are measured upstream and downstream of the feed nozzle.

Figure 7.11: Typical pressure and temperature traces for cooled tests.

The temperature measured by the downstream thermocouples is around 7 K lower than the upstream measurement. The temperature change of a gas on adiabatic expansion is described by the Joule-Thomson coefficient μ_{JT}:

$$\mu_{\mathrm{JT}} = \left(\frac{\partial T}{\partial p}\right)_h . \tag{7.5}$$

The Joule-Thomson coefficient is 2.1789 K MPa^{-1} for the given temperature and pressure before the expansion (Green and Perry, 2007). For the pressure ratio across the feed nozzle, the expected drop in temperature is 5.4 K, which corresponds very well to the experimental results.

7.3.3 Data acquisition

The HTA3 thin film signal conditioning amplifier is used to power the thin film gauges and to record the heat transfer signal (see section 5.4). Each HTA3 has an DC output and a AC output. It is desirable to use the voltage trace from the AC output, as it has a much better signal-to-noise ratio (Oldfield and Beard, 2014). However, for tests with heated gauges the DC offset data is necessary to determine the gauge temperatures at the start of the run. The DC offset and AC voltage trace can be combined to give the temperature traces that have been shown in chapter 6. When testing the fully instrumented cassette the data acquisition was limited by the number of available channels. For this reason the acquisition of DC data was prioritised and AC data was acquired only on a number of selected channels. A comparison of the temperature traces obtained from the DC and AC outputs is shown in figure 7.12 for a double-sided thin film gauge (NGV B PS8).

As can be seen, the temperature traces from the DC output are much noisier, because of the lower signal-to-noise ration of the amplifier. It would hence be preferable to use the AC data for all runs, but for this particular gauge only two AC runs are available, while the left panel shows the results for eight DC runs. It is nevertheless possible to use the DC data if the temperature traces are filtered. A fast Fourier transform (FFT) of the data was performed

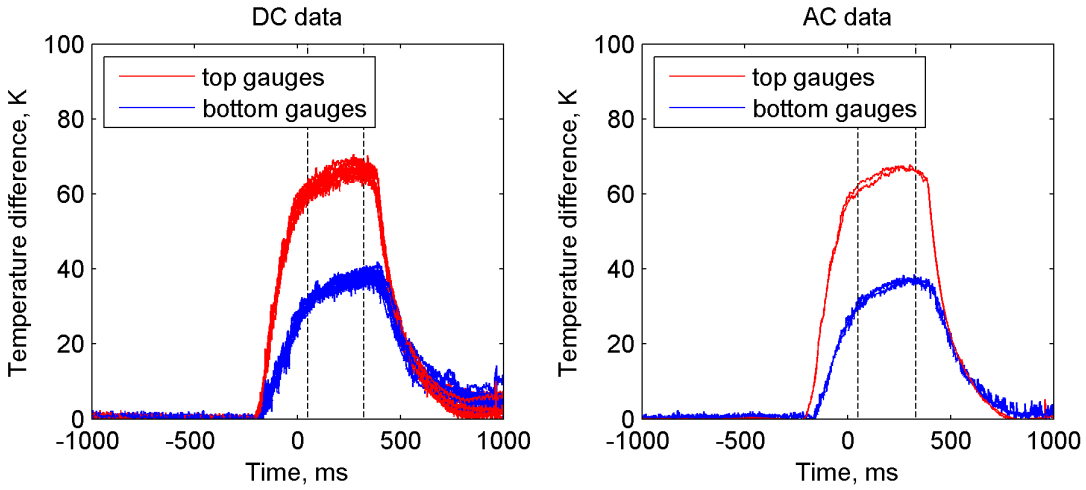

Figure 7.12: Comparison of the temperature traces obtained using data from the AC output or data from the DC output of the HTA3 thin film signal conditioning amplifier.

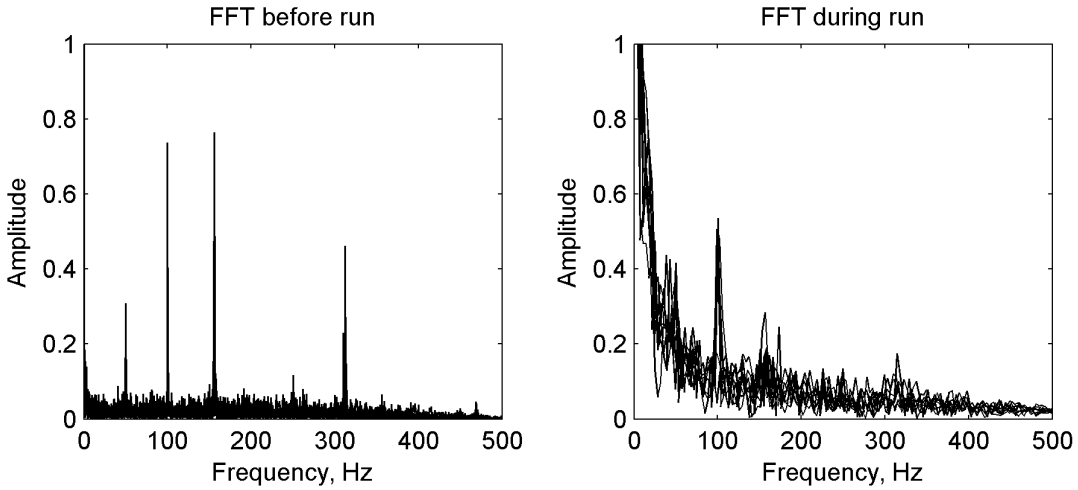

Figure 7.13: Characteristic amplitude spectrum of the DC data from double-sided gauges.

to find the frequency components of the noise (see figure 7.13). In the frequency domain the main noise frequencies are clearly identified. The amplitude before the run (left panel) peaks at 50 Hz, 100 Hz, 150 Hz and 300 Hz, which are all multiples of the 50 Hz power supply. During the run (in the stable run period), the low frequency region is predominant, but the peaks are still visible (right panel). The FFT results were identical for the top and bottom gauges. When filtering data it is important to maintain the general shape of the signal. The correct behaviour of the filter was verified by applying it to the DC and AC data. Figure 7.14 shows the results of filtering the DC and AC data with a low-pass filter at 45 Hz. The filtered data agrees very well with the original data and there is good agreement between the DC and AC data.

In this chapter the results of the DC data will be presented, because given the reduced number of AC runs, good AC data is only available for a small fraction of the gauges. If required the temperature traces can be filtered using the method described above.

7.4 Uncooled results

The analysis of the data from uncooled NGVs is based on the work presented in chapter 5 on the casing measurements. The four gauge types investigated are presented separately. NGV A was instrumented with single-sided thin film gauges, NGV B was instrumented with double-sided thin film gauges, NGV C was instrumented with self-heating double-sided thin film gauges

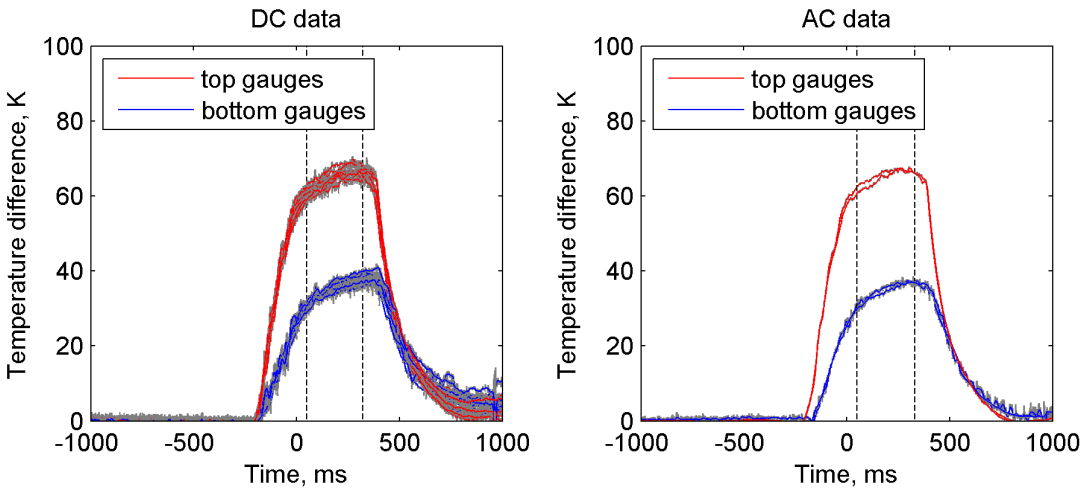

Figure 7.14: Filtered temperature traces using a low-pass filter.

and NGV D was instrumented with double-sided thin film gauges with an underside thin film heater. 28 uncooled runs were conducted. To allow a comparison of measurement techniques, measurements were taken on at least two vanes on identical sides (pressure or suction side). The data acquisition continued on uncooled NGVs A and B after swapping NGVs C and D for their cooled counterparts.

7.4.1 Single-sided thin film gauges

The configuration and principle of operation of the single-sided thin film gauges has been discussed in chapter 5. The gauges were sputtered onto an insulating layer, which was wrapped around the aerofoil. While all gauges calibrated well, the single-sided gauges on the pressure side of NGV A gave unphysical and inconsistent results after installation, so that the possibility must be considered that the gauges were damaged during this process, although no visible signs of damage could be observed. Fortunately, the gauges on the suction side were not affected by this issue.

Typical temperature traces for the singles-sided thin film gauges on the suction side are shown in figure 7.15 for gauges 4 and 12. As for the casing tests, it is assumed that the rig is still at isothermal conditions just prior to the run and the voltage at the start of the run is used as the reference value corresponding to the temperature measurement from the cassette thermocouples.

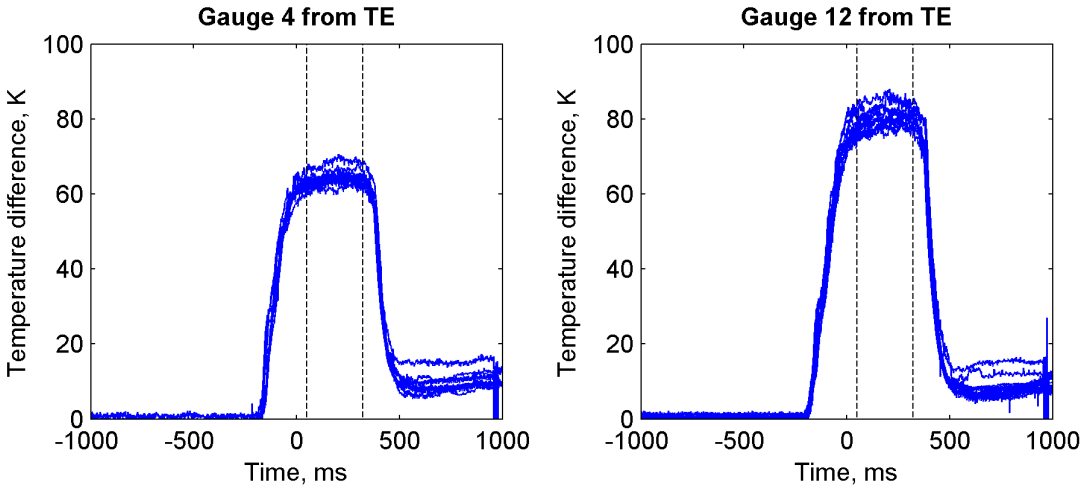

Figure 7.15: Temperature traces for two single-sided thin film gauges on the NGV A **suction side**. The results for eleven runs are overlapped in this plot. The dashed lines mark a typical stable period used for the regression of one run

The temperature profile for the single-sided gauges is very flat – less than 5 K temperature increase were recorded during the stable run time. The total temperature rise is around 80 K. A higher temperature is achieved at gauge 12 near the vane leading edge, which corresponds to a higher heat flux. Overall the run-to-run agreement is very good with a maximum variation of 10 K. The temperature spread at the end of the run (from 500 ms onwards) is caused by the combination of uncooled and cooled runs – NGV A is not cooled, but when cooling air is introduced in NGVs C and D the drop in temperature is noticeable.

Figure 7.16 shows the heat flux traces obtained from the temperature traces using the impulse response method.[1] The gauge 12 near to the leading edge (right plot) has a higher heat flux, as expected from the raw temperature data. Finally, figure 7.17 shows the heat flux versus the wall temperature. Even though the run-to-run agreement is good, it is necessary to make an assumption on the recovery temperature to obtain the heat transfer coefficient at both gauge locations. The recovery temperature was calculated following equation 6.1 from the static temperature and isentropic Mach number at the gauge location (see figures 7.6 and 7.9). A recovery factor of $Pr^{1/3}$ for a turbulent boundary layer was assumed. The heat transfer

[1]The noise level can be considerably reduced by filtering the temperature traces as described in section 7.3, but it was not deemed necessary, as the single-sided gauges were not further investigated.

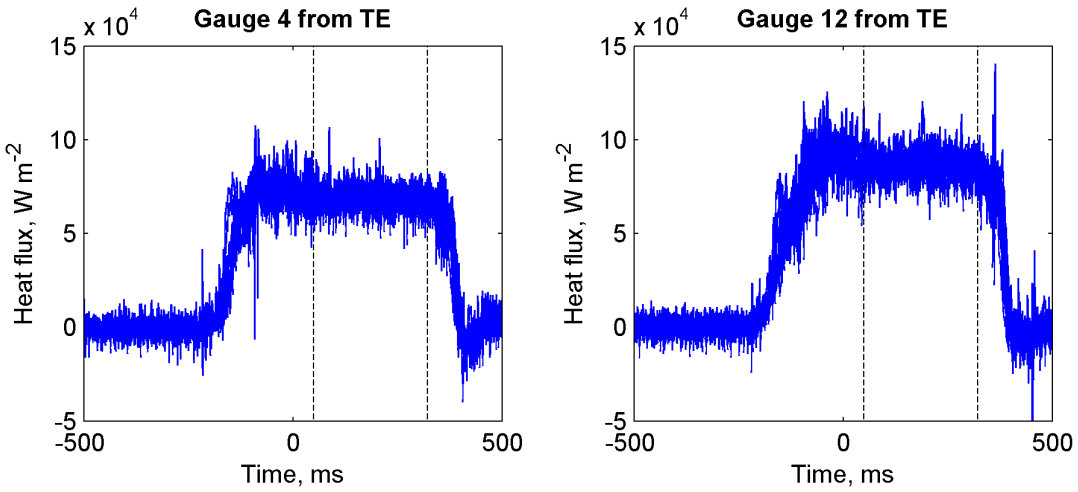

Figure 7.16: Heat flux for two single-sided thin film gauges on the NGV A **suction side**. The dashed lines mark a typical stable period used for the regression of one run.

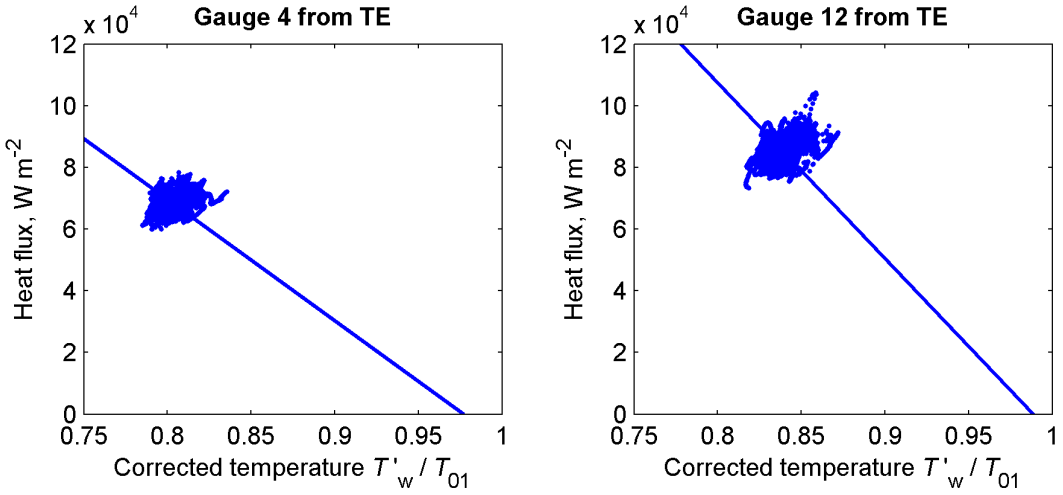

Figure 7.17: Regression data for two single-sided thin film gauges. The regression is performed on data from the stable run period.

coefficient is much larger for gauge 12 closest to the leading edge of the vane (right plot).

In conclusion, it is possible to obtain the heat transfer coefficient from the single-sided thin film gauges if a recovery temperature is assumed. However, for the chosen thickness of the gauge substrate the range of the regression is very small and the uncertainty in the heat transfer coefficient is very large. Given the poor performance of the single-sided gauges on the pressure side and the low quality of the regression on the suction side, the Nusselt number distribution is not presented.

7.4.2 Double-sided thin film gauges

On all 49 runs data was taken with unheated double-sided thin film gauges on NGV B as a comparison for the heated gauges. The unheated double-sided gauges were processed in the same way as the single-sided gauges, i.e. with the same pre-run isothermal assumptions. As the gauge package is thicker, the gauges are expected to achieve a larger temperature increase during the run and thus a better regression. Runs with unphysical results are left out from the post-processing. The bottom gauges were more frequently affected by issues like resistance variability giving unreliable data, which points to sensitivities in the copper-platinum contacts. Other reasons to exclude runs relate to the quality of the run, for example plug valve oscillations or temperature variations.

The temperature traces for four double-sided gauges on the pressure side of NGV B are shown in figure 7.18. These traces were obtained from filtered DC data (see section 7.3). As the distance to the leading edge decreases the surface temperature first decreases and then strongly increases. A similar phenomenon is observed on the suction side (see figure 7.19). Gauges 6 and 7 on the suction side see the highest surface temperature. The temperature plot for gauge 14 also includes data acquired with neighbouring cooled vanes (NGVs C and D). NGV C was the neighbouring vane such that its pressure side was adjacent to the suction side of NGV B. The effect of the coolant lowering the post-run temperature of gauge 14 is visible at the end of the run. On the gauges nearer the trailing edge a larger effect of the coolant was observed before the run (not shown). The heat flux traces corresponding to the temperature traces measured on the pressure side are shown in figure 7.20. The heat flux is highest at the gauge closest to the leading edge, which is also the gauge with the greatest temperature variations. The heat transfer rates on the suction side show similar behaviour.

The regression of the heat flux against wall temperature is shown in figures 7.21 and 7.22 for the pressure and suction side gauges respectively. As for the single-sided thin film gauges the regression is forced through a known recovery temperature which is obtained from the static temperature and isentropic Mach number at the surface (see equation 6.1). The heat transfer coefficient decreases from gauge 2 to 9 on the pressure side and then steadily increases. On the

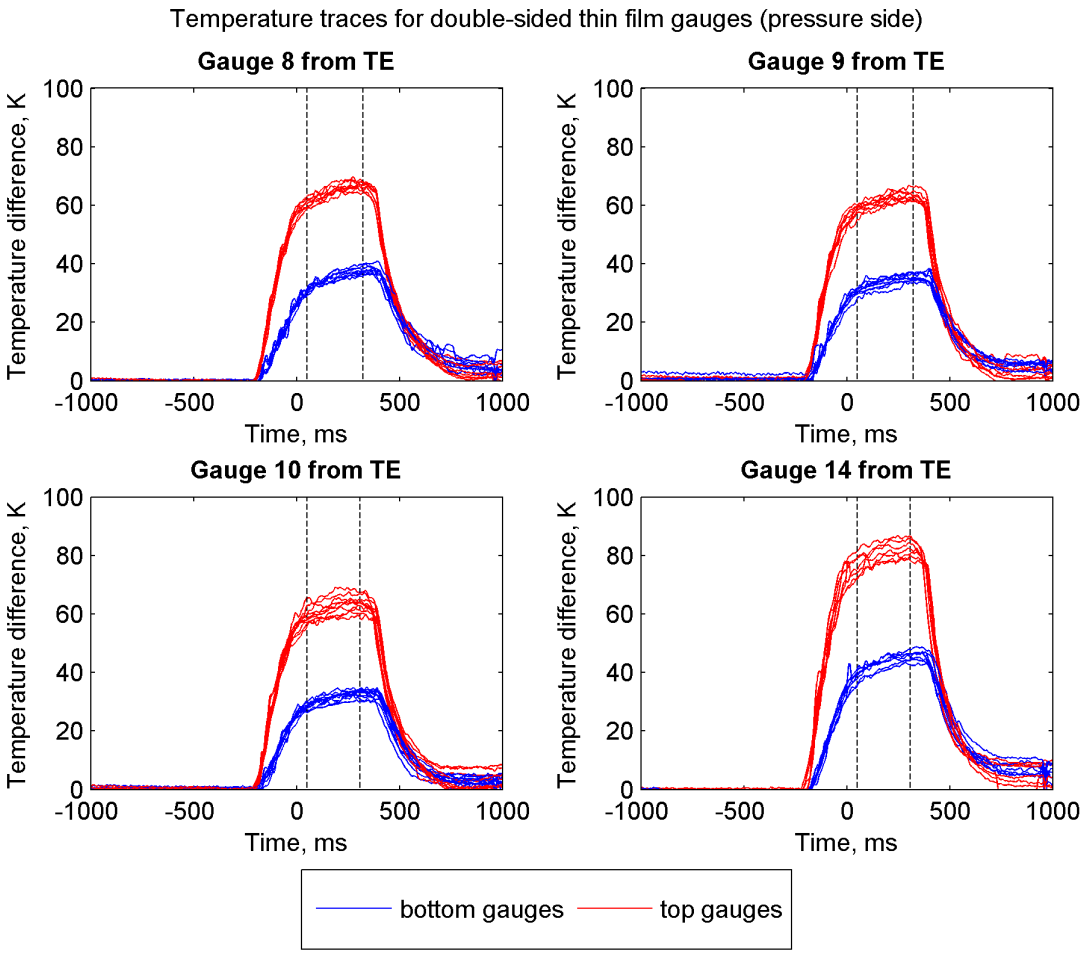

Figure 7.18: Temperature traces for four double-sided thin film gauges on the NGV B **pressure side**. The results for up to ten runs are shown. The dashed lines mark a typical stable period used for the regression of one run.

suction side the heat transfer rates are larger than on the pressure side and peak at gauges 5 to 7. Gauges 6 and 7 show nearly identical results. The heat flux then reaches a local minimum and rises towards the leading edge.

The heat transfer results are summarised in figure 7.23 in terms of a distribution of the Nusselt number over the surface distance. The conductivity of air is calculated at the inlet total temperature (Oldfield and Guo, 1997) and the characteristic length is the NGV true chord. The trend corresponds to that of the heat flux discussed above. The leading edge heat transfer is given by gauge 15 on the pressure side at a surface distance of 0 mm. The heat transfer distribution from the double-sided gauges is compared to that obtained using single-sided gauges

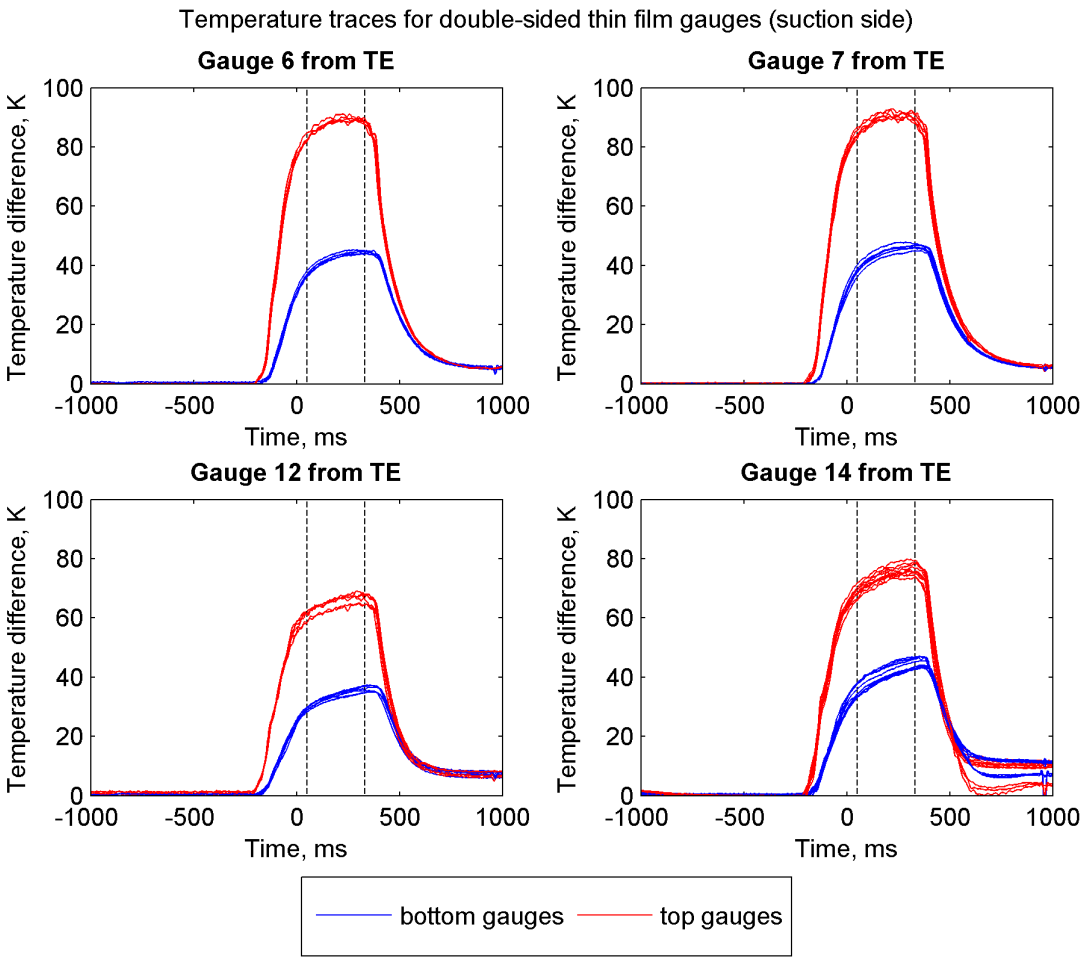

Figure 7.19: Temperature traces for four double-sided thin film gauges on the NGV B **suction side**. The results for up to ten runs are shown. The dashed lines mark a typical stable period used for the regression of one run.

during the TATEF I test campaign (Chana and Mole, 2000). Both sets of data capture the same trend well, but the new gauges tend to show lower Nusselt numbers compared to previous data.

In summary, double-sided thin film gauges have been used to obtain Nusselt number distributions over the aerofoil chord. Given the thicker substrate layer the range for the regression is larger than for the single-sided gauges, but most importantly double-sided gauges do not require to make an assumption on the heat conduction into the wall and can thus be used on cooled aerofoil walls. The range of the regression has to be further increased to be able to separate the adiabatic wall temperature and the heat transfer coefficient, as the next section will show.

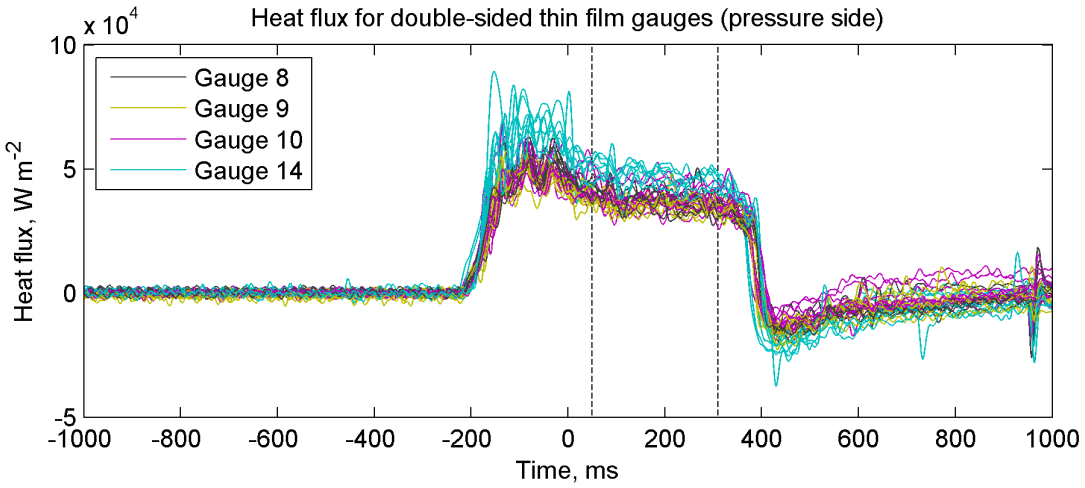

Figure 7.20: Heat flux for four double-sided thin film gauges on the NGV B. The dashed lines mark a typical stable period used for the regression of one run and one gauge.

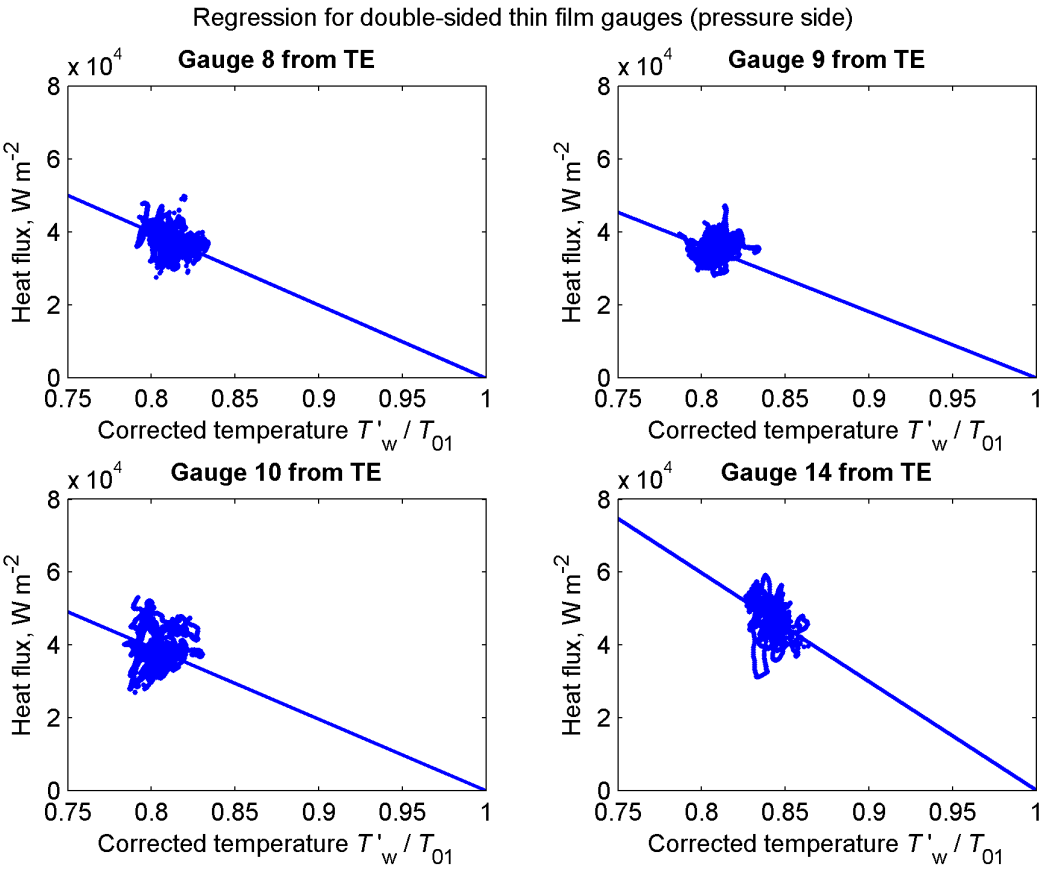

Figure 7.21: Regression data for four double-sided thin film gauges on the NGV B **pressure side**. The regression is performed on data from the stable run period.

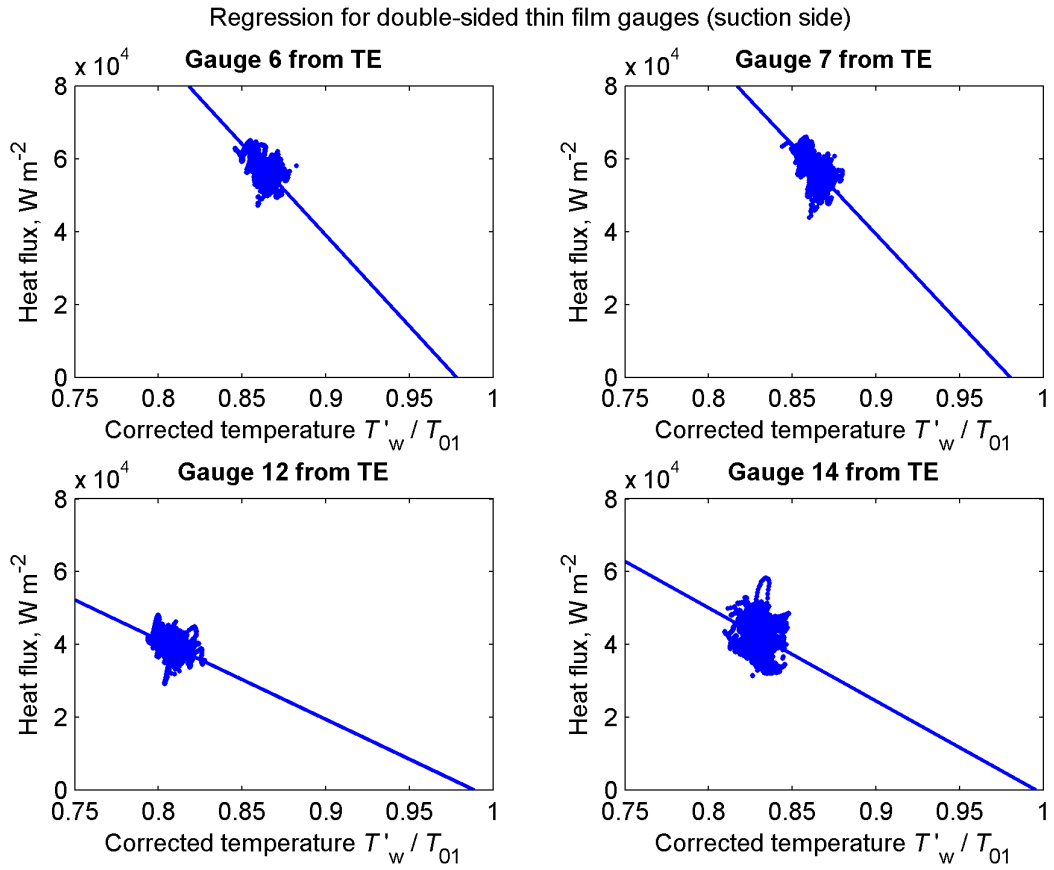

Figure 7.22: Regression data for four double-sided thin film gauges on the NGV B **suction side**. The regression is performed on data from the stable run period.

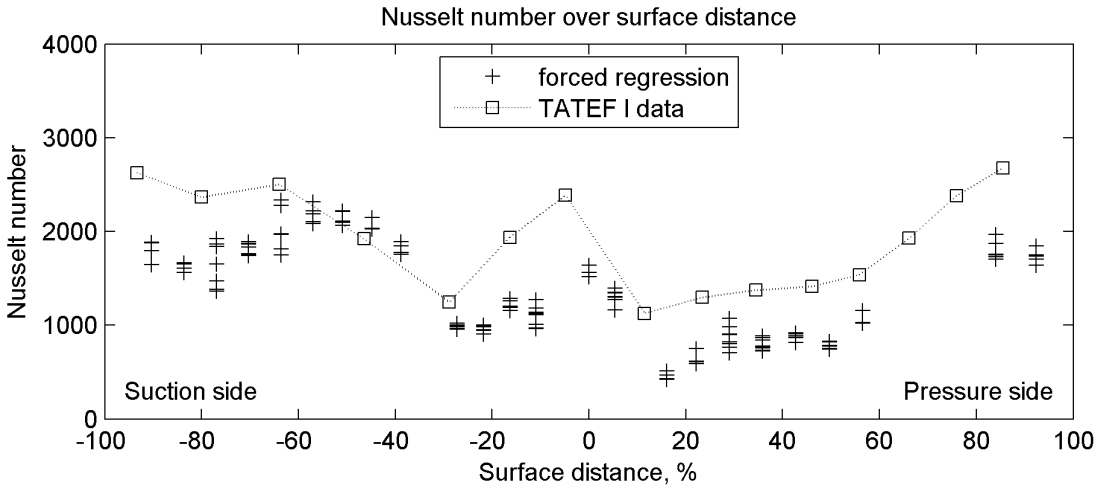

Figure 7.23: Nusselt number plotted against surface distance from the NGV leading edge for unheated double-sided thin film gauges. The current results are compared to data from TATEF I.

7.4.3 Double-sided thin film gauges with an underside thin film heater

The double-sided thin film gauges with an underside heater element on NGV D were tested over a range of heater currents from 0 A to 2.0 A (see table 7.3). The data was acquired in different test runs for the pressure and suction sides. The maximum heater current was lower for the tests measuring the heat transfer on the suction side, as the temperature range achieved during the stable part of the run was deemed large enough for an accurate regression. The maximum heating heat flux was 63 kW m^{-2} on the pressure side and 41 kW m^{-2} on the suction side. Before the analysis of the results is presented, it is important to understand in detail the effect of the heating. For the single-sided and unheated double-sided gauges the assumption has been made that the rig is still at isothermal conditions just prior to the run after taking into consideration all possible effects. For the heated gauges the underlying assumptions need to be revisited.

In principle the advantage of double-sided thin film gauges with an underside thin film heater

	Heater current	**Number of runs**
Pressure side	unheated	4
	0.4 A	1
	0.8 A	1
	1.2 A	4
	1.6 A	2
	2.0 A	2
Suction side	unheated	2
	0.4 A	1
	0.8 A	3
	1.2 A	2
	1.6 A	2

Table 7.3: Heater settings for double-sided thin film gauges with an underside thin film heater.

compared to self-heating gauges is the possibility to measure directly the surface temperature during heating, as the gauge current is unchanged. However, there is a spread in the top gauge temperatures measured at the start of the run, which does not appear to be physical. In particular, for some gauges the top gauge temperature is higher than the bottom gauge temperature in spite of the heater being placed underneath the bottom gauge.[1] Similar temperature variations were observed for the unheated gauges in the casing tests in chapter 6, where the issue was solved by assuming isothermal conditions at the start of the run. In analogy it is desirable to develop a model that can predict the top gauge temperature in terms of the bottom gauge temperature and the heating power. Such a model will be discussed next and compared to experimental data.

Substrate preheating using a heater element

The preheating temperature of the substrate of a double-sided thin film gauge on a heating element can be calculated from the heat flux from the heating element, which is given by the voltage and current across the heater (see also section 5.5). A schematic of a double-sided thin film gauge on a heating element is depicted in figure 5.3a. The heat flux can be described using Fourier's law of thermal conduction as the heat dissipated into the substrate and into the wall

$$\dot{q}_{\mathrm{H}} = k\frac{T_{\mathrm{H}} - T_{\mathrm{g2}}}{x_2} + k\frac{T_{\mathrm{H}} - T_{\mathrm{w}}}{x_3} \,, \tag{7.6}$$

where k is the conductivity of the substrate layer. T_{H} is the temperature of the heater, T_{g2} is the temperature of the bottom gauge and T_{w} is the temperature of the aerofoil wall. x_2 and x_3 are the thicknesses of the corresponding insulating layers. The heat flux through both top insulating layers is assumed to be constant and lateral conduction effects are neglected (as the heater heats evenly over the chord length of the aerofoil):

$$k\frac{T_{\mathrm{g2}} - T_{\mathrm{g1}}}{x_1} = k\frac{T_{\mathrm{H}} - T_{\mathrm{g2}}}{x_2} \tag{7.7}$$

with the distance between the top and bottom gauges x_1.

[1] An obvious explanation would be an instability in the constant current supply in the time between taking the reference measurement and the start of the run. This possibility was disregarded, as a stability check of the current supply gave very constant results (see figure 6.5).

Before the start of the run, the preheated substrate may lose heat into the working section by convection and radiation, potentially cooling the top gauge relative to the bottom gauge. The total power radiated by a black body per unit area is $E = \sigma T^4$ with the Stefan-Boltzmann constant $\sigma = 5.67 \cdot 10^{-8}\,\mathrm{Wm^{-2}K^{-4}}$. For the maximum allowable preheating temperature difference of 100 K, the radiative effect is $1.3\,\mathrm{kW\,m^{-2}}$, which is only about 3% of the heating power, not accounting for the reduced radiation due to the lower emissivity of the surface.

The heat transfer rate into the working section due to natural convection is a function of the convective heat transfer coefficient h and the temperature difference between the gauge surface T_{g1} and the rig temperature $T_\infty = 290\,\mathrm{K}$ at the start of the run:

$$\dot{q}_{\mathrm{conv}} = h(T_{\mathrm{g1}} - T_\infty) = k\frac{T_{\mathrm{g2}} - T_{\mathrm{g1}}}{x_1}\ . \tag{7.8}$$

The heat transfer coefficient before the run can be obtained from a correlation for the Nusselt number for a surface in natural convection. The Nusselt number can be expressed as a function of Grashof number and Prandtl number (see equation 5.36). When calculating the Grashof number, however, the reduced kinematic viscosity due to the reduced rig pressure before the run (approximately 10 mbar) has to be taken into account, which implies $\mathrm{Gr} \propto p^2$. As a result, the Nusselt number is expected to be proportional to $p^{1/2}$–$p^{2/3}$. Since the pressure during preheating is of order 10 mbar, the resulting Nusselt numbers are very small (typically $\mathrm{Nu} \approx 1$) and hence natural convection gives a negligible heat loss. It is to be expected that these arguments underpredict the Nusselt number, as they only consider natural convection effects. With the rotor being spun up to 9500 rpm in near vacuum before the run, forced convection will also occur and may give an additional contribution to the heat flux from the surface into the working section.

Nevertheless, heat losses due to radiation and convection are expected to be small and as a result the model predicts essentially isothermal conditions, i.e. $T_{g1} = T_{g2} = T_{\mathrm{H}}$, with the magnitude of these temperatures determined by the heating heat flux $\dot{q}_{\mathrm{H}}$ and the wall temperature T_{w}. This very simple model prediction can be directly compared to measurements of the top and bottom gauge temperatures.

Figure 7.24 shows the bottom gauge temperatures before the run for the double-sided thin film

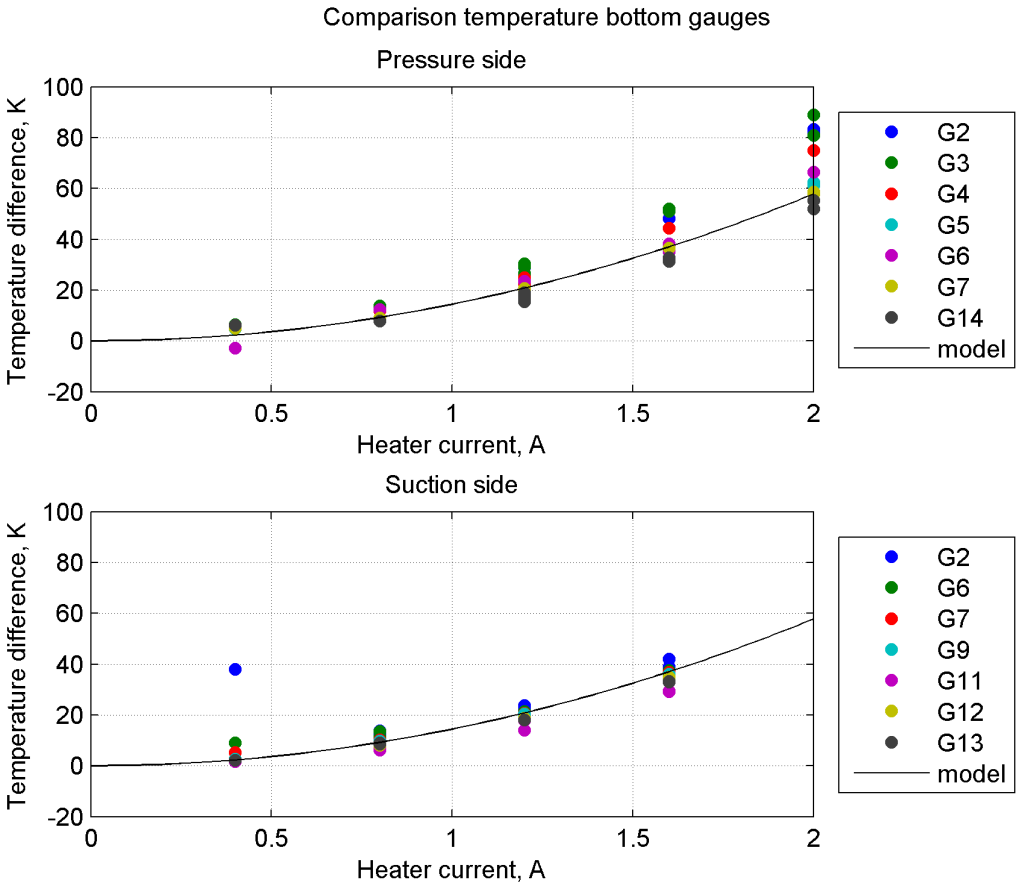

Figure 7.24: Preheating temperature difference of the bottom gauges on NGV D compared to model prediction.

gauges with a heater for a range of heater settings over different tests. The achieved temperature increases as the heating power increases and good repeatability was achieved between consecutive runs. The bottom gauge temperatures follow a clear trend which is proportional to I^2. Also (with exception of two outliers), the gauges near the trailing edge achieve higher temperatures than the gauges nearer the leading edge at the same heater settings, because of backwall heating due to the thinner wall. This effect can be observed both on the pressure side as well as on the suction side and is more obvious at higher current settings. For comparison, the experimental results are compared to the prediction of the bottom gauge temperature from the model discussed above, assuming the heat flux into the working section to be negligible. Good agreement between model prediction and experimental data is found.

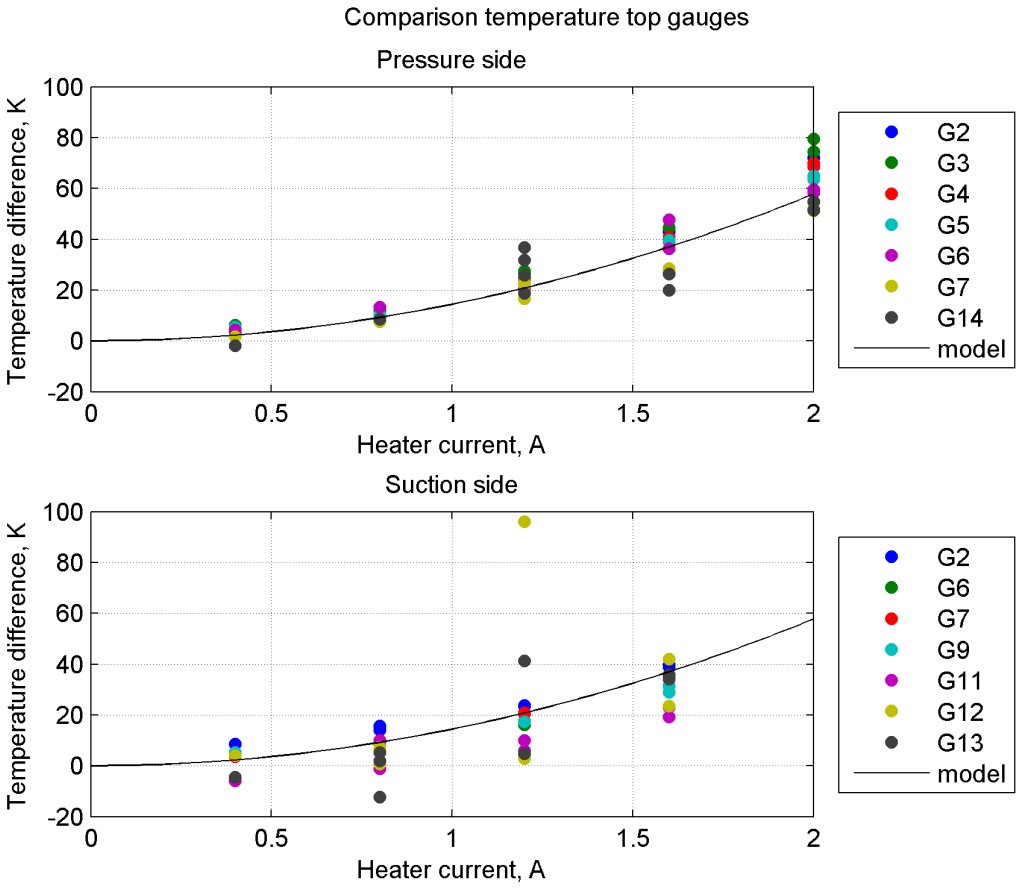

Figure 7.25: Preheating temperature difference of the top gauges on NGV D as measured and compared to model prediction.

The corresponding top gauge temperatures are shown in figure 7.25. In agreement with the model prediction, these temperatures follow the same trend and are comparable in magnitude to the bottom gauge temperatures. Nevertheless, in contrast to the bottom gauges, the surface temperatures measured by the top gauges do not show a clear correlation with the position of the gauge on the aerofoil. While some of the top gauges have a temperature that is slightly smaller than the bottom gauge temperature, indicating a non-zero heat flux into the working section, this observation cannot be made for all. In fact, in some cases, the top gauge temperature is higher than the corresponding bottom gauge temperature. In order to process this data there are two possibilities, either to manually pick only gauges whose top gauges show an expected physical trend or to calculate the top gauge temperature from the bottom gauge temperature.

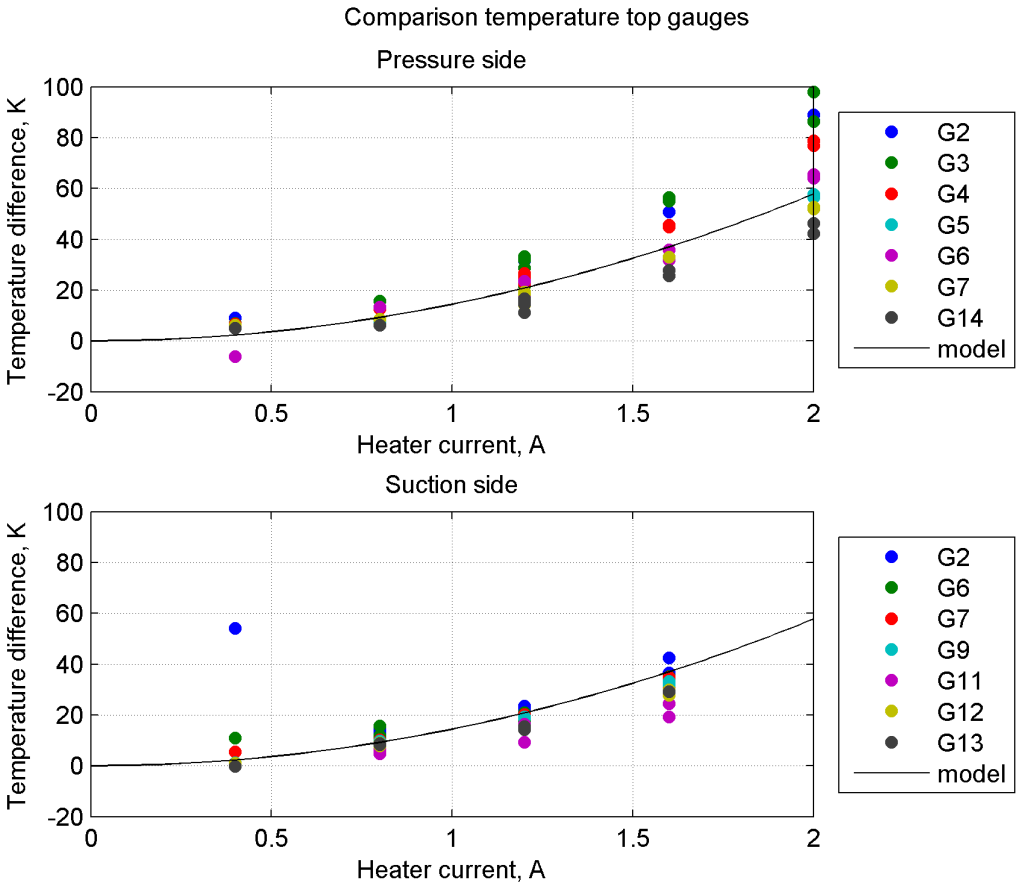

Figure 7.26: Preheating temperature difference of the top gauges on NGV D calculated from the bottom gauge temperatures and the heat flux from the heater. The results are compared to the model prediction.

There are two options to calculate the top gauge temperatures. The first option is to simply calculate the top gauge temperature from the heating heat flux and the conduction through the substrate layers using equations 7.6 and 7.7 for given T_w and T_{g2}. The advantage of this method is that it requires no knowledge on the heat transfer coefficient. However, it presumes that the cassette temperature stays constant.[1] The second option is to make an assumption on h and then calculate the top gauge temperature in terms of the bottom gauge temperature.

The results for the first option are shown in figure 7.26. As expected, the top gauges now follow the pattern of the bottom gauges. Nevertheless, the spread is larger and in some cases

[1]For this calculation it is necessary to know accurately the thickness of the three substrate layers and the uncertainty in the glue thickness cannot be reduced for x_2 and x_3, whereas in future it can be eliminated for x_1 by using the double-sided manufacturing process (see section 5.1).

unphysical top gauge temperatures are inferred.

These problems are avoided by the second option, where the top gauge temperature is calculated by making an assumption on the heat transfer coefficient. As argued above, the heat transfer coefficient before the start of the run is small and it is a good approximation to assume $h = 0$, such that the substrate layer is isothermal. In this case the top gauge temperature is simply set equal to the bottom gauge temperature.

The heat flux regressions for both approaches are illustrated in figure 7.27. For all three options the heat flux was calculated from the temperature history using the impulse response method based on the temperature change from the start of the run. The reduced heat flux does not include the pre-run heat flux and is zero at the start of the run. It is identical for all three options, as uncertainties in the initial temperature difference do not affect measurements of $\dot{q}$ (see section 5.6). The higher the current through the heater, the lower the reduced heat flux during the run. Figure 7.27a shows the heat transfer that is obtained from using the measured top and bottom gauge temperatures. Figure 7.27b corresponds to the case in which the top gauge temperature is calculated from the bottom gauge temperature and the heating heat flux. Finally, the heat transfer results when assuming $h = 0$ are shown in figure 7.27c. The regression results look similar, but the assumption of an isothermal substrate layer has been found to give more reliable results. This assumption will be used in the following results section. Compared to the data shown in figure 7.20, it is clear that preheating over a wide range of pre-run surface temperatures resulted in an increased range for the data regression.

Results

The temperature traces for four double-sided thin film gauges with an underside thin film heater on NGV D are shown in figure 7.28 (pressure side) and figure 7.29 (suction side). For this vane the quality of the DC data was very high and it is used to present the results. Comparing the temperature traces is not straightforward, because the level of preheating depends on the heater current and the location of the gauge on the aerofoil. However, as for the unheated double-sided gauges a decrease in surface temperature along the aerofoil is followed by an increase in surface temperature.

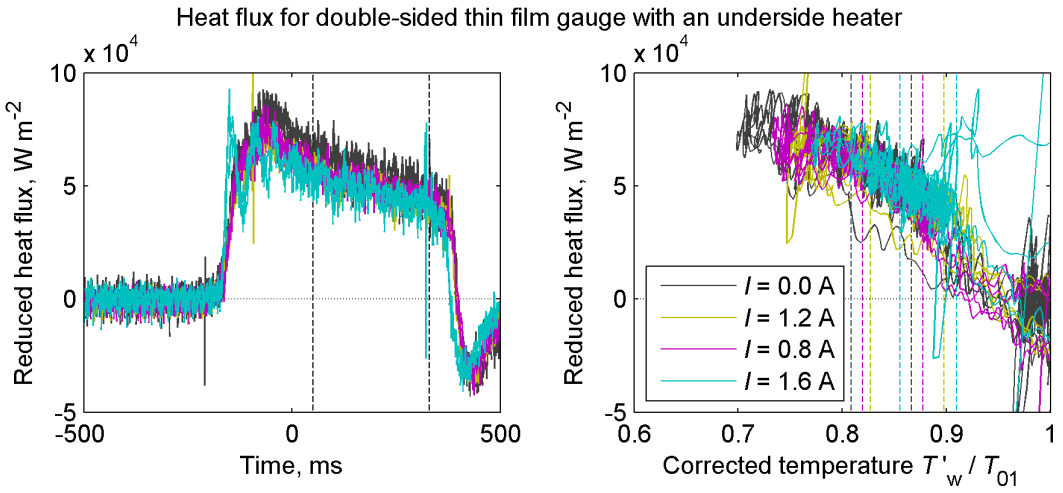

(a) Measured top and bottom gauge temperatures.

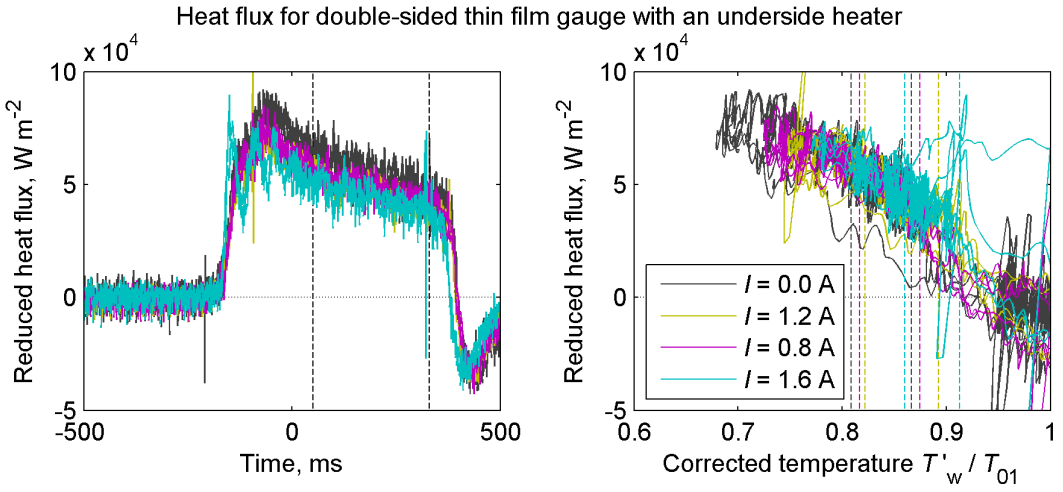

(b) Top gauge temperatures calculated from bottom gauge temperatures.

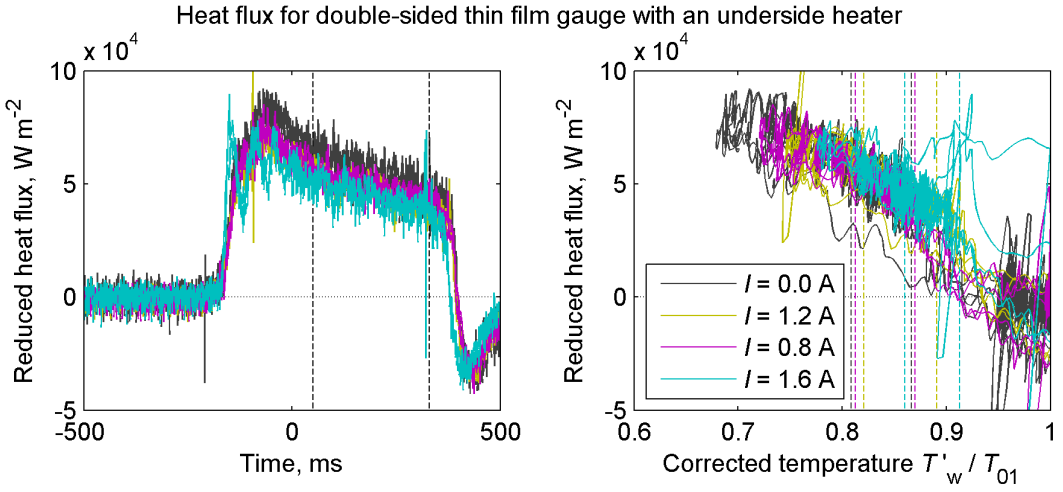

(c) Isothermal substrate layer.

Figure 7.27: Comparison of the heat flux of a double-sided thin film gauge with an underside heater (NGV D SS2) using different assumptions for the top gauge temperature.

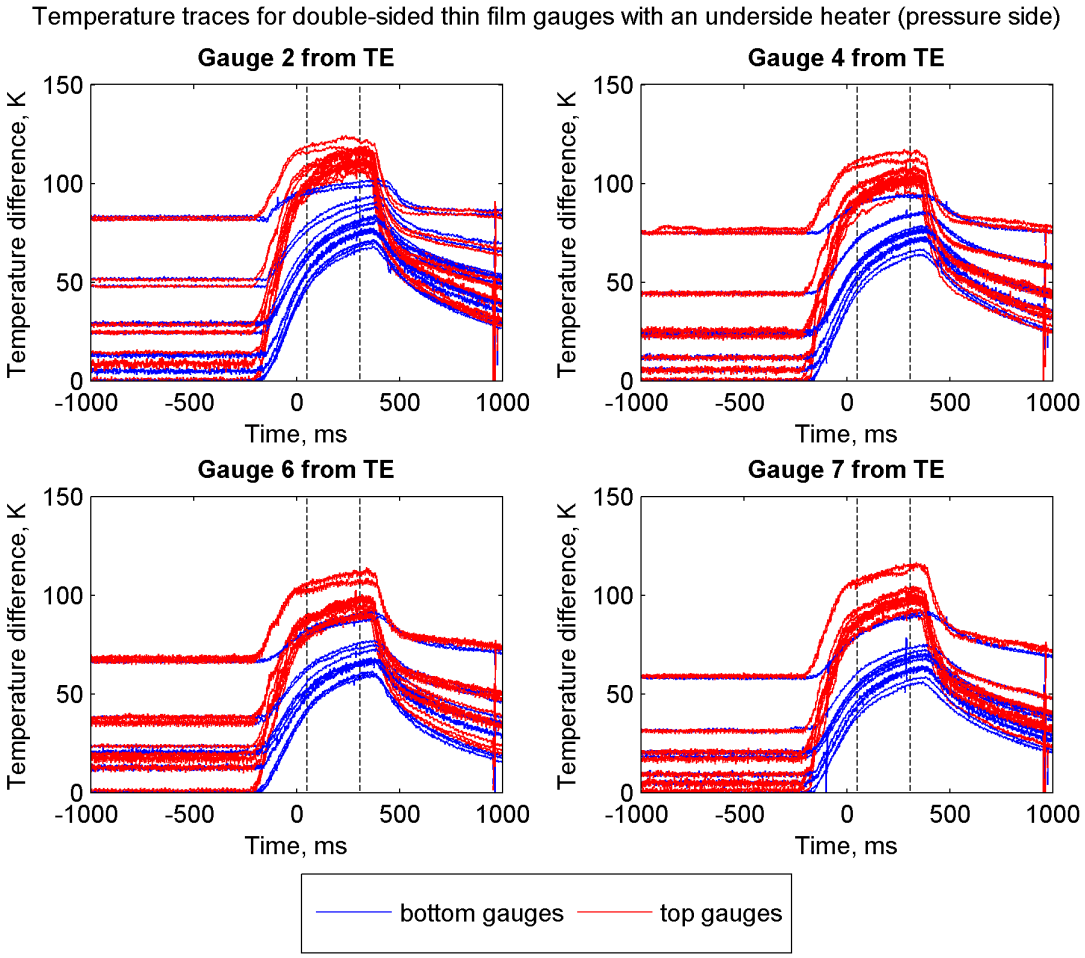

Figure 7.28: Temperature traces for four double-sided thin film gauges with an underside thin film heater on the NGV D **pressure side**. The results for up to fourteen runs are shown (see table 7.3). The dashed lines mark a typical stable period used for the regression of one run.

Due to several gauge failures, the heat transfer in the leading edge region was not well resolved. A few gauges failed at the beginning of the test campaign due to poor manufacture. Other gauges showed large changes in film resistance during the test campaign, which is interpreted as a change in the gauge substrate and is also a reason for dismissal. Finally, some gauges performed well, but calibrated very poorly and gave erroneous results. A failure of the top or bottom gauge in a set discards the whole gauge.

The regression results are shown in figure 7.30 (pressure side) and figure 7.31 (suction side). The results of the double-sided thin film gauges with an underside thin film heater are compared

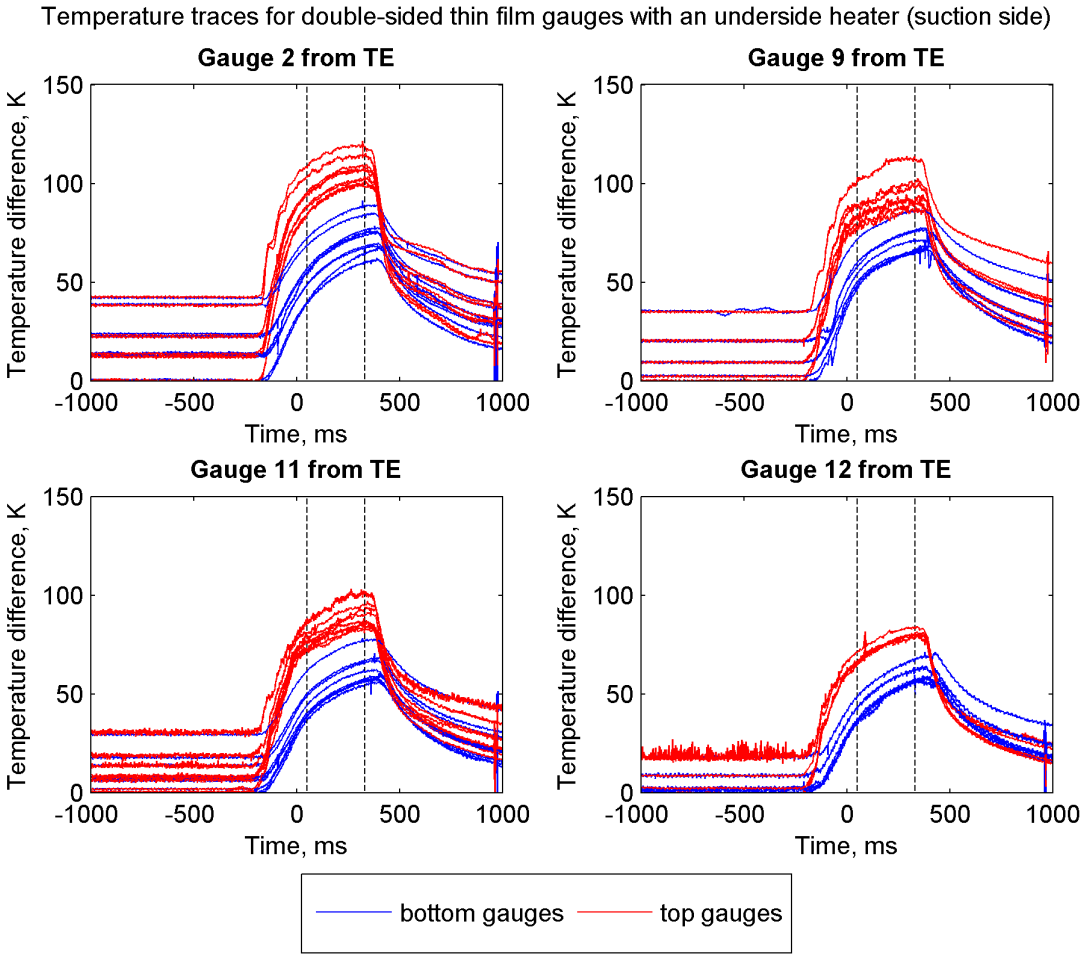

Figure 7.29: Temperature traces for four double-sided thin film gauges with an underside thin film heater on the NGV D **suction side**. The results for up to nine runs are shown (see table 7.3). The dashed lines mark a typical stable period used for the regression of one run.

to the results of the corresponding unheated double-sided gauges on NGV B (when available). With a wide range of preheating settings it was possible to obtain the adiabatic wall temperature and the heat transfer coefficient from a multiple regression of the pressure side gauge results. Hence, the regression of the heated gauges is much more accurate. There is generally good agreement in the adiabatic wall temperature on the pressure side. The evaluated heat transfer coefficient tends to be larger for the heated than for the unheated double-sided gauges. A large mismatch in heat transfer coefficient between NGV B and D is observed on gauge 7 from the trailing edge on the pressure side. This variation is unexpected as the heat transfer gradient is

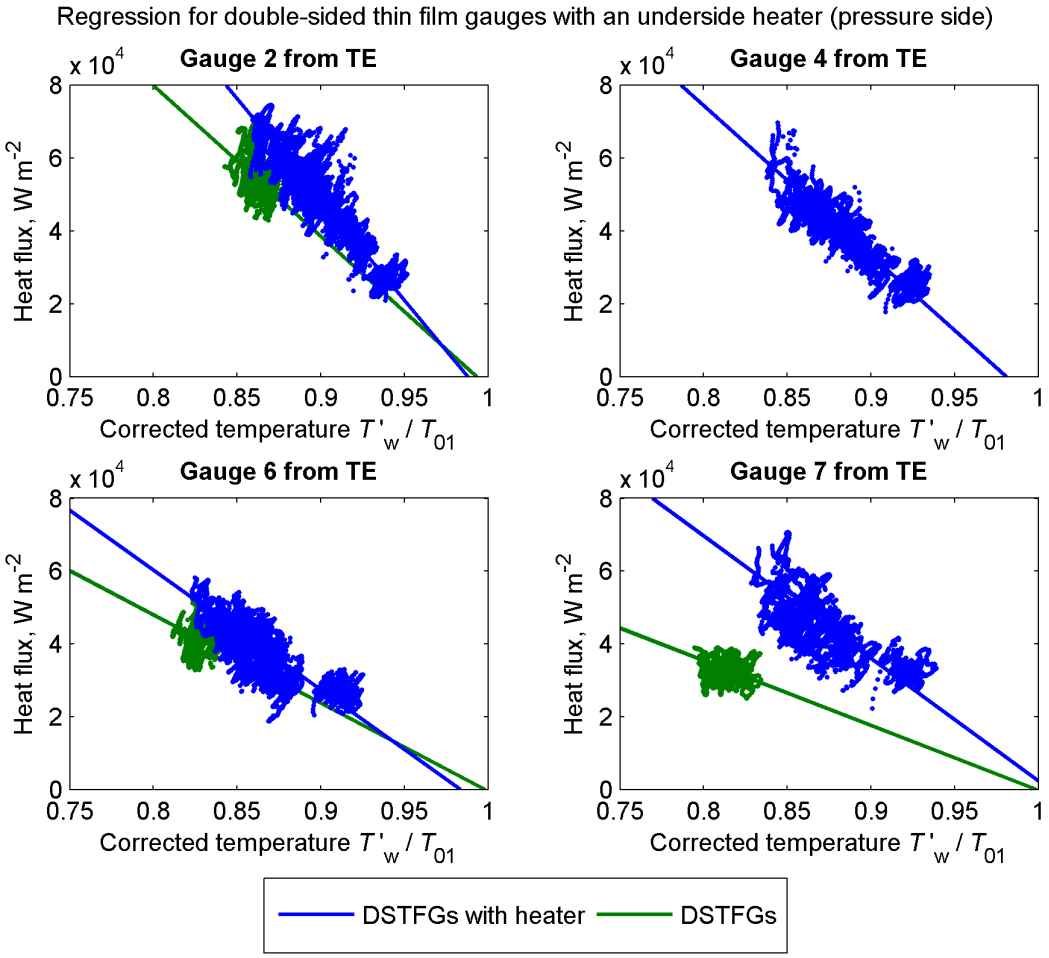

Figure 7.30: Regression data for four double-sided thin film gauges with an underside heater on the NGV D **pressure side** compared to corresponding unheated double-sided gauges on NGV B. The regression is performed on data from the stable run period.

rather flat in this region.

On the suction side the run quality is lower, because there was more noise pick-up than on the pressure side, and fewer runs are available for analysis.[1] For this reason it is necessary to calculate the recovery temperature from equation 6.1 to get a regression (except for gauge 2 from the trailing edge). The temperature range of the regression is still larger for the heated gauges than for their unheated counterparts, but an inconsistent run performance of some of the gauges caused a large variability in the heat transfer coefficient. For gauges 9 and 12 from the trailing edge a single run does not align with the rest of the data. In both cases it is a heated

[1]Table 7.3 shows the range of heater settings for all runs, but not every run can be used for every gauge.

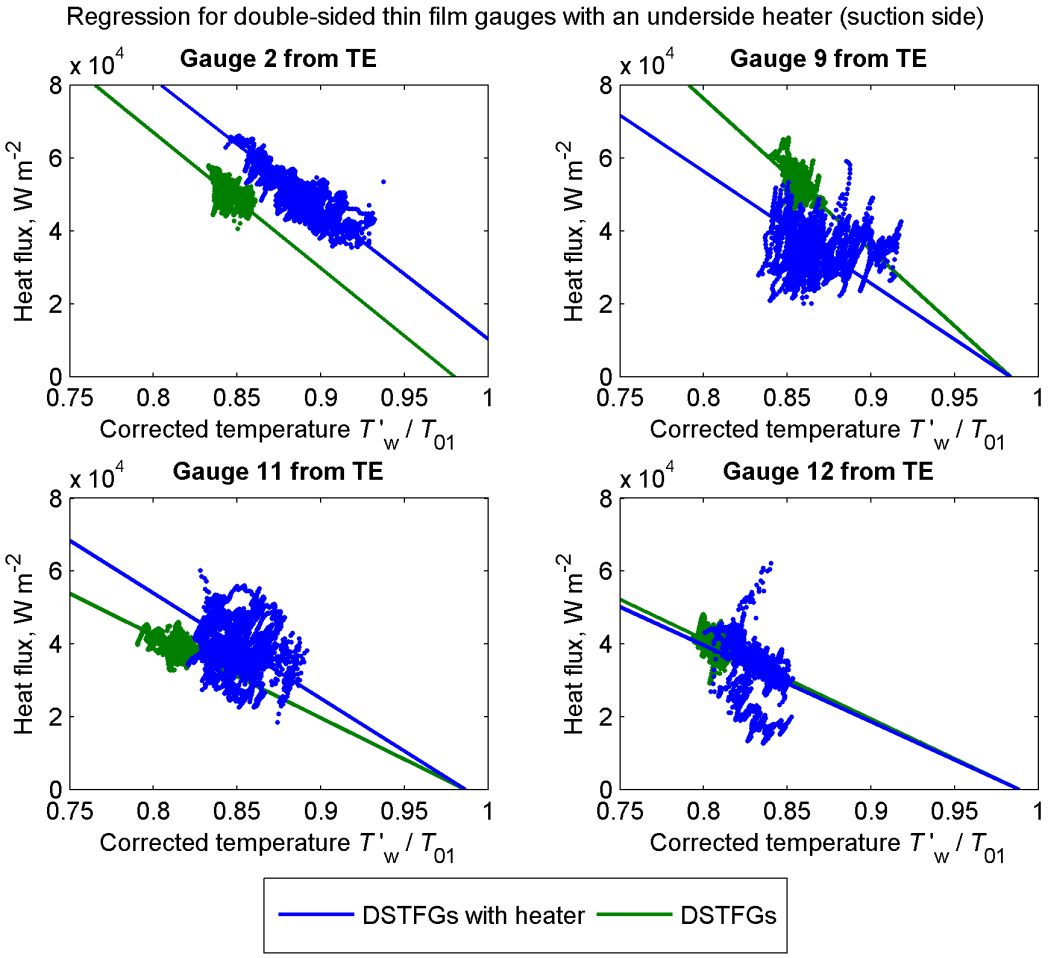

Figure 7.31: Regression data for four double-sided thin film gauges with an underside heater on the NGV D **suction side** compared to corresponding unheated double-sided gauges on NGV B. The regression is performed on data from the stable run period.

run for which there is unfortunately no repeat measurement, as the gauges showed an errant or very sensitive behaviour.

The regression results are summarised in figure 7.32 as a plot of Nusselt number distribution over surface distance. The heat transfer results obtained using the temperature measurement of the top and bottom gauges are compared to the results obtained when an isothermal substrate layer is assumed and the initial top gauge temperature is set equal to the bottom gauge temperature. The error in Nusselt number has been calculated for the results from the multiple regression based on the uncertainty analysis presented in section 5.6 and is also displayed in figure 7.32. While it is reassuring that the results for the measured temperatures and the

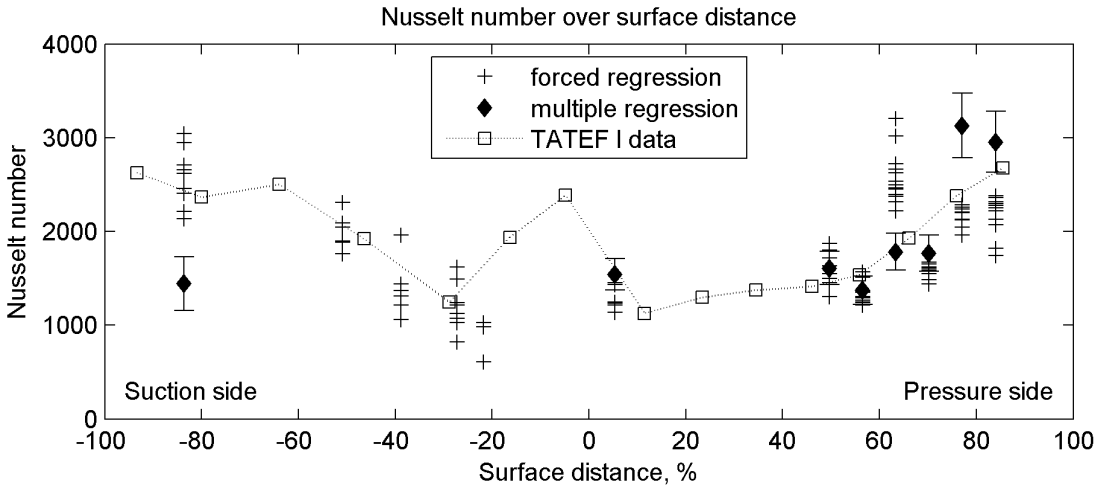

(a) Measured top and bottom gauge temperatures.

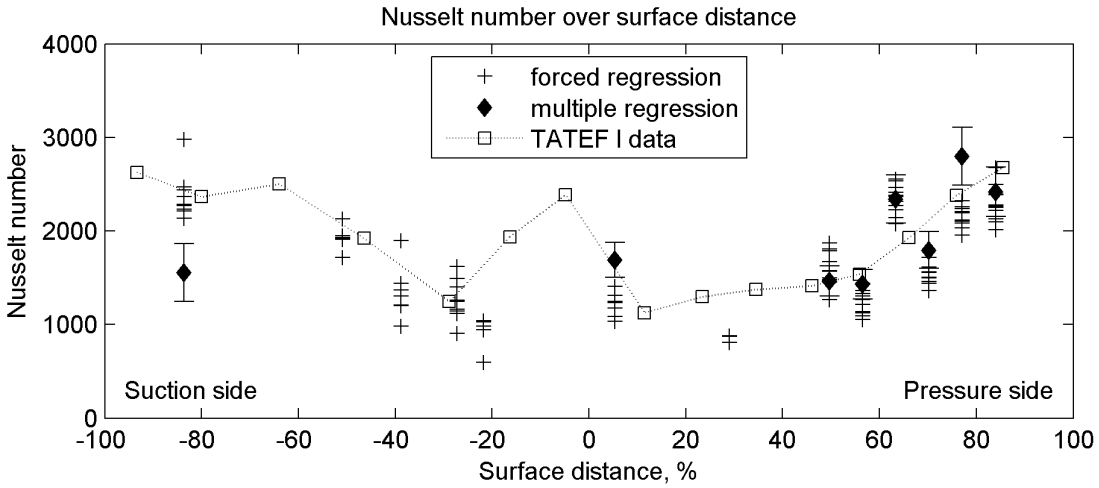

(b) Isothermal substrate layer.

Figure 7.32: Nusselt number plotted against surface distance from the NGV leading edge for double-sided thin film gauges with an underside heater. The current results are compared to data from TATEF I.

assumed isothermal substrate layer are similar, there are several improvements achieved by calculating the top gauge temperature from $T_{g1} = T_{g2}$. Firstly, the run-to-run agreement for the gauges improves and the forced regressions (i.e. when the adiabatic wall temperature is defined as the recovery temperature) and the multiple regression are better matched. Secondly, additional data that was dismissed because of large pre-run temperature variations can be included.

The data from the double-sided thin film gauges with an underside heater agrees well with the TATEF I data. In general, gauges for which more runs are available should be considered more trustworthy, as they have behaved more consistently. In comparison to the unheated double-sided gauges the agreement with the previous data is much better, as not only the general trend is captured, but also the absolute value of the Nusselt number. The single deviations have already been commented on – it is often in the same run that a higher heat transfer coefficient is measured for several gauges (as observed for example in gauges 9 and 12 on the suction side). There is an interesting local peak in heat transfer on the late pressure side, which has been recorded on all runs.

For three of the eight gauges for which it was possible to perform a regression on multiple runs to separate the adiabatic wall temperature and the heat transfer coefficient, the results agree poorly with those obtained performing a forced regression for each run. The regression results for the three gauges are shown in figure 7.33. On gauges 3 and 14 on the pressure side the adiabatic wall temperatures that follow from a multiple regression are smaller than the recovery temperature calculated from the isentropic Mach number and the static temperature. The uncertainty in the intercept of 2% and 3% respectively agrees well with the 2% error predicted by the uncertainty analysis in section 5.6. The error is larger for gauge 14 than gauge 3 due to uncertainties in the data fit (such as caused by outliers), which were not included in the analysis. On gauge 2 on the suction side the results from the forced regression do not match the experimental data very well. The multiple regression gives a much better fit with an adiabatic wall temperature which is larger than that predicted and actually larger than the hot gas temperature. The maximum preheating temperature this gauge achieved was around 40 K and thus smaller than the 80 K assumed for the uncertainty analysis. As a result, the regression will be less reliable and larger errors in adiabatic wall temperature are to be expected.

In conclusion, the double-sided thin film gauges with an underside thin film heater have shown to be able to separate the adiabatic wall temperature and the heat transfer coefficient when good data is available over a wide range of heater settings. This separation could not be achieved with unheated double-sided gauges. The results obtained from the multiple regressions generally compare well with the results where the recovery temperature has been set, but they

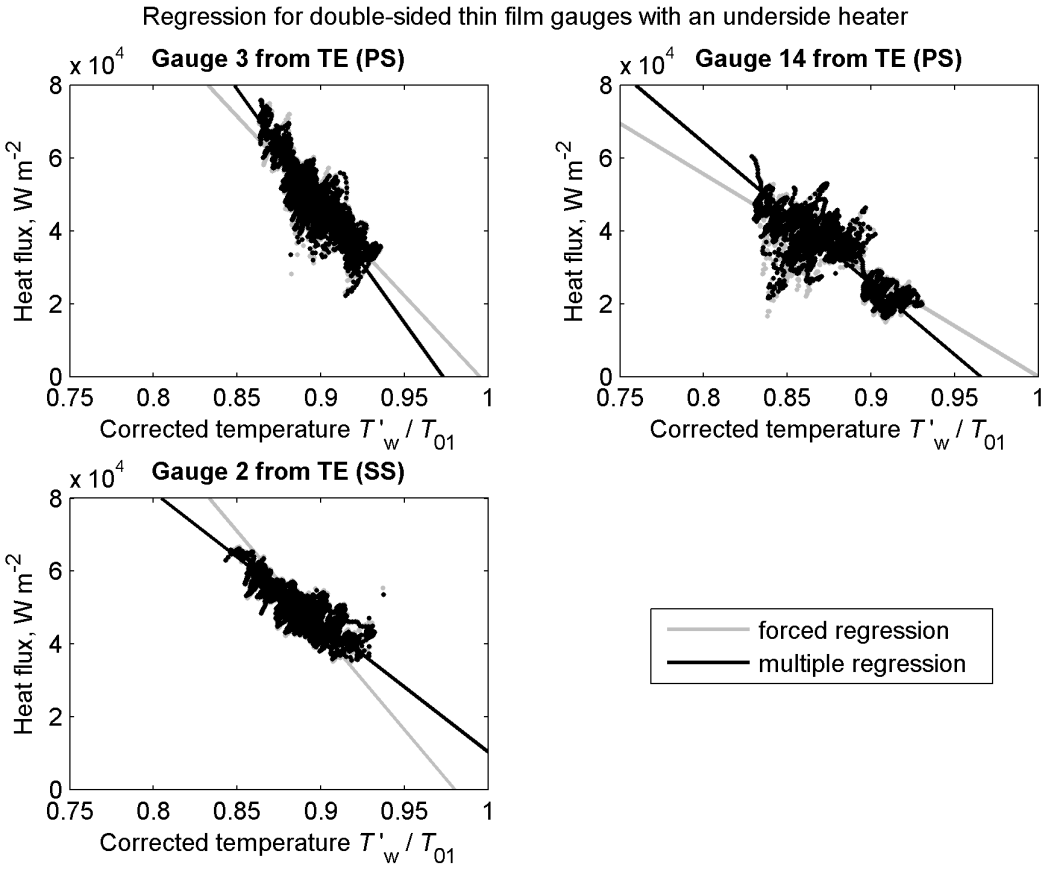

Figure 7.33: Comparison of the regression results obtained performing a forced regression for each run to the regression results obtained from a multiple regression on all runs for one gauge.

often reflect the heat transfer much more accurately. The resulting Nusselt number distributions match the expectations and agree with previous experimental data. Finally, the gauges on the suction side are expected to perform as well as the gauges on the pressure side when good data is obtained over a wide range of preheating.

7.4.4 Double-sided thin film gauges with variable heating current

The instrumentation of NGV C with self-heating double-sided thin film gauges is identical to that of NGV B. The current through the top gauges of the self-heating double-sided thin film gauges was set between 40 mA and 100 mA (see table 7.4). For comparison, the unheated gauges are set at a nominal voltage of 0.25 V, which typically corresponds to currents between 5 mA

	Gauge current	Number of runs	Heated gauges
Pressure side	unheated	4	–
	60 mA	4	1, 5, 6, 8, 12, 14
	80 mA	3	1, 5, 6, 8, 12, 14
	100 mA	2	1, 5, 6, 8, 12, 14
Suction side	unheated	2	–
	40 mA	3	1, 2, 5–9, 11–15
	60 mA	3	1, 2, 5–9, 11–15
	80 mA	2	5, 7, 9, 11, 13, 15

Table 7.4: Top gauge current settings for self-heating double-sided thin film gauges.

and 10 mA. The DC data was acquired in different test runs for the pressure and suction sides. The gauge current was limited to 80 mA for the tests on the suction side, as the gauges on the pressure side overheated at 100 mA: After the final test at a top gauge current of 100 mA the gauges showed an erratic behaviour and the resistance dropped drastically. The following analysis is limited to the heated tests below 100 mA. Due to the reduced number of modified HTA3 channels only six gauges could be heated simultaneously.

The bottom gauge temperatures can be reliably measured as the gauge current is constant. They are plotted in figure 7.34 as a function of the top gauge voltage for the pressure and suction sides. The unheated gauges were set to a voltage of 0.25 V. For the heated gauges the voltage settings were 2.4 V, 3.6 V and 4.8 V – with some variation between different gauges, because they were individually set. These voltages correspond to nominal gauge currents of 40 mA, 60 mA and 80 mA. The actual gauge current depends on the gauge resistance and the achieved temperature depends on the location of the gauge on the aerofoil. When heated, the gauges near the trailing edge tend to be hotter than the gauges on the leading edge. In general, the gauges on the suction side were better behaved and a greater variability of the preheating temperature is observed on the pressure side.

As for the casing tests, the temperature of the top gauge was inferred from the bottom gauge

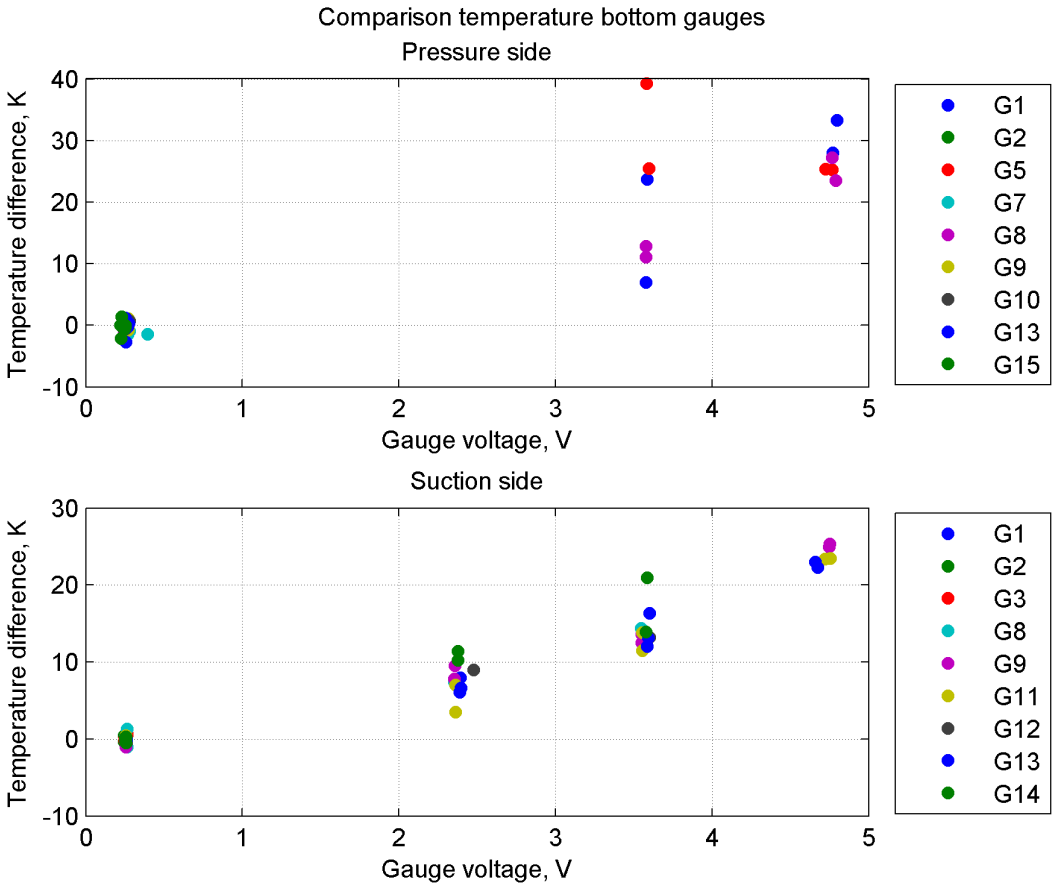

Figure 7.34: Temperature difference of the bottom gauges on NGV C achieved through ohmic heating of the top gauges.

temperature and the heating heat flux using the 2D thermal conduction model. The motivation and assumptions needed to calculate the initial gauge temperature are detailed in sections 5.5 and 6.4. The bottom gauge preheating temperature difference is plotted in figure 7.35 for three gauges and compared to the 2D model predictions. As for the self-heating double-sided thin film gauges on the casing, the model predictions agree very well with the experimental results up to 2.5 V. At higher voltages the modelling uncertainties increase.

The temperature traces following from the calculation of the top gauge temperature are shown in figures 7.36 and 7.37 for the pressure and suction sides. Given the different location of the gauges on the aerofoil and the individual setting of the gauge current, it is difficult to directly compare gauges. At the highest current setting temperature differences up to 90 K are

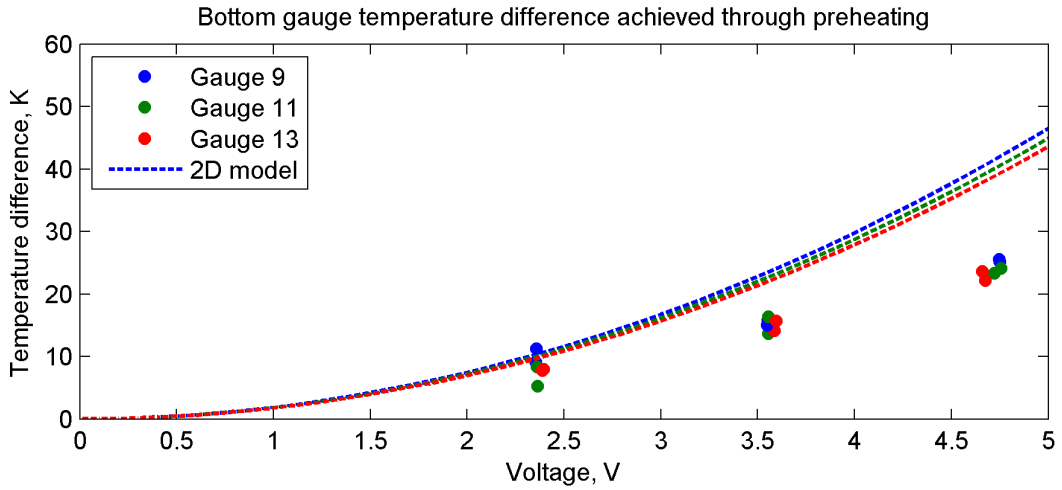

Figure 7.35: The bottom gauge temperature difference achieved for different gauge settings by three gauges on the suction side of NGV C is plotted over the voltage across the top gauge and superimposed to the 2D (dashed line) model results.

achieved. It is important to note that the heating of the gauges with variable gauge current also affects neighbouring gauges. These gauges are not self-heating, but they are preheated by the hot gauges before the run. The effect can be seen on gauges 2 and 9 on the pressure side and on gauges 1 and 14 on the suction side (which were only heated for two runs).

The heat flux was calculated using the impulse response method on the temperature change from the start of the run. For this calculation the temperature difference – and hence the heat flux – is set to zero at the start of the run. A typical heat flux trace is shown in figure 7.38 for gauges 9 and 14 on the suction side. The results for the nominal current setting are plotted in grey. At higher values of the current through the gauge a lower heat flux is observed during the run. Gauge 14, which was only heated for two runs, already achieves an improved regression range by the heating through the neighbouring gauges. This preheating temperature is recorded by the bottom gauge and an isothermal gauge substrate is assumed (see figure 7.37). Overall the data quality is very good and a good regression is possible.

The regression results are shown in figure 7.39 for the pressure side and in figure 7.40 for the suction side. The results are compared to data from the unheated double-sided thin film gauges (when available), whose configuration is identical. As the quality of the data was very good, it was possible to separate the adiabatic wall temperature and heat transfer coefficient

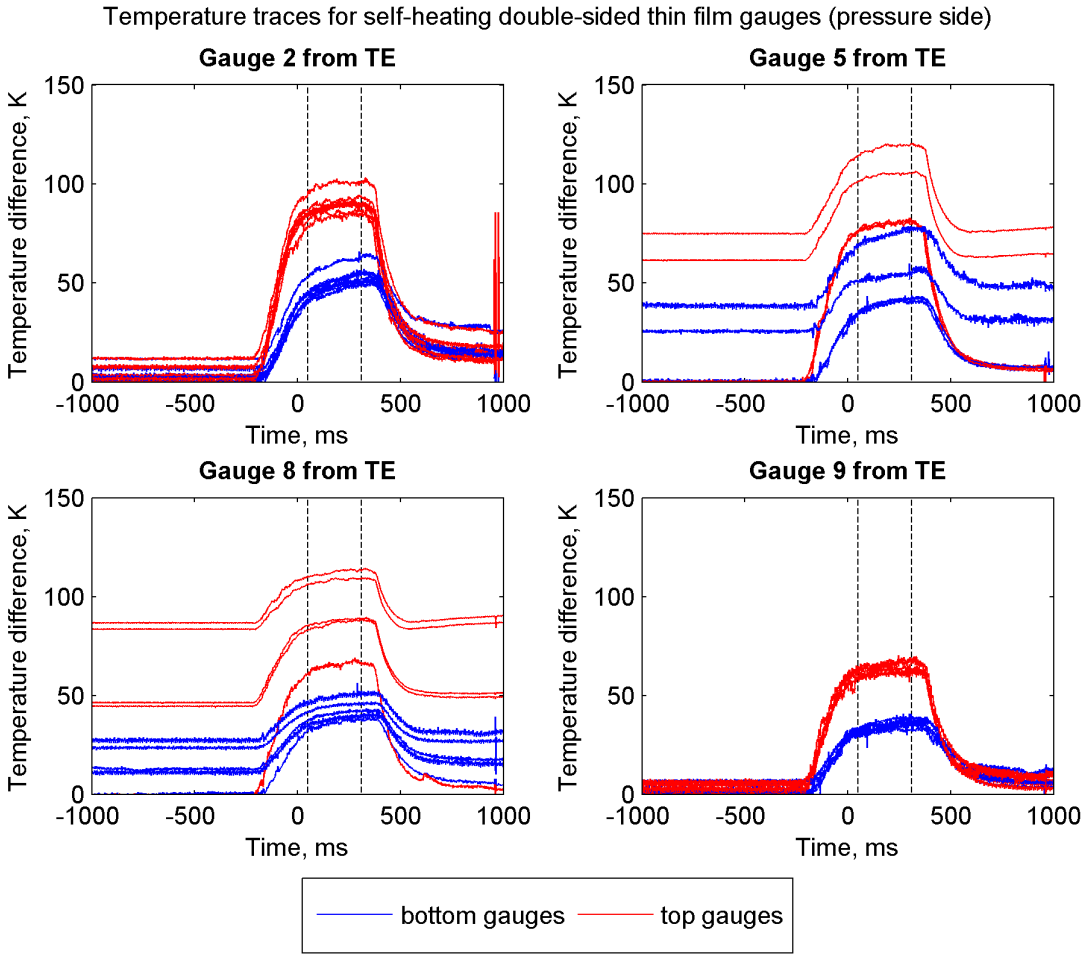

Figure 7.36: Temperature traces for four self-heating double-sided thin film gauges on the NGV C **pressure side**. The results for up to eight runs are shown (see table 7.4). The dashed lines mark a typical stable period used for the regression of one run.

for 13 out of the 27 gauges. Given the reduced number of heated gauges per run this is a very encouraging result. Where the multiple regression does not converge, the recovery temperature was calculated (see equation 6.1). Gauges 2 and 9 on the pressure side are unheated. Their heat transfer results agree very well with those of the unheated double-sided thin film gauges (for both sets of gauges it was necessary to specify the recovery temperature). Gauges 5 and 8 are heated. Again the unheated results agree very well. A much more accurate regression is obtained when the heated results are included. On the suction side gauges 9 and 11 are heated over the full range of currents and they achieve the best regression range. Gauges 1 and 14 were heated for two runs only and still achieve an improved regression compared to their unheated

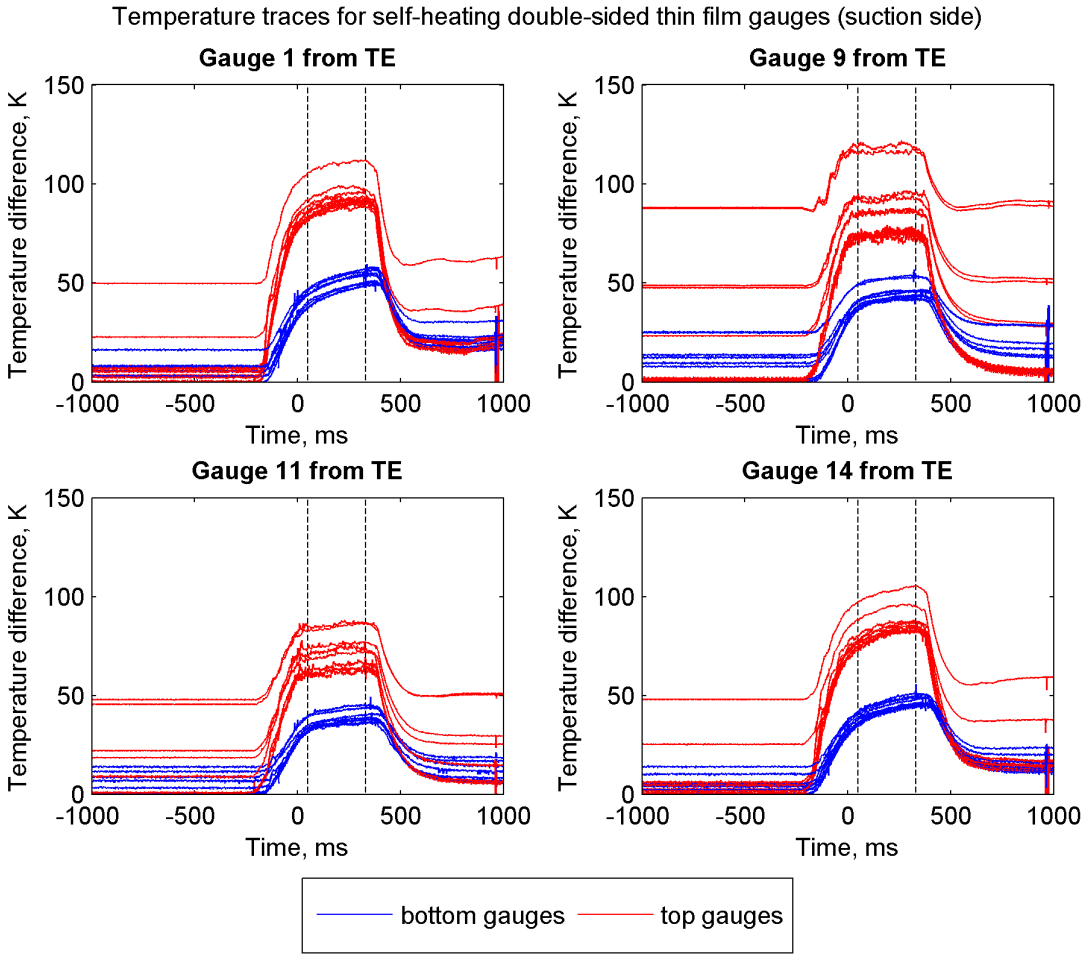

Figure 7.37: Temperature traces for four self-heating double-sided thin film gauges on the NGV C **suction side**. The results for up to ten runs are shown (see table 7.4). The dashed lines mark a typical stable period used for the regression of one run.

counterparts.

As for the gauges on the casing, the top gauge temperatures calculated from the bottom gauge temperatures using the 2D model generally appear to be too low at higher heating power. This results in an underprediction of the adiabatic wall temperature and an overprediction of the heat transfer coefficient compared to the results from the unheated double-sided gauges. This observation agrees with the fact that at higher heating currents the bottom gauge temperature is measured low in comparison to the prediction of the conductive model (see figure 7.35) and a lower bottom gauge temperature results in a lower top gauge temperature. The observed difference is large enough to account for the differences in the inferred adiabatic wall temperatures.

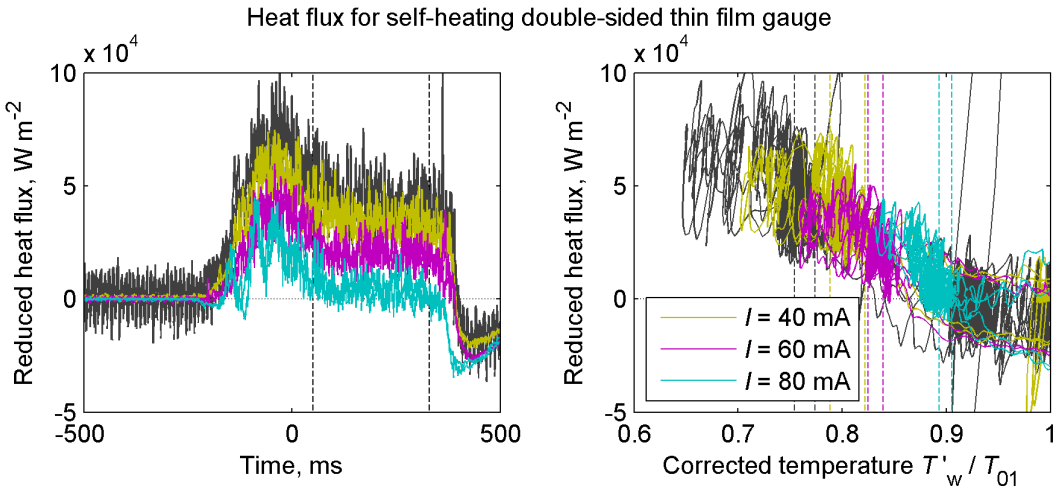

(a) Gauge 9 from trailing edge.

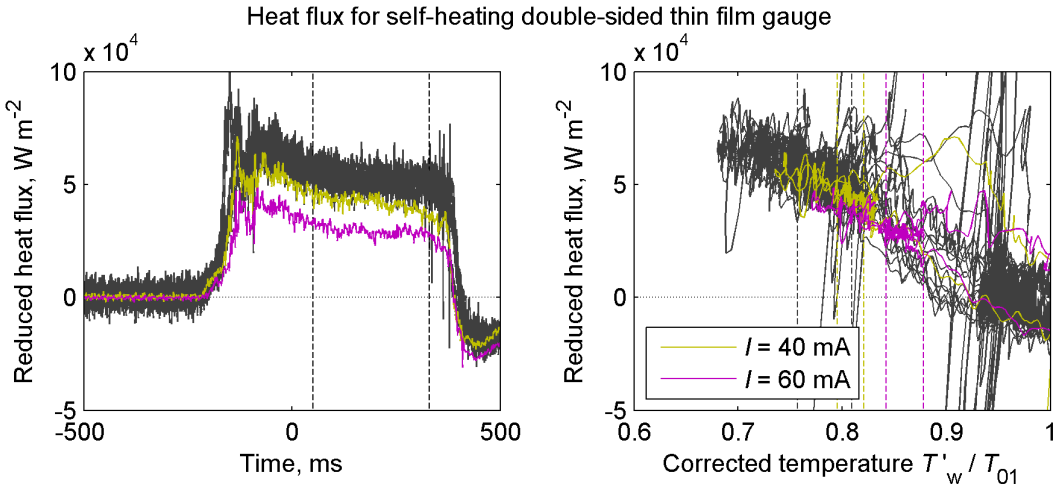

(b) Gauge 14 from trailing edge.

Figure 7.38: Heat flux for two self-heating double-sided thin film gauges on the NGV C **suction side**. The dashed lines mark a typical stable period used for the regression of one run and one gauge. The unheated results are plotted in grey.

A summary of the heat transfer results is given in figure 7.41 as a distribution of the Nusselt number over the surface distance. As explained above, the multiple regressions result in higher heat transfer coefficients compared to those obtained from unheated double-sided gauges. Conversely, when the regression is forced through a set recovery temperature, the underprediction of the surface temperature results in heat transfer coefficients that tend to be low. The difference between the Nusselt number from multiple regressions and forced regressions

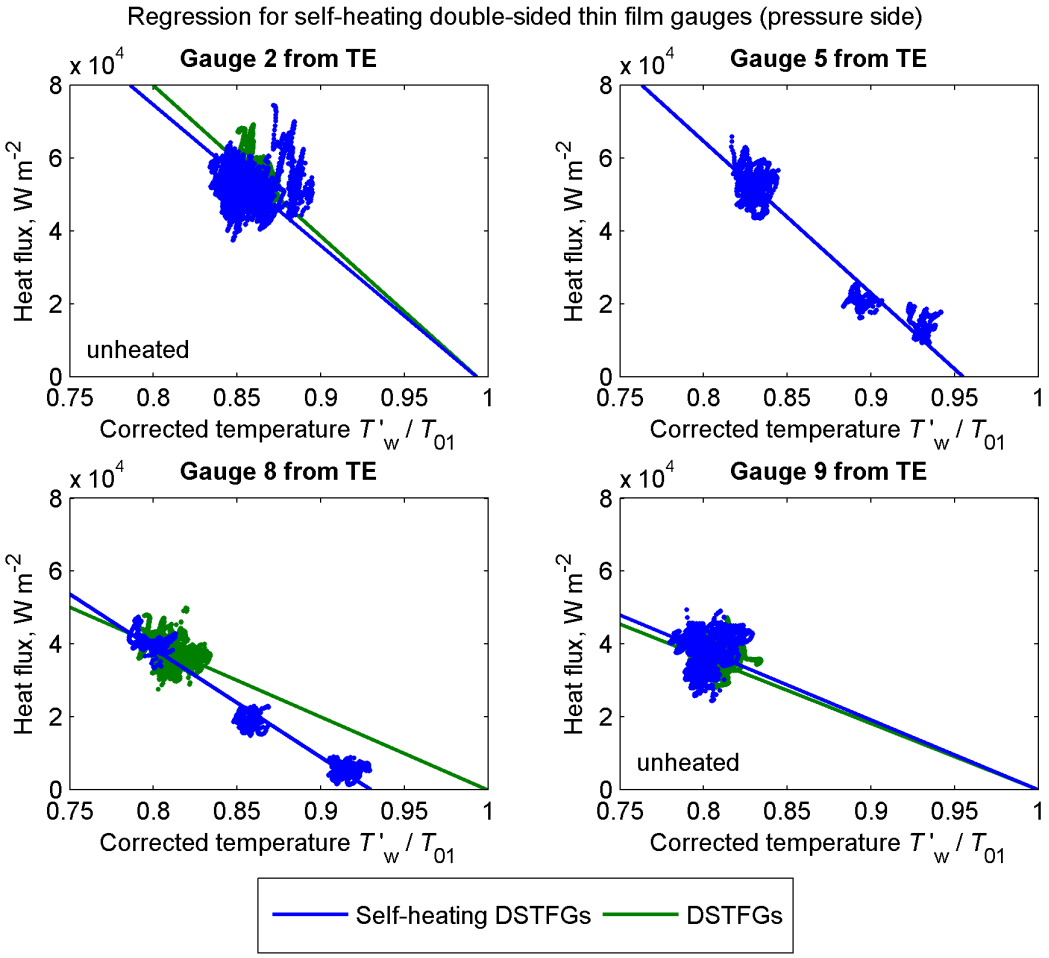

Figure 7.39: Regression data for four self-heating double-sided thin film gauges on the NGV C **pressure side** compared to corresponding unheated double-sided gauges on NGV B. The regression is performed on data from the stable run period.

varies from gauge to gauge, as runs at higher currents will cause a more pronounced discrepancy. At lower gauge currents the results from the self-heating gauges agree better with the unheated double-sided thin film gauges. The effect of modelling uncertainties on the regression results are discussed in section 5.6.

Given the difficulties in determining the initial gauge temperature, the heat transfer results obtained by setting the recovery temperature are expected to be more accurate. Indeed, the forced regressions for the self-heating double-sided thin film gauges lead to a very good agreement with the trend described by the TATEF I data. It is important to note that the TATEF I data consistently shows a larger heat transfer on the pressure side. This discrepancy is not an

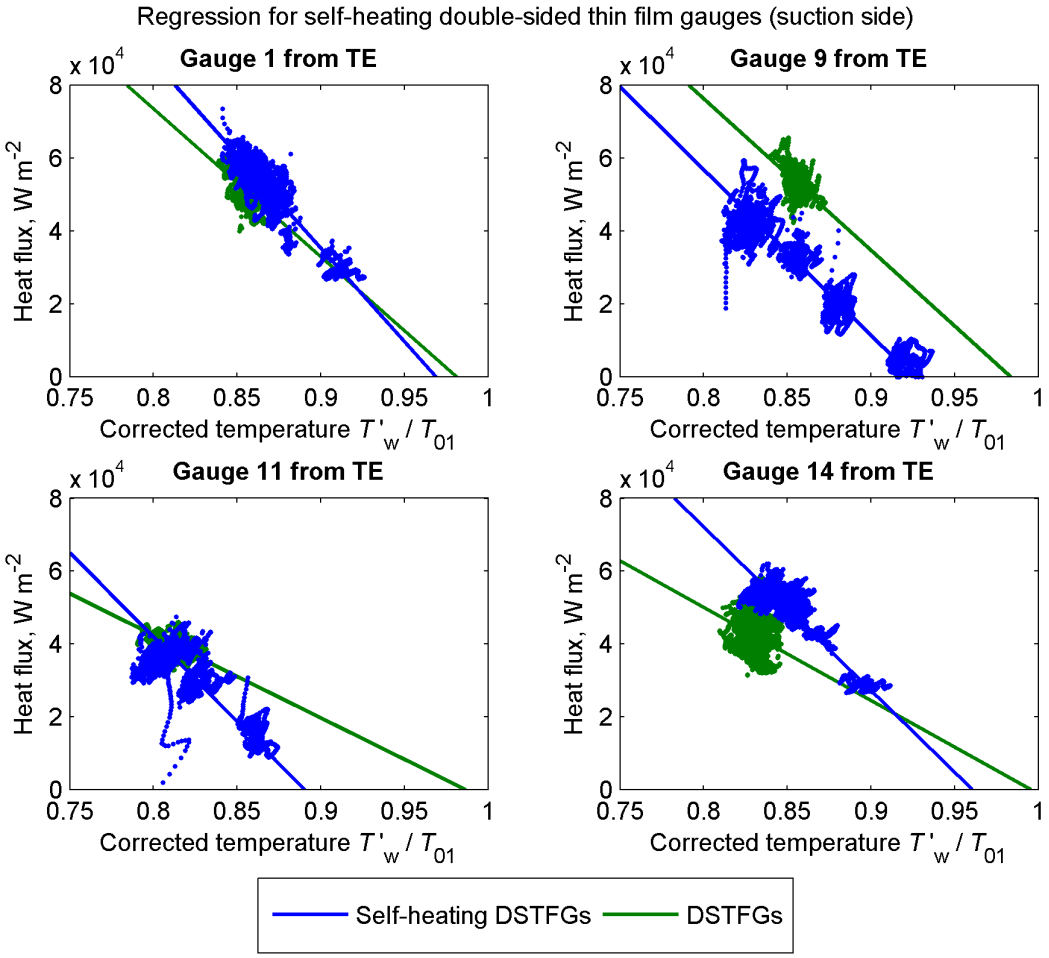

Figure 7.40: Regression data for four self-heating double-sided thin film gauges on the NGV C **suction side** compared to corresponding unheated double-sided gauges on NGV B. The regression is performed on data from the stable run period.

effect of the uncertainty in the top gauge temperature and has already been observed with the unheated double-sided thin film gauges (see figure 7.23).

To sum up, self-heating double-sided gauges have been successfully used to separately determine the adiabatic wall temperature and the heat transfer coefficient. The Nusselt number distributions agree well with those measured by the unheated double-sided gauges. In comparison to the double-sided gauges with an underside thin film heater the self-heating gauges are thinner and do not require separate instrumentation of the heating system. However, in order to reduce the modelling uncertainties it will be necessary to further investigate the thermal conduction in the substrate layer, as described in section 8.2.

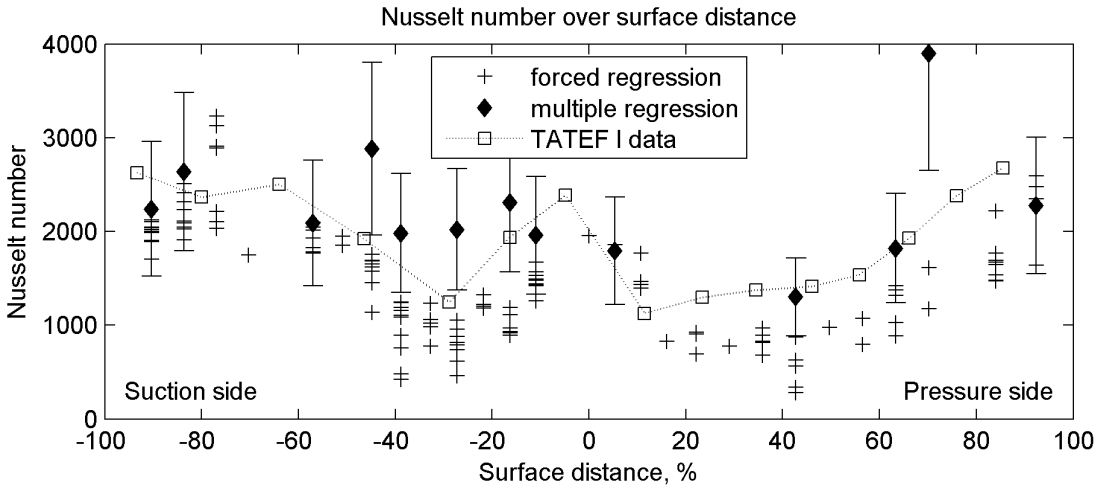

Figure 7.41: Nusselt number plotted against surface distance from the NGV leading edge for self-heating double-sided thin film gauges. The current results are compared to data from TATEF I.

7.5 Cooled results

In this section the results from the two cooled NGVs are presented. NGV C was instrumented with double-sided thin film gauges with an underside thin film heater and NGV D was instrumented with self-heating double-sided thin film gauges. The cooling configuration and coolant delivery system have been described in section 7.2. In total 18 cooled runs were conducted. The heat transfer measurements were taken simultaneously on all four vanes (including uncooled NGVs A and B) on the same side of the aerofoil to monitor the run conditions and to have a comparison.

The aim of this section is to develop a measurement technique to obtain accurate distributions of Nusselt number and film cooling effectiveness on cooled NGVs. These results can be compared to the corresponding data from the uncooled vanes and literature. A qualitative comparison with the tests performed by Chana and Mole (2000) on cooled MT1 NGVs within the TATEF I programme is also provided.[1]

[1]It is not possible to give a quantitative comparison, because of the different regressions and Nusselt number definitions.

	Heater current	Number of runs
Pressure side	unheated	2
	1.2 A	2
	1.6 A	2
	2.0 A	2
Suction side	unheated	2
	1.2 A	2
	1.6 A	2
	2.0 A	2

Table 7.5: Heater settings for double-sided thin film gauges with an underside thin film heater on cooled NGV C.

7.5.1 Double-sided thin film gauges with an underside thin film heater

The cooled NGV C was instrumented with two rectangular heaters (see figure 5.4 for details) underneath eight double-sided thin film gauges on the pressure and suction sides – as per the gauge configuration in figure 5.3a. In order to minimise the step size the substrate layers were staggered. Each heater had an area of 525 mm^2 and a resistance of 8.2 Ω. The current through the heater was set for each run, as detailed in table 7.5. A maximum heating heat flux of about 100 $\mathrm{kW\,m^{-2}}$ was achieved. The data was acquired separately on the pressure and suction sides.

Two major issues affected the performance of the double-sided thin film gauges with an underside heater on a cooled NGV. The first issue relates to the manufacture of the gauges. A flickering of the vacuum pump used for the deposition of the platinum films caused a very uneven sputtering of the films. The uneven sputtering resulted in a large variance of the thickness and hence the resistance of the gauges, ranging from 20 Ω to 50 Ω. The behaviour of these gauges during the calibration was not very consistent and resulted in a wide range of temperature coefficients of resistance. The contact in the copper-platinum joint was also severely affected by the bad sputtering. A few of the gauges could be fixed by painting over the joint with silver paint. Still, out of the eight double-sided gauges on the pressure side of the vane three failed

because of the poor gauge quality.

The second issue affected the reference measurement of the gauges. In chapter 6 it was demonstrated that the HTA3 boxes used as the current supply for the thin film gauges are stable in the required time scales (figure 6.5). However, one of the boxes used for some of the gauges on the cooled NGV C did not provide a reliable reference measurement. This problem was not spotted during the test campaign, because the voltage records looked (and indeed behaved) correctly. Nevertheless, the faulty reference measurement gave unphysically high or low initial gauge temperatures. The box has since been repaired and re-calibrated. The temperatures of the remaining good bottom gauges connected to a reliable HTA3 box are shown in figure 7.42 over a range of heater settings.

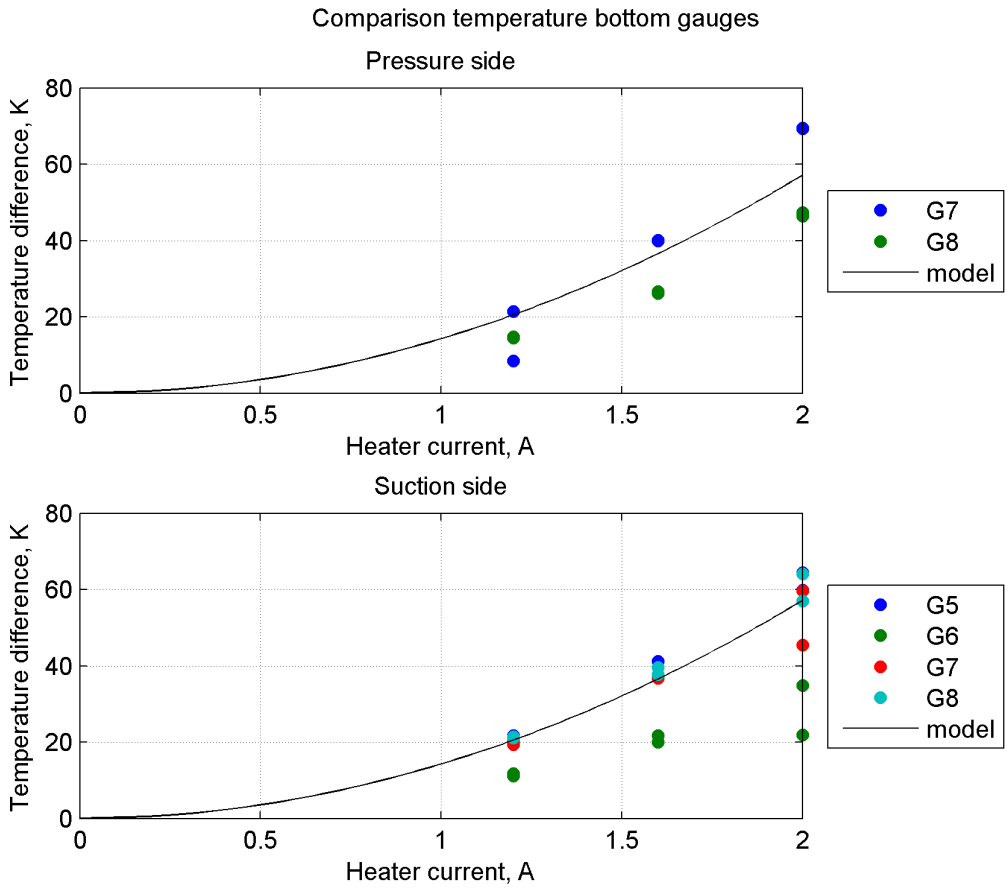

Figure 7.42: Preheating temperature of the bottom gauges on cooled NGV C compared to model prediction.

As discussed for the double-sided gauges with an underside thin film heater on an uncooled NGV, the top gauge temperature is less well behaved than the bottom gauge temperature (see figure 7.43). In the following analysis, the top gauge temperature is assumed to be the same as the bottom gauge temperature. Since the absolute temperature is available only for a few of the bottom gauges due to the bad HTA3 box, the bottom gauge temperature is assumed to be the same for all gauges. This assumption is valid because the surface is heated uniformly and the gauges are on the central part of the aerofoil – far away from the leading or trailing edge. The top gauge temperatures confirm this assumption. On the suction side, where more data was obtained, an average bottom gauge temperature is calculated.

The temperature traces are shown in figure 7.44 and figure 7.45 for the pressure and suction

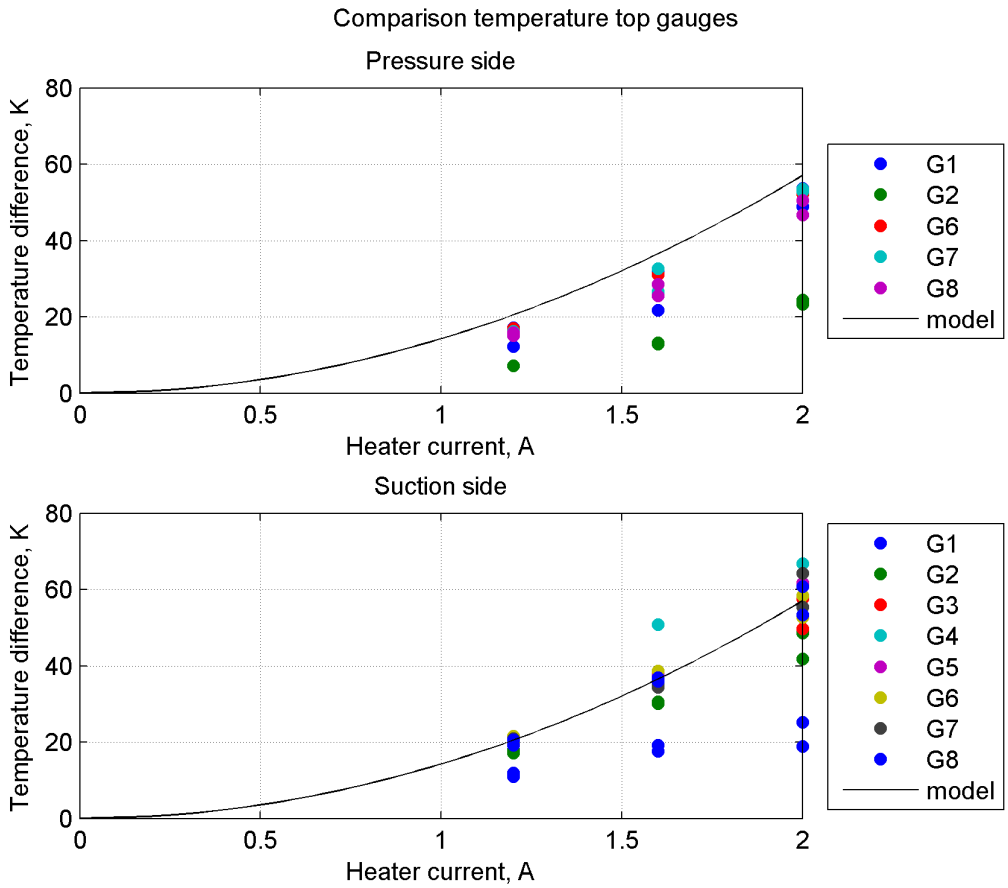

Figure 7.43: Preheating temperature of the top gauges on cooled NGV C compared to model prediction.

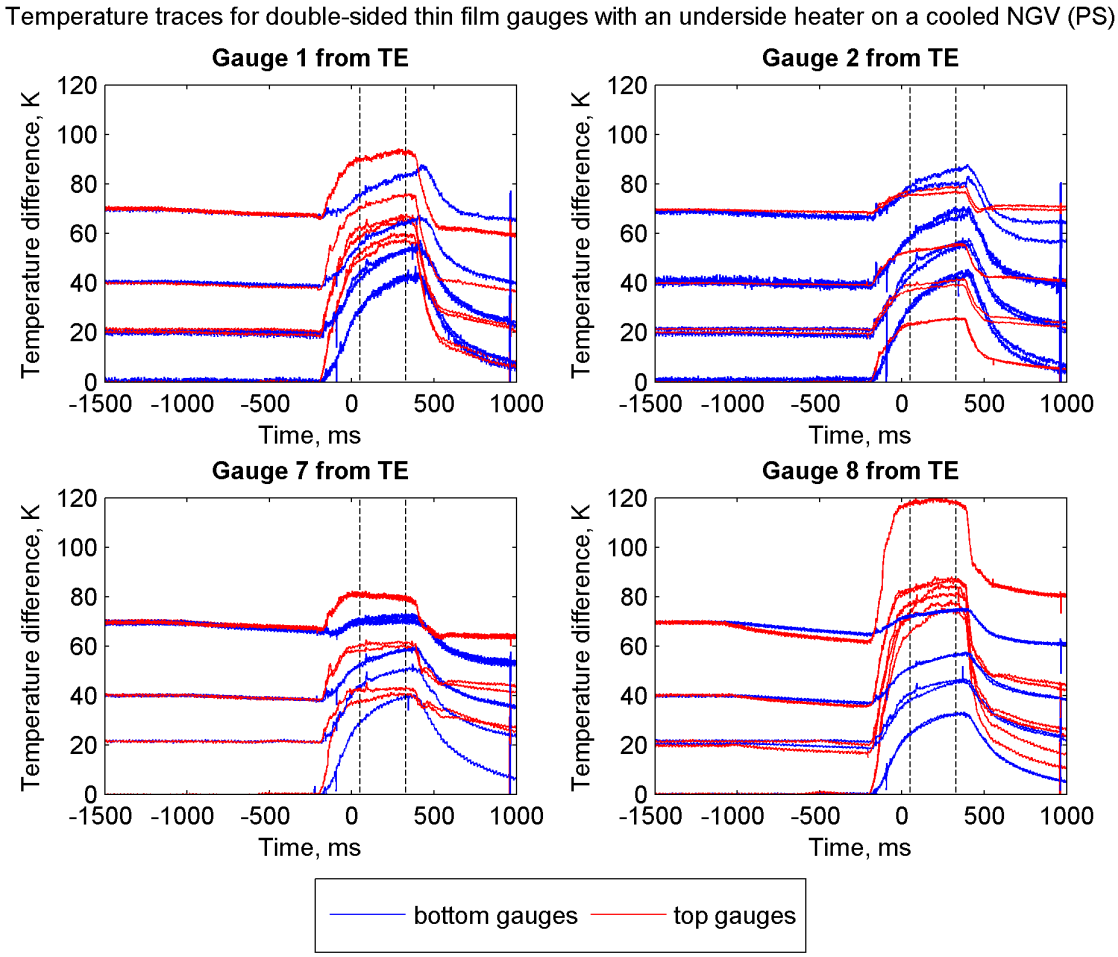

Figure 7.44: Temperature traces for four double-sided thin film gauges with an underside thin film heater on the cooled NGV C **pressure side**. The results for up to eight runs are shown (see table 7.5). The dashed lines mark a typical stable period used for the regression of one run.

side respectively. At approximately 1 s before the start of the run, the cooling air starts blowing, resulting in a reduction of the surface temperature. The quality of the data on the pressure side is poor. Out of the four "good" gauges two show erratic behaviour. Gauge 2 from the trailing edge has a hotter bottom than top gauge during the run, which would be possible for a gauge in a region of high local film effectiveness, but is unexpected for a gauge far from the film cooling holes. The temperature rise of the top gauge corresponding to gauge 7 from the trailing edge is too low. Both gauges have inconsistent regression results. The data from the suction side gauges is much better and the development of the cooling film along the aerofoil can be

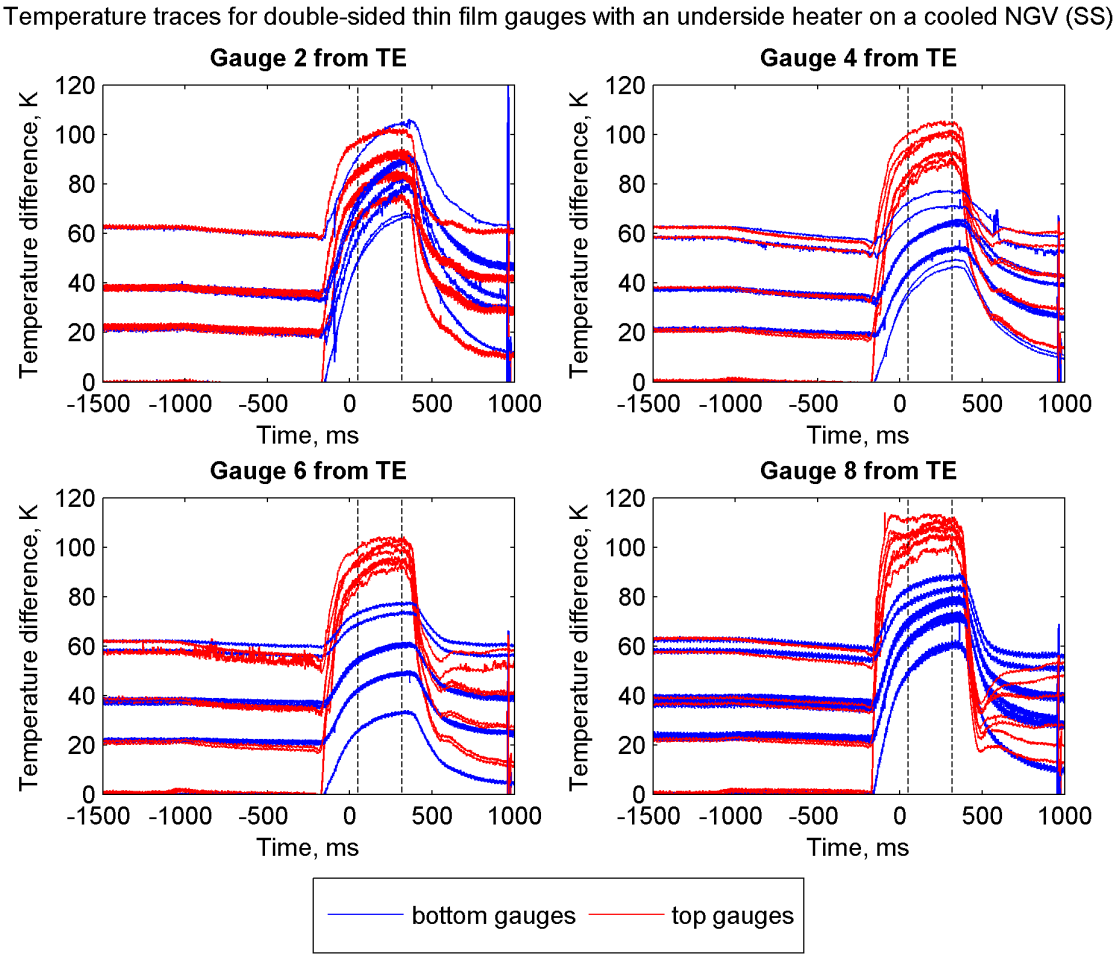

Figure 7.45: Temperature traces for four double-sided thin film gauges with an underside thin film heater on the cooled NGV C **suction side**. The results for up to eight runs are shown (see table 7.5). The dashed lines mark a typical stable period used for the regression of one run.

observed (discussion to follow).

The results for the heat flux are shown in figure 7.46 for the suction side gauges. The increase in the temperature range for the regression can be seen best for gauge 4 from the trailing edge. The effect is, however, more critical for gauge 8 from the trailing edge, which is closest to the film cooling holes. In this region the surface temperature stays nearly constant during the run and the regression range is very short. The regression results for the suction side gauges are summarised in figure 7.47 for four selected gauges.

The key advantage of using heated gauge configurations is that it is possible to separately

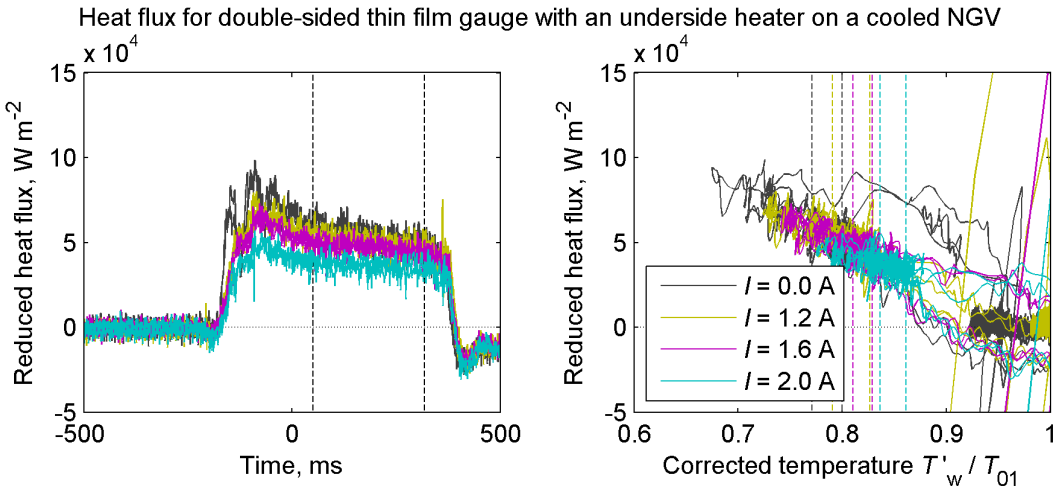

(a) Gauge 4 from trailing edge.

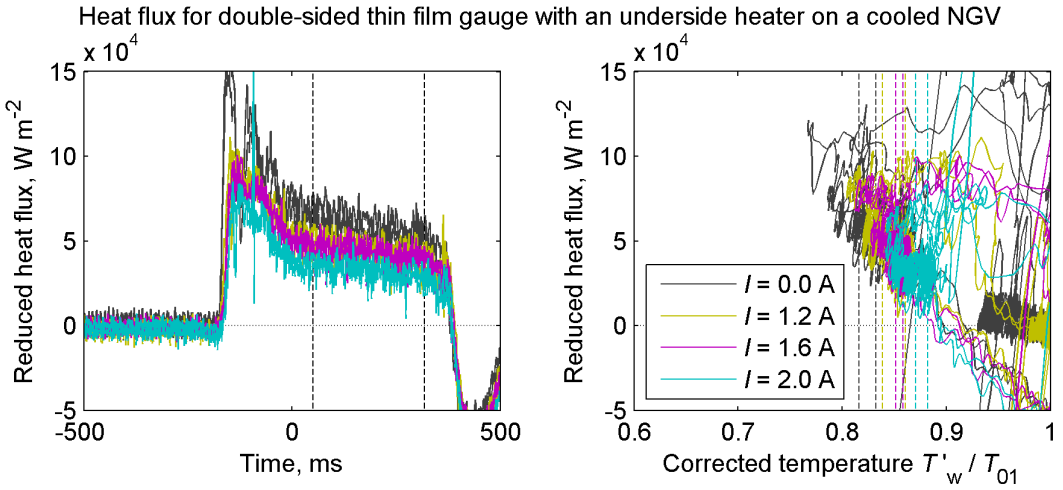

(b) Gauge 8 from trailing edge (closest to film cooling holes).

Figure 7.46: Heat flux for two double-sided thin film gauges with an underside thin film heater on the cooled NGV C **suction side**. The dashed lines mark a typical stable period used for the regression of one run and one gauge.

determine the adiabatic wall temperature and the heat transfer coefficient. For a cooled aerofoil the recovery temperature is unknown, so a forced regression would require an assumption on the heat transfer coefficient based on a model describing the effect of the cooling film. Such strong assumptions are not necessary if the range of the regression can be increased sufficiently to obtain the adiabatic wall temperature and the heat transfer coefficient from multiple regressions.

The resulting heat transfer coefficient first increases downstream of the row of film cooling

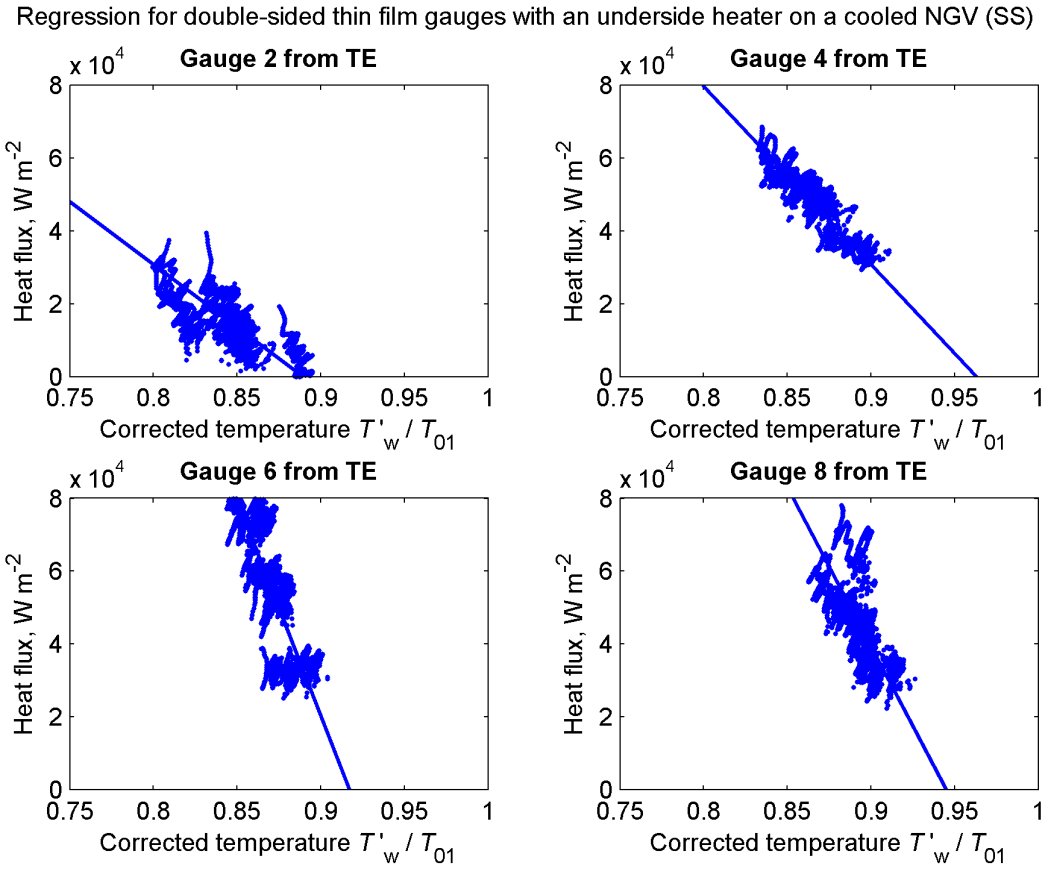

Figure 7.47: Regression data for four double-sided thin film gauges with an underside heater on the cooled NGV C **suction side**. The regression is performed on data from the stable run period.

holes and then decreases. In order to understand this behaviour an analysis of the film decay is necessary.

Cooling film performance

The performance of the cooling film can be described through a non-dimensional adiabatic film effectiveness (see equation 4.3). The coolant temperature at the cooling hole exit is assumed to be constant 290 K, as the cooling system was designed to minimise internal heat transfer and the pipework is at ambient conditions. The value of the film cooling effectiveness depends on the coolant parameters, namely the density ratio, the blowing ratio and the momentum flux ratio of the coolant jet and the local mainstream flow. Other factors that affect the film

effectiveness are the hole geometry and configuration as well as mainstream flowfield effects such as pressure gradients, curvature and freestream turbulence (Bogard and Thole, 2006).

At low blowing ratios the decay of a cooling film can be modelled with an exponential decay function, which provides a reasonable approximation to real film effectiveness decay:

$$\eta_{\mathrm{f}}(x) = \frac{T_{0\mathrm{h}} - T_{\mathrm{aw}}(x)}{T_{0\mathrm{h}} - T_{0\mathrm{c}}} = \eta_0 e^{-\lambda x^\star} \ , \tag{7.9}$$

where $T_{\mathrm{aw}}(x)$ is the film temperature (or adiabatic wall temperature), η_0 is the initial adiabatic film effectiveness, $\lambda = aL$ is the non-dimensional film decay rate (where a is the decay rate and L is the length of the system), and $x^\star = x/L$ is the normalised surface distance.

However, at high blowing ratios the coolant jets separate and reattach further downstream, resulting in lower values of film effectiveness. Studies on the spatial distribution of film effectiveness for varying blowing ratios by Baldauf et al. (2001) show the behaviour of cooling films over a range of blowing ratios. With increasing blowing ratio the peak in film effectiveness is separated from the start of the cooling film and lower maximum values are achieved. In the current test campaign at a blowing ratio of 2.07 on the suction side (see table 7.2) a maximum effectiveness of 0.25 is achieved at a distance of 13 diameters downstream of the cooling hole exit location (see figure 7.48). There is a plateau of about 9 diameters length after which the film effectiveness decays rapidly. The measured values are well within expectation. Given the 0.6 mm cooling hole diameter, the 3 mm wide gauges measure actually a laterally averaged film cooling effectiveness, which for a pitch over diameter ratio $p/d = 3$ can be maximally 0.33.

In figure 7.48 the results from the present study are compared with those reported by Baldauf et al. (2001). Both sets of experiments have measured the film cooling effectiveness downstream of one row of cylindrical film cooling holes of identical p/d and very similar cooling parameters (DR, BR and MFR). The qualitative agreement of the film cooling decay is very good. The differences can be explained by the effects of the convex surface and the increased freestream turbulence, which were not replicated in the flat-plate study.

Figure 7.49 shows a comparison of the Nusselt number over the suction surface distance between the uncooled and the cooled aerofoils. In both cases, the results for double-sided thin film gauges with an underside thin film heater are presented. For the uncooled case, the Nusselt

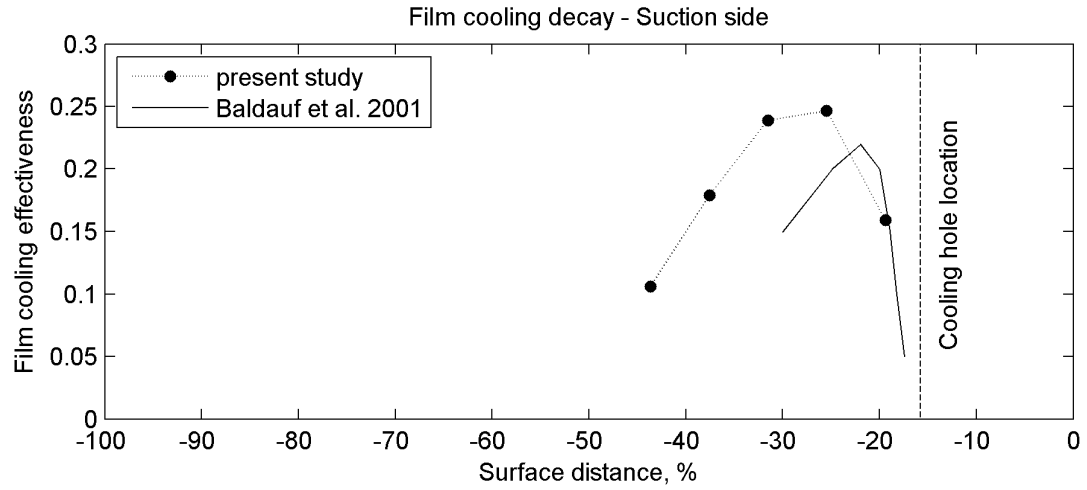

Figure 7.48: Cooling film development at mid-span for a cooling hole inclination of 50° and a blowing ratio BR = 2.07.

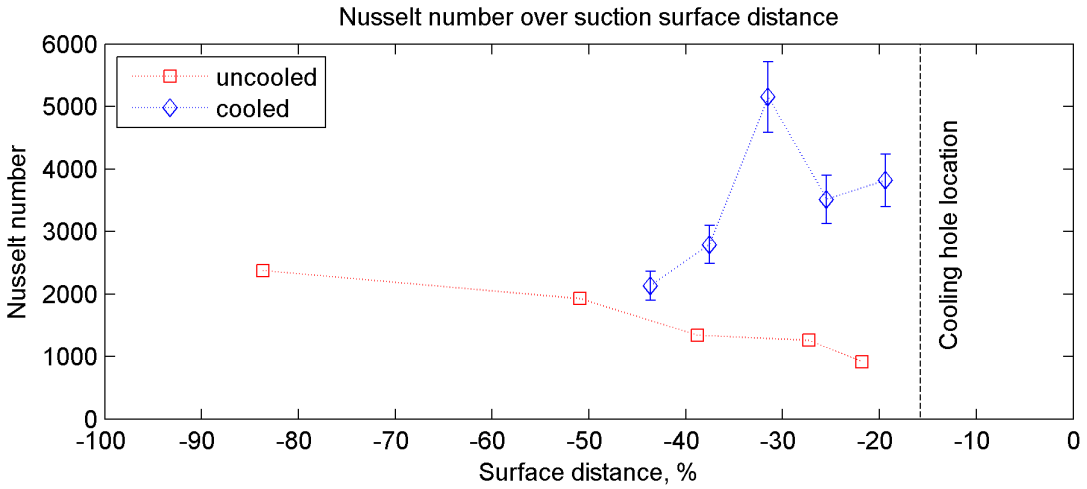

Figure 7.49: Nusselt number plotted against suction surface distance from NGV leading edge for double-sided thin film gauges with an underside heater.

number increases along the aerofoil from the transition point. The cooled results start at a higher value of the Nusselt number and then peak sharply before decreasing rapidly. The coolant is injected in the region of boundary layer transition on the uncooled vane. However, the coolant injection trips the boundary layer and there is no transitional region on the cooled vane.

Due to the simple cooling feed arrangement, the blowing ratio on the suction side is higher than desirable. Consequently, the film lifts off the surface enhancing the local heat transfer rate. This peak in Nusselt number was also observed by Chana and Mole (2000), who reported a

maximum Nusselt number at 30% surface distance. The peak corresponds to gauge 6 from the leading edge. The larger decrease in temperature difference between top and bottom gauges with increasing surface temperature already suggested a large heat transfer coefficient (see figure 7.45), which was confirmed by the regression results on figure 7.47. The benefits of film cooling can be seen on the late suction side.

Comparison of adiabatic and isothermal film cooling effectiveness

So far the film cooling effectiveness has been expressed as a function of the adiabatic wall temperature (see equation 4.3). This "adiabatic" film cooling effectiveness $\eta_{\mathrm{f,ad}}$ represents the degree to which the adiabatic surface temperature approaches the coolant temperature with respect to the freestream temperature. This definition does not account for any changes in temperature of the cooling film along the aerofoil surface. However, for the current experimental set-up heat will be transferred from the preheated surface into the coolant. As a result the adiabatic wall temperature will be different from that inferred in a perfect adiabatic set-up. Denoting the adiabatic wall temperature for an isothermal wall by $T_{\mathrm{aw,iso}}$ the corresponding isothermal film cooling effectiveness is given by

$$\eta_{\mathrm{f,iso}} = \frac{T_{0\mathrm{h}} - T_{\mathrm{aw,iso}}}{T_{0\mathrm{h}} - T_{0\mathrm{c}}} \,, \tag{7.10}$$

where both $T_{\mathrm{aw,iso}}$ and $\eta_{\mathrm{f,iso}}$ depend implicitly on the temperature of the isothermal wall T_{w}.

The quantity that determines the heat pick-up of the coolant is the Stanton number

$$\mathrm{St} = \frac{h}{\rho\, u\, c_p} \,, \tag{7.11}$$

which characterises the ratio of the heat transferred into a fluid and its thermal capacity. It has been shown (Jones and Telisinghe, 2010) that $\eta_{\mathrm{f,iso}}$ and $\eta_{\mathrm{f,ad}}$ are related by

$$\frac{\eta_{\mathrm{f,iso}}}{\eta_{\mathrm{f,ad}}} = 1 + \int_0^x \frac{\mathrm{St}}{\mathrm{BR}\, s} \left(\frac{T_{0\mathrm{h}} - T_{\mathrm{w}}}{T_{0\mathrm{h}} - T_{0\mathrm{c}}} - \eta_{\mathrm{f,ad}} \right) \mathrm{d}x \,, \tag{7.12}$$

where BR is the blowing ratio. The cooling hole geometry is included via the equivalent slot width $s = \pi d^2/4p$ with the hole diameter d and pitch p for a single row of cooling holes. For $T_{\mathrm{w}} = T_{\mathrm{aw}}$ the expression in the parenthesis cancels and therefore $\eta_{\mathrm{f,iso}} = \eta_{\mathrm{f,ad}}$. For smaller T_{w}

the expression is positive and therefore the measured film cooling effectiveness $\eta_{\mathrm{f,iso}} > \eta_{\mathrm{f,ad}}$.

For the experimental set-up under consideration, one finds

$$\frac{\mathrm{St}}{\mathrm{BR}\, s} \approx 0.01\,\mathrm{mm}^{-1}\,. \tag{7.13}$$

For the unheated case, $T_{\mathrm{w}} = 290\,\mathrm{K}$, the maximum difference obtained from equation 7.12 is then $\eta_{\mathrm{f,iso}} - \eta_{\mathrm{f,ad}} \approx 0.03$. With increasing heating power, this effect will become smaller.

7.5.2 Double-sided thin film gauges with variable heating current

The cooled NGV D was instrumented with 12 self-heating double-sided gauges on the pressure side and 13 self-heating double-sided gauges on the suction side. As for cooled NGV C, the substrate layers were staggered in order to reduce the step size after the cooling hole. When heated, the current through the top gauge was varied between 40 mA and 80 mA (see table 7.6).

Unfortunately, 10 out of 13 gauges on the suction side failed. The fact that 80% of the gauges failed on the first run and the high correlation of faulty top and bottom gauges suggests it was not a manufacturing issue (the top and bottom gauges were manufactured in different batches), but that the gauges were damaged during testing. This failure would explain why the problematic gauges were not identified during the calibration. The gauges on the pressure side, which were manufactured together with the suction side gauges, but tested first, performed well. A problem with the HTA3 boxes can be excluded, as they were successfully used on other tests. Also, in the majority of the bad gauges a drastic change in gauge resistance was measured. Possible explanations for gauge failure during operation are external gauge damage or changes in the gauge substrate, such as outgassing of the glue at low pressures, which in the worst case can lead to film delamination. In the following the results for the pressure side are presented.

The top gauge temperature was calculated from the bottom gauge temperature and the heating heat flux, which is given by the voltage across the top gauge and the top gauge resistance, using the 2D thermal conduction model. The voltage across the top gauges was varied between 1.2 V and 2.4 V. In comparison to the gauges on the uncooled NGV C, the voltage across the gauges was reduced to account for the reduced gauge resistance. The temperatures achieved by different bottom gauges are comparable, but no clear patterns can be recognised (see figure 7.50).

	Gauge current	Number of runs
Pressure side	unheated	2
	40 mA	2
	60 mA	2
	80 mA	2
Suction side	unheated	2
	40 mA	2
	60 mA	2
	80 mA	2

Table 7.6: Top gauge current settings for self-heating double-sided thin film gauges on cooled NGV D.

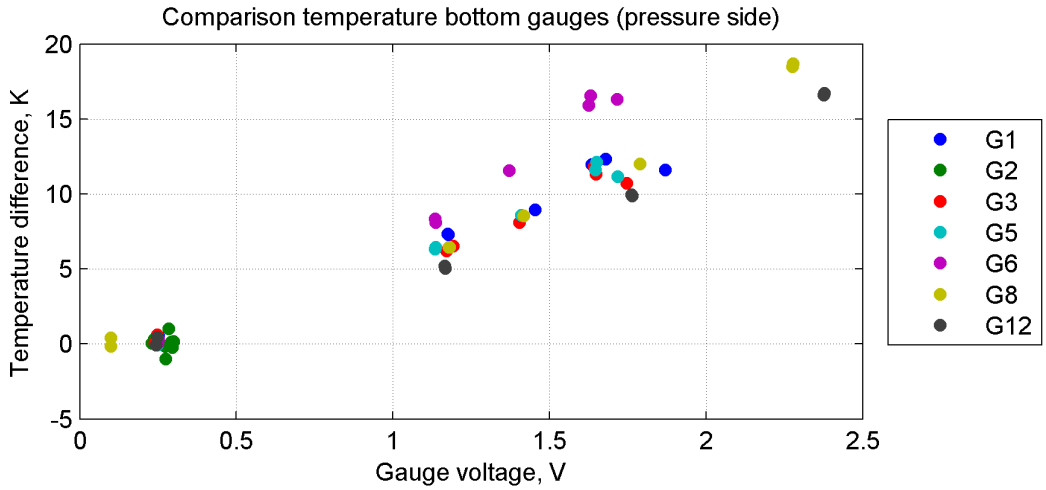

Figure 7.50: Temperature difference of the bottom gauges on cooled NGV D achieved through ohmic heating of the top gauges.

The temperature difference achieved through preheating is shown in figure 7.51 for three gauges and compared to the 2D model predictions. The temperature differences agree well with the model predictions even at higher voltages. The preheating measurements are taken before the cooling air starts to blow. Nevertheless, the hollow wall leads to an increase of the bottom gauge temperature with increasing heating power, which is in better agreement with the 2D

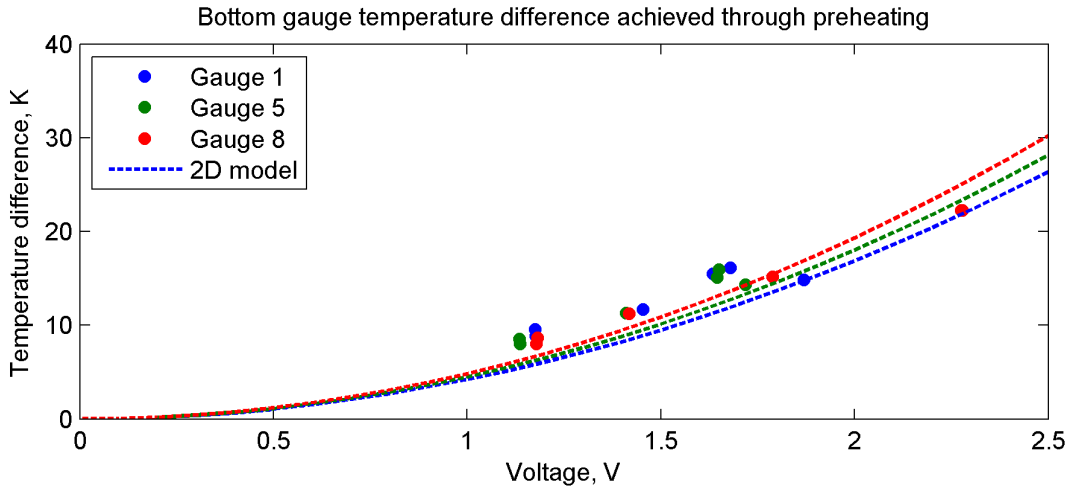

Figure 7.51: The bottom gauge temperature difference achieved for different gauge settings by three gauges on the pressure side of cooled NGV D is plotted over the voltage across the top gauge and superimposed to the 2D (dashed line) model results.

predictions.[1]The flattening of the temperature curve at high current settings is less pronounced than on the uncooled aerofoil.

Figure 7.52 shows the corresponding temperature traces. The effect of the coolant is clearly visible at -1000 ms when the cooling air starts blowing and the surface temperature decreases. One can also identify the temperature spike caused by the compression of the air in the coolant supply system (explained in figure 7.11b). For the first three runs, the cooling injection was started only 500 ms before the run and the spike occurs later. The gauge closest to the row of film cooling holes (gauge 12) has a nearly constant temperature during the run. The different gauge settings do not allow for any further comparisons at this point.

The heat flux traces are shown in figure 7.53 for the gauge closest to the film cooling holes on the pressure side (gauge 12) and for a gauge further downstream (gauge 8). Near the cooling hole exit location the temperature stays approximately constant during the run and the range for the regression is shorter. It is nevertheless possible to perform a regression and the expectation of a very high heat transfer coefficient is confirmed. Further downstream a slower increase in surface temperature during the run is observed. The corresponding regression results are

[1]The uncooled NGVs also have an inner cavity, but it is used to lead the wires out and hence it is blocked with sealant.

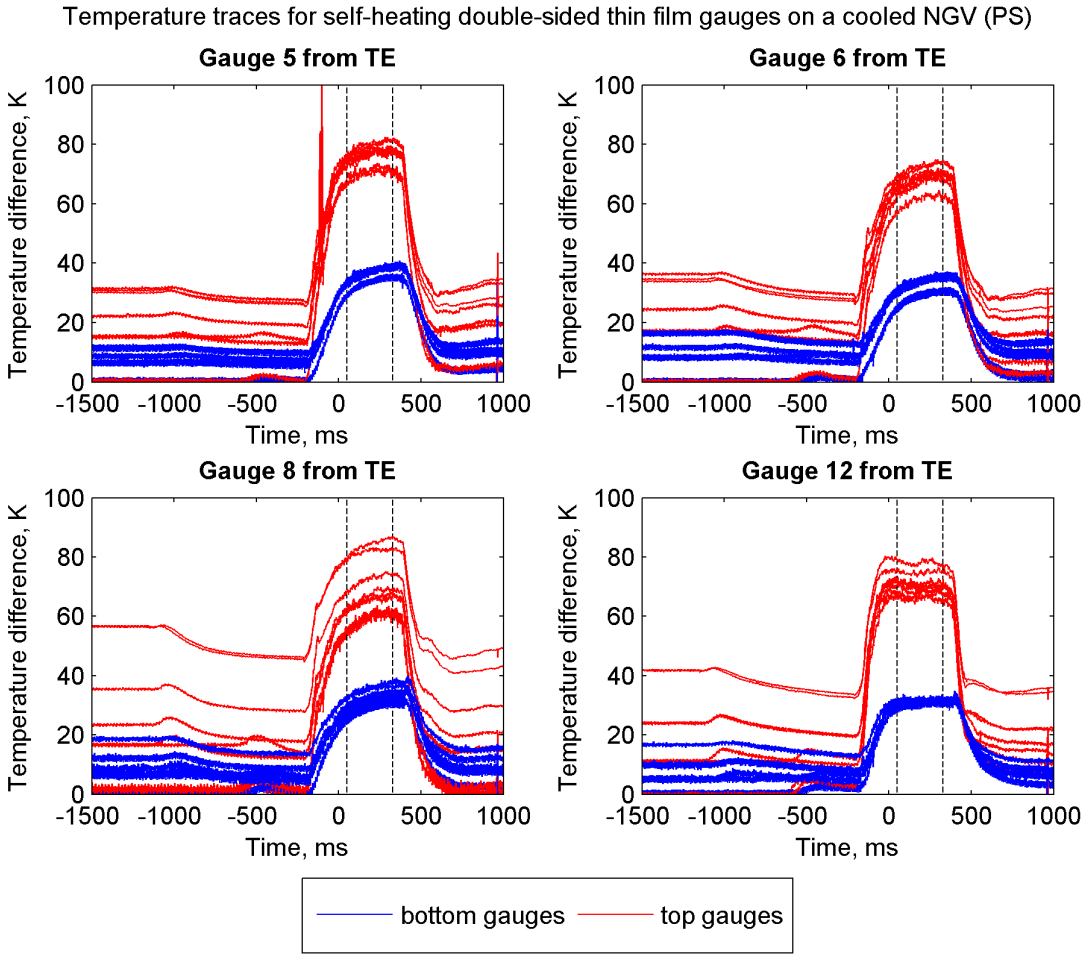

Figure 7.52: Temperature traces for four self-heating double-sided thin film gauges on the cooled NGV D **pressure side**. The results for up to eight runs are shown (see table 7.6). The dashed lines mark a typical stable period used for the regression of one run.

shown in figure 7.54. The data for the regression is very neat and it is possible to separate the heat transfer coefficient and the adiabatic wall temperature for the shown gauges. As for the self-heating double-sided gauges on the uncooled NGV C, the 2D prediction of the top gauge temperature gives a higher heat transfer coefficient than expected from the unheated measurements (see section 5.5).

The Nusselt number distribution is compared in figure 7.55 to the results from an uncooled NGV instrumented with self-heating double-sided thin film gauges. The uncooled results were obtained defining the recovery temperature. The results on cooled NGVs presented by Chana and Mole (2000) also reported a steep decrease in Nusselt number from Nu = 2500 to Nu = 1000

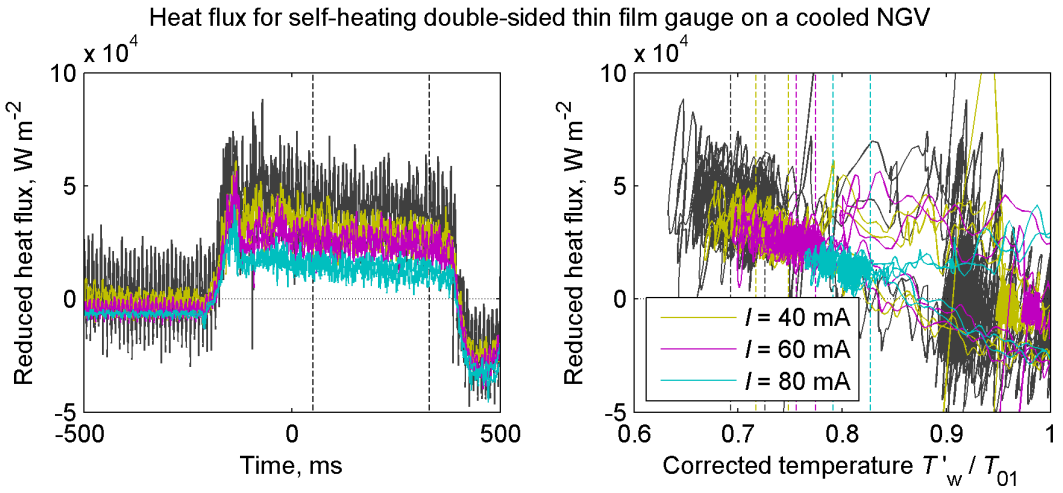

(a) Gauge 8 from trailing edge.

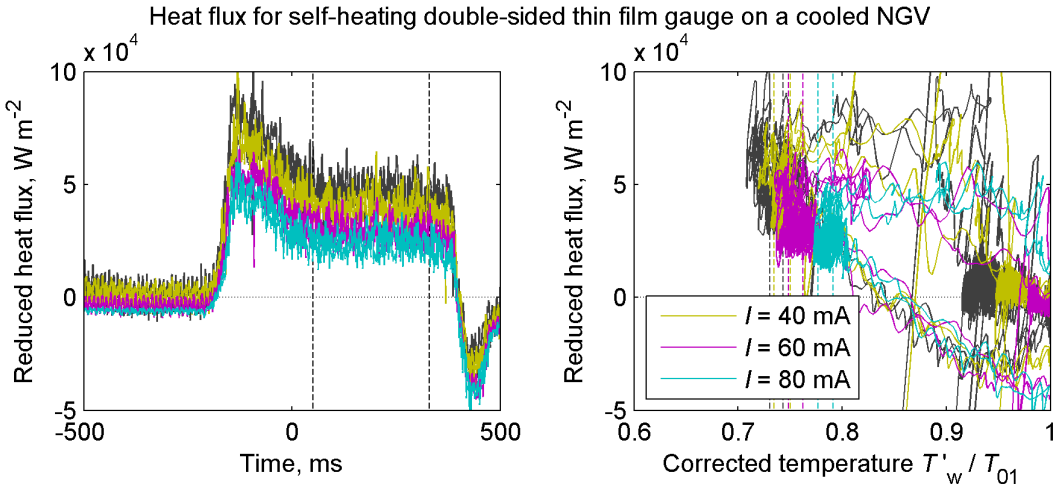

(b) Gauge 12 from trailing edge (closest to film cooling holes).

Figure 7.53: Heat flux for two self-heating double-sided thin film gauges on the cooled NGV D **pressure side**. The dashed lines mark a typical stable period used for the regression of one run and one gauge. The unheated results are plotted in grey.

up to 50% surface distance downstream of the pressure side cooling holes. Near the trailing edge the cooling films have usually dissipated and the heat transfer coefficient is expected to be similar to that of the uncooled vane. However, at very high blowing ratios (detailed in table 7.2) the film lifts off and persist further downstream at higher values of film effectiveness. This behaviour is confirmed by an analysis of the cooling film decay.

The performance of the pressure side cooling film is described by the adiabatic film effectiveness

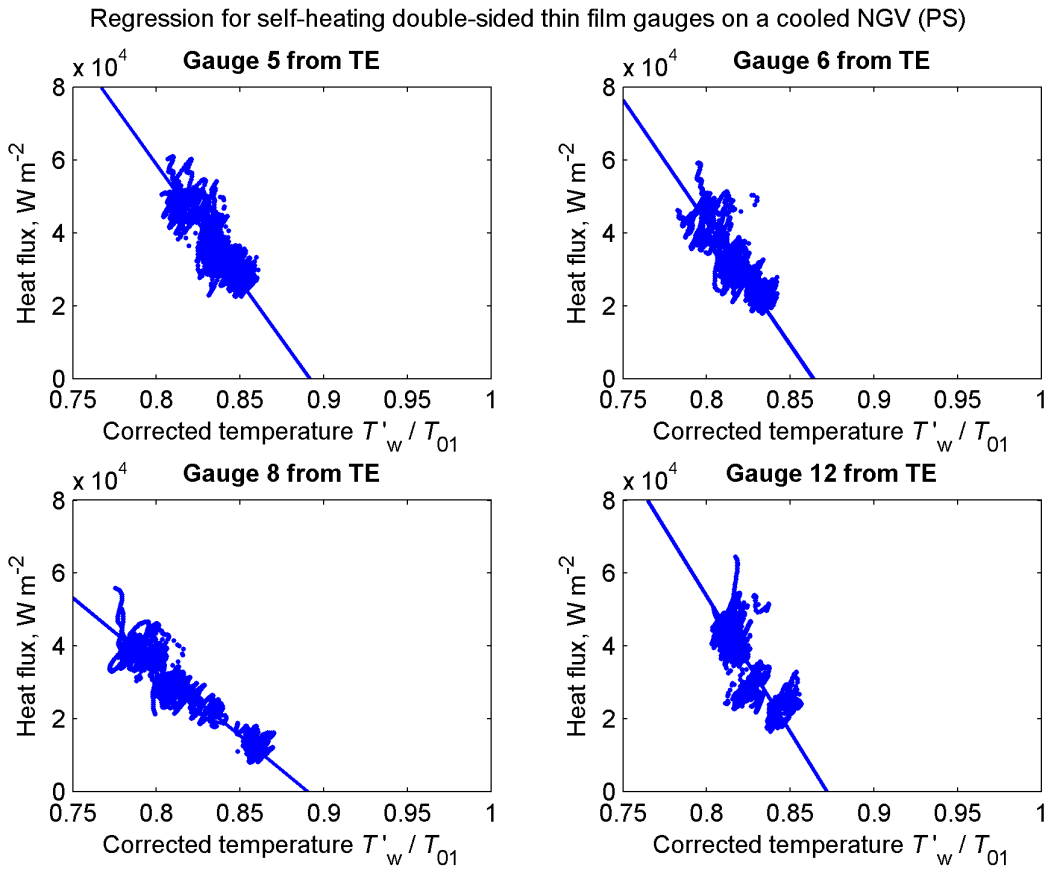

Figure 7.54: Regression data for four self-heating double-sided thin film gauges on the cooled NGV D **pressure side**. The regression is performed on data from the stable run period.

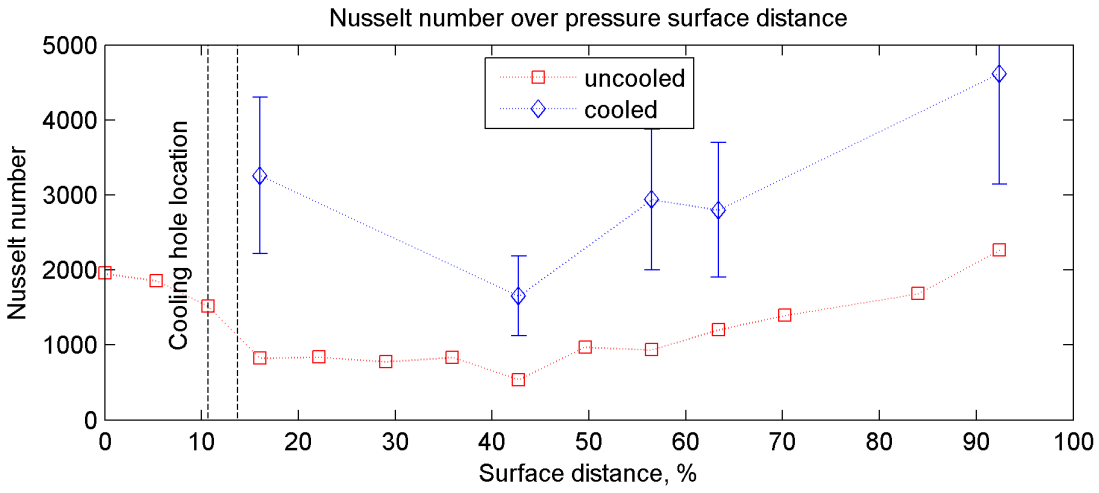

Figure 7.55: Nusselt number plotted against pressure surface distance from NGV leading edge for self-heating double-sided thin film gauges.

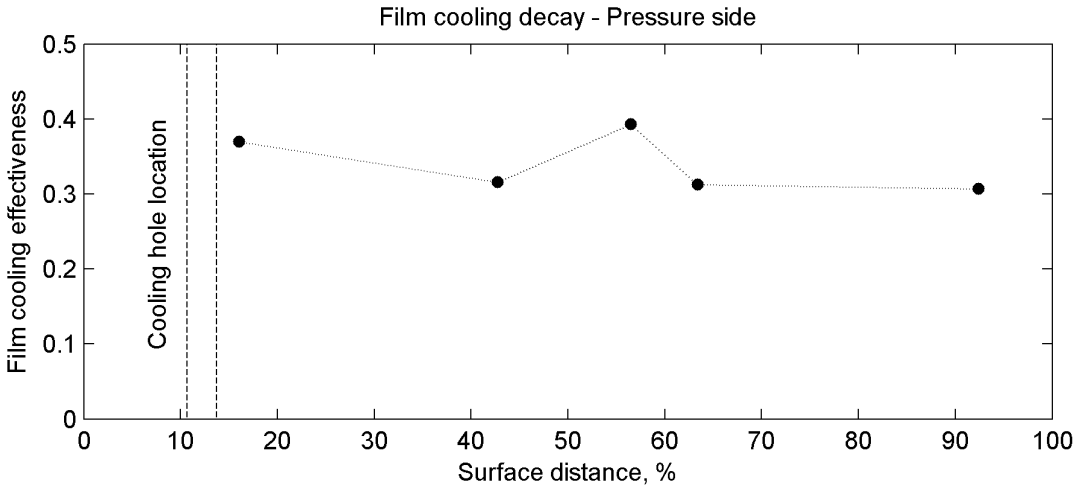

Figure 7.56: Cooling film development at mid-span for a cooling hole inclination of 50° and a blowing ratio BR = 11.8.

(see figure 7.56). At a blowing ratio of 11.8 an effectiveness of 0.37 is achieved 2 diameters downstream of the cooling hole exit location. The resolution is not high enough to resolve flow phenomena near the cooling hole, but the decay is very slow and flattens out at mid distance. This behaviour is typical for jet lift-off at high blowing ratios. It is very unfortunate that the gauges on the suction side failed, because it will not be possible to show a comparison of the performance of the cooling film and the cooled heat transfer results between NGVs C and D.

7.6 Summary aerofoil measurements

Four different types of thin film gauges have been used to perform heat transfer measurements on NGV aerofoils, namely single-sided gauges, double-sided gauges, double sided gauges with an underside heater and self-heating double-sided gauges. Nusselt number distributions along the aerofoil chord have been obtained from all four gauge types. For the single-sided and double-sided gauges it was necessary to define the adiabatic wall temperature to obtain the heat transfer coefficient. In contrast, using heated configurations extends the range of the regression and makes it possible to separate the adiabatic wall temperature and the heat transfer coefficient. Such a separation is crucial in the presence of cooling, where no reliable assumption on the heat transfer coefficient can be made.

Moreover, it requires special instrumentation such as double-sided thin film gauges to measure the heat transfer on a cooled thin wall. In this chapter, heated double-sided thin film gauges were successfully used to study cooled aerofoils and in particular to investigate the film cooling effectiveness. The accurate determination of non-dimensional parameters of heat transfer on cooled aerofoils is of great importance for the design of turbine cooling systems and for the validation of CFD data.

CHAPTER 8

Conclusions

Improving the cooling systems in HP turbine stages presents a key challenge for increasing the thermal efficiency of gas turbines. For this purpose it is crucial to understand the interaction of cooling flows with engine-realistic inlet flows (with temperature distortion and high swirl). Transient turbine facilities with engine-size turbine stages offer a unique opportunity for performing this kind of measurements. Nevertheless, making the best use of these facilities and accurately studying such a complex environment requires the development of improved instrumentation. The work presented in this thesis has contributed significantly to advancing heat transfer measurements for cooled turbine stages. A novel gauge configuration based on double-sided thin film gauges has been designed to measure the heat transfer at low temperature differences on non-isothermal surfaces. The heating of the gauge substrate allows to accurately determine the adiabatic wall temperature and the heat transfer coefficient on cooled aerofoils. The combination of double-sided gauges with local surface heating arrangements is unique in that it allows measurements to be taken on intricate geometries without the need for complex heating systems.

The results presented in this thesis are summarised in section 8.1. An overview of future work regarding the use of heated double-sided gauges in the OTRF is given in section 8.2.

8.1 Summary

This thesis can be divided into three distinct parts: the design of a fully cooled HP turbine stage for the OTRF (chapter 3), the development and the implementation of the gauge concept

(chapters 4 and 5) and finally the testing of the new gauges in the OTRF (chapters 6 and 7). The first part can be considered a separate project, as the turbine stage will not be tested in the OTRF until late 2016.

A new fully cooled turbine stage was designed within the Rolls-Royce SILOET programme. The turbine stage will have a fully cooled HP NGV and HP rotor (including TE slots and the blade root seal leakage flow). The design of the turbine stage considered aerodynamics and heat transfer as well as mechanical aspects. It is the first turbine designed for lean-burn combustor exit flows with combined temperature distortion and swirl. A mechanical assessment of a bladed disc was conducted to determine the steady-state stresses and the fatigue life. The natural frequencies of the system were obtained from a dynamic analysis and a safe operation at the design speed was confirmed. The cooling capacities were predicted using Rolls-Royce models. The turbine stage has since been manufactured and is now ready for installation.

Thin film gauges are widely used to measure the heat transfer in short-duration rotating facilities. In comparison to traditional single-sided gauges, double-sided gauges have the advantage that they do not require a 1D assumption of the heat conduction into the wall making them particularly well suited to record the heat transfer data on a cooled geometry. The transient behaviour of a double-sided thin film gauge was investigated with a 1D FE multi-layer model. This model served to define the gauge design parameters, such as the substrate thickness, and to evaluate the performance of the double-sided gauges compared to a baseline case with a semi-infinite wall. Heating the substrate allows to improve the regression used to obtain the adiabatic wall temperature and the heat transfer coefficient from the measured wall temperature and heat transfer rate. The magnitude of this potential improvement was assessed with a stability criterion for the regression. The effect of lateral conduction in the substrate of heated gauges was discussed and an analytical model to investigate it was introduced.

The final gauge design was based on the latest thin film gauge manufacturing technology. Two heating configurations were developed, namely double-sided gauges with an underside thin film heater and self-heating double-sided gauges, which use the ohmic heating of the gauges to create a pre-run temperature distribution. Due to the change in current for the self-heating gauges, the two heating arrangements require different measurement strategies to compute the

temperature from the recorded voltage trace. These measurement strategies have been detailed for further use of these gauges in a similar experimental set-up, as outlined in figure 5.8. The main challenge of the heated gauges is the determination of the gauge initial temperature. For the double-sided gauges with a heater the initial temperature achieved over a range of heater settings was measured on the bench and used to validate models of the thermal conduction in the gauge substrate. For self-heating double-sided gauges more complex models were required which described the thermal conduction in the gauge substrate taking into account 2D and 3D effects.

The experimental uncertainties related to the acquisition of heat transfer data using heated gauges were investigated. The systematic error sources for a single run were identified and evaluated (see table 5.1). The effect on the regression of the uncertainties in the measurement of the initial gauge temperature – including modelling uncertainties – and the heating heat flux as well as in the calculation of the temperature difference were analysed (see figure 5.21). Heating the gauge substrate improves the reliability of the linear regression, despite leading to larger systematic uncertainties due to the need to compare runs with different initial temperatures. The uncertainty in the heat transfer coefficient and the adiabatic wall temperature was computed for a combination of unheated and heated runs (see table 5.2). With the current thermal models for the self-heating gauges, the uncertainties affecting the determination of the initial gauge temperature are high, and the gauges with an underside heater achieve more accurate results.

The double-sided gauges with both heating arrangements were tested in the OTRF under engine-realistic conditions on the turbine casing of a simple nozzle configuration. The heat transfer results were compared to those obtained from single-sided and unheated double-sided gauges. These experiments served as a proof of concept for the new gauge system and validated the thermal models introduced before. With both heated systems it was possible to separately determine the adiabatic wall temperature and the heat transfer coefficient. In general good agreement was achieved with correlations from literature and with the predictions from a boundary layer code. The improvement in the regression from the single-sided and unheated double-sided gauges to the heated gauge configurations was quantified in terms of the stability criterion (see table 6.5).

Finally, the double-sided gauges with an underside thin film heater and the self-heating double-sided gauges were used to measure the heat transfer on uncooled and cooled HP NGVs. For comparison, two additional vanes were instrumented with single-sided and unheated double-sided gauges. The Nusselt number distribution over the surface distance at mid-span was measured with each gauge type and compared to previous experimental data (see for example figures 7.41 and 7.49). The wide range of pre-run temperatures achieved with the heated arrangements resulted in a very accurate regression, which allowed to separate the adiabatic wall temperature and the heat transfer coefficient. Most importantly, it was also possible to measure the heat transfer on the cooled aerofoils and determine the film cooling effectiveness on the cooled NGVs to observe the decay of the cooling film. The new gauges have shown to perform very well at low temperature differences and are thus ideally suited to measure the heat transfer on future fully cooled geometries.

8.2 Outlook

The work presented in this thesis contributes to two major test programmes on the OTRF. The LEMCOTEC turbine stage is currently being commissioned (see section 2.3). The HP NGVs are heavily cooled and have engine-realistic external cooling features. The heat transfer will be measured with double-sided thin film gauges with an underside heater. The shower head cannot be instrumented, but in order to fit gauges between the rows of film cooling holes, their lateral extent has been reduced to 1.1 mm. These gauges have been manufactured using the double-sided manufacturing process described in section 5.1. Furthermore, to minimise flow disruption, pockets have been machined on the aerofoil surface for the thin film heater and the gauges. Bespoke heaters have been designed for each gauge location. The first measurements are expected to be taken from April 2016 under uniform conditions and then tests will be conducted with inlet temperature distortion and swirl. The SILOET turbine stage designed for this thesis (see chapter 3) will be tested next.

The crux of using heated thin film gauge configurations is the measurement of the initial gauge temperature. The heat transfer measurements using double-sided thin film gauges with a

heater element on the LEMCOTEC NGVs can be performed as discussed in section 5.4. It is desirable to conduct bench tests of the new heater designs to measure the achievable surface temperature over a range of heater currents. However, it is also important to better understand the heat losses into the working section prior to the run, so that the data from the bench tests can be applied on the rig. Ideally the initial gauge temperature could also be inferred externally (e.g. with a thermocouple) and compared to the rig measurement.

For the self-heating gauges the accurate determination of the initial gauge temperature is critical. To reduce the modelling uncertainties it is suggested to perform a 3D FEA model of the thermal conduction in the gauge substrate. The predictions of the model would allow to better interpret the measured bottom gauge temperatures. The resulting model can be validated on the bench by measuring the (bottom) gauge temperatures for different top gauge currents. In addition it is desirable to take temperature measurements on the wall at the gauge location with thermocouples and to measure the top gauge temperature using IR thermography. This information can then be used together with knowledge of the heat loss into the working section to determine the initial top gauge temperature at the start of the run for a given gauge current. With these improvements the accuracy and reliability of the self-heating gauges is expected to be as high as that of the gauges with an underside heater.

Thin film gauges will continue to play a very important role in the heat transfer measurements in experimental facilities. For the study of cooled engine parts there are three key challenges: to improve the manufacturing technology in order to increase the spatial resolution of the measurements, to reduce the uncertainties arising from the assumption of a simplified geometry to model the thermal conduction in the gauge substrate, and to develop methods to accurately determine the Nusselt number and the film cooling effectiveness. This thesis has made important contributions to each of these areas and it is to be expected that heated double-sided gauges will yield interesting results in the near future.

Appendices

A.1 HTA3 Heat Transfer Amplifier

The HTA3 thin film signal condition amplifier is described in (Oldfield and Beard, 2014). It consists of a two-breakpoint, gain-shaping differential amplifier and it has a built-in constant current source. The HTA3 is used to power the thin film gauges and to record the heat transfer signal. For the self-heating double-sided gauges it was necessary to increase the basic 20 mA maximum current source up to 150 mA maximum by modifying the circuit (see figure A.1). For completeness the original circuit diagram is shown in figure A.2

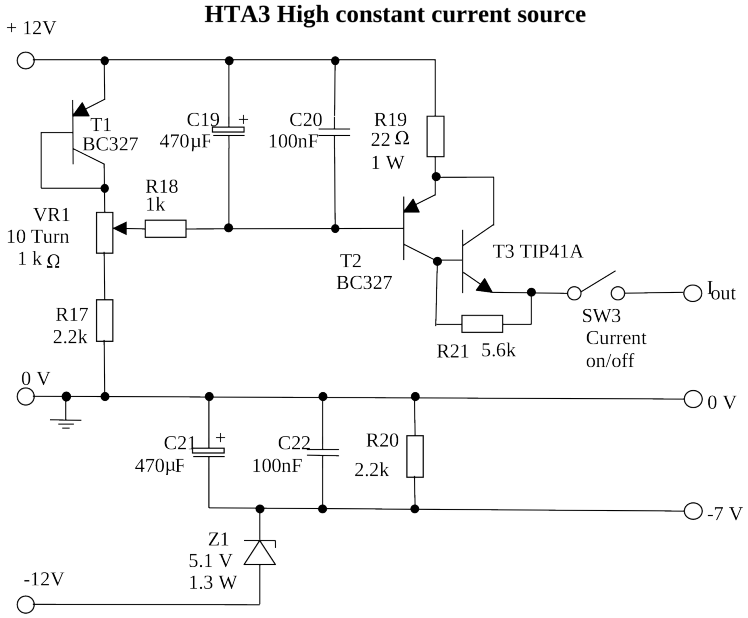

Figure A.1: High constant current source modification.

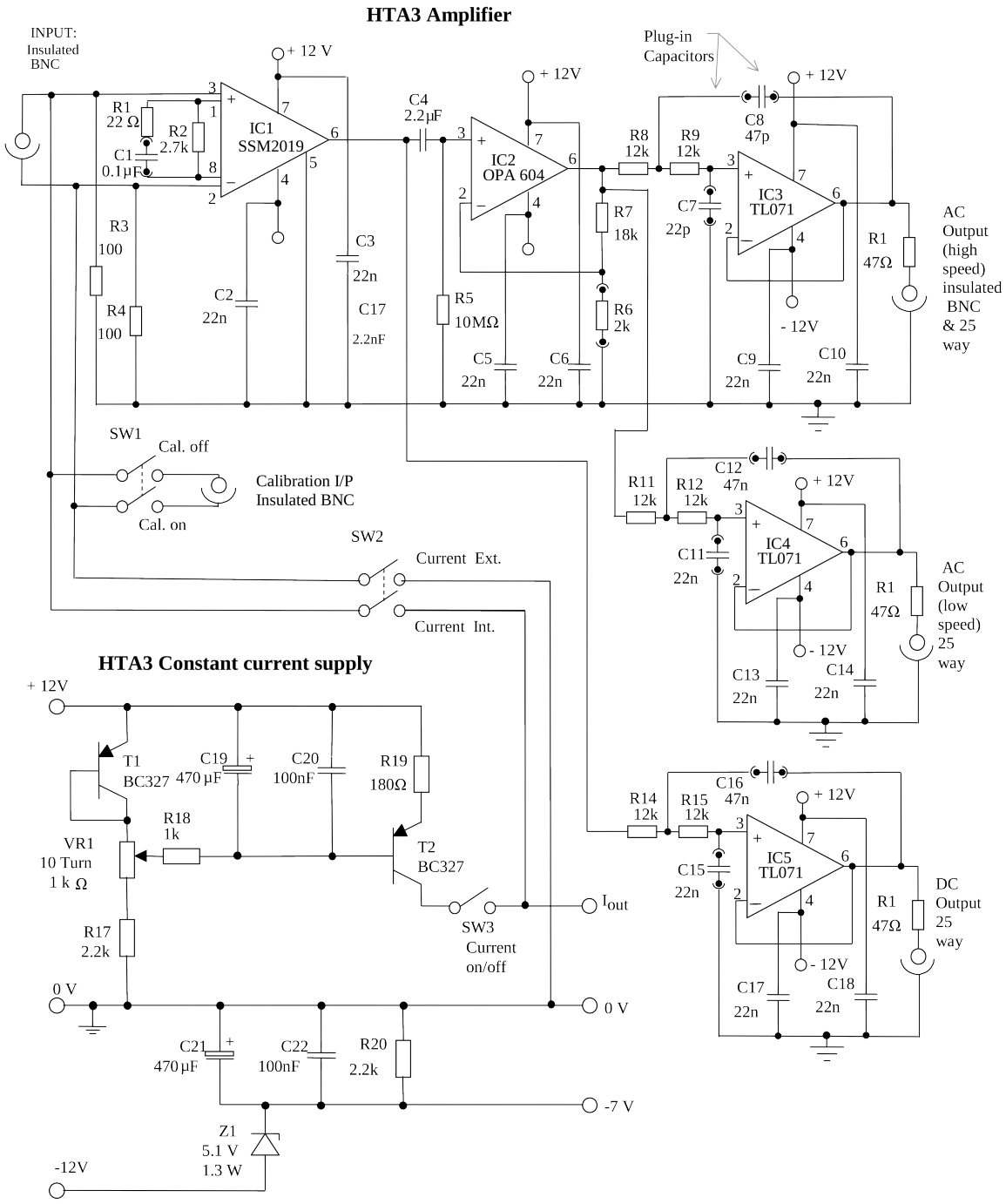

Figure A.2: Circuit diagram of single channel of HTA3 thin film gauge signal conditioning unit.

A.2 Issues with the reference voltage measurement

The heat transfer on a turbine casing was measured using double-sided thin film gauges and self-heating double-sided thin film gauges, where the latter are connected to the modified HTA3 box (see chapter 6). It is expected that the unheated self-heating gauges will see the same temperature rise during the run as the double-sided gauges, which are placed on the same axial location and have an identical configuration. However, an issue with the reference voltage measurement of the self-heating gauges was observed and the expectation could not be confirmed. The voltage traces for both sets of gauges are shown in figure A.3. The double-sided gauges and bottom gauges of the self-heating double-sided gauges are set to 0.25 V prior to the run. For this comparison the current through the top gauges of the self-heating gauges was set at about 5 mA for the duration of the run – they are unheated.

If the reference voltage measurement, which is taken about 3 min before the run, is subtracted from the voltage trace, the result should be proportional to the change in temperature since the acquisition of the reference measurement. This approach works very well for the unheated thin film gauges as well as the bottom gauges of the self-heating thin film gauges (see figure A.4). The top gauges of the self-heating gauges, however, show a change in voltage between the reference measurement and the beginning of the run, which has no external origin.[1] The recorded variation in voltage agrees with the larger voltage instability observed with the modified HTA3 boxes used for the current supply.

If the voltage measurement at the start of the run is subtracted from the voltage trace, very similar results are obtained for the unheated double-sided and for the self-heating double-sided gauges (figure A.5). Two observations can be made from this plot: First, that the unheated and self-heating gauges experience the same voltage change during a run; second, that in spite of the variation of the absolute voltage at the beginning of the run all self-heating gauges give consistent results for the change in voltage during the run.

In order to obtain the temperature difference, the voltage difference is divided by the absolute

[1] The physical effects that could lead to a heating (or cooling) of the gauge surface before the run were discussed in chapter 6, leading to the conclusion that in the absence of heating the rig is still at isothermal conditions at the start of the run.

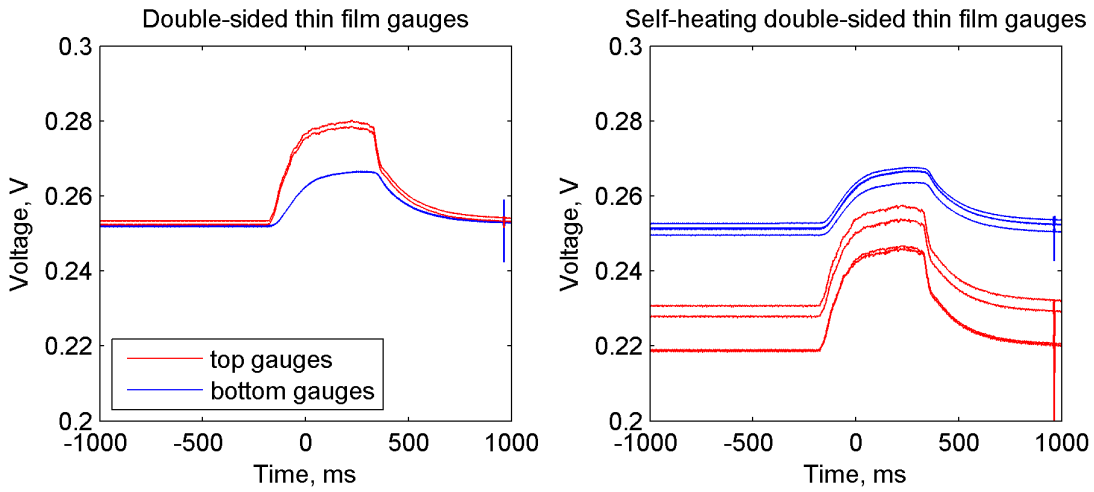

Figure A.3: Voltage traces for two double-sided thin film gauges compared to voltage traces for four self-heating double-sided thin film gauges (unheated case).

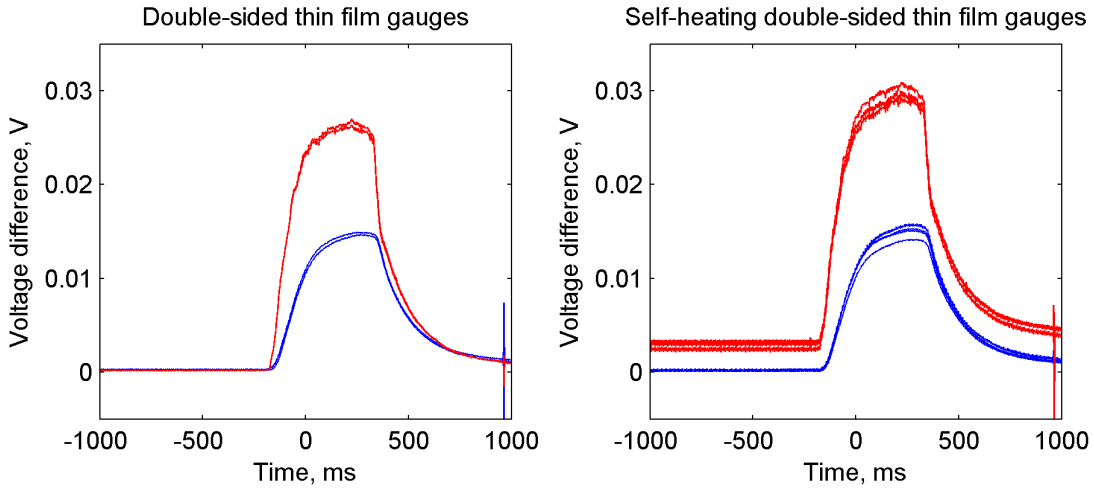

Figure A.4: Voltage difference from the acquisition of the reference measurement for two double-sided and four self-heating double-sided thin film gauges (unheated case).

voltage at the start of the run following equation 5.17. Since all top gauges were manufactured in the same batch, they have similar resistances and temperature coefficients of resistance. The temperature difference should therefore be proportional to the ratio $\Delta V/V_{\mathrm{gi}}$. The voltage ratios shown in figure A.6 however are clearly inconsistent, because they suggest that the self-heating gauges heat up more during the run and thus observe a higher heat flux. Moreover, two of the gauges seem to see a significantly higher temperature than the others, which is not physical (and not reproduced by the bottom gauges). This result can be traced back to the lower absolute

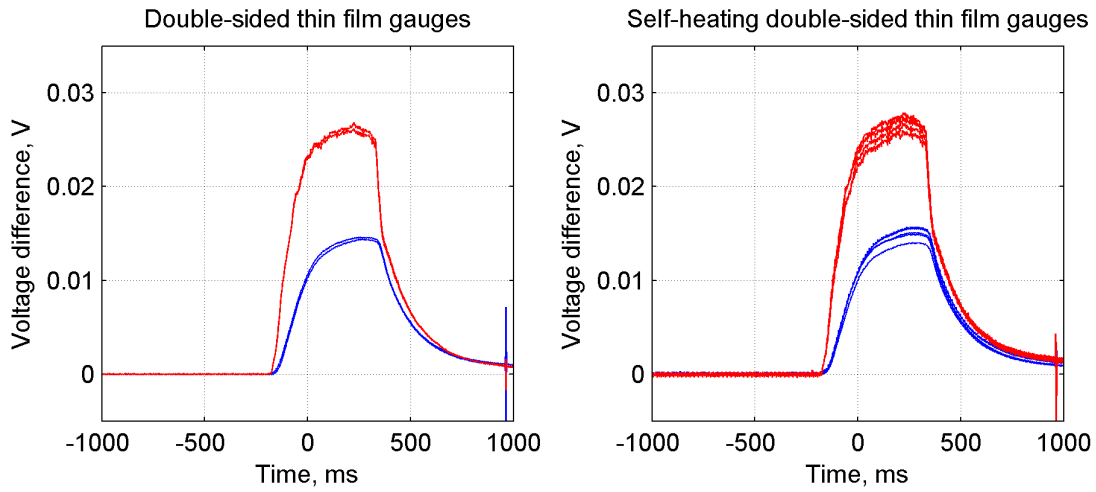

Figure A.5: Voltage difference from the start of the run for two double-sided and four self-heating double-sided thin film gauges (unheated case).

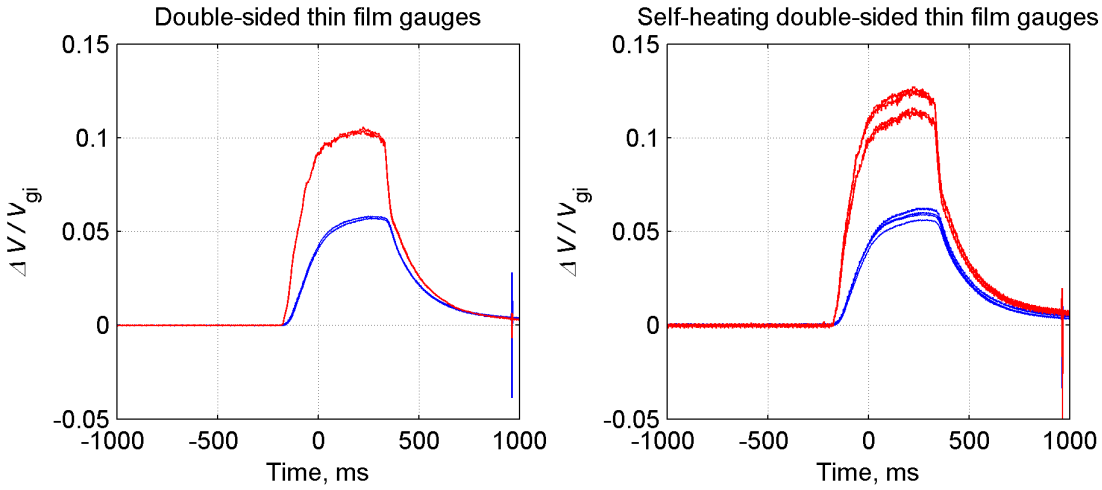

Figure A.6: Voltage difference divided by voltage at the start of the run for two double-sided and four self-heating double-sided thin film gauges (unheated case).

voltage (see figure A.3), i.e. the discrepancies observed in figure A.6 result from the variation in the initial voltage measurements.

For future test campaigns the HTA3 boxes have been modified to provide the possibility to directly measure the current through the gauges, which can be used to infer the reference voltage. For the measurements on the aerofoils presented in chapter 7, the issue was avoided by ensuring that the reference voltage is set to 0.25 V for all gauges and for all runs.

Bibliography

3M. VHB^{TM} Adhesive Transfer Tapes with Adhesive 100MP. Technical Data Sheet, 2005.

Anthony, R. J. *Boundary Layer Transition under Freestream Turbulence, Pressure Gradient and Crossflow*. DPhil thesis, 2002.

Anthony, R. J., Clark, J. P., Kennedy, S. W., Finnegan, J. M., Johnson, D., Hendershot, J., and Downs, J. Flexible Non-Intrusive Heat Flux Instrumentation on the AFRL Research Turbine. In *Proceedings of the ASME Turbo Expo*, volume 5, 2011. GT2011-46853.

Anthony, R. J., Clark, J. P., Finnegan, J. M., and Johnson, D. Modifications and Upgrades to the AFRL Turbine Research Facility. In *Proceedings of the ASME Turbo Expo*, volume 4, 2012. GT2012-70084.

Baldauf, S., Schulz, A., and Wittig, S. High-Resolution Measurements of Local Effectiveness from Discrete Hole Film Cooling. *Journal of Turbomachinery*, 123(4):758–765, 2001.

Beard, P. F., Povey, T., and Chana, K. S. Effect of Aggressive Inlet Swirl on Heat Transfer and Aerodynamics in an Unshrouded Transonic HP Turbine. *Journal of Turbomachinery*, 132(1): 011002, 2010.

Bogard, D. G. and Thole, K. A. Gas Turbine Film Cooling. *Journal of Propulsion and Power*, 22(2):249–270, 2006.

Brooks, A. J., Colbourne, D. E., Wedlake, E. T., Jones, T. V., Oldfield, M. L. G., Schultz, D. L., and Loftus, P. J. The Isentropic Light Piston Annular Cascade Facility at REA Pyestock. In *AGARD Heat Transfer and Cooling in Gas Turbines*, 1985.

Buttsworth, D. R. and Jones, T. V. Radial Conduction Effects in Transient Heat Transfer Experiments. *The Aeronautical Journal*, 101(1005):209–212, 1997.

Buttsworth, D. R. and Jones, T. V. A Fast-Response Total Temperature Probe for Unsteady Compressible Flows. *Journal of Engineering for Gas Turbines and Power*, 120(4):694–702, 1998a.

Buttsworth, D. R. and Jones, T. V. A Fast-Response High Spatial Resolution Total Temperature Probe Using a Pulsed Heating Technique. *Journal of Turbomachinery*, 120(3):601–607, 1998b.

Buttsworth, D. R., Jones, T. V., and Chana, K. S. Unsteady Total Temperature Measurements Downstream of a High-Pressure Turbine. *Journal of Turbomachinery*, 120(4):760–767, 1998.

Chana, K. S. Fluid Temperature Measurement. Patent, 2004. US 20050281312 A1.

Chana, K. S. and Haller, B. R. Novel Turbine Rotor Shroud Film-Cooling Design and Validation: Part 1. In *Proceedings of the ASME Turbo Expo*, volume 3, 2009a. GT2009-60242.

Chana, K. S. and Haller, B. R. Novel Turbine Rotor Shroud Film-Cooling Design and Validation: Part 2. In *Proceedings of the ASME Turbo Expo*, volume 3, 2009b. GT2009-60246.

Chana, K. S. and Haller, B. R. Prediction of the Influence of Upstream Wake Passing on Downstream Blade Row External Heat Transfer Coefficient – A New Physically-Based Method. In *Proceedings of the ASME Turbo Expo*, volume 4, 2010. GT2010-23314.

Chana, K. S. and Jones, T. V. An Investigation on Turbine Tip and Shroud Heat Transfer. *Journal of Turbomachinery*, 125(3):513–520, 2003.

Chana, K. S. and Mole, A. H. A Summary of Cooled NGVs and Un-cooled Rotor Measurements from the MT1 Single Stage High Pressure Turbine in the DERA Isentropic Light Piston Facility (UL). *TATEF Project (BRPR-CT97-0519)*, 2000.

Chana, K. S., Hurrion, J. R., and Jones, T. V. The Design, Development and Testing of a Non-Uniform Inlet Temperature Generator for the QinetiQ Transient Turbine Research Facility. In *Proceedings of the ASME Turbo Expo*, volume 6, 2003a. GT2003-38469.

Chana, K. S., Povey, T., and Jones, T. V. Heat Transfer and Aerodynamics of an Intermediate Pressure Nozzle Guide Vane with and without Inlet Temperature Non-Uniformity. In *Proceedings of the ASME Turbo Expo*, volume 6, 2003b. GT2003-38466.

Chana, K. S., Cardwell, D., and Jones, T. V. A Review of the Oxford Turbine Research Facility. In *Proceedings of the ASME Turbo Expo*, volume 3C, 2013. GT2013-95687.

Collins, M., Chana, K. S., and Povey, T. New Technique for the Fabrication of Miniature Thin Film Heat Flux Gauges. *Measurement Science and Technology*, 26(2):025303, 2015a.

Collins, M., Chana, K. S., and Povey, T. Improved Methodologies for Time Resolved Heat Transfer Measurements, Demonstrated on an Unshrouded Transonic Turbine Casing. In *Proceedings of the ASME Turbo Expo*, volume 5B, 2015b. GT2015-43346.

Crawford, M. E. and Kays, W. M. STAN5: A Program for Numerical Computation of Two-Dimensional Internal and External Boundary Layer Flows. Technical Report CR-2742, NASA, 1976.

CS-E. Certification Specification for Engines. Technical report, European Aviation Safety Agency, 2010.

Doorly, J. E. and Oldfield, M. L. G. New Heat Transfer Gages for use on Multilayered Substrates. *Journal of Turbomachinery*, 108(1):153–160, 1986.

Doorly, J. E. and Oldfield, M. L. G. The Theory of Advanced Multi-Layer Thin Film Heat Transfer Gauges. *International Journal of Heat and Mass Transfer*, 30(6):1159–1168, 1987.

Dunn, M. G. Heat-Flux Measurements and Analysis for a Rotating Turbine Stage. In *AGARD Heat Transfer and Cooling in Gas Turbines*, 1985.

Dunn, M. G. Heat-Flux Measurements for the Rotor of a Full-Stage Turbine: Part I – Time-Averaged Results. *Journal of Turbomachinery*, 108(1):90–97, 1986.

Dunn, M. G. and Stoddard, F. J. Application of Shock-Tube Technology to the Measurement of Heat-Transfer Rate to Gas Turbine Components. In *Shock Tube and Shock Wave Research: Proceedings of the 11th International Symposium on Shock Tubes and Waves*, 1977.

DuPont™. Pyralux® AP Flexible Circuit Materials. Technical Data Sheet, 2012.

Epstein, A. H. and Guenette, G. R. The MIT Blowdown Turbine Facility. In *Proceedings of the ASME Turbo Expo*, volume 4, 1984. 84-GT-116.

Epstein, A. H., Guenette, G. R., Norton, R. J. G., and Yuzhang, C. High-Frequency Response Heat-Flux Gauge. *Review of Scientific Instruments*, 57(4):639–649, 1986.

Fowler, A. *A New Advanced Turbine-Stage Test Facility.* DPhil thesis, 1994.

Goodisman, M. I. *Turbine Turbobrake Systems.* DPhil thesis, 1991.

Goodisman, M. I., Oldfield, M. L. G., Kingcombe, R. C., Jones, T. V., Ainsworth, R. W., and Brooks, A. J. An Axial Turbobrake. *Journal of Turbomachinery*, 114(2):419–425, 1992.

Green, D. W. and Perry, R. H. *Perry's Chemical Engineers' Handbook.* McGraw-Hill, 8th edition, 2007. ISBN 978-0-071-42294-9.

Grote, K.-H. and Feldhusen, J., editors. *Dubbel – Taschenbuch für den Maschinenbau.* Springer, 22nd edition, 2007. ISBN 978-3-540-68191-5.

Gunther, C. K. Cast Aluminum Primary Aircraft Structure. In *Boeing Miliary Airplane Development.* Boeing Aerospace Company, 1979.

Guo, S. M., Spencer, M. C., Lock, G. D., Jones, T. V., and Harvey, N. W. The Application of Thin Film Gauges on Flexible Plastic Substrates to the Gas Turbine Situation. In *Proceedings of the ASME Turbo Expo*, volume 4, 1995. 95-GT-357.

Guo, S. M., Lai, C. C., Jones, T. V., Oldfield, M. L. G., Lock, G. D., and Rawlinson, A. J. The Application of Thin-Film Technology to Measure Turbine-Vane Heat Transfer and Effectiveness in a Film-Cooled, Engine-Simulated Environment. *International Journal of Heat and Fluid Flow*, 19(6):594–600, 1998.

Haldeman, C. W., Dunn, M. G., MacArthur, C. D., and Murawski, C. G. The USAF Advanced Turbine Aerothermal Research Rig (ATARR). In *AGARD Conference Proceeding No. 319*, 1992.

Hall, B. F., Chana, K. S., and Povey, T. Design of a Nonreacting Combustor Simulator with Swirl and Temperature Distortion with Experimental Validation. *Journal of Engineering for Gas Turbines and Power*, 136(8):081501, 2014.

Haller, B. R. and Hilditch, M. A. External Heat Transfer on a Shrouded HP Gas Turbine Stage. In *Proceedings of the ASME Turbo Expo*, volume 4, 2007. GT2007-27168.

Han, J.-C., Dutta, S., and Ekkad, S. V. *Gas Turbine Heat Transfer and Cooling Technology*. Taylor & Francis, 2nd edition, 2012. ISBN 978-1-439-85568-3.

Hilditch, M. A., Fowler, A., Jones, T. V., Chana, K. S., Oldfield, M. L. G., Ainsworth, R. W., Hogg, S. I., Anderson, S. J., and Smith, G. C. Installation of a turbine stage in the Pyestock Isentropic Light Piston Facility. In *Proceedings of the ASME Turbo Expo*, volume 4, 1994. 94-GT-277.

Hilditch, M. A., Chana, K. S., and Anderson, S. J. A Summary of Phase II Measurements: Cooled NGV and Uncooled Rotor from the MT1 Single Stage High Pressure Turbine in the DRA Pyestock Isentropic Light Piston Facility. *IMT Area 3 Turbine Project (AER2-CT92-0044)*, 1996.

Howatson, A. M., Lund, P. G., and Todd, J. D. Engineering Tables and Data. University of Oxford, 2009.

Jones, T. V. The Thin Film Heat Transfer Gauge – A History and New Developments. In *Proceedings of the 4th National UK Heat Transfer Conference*, 1995. C510/150/95.

Jones, T. V. Preheated model using thin film gauges. Private communication (attached), 2013.

Jones, T. V. and Schultz, D. L. Film Cooling in Subsonic and Supersonic Flows Using a Shock Tunnel. In *Shock Tube and Shock Wave Research: Proceedings of the 8th International Symposium on Shock Tubes and Waves*, 1971.

Jones, T. V. and Telisinghe, J. Approximate Analysis of Thermal Boundary Conditions in Film Cooling. Unpublished, 2010.

Jones, T. V., Schultz, D. L., and Hendley, A. D. *On the Flow in an Isentropic Light Piston Tunnel*. Reports and Memoranda. Aeronautical Research Council (Great Britain), 1973.

Kahveci, H. S., Haldeman, C. W., Mathison, R. M., and Dunn, M. G. Heat Transfer for the Film-Cooled Vane of a 1-1/2 Stage High-Pressure Transonic Turbine – Part I: Experimental Configuration and Data Review with Inlet Temperature Profile Effects. *Journal of Turbomachinery*, 135(2):021027, 2013.

Kays, W. M., Crawford, M. E., and Weigand, B. *Convective Heat and Mass Transfer*. McGraw-Hill Higher Education, 4th edition, 2005. ISBN 978-0-072-46876-2.

Lakshminarayana, B. *Fluid Dynamics and Heat Transfer of Turbomachinery*. John Wiley & Sons, 1996. ISBN 978-0-471-85546-0.

Lam, C. G. and Bremhorst, K. K. A Modified Form of the k-ϵ Model for Predicting Wall Turbulence. *Journal of Fluids Engineering*, 103(3):456–460, 1981.

Lubbock, R. *Turbulent Velocity and Temperature Measurements in Gas Turbine Hot Sections*. DPhil thesis, 2014.

Lundbladh, A., von der Bank, R., Donnerhack, S., A., R., Stokes, M., Bourgois, S., Caballero, O., Soldevilla, N., Avellan, R., Forsman, S., Sturm, W., Versluis, J., Ornat, A., Mrugala, T., and Kraj, L. Turbines and Structures for Ultra-High Pressure Ratio Aero-Engines. In *Proceedings of the ASME Turbo Expo*, 2016. GT2016-57307.

Luque Martínez, S. G. *A Fully-Integrated Approach to Gas Turbine Cooling System Research*. DPhil thesis, 2011.

Mathison, R. M., Haldeman, C. W., and Dunn, M. G. Heat Transfer for the Blade of a Cooled Stage and One-Half High-Pressure Turbine – Part I: Influence of Cooling Variation. *Journal of Turbomachinery*, 134(3):031014, 2012.

Matthews, A., Chapman, C., White, A., Rawlinson, A., Povey, T., Chana, K. S., Beard, P. F., and Usandizaga, I. OTRF Cooled Turbine Design Report. Technical Report DNS177975, Rolls-Royce plc, 2012.

MIL-HDBK-5H. *Military Handbook: Metallic Materials and Elements for Aerospace Vehicle Structures*. US Department of Defense, 1998.

Moffat, R. J. What's new in convective heat transfer? *International Journal of Heat and Fluid Flow*, 19(2):90–101, 1998.

Ng, W. F. and Epstein, A. H. High-Frequency Temperature and Pressure Probe for Unsteady Compressible Flows. *Review of Scientific Instruments*, 54(12):1678–1683, 1983.

O'Brien, J. A Technique for Measurement of Instantaneous Heat Transfer in Steady-Flow Ambient-Temperature Facilities. *Experimental Thermal and Fluid Science*, 3(4):416–430, 1990.

Oldfield, M. L. G. Impulse Response Processing of Transient Heat Transfer Gauge Signals. *Journal of Turbomachinery*, 130(2):021023, 2008.

Oldfield, M. L. G. Guide to Impulse Response Heat Transfer Signal Processing Version 6.1. Technical Report 2233/2000, OUEL, 2012.

Oldfield, M. L. G. and Beard, P. F. HTA3 Heat Transfer Amplifier 3 Version 1.5, 2014.

Oldfield, M. L. G. and Guo, S. M. Aero-thermal Properties of Foreign Gas (SF_6/Ar) and Air: Recommended Formulae from 160-1000 K. Technical Report 2141/1997, OUEL, 1997.

Oldfield, M. L. G., Jones, T. V., and Schultz, D. L. On-Line Computer for Transient Turbine Cascade Instrumentation. *IEEE Transactions on Aerospace and Electronic Systems*, 14(5): 738–749, 1978.

Oldfield, M. L. G., Burd, H. J., and Doe, N. G. Design of Wide-Bandwith Analogue Circuits for Heat Transfer Instrumentation in Transient Tunnels. In *Heat and Mass Transfer in Rotating Machinery*, pages 233–258, 1984.

Passaro, A., LaGraff, J. E., Oldfield, M. L. G., Biagioni, L., Moss, R. W., and Battelle, R. J. Measurement of Turbulent Pressure and Temperature Fluctuations in a Gas Turbine Combustor. Technical Report 20030106574, NASA, 2003.

Piccini, E., Guo, S. M., and Jones, T. V. The Development of a New Direct-Heat-Flux Gauge for Heat-Transfer Facilities. *Measurement Science and Technology*, 11(4):342, 2000.

Pinilla, V. V., Solano, J. P., Paniagua, G. G., and Anthony, R. J. Adiabatic Wall Temperature Evaluation in a High Speed Turbine. *Journal of Heat Transfer*, 134(9):091601, 2012.

Povey, T. *On Advances in Annular Cascade Techniques*. DPhil thesis, 2003.

Povey, T. and Qureshi, M. I. Developments in Hot-Streak Simulators for Turbine Testing. *Journal of Turbomachinery*, 131(3):031009, 2009.

Qureshi, M. I. *Effects of Engine-Realistic Temperature Profile and Swirl on HP Turbine Heat Transfer and Aerodynamics*. DPhil thesis, 2010.

Qureshi, M. I. and Povey, T. A Combustor-Representative Swirl Simulator for a Transonic Turbine Research Facility. *Proceedings of the Institution of Mechanical Engineers*, 2011. 0954410011400817.

Qureshi, M. I., Beretta, A., Chana, K. S., and Povey, T. Effect of Aggressive Inlet Swirl on Heat Transfer and Aerodynamics in an Unshrouded Transonic HP Turbine. *Journal of Turbomachinery*, 134(6):061023, 2012.

Ralph, C. Development of a New Total Temperature Probe for Transient Turbomachinery Testing. Master thesis, University of Oxford, 2000.

Ron, E. *Entropy Noise*. DPhil thesis, 2015.

Rowbury, D. *Discharge Coefficients of Nozzle Guide Vane Film Cooling Holes*. DPhil thesis, 1998.

RR Stress Criteria. Preliminary Firtree Root Assessment, Criteria and Defintions. Rolls-Royce plc internal document, 2011.

SAE. Aerospace Material Specification. AMS2175 Standard, 2010.

Saravanamuttoo, H. I. H., Rogers, G. F. C., Cohen, H., and Straznicky, P. V. *Gas Turbine Theory*. Pearson Education, 6th edition, 2009. ISBN 978-0-132-22437-6.

sc03 Manual. *sc03 User's Guide*. Rolls-Royce plc, 1999.

Schultz, D. L. and Jones, T. V. Heat-Transfer Measurements in Short-Duration Hypersonic Facilities. *AGARDograph*, 165, 1973.

Schultz, D. L., Jones, T. V., Oldfield, M. L. G., and Daniels, L. C. A New Transient Facility for the Measurement of Heat Transfer Rate. In *AGARD Conference Proceeding No. 229*, 1977.

Sieverding, C. H. and Arts, T. The VKI Compression Tube Annular Cascade Facility CT3. In *Proceedings of the ASME Turbo Expo*, 1992. 92-GT-336.

Solano, J. P. and Paniagua, G. G. Novel Two-Dimensional Transient Heat Conduction Calculation in a Cooled Rotor: Ventilation Preheating – Blow-Down Flux. *Journal of Heat Transfer*, 131 (8):081601, 2009.

Thorpe, S. J., Yoshino, S., Ainsworth, R. W., and Harvey, N. W. Improved Fast-Response Heat Transfer Instrumentation for Short-Duration Wind Tunnels. *Measurement Science and Technology*, 15(9):1897, 2004a.

Thorpe, S. J., Yoshino, S., Ainsworth, R. W., and Harvey, N. W. An Investigation of the Heat Transfer and Static Pressure on the Over-Tip Casing Wall of an Axial Turbine Operating at Engine Representative Flow Conditions. (I). Time-Mean Results. *International Journal of Heat and Fluid Flow*, 25(6):933–944, 2004b.

Thorpe, S. J., Yoshino, S., Ainsworth, R. W., and Harvey, N. W. An Investigation of the Heat Transfer and Static Pressure on the Over-Tip Casing Wall of an Axial Turbine Operating at Engine Representative Flow Conditions. (II). Time-Resolved Results. *International Journal of Heat and Fluid Flow*, 25(6):945–960, 2004c.

Tritech. EPIC Advances. Tritech Group Internal Document, 2011.

Vidal, R. J. *Model Instrumentation Techniques for Heat Transfer and Force Measurements in a Hypersonic Shock Tunnel*. Cornell Aeronautical Laboratory, 1956.

Jones, T. V. Preheated model using thin film gauges. Private communication, 2013.

The problem is considered in two parts

(1) The uniform heating of the test surface prior to the run. Any surface temperature state could be chosen and the heat transfer coefficient defined for similar temperature distributions. However, a uniform surface temperature is perhaps not too far from the engine state.

The heating in this case is produced by an array of heat transfer gauges used as heaters or by dedicated heaters of the same size,

i.e.

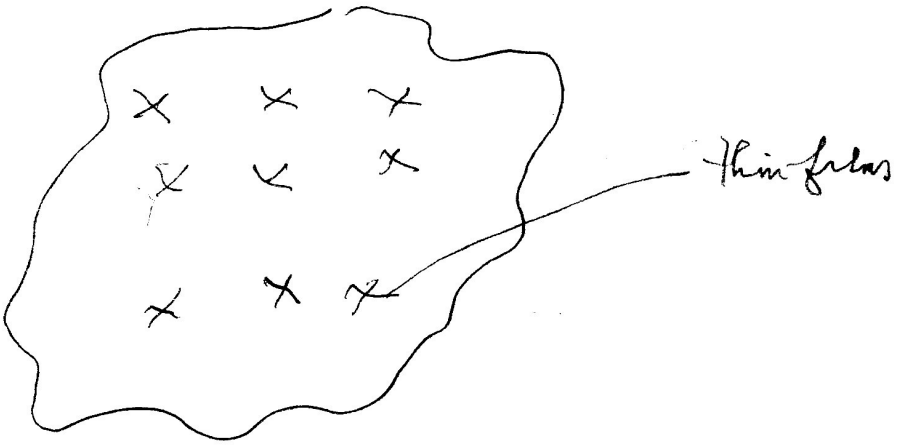

Of course the surface temperature will peak at the heaters (thin films) but this temperature rise is small compared to the difference between gas and surface

i.e

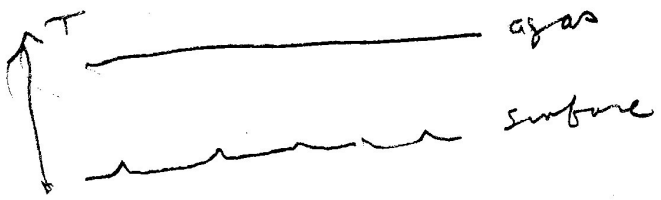

The above is the steady state with individual films currents being adjusted to give the uniform surface temperature.

Assessment needs to be made as to the size of the temperature non uniformity.

i.e.

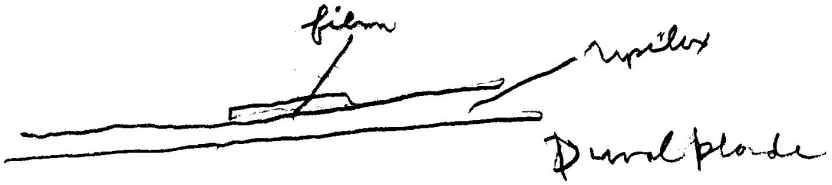

Before the run the model is in equilibrium i.e. The electrical power in equals the heat-conducted and convected from the model The electrical power remains constant The conduction field should remain nearly constant and the change is in the convective surface heat flux from the pre-run value to the run value.

The surface temperature is being measured by the thin film gauges. So long as the surface variation of the convective heat flux is not too high then the

local heat-flux can be found by conventional 1D conduction analysis i.e. Using our standard techniques. Thus the measured heat transfer is equal to the surface heat-flux minus the pre-run heat-flux. The latter has to be evaluated therefore. It may be that this quantity is small and may be ignored. Nevertheless the pre-run convective heat transfer can be determined and in fact was done routinely on the small piston tunnel 20 years back when pre-heating was effected by passing hot gas over the test surface.

Note

As shown in Jim O'Brien's paper and in my analysis in this paper the use of a thin film gauge with a large current to heat the surface is valid for a single gauge. However the surface temperature in the steady state will be far from uniform. The method proposed here uses many gauges to achieve this and the surface temperature is the result of the sum of all the heating elements